

**PROBING STRUCTURE FUNCTION RELATIONSHIPS IN NOVEL
SILICON CONTAINING MACROMOLECULES WITH
NONLINEAR OPTICAL AND ULTRA-FAST SPECTROSCOPY**

by

Jin Zhang

**A dissertation submitted in partial fulfillment
of the requirements for the degree of
Doctor of Philosophy
(Macromolecular Science and Engineering)
in The University of Michigan
2014**

Doctoral Committee:

**Professor Theodore G. Goodson III, Chair
Professor Jinsang Kim
Professor Richard M. Laine
Professor Ayyalusamy Ramamoorthy**

© Jin Zhang 2014

All Rights Reserved

DEDICATION

This dissertation is dedicated to all my loved ones:
my son, my parents and my husband.
You make my life so beautiful, so meaningful, so enjoyable, and so complete.

ACKNOWLEDGEMENTS

I would like to express the deepest appreciation to my committee chair, Professor Theodore Goodson III, who led me to the field of ultrafast spectroscopy meanwhile encouraged me and continually inspired me with his attitude, wisdom, encourage and enthusiasm. Without his supervision and constant help this dissertation would not have been possible.

I am also grateful to the members on my dissertation committee Professor Jinsang Kim, Professor Richard M. Laine and Professor Ayyalusamy Ramamoorthy, whose valuable expertise, excellent insights and passionate exploration in this field deeply influenced me.

In addition, a thank you to Professor to Professor Richard M. Laine and Dr. Santy Sulaiman, who provided me with the opportunity to apply my skills and knowledge on their samples. Three of our articles are included in Chapter 3, where were originally published in Chemistry of Materials, Journal of the American Chemical Society and Journal of Materials Chemistry, respectively. I am also thankful to Dr. Weiming Wang and Professor Jamie D. Phillips from EECS department, and Professor Peter Bauerle from The University of Ulm for making and sharing materials that made this work possible.

I would also like to thank all Professor Goodson's group members past and present, who have been consistently providing help and making the lab a pleasant place to work. In particular, I would like to thank Professor Ramakrishna Guda, Dr. Oleg Varnavski, who had been constantly helping, training and guiding me with various laser tools and experimental procedures.

Special thanks go to Nonna Hamilton who giving herself fully to macro students and taking such a good care of all her students, and Linda VanBlaircum who continuously providing help and making my working environment extremely pleasant.

Last, but never least, I would like to express my greatest gratitude to my family. To my little boy Alex, who missed out a lot time with Mommy while I am writing this dissertation. To my husband Yin, who inspired me, supported me and encouraged me during the entire process. To my parents and in laws, who took care of little Alex while I am not able to. I thank you all for your patience, love and support.

TABLE OF CONTENTS

DEDICATION.....	ii
ACKNOWLEDGEMENTS.....	iii
LIST OF FIGURES.....	viii
LIST OF TABLES.....	xiv
LIST OF APPENDICES.....	xvi
ABSTRACT.....	xvii
CHAPTER 1 INTRODUCTION AND BACKGROUND.....	1
1.1 MOTIVATION AND BACKGROUND.....	1
1.2 PHOTOVOLTAIC TECHNIQUES.....	4
1.2.1. <i>Basic Physical Principles</i>	4
1.2.2. <i>Organic Photovoltaic Materials</i>	11
1.3 TWO-PHOTON ABSORPTION.....	18
1.3.1. <i>The Main Concepts of Two-Photon Absorption</i>	18
1.3.2. <i>Theoretical Consideration</i>	25
1.4 SILSESQUIOXANES.....	29
1.5 ORGANIZATION OF THESIS.....	38
REFERENCES.....	39
CHAPTER 2 EXPERIMENTAL TECHNIQUES.....	62
2.1 OVERVIEW.....	62
2.2 OPTICAL ABSORPTION AND EMISSION MEASUREMENT.....	62
2.3 FLUORESCENCE QUANTUM YIELD MEASUREMENT.....	65
2.4 TWO-PHOTON EXCITED FLUORESCENCE METHOD.....	66
2.5 FLUORESCENCE UP-CONVERSION.....	71
2.6 ULTRAFAST TRANSIENT ABSORPTION SPECTROSCOPY.....	75
2.7 TWO PHOTON NONLINEAR TRANSMISSION.....	78
REFERENCES.....	80

CHAPTER 3 BASIC CHARACTERIZATIONS AND TWO-PHOTON ABSORPTION OF T₈ SILSESQUIOXANES	82
3.1 OVERVIEW.....	83
3.2 OCTAVINYLSILBENESILSESQUIOXANE DERIVATIVES (GEN2 T ₈).....	84
3.2.1. <i>Basic Characterization</i>	86
3.2.2. <i>Steady-State Measurements</i>	88
3.2.3. <i>Two-Photon Cross-Section Measurements</i>	91
3.3 POLYFUNCTIONAL PHENYLSILSESQUIOXANES: [O-RPHSiO _{1.5}] ₈ , [2,5- R ₂ PHSiO _{1.5}] ₈ AND [R ₃ PHSiO _{1.5}] ₈	93
3.3.1. <i>Basic Characterization</i>	94
3.3.2. <i>Steady-State Measurements</i>	95
3.3.3. <i>Two-Photon Cross-Section Measurements</i>	103
3.4 SUMMARY	106
REFERENCES	107
CHAPTER 4 ULTRAFAST FLUORESCENCE DYNAMICS AND EXCITED STATE CHARGE TRANSFER PROCESS OF FUNCTIONALIZED SILSESQUIOXANES INVESTIGATED BY TIME-RESOLVED ABSORPTION AND EMISSION SPECTROSCOPY	111
4.1 INTRODUCTION.....	112
4.2 RESULTS AND DISCUSSION	115
4.2.1. <i>Steady-State Measurements</i>	115
4.2.2. <i>Two-Photon Cross-Section Measurements</i>	118
4.2.3. <i>Fluorescence Up-Conversion Measurements</i>	122
4.2.4. <i>Ultrafast Transient Absorption Measurements</i>	131
4.3 CONCLUSION.....	142
REFERENCES	143
CHAPTER 5 OTHER PHOTOVOLTAIC MATERIALS: ENERGY MIGRATION IN DENDRITIC OLIGOTHIOPHENE-PERYLENE BISIMIDES	154
5.1 INTRODUCTION.....	155
5.2 RESULTS AND DISCUSSION	158
5.2.1. <i>Steady State Photophysical Properties</i>	159
5.2.2. <i>Two-Photon Cross-Section Measurements</i>	162
5.2.3. <i>Fluorescence Up-Conversion Measurements</i>	164
5.2.4. <i>Transient Absorption Measurements</i>	174
5.3 CONCLUSION.....	182
REFERENCES	182
CHAPTER 6 OTHER PHOTOVOLTAIC MATERIALS: Z_nT_eO THIN FILMS – TWO PHOTON MEASUREMENTS USING NONLINEAR TRANSMISSION METHODS	193
6.1 INTRODUCTION.....	193
6.2 OPTICAL PROPERTIES OF ZNTEO	198
6.3 TWO PHOTON TRANSMISSION MEASUREMENT	200
6.4 SUMMARY	203
REFERENCES	204

CHAPTER 7 OVERALL SUMMARY AND FUTURE DIRECTION	209
7.1 OVERALL SUMMARY	209
7.2 FUTURE DIRECTION	213
REFERENCES	217
APPENDICES	219

LIST OF FIGURES

FIGURE 1.1 ENERGY CONSUMPTION, 2011 ⁵	2
FIGURE 1.2 ENERGY CONSUMPTION PREDICTION TO 2025 ⁵	3
FIGURE 1.3 FLEXIBLE ORGANIC SOLAR CELL ¹⁶	4
FIGURE 1.4 AMERICAN SOCIETY FOR TESTING AND MATERIALS (ASTM) TERRESTRIAL REFERENCE SPECTRA FOR PHOTOVOLTAIC PERFORMANCE EVALUATION ¹⁸	5
FIGURE 1.5 EQUIVALENT CIRCUIT FOR A SOLAR CELL ¹⁷	7
FIGURE 1.6 CURRENT DENSITY–VOLTAGE (J–V) CHARACTERISTICS FOR A GENERIC PHOTOVOLTAIC DEVICES ²¹	8
FIGURE 1.7 ENERGY BAND DIAGRAM ILLUSTRATING THE FIVE CONSECUTIVE STEPS AND HOMO /LUMO LEVELS IN A HYBRID SOLAR CELL ²⁵	10
FIGURE 1.8 SCHEMATIC DIAGRAM OF BI-LAYER AND BULK HETEROJUNCTION STRUCTURE PHOTOACTIVE LAYERS ²⁵	10
FIGURE 1.9 ORGANIC SEMICONDUCTOR MATERIALS IN ORGANIC SOLAR CELLS ⁴⁷	14
FIGURE 1.10 STRUCTURE OF POLYTHIOPHENE AND SUBSTITUTED DERIVATES OF POLYTHIOPHENE IN HH, HT AND TT COUPLINGS ⁷⁸	15
FIGURE 1.11 BAND STRUCTURE DIAGRAM ILLUSTRATING THE HOMO AND LUMO ENERGIES OF P3HT, MDMO-PPV AND AN IDEAL DONOR WITH RESPECT TO THE BAND STRUCTURE OF PCBM ³⁶	16
FIGURE 1.12 CHARGE PHOTOGENERATION DIAGRAM IN POLYTHIOPHENE:PCBM BLEND FILMS ¹¹⁸	18
FIGURE 1.13 SCHEMATIC REPRESENTATION OF SIMULTANEOUS TPA PROCESS	19
FIGURE 1.14 OUTPUT INTENSITY WITH RESPECT TO INPUT EXCITATION INTENSITY IN ONE-PHOTON AND TWO-PHOTON PROCESS	20

FIGURE 1.15 DEMONSTRATION OF ONE-PHOTON EXCITATION PROCESS (LEFT) AND TWO-PHOTON PROCESS (RIGHT) ¹⁴⁴	21
FIGURE 1.16 SEM IMAGES OF WOODPILE-TYPE PHOTONIC CRYSTAL (PC) STRUCTURES FABRICATED WITH 520 NM EXCITATION AT (A) 0.60 MW AND AT (B) 0.45 MW USING THE 4,4'-BIS(DI-N-BUTYLAMINO)BIPHENYL(DABP)-TRIACRYLATE RESIN. ¹⁴⁵	22
FIGURE 1.17 DIFFERENT VIEW-ANGLE SEM IMAGES OF A MICRO-BULL SCULPTURE THAT WAS TWO-PHOTON PHOTOPOLYMERIZED WITH SUB-DIFFRACTION-LIMIT ACCURACY ^{140, 146}	23
FIGURE 1.18 IN VIVO TWO-PHOTON IMAGING IN THE INTACT NEOCORTEX. (A) DIFFERENT TYPES OF BRAIN ACCESS. (B) EXAMPLE OF DEEP TWO-PHOTON IMAGING IN MOUSE NEOCORTEX ¹⁴⁷	24
FIGURE 1.19 SCHEMATIC DIAGRAM OF TRANSITION DIPOLE MOMENT DIFFERENCE IN ONE-PHOTON ABSORPTION AND TWO-PHOTON ABSORPTION PROCESS	29
FIGURE 1.20 STRUCTURES OF SILSESQUIOXANES ¹⁷⁰	30
FIGURE 1.21 STRUCTURE EXAMPLE OF CUBIC T ₈ SQ	31
FIGURE 1.22 SINGLE-CRYSTAL STRUCTURE OF RECRYSTALLIZED [P-IC ₆ H ₄ SiO _{1.5}] ₈ ¹⁹⁷	32
FIGURE 1.23 EXPERIMENTAL PROCEDURE FOR SYNTHESIS OPS ²⁰⁸	33
FIGURE 1.24 SYNTHESIS OF OCTAVINYLSILSESQUIOXANE AND OCTA(STYRENYL)SILSESQUIOXANES DERIVATIVES ²¹¹	34
FIGURE 1.25 THE ABSORPTION OF THE T ₈ CAGE WITHOUT CHROMOPHORES. THE ABSORPTION BAND IS DUE TO EXCITATION OF AN ELECTRON FROM THE NON-BONDING N ORBITAL TO THE ANTBONDING Σ* ORBITAL ¹³²	35
FIGURE 1.26 STRUCTURE OF POSS ANCHORED POLY(2-METHYOXY-5-(2-ETHHEXYLOXY)-1,4-PHENEVINYLENE)	36
FIGURE 1.27 ISOSURFACES (DARK, POSITIVE; LIGHT, NEGATIVE VALUES) FOR HOMO AND LUMO STATES OF CUBIC SILSESQUIOXANES (HSiO _{1.5}) ₈ ²²⁹	37
FIGURE 1.28 HOMO AND LUMO STATES OF OCTASTILBENE-FUNCTIONALIZED OS, RESIDING ON THE STILBENE TETHERS ²²⁸	37
FIGURE 2.1 TYPES OF ELECTRONIC TRANSITIONS	63
FIGURE 2.2 ILLUSTRATION OF ABSORPTION AND FLUORESCENCE PROCESS USING JABLONSKI ENERGY DIAGAMS.....	64

FIGURE 2.3 OPTICAL DIAGRAM OF TWO-PHOTON SETUP I WITH KM LASER WITH WAVELENGTH RANGE FROM 770-830NM.....	67
FIGURE 2.4 OPTICAL DIAGRAM OF TWO-PHOTON SETUP II WITH SELECTIVE PATHWAYS INVOLVING MAI-TAI AND OPAL LASER. WAVELENGTH RANGE FROM 250 TO 2250NM CAN BE ACHIEVED BY SELECTING DIFFERENT OPTICAL PATHWAYS.....	68
FIGURE 2.5 THE OPAL CAVITY LAYOUT	68
FIGURE 2.6 PHOTO ILLUSTRATION OF (A) KAPTEYN MURNANE LASER, (B) SAMPLE HOLDER AND PMT, (C) MAI-TAI LASER AND (D) OPAL LASER	69
FIGURE 2.7 SCHEMATIC DIAGRAM OF FLUORESCENCE UPCONVERSION MECHANISM ⁴	72
FIGURE 2.8 OPTICAL DIAGRAM FOR TIME RESOLVE FLUORESCENCE UP-CONVERSION MEASUREMENTS	73
FIGURE 2.9 FEMTOSECOND FLUORESCENCE UPCONVERSION SET-UP UNDER OPERATION	74
FIGURE 2.10 BASIC PRINCIPLE OF TRANSIENT ABSORPTION SPECTROSCOPY	76
FIGURE 2.11 SCHEMATIC ILLUSTRATION OF THE TRANSIENT ABSORPTION PUMP-PROBE PROCESS ¹¹	76
FIGURE 2.12 OPTICAL DIAGRAM OF TRANSIENT ABSORPTION EXPERIMENTAL SETUP IN OUR LAB.....	78
FIGURE 2.13 SCHEMATIC DIAGRAM OF TWO-PHOTON TRANSMISSION MEASUREMENT SETUP	79
FIGURE 3.1 STRUCTURE EXAMPLES OF SILSESQUIOXANES WITH DIFFERENT CORE, SYMMETRY, CHROMOPHORES AND GENERATION	84
FIGURE 3.2 MOLECULAR STRUCTURE OF R-VINYLSILBENEOS.....	85
FIGURE 3.3 SYNTHESIS OF R-VINYLSILBENEOS.....	85
FIGURE 3.4 UV-VIS AND PL SPECTRA OF R' VINYLSTILBENEOS (A: R' = -H,-ME, AND -MEO; B: R' = -NH ₂) IN THF	87
FIGURE 3.5 UV-VIS AND PL SPECTRA OF HSTYRENYLOS AND HVINYLSILBENOS	88
FIGURE 3.6 STEADY STATE ABSORPTION SPECTRA OF SOVS, OSOVS AND NSOVS	89
FIGURE 3.7 STEADY STATE FLUORESCENCE EMISSION SPECTRA OF SOVS, OSOVS AND NSOVS.....	89
FIGURE 3.8 TWO PHOTON ABSORPTION CROSS-SECTION MEASUREMENT CALCULATION OF NSOVS, OSOVS AND SOVS.....	92
FIGURE 3.9 TWO-PHOTON ABSORPTION CROSS-SECTION SPECTRA FOR SOVS , OSOVS AND NSOVS.....	92

FIGURE 3.10 MOLECULAR STRUCTURES OF INVESTIGATED SYSTEMS: O-NBOCSTIL ₈ OS, NBOCSTIL ₁₆ OS, NBOCSTIL ₂₃ OS, O-ACESTIL ₈ OS, O-ACESTIL ₁₆ OS AND O-ACESTIL ₂₃ OS	93
FIGURE 3.11 ABSORPTION AND EMISSION SPECTRA FOR MESTYR _x OPS	96
FIGURE 3.12 ABSORPTION AND EMISSION SPECTRA FOR NBOCSTYR _x OPS.....	96
FIGURE 3.13 ABSORPTION AND EMISSION SPECTRA FOR ACESTYR _x OS.....	97
FIGURE 3.14 TWO POSSIBLE CONFIGURATIONS OF RSTILBENE ₂₄ OS CORNER	101
FIGURE 3.15 INTERACTIONS OF “FRAGMENTS” OF TRISTYRENYLPHENYL GROUPS ON EACH CORNER OF RSTYR ₂₄ OS.....	102
FIGURE 3.16 TPA CROSS-SECTION MEASUREMENTS OF O-NBOCSTIL ₈ OS, NBOCSTIL ₁₆ OS, NBOCSTIL ₂₃ OS, O-ACESTIL ₈ OS, O-ACESTIL ₁₆ OS AND O-ACESTIL ₂₃ OS	104
FIGURE 3.17 TPA CROSS SECTION MEASUREMENTS OF O-NBOCSTIL ₈ OS, NBOCSTIL ₁₆ OS, NBOCSTIL ₂₃ OS, O-ACESTIL ₈ OS, O-ACESTIL ₁₆ OS AND O-ACESTIL ₂₃ OS	105
FIGURE 4.1 MOLECULAR STRUCTURE OF INVESTIGATED CORNER, HALF AND CUBE SILSESQUIOXANE SYSTEMS.....	115
FIGURE 4.2 STEADY STATE ABSORPTION SPECTRUM OF CORNER, HALF AND CUBE.....	116
FIGURE 4.3 STEADY STATE FLUORESCENCE EMISSION SPECTRA OF CORNER, HALF AND CUBE	117
FIGURE 4.4 TWO-PHOTON CROSS SECTION MEASUREMENTS OF CORNER, HALF AND CUBE	119
FIGURE 4.5 TWO-PHOTON ABSORPTION CROSS-SECTION SPECTRA FOR THE INVESTIGATED CHROMOPHORES.	119
FIGURE 4.6 (A) FLUORESCENCE DECAY, (B)FLUORESCENCE RISE TIME,(C)FLUORESCENCE ANISOTROPY FOR THE INVESTIGATED SYSTEMS.....	126
FIGURE 4.7 SCHEMATIC ILLUSTRATION OF TWISTED SINGLE-BOND (T*) AND TWISTED DOUBLE-BOND (P*) CONFORMATION OF CORNER. STARTING FROM A FULLY PLANAR GEOMETRY, THE T* AND P* GEOMETRIES WERE DRIVED BY TWISTING BY 90° AROUND THE RESPECTIVE SINGLE OR DOUBLE BOND.	127
FIGURE 4.8 THREE-STATE KINETIC SCHEME PROPOSED FOR THE INTERPRETATION OF THE PHOTOPHYSICAL BEHAVIOR OF DONOR-ACCEPTOR SUBSTITUTED STILBENES.....	127
FIGURE 4.9 PHOTOISOMERIZATION PROCESSE IN SILBENE AND CORNER SYSTEM.....	128

FIGURE 4.10 FEMTOSECOND TRANSIENT ABSORPTION SPECTRA OF CORNER SAMPLE (A) AT TIME DELAYS BEFORE 1.2PS AND (B) AT TIME DELAYS BETWEEN 1.2PS TO 350PS	133
FIGURE 4.11 FEMTOSECOND TRANSIENT ABSORPTION SPECTRA OF HALF SAMPLE (A) AT TIME DELAYS BEFORE 0.5PS AND (B) AT TIME DELAYS BETWEEN 0.5PS TO 340PS	133
FIGURE 4.12 FEMTOSECOND TRANSIENT ABSORPTION SPECTRA OF CUBE SAMPLE (A) AT TIME DELAYS BEFORE 0.3PS AND (B) AT TIME DELAYS BETWEEN 0.3PS TO 250PS	134
FIGURE 4.13 TRANSIENT ABSORPTION KINETICS OF CORNER, HALF AND CUBE AND MODEL COMPOUND CF ₃ STILBENENH ₂	135
FIGURE 4.14 TRANSIENT ABSORPTION KINETICS OF CORNER AT 467 NM, HALF AT 470 NM AND CUBE AT 467 NM.	136
FIGURE 4.15 FEMTOSECOND TRANSIENT ABSORPTION SPECTRUM OF CUBE IN DMSO.....	139
FIGURE 4.16 SIMPLIFIED SCHEMATIC ENERGY DIAGRAM OF INVESTIGATED SYSTEMS	142
FIGURE 5.1 MOLECULAR STRUCTURE OF INVESTIGATED THIOPHENE DENDRIMER FUNCTIONALIZED PERYLENE IMIDES (PDI-G0, PDI-G1 AND PDI-G2)	158
FIGURE 5.2 (A)NORMALIZED OPTICAL ABSORPTION AND EXTINCTION COEFFICIENT AND (B) NORMALIZED STEADY-STATE FLUORESCENCE SPECTRA OF THE INVESTIGATED DERIVATIVES OF G0, G1 AND G2 ..	160
FIGURE 5.3 THE TWO-PHOTON ABSORPTION CROSS SECTION FOR THIOPHENE DENDRIMER FUNCTIONALIZED PERYLENE BISIMIDES.....	163
FIGURE 5.4 (A)G0 ,(B)G1 AND (C)G2 FLUORESCENCE OF DIFFERENT TIME SCALE WITH AN EXCITATION AT 420NM, AND (D)FLUORESCENCE ANISOTROPY FOR G0, G1 AND G2	167
FIGURE 5.5 (A) PLANAR SHAPE AREAS MARKED IN G2, (B) ILLUSTRATION THE ANGLE BETWEEN THE PDI AND DOT AND (C) ILLUSTRATION OF THE TWISTING OF THE PDI.....	168
FIGURE 5.6 (A)G0, (B)G1 AND (C)G2 FLUORESCENCE OF DIFFERENT TIME SCALE WITH AN EXCITATION OF 266NM AND (D) FLUORESCENCE ANISOTROPY FOR G0, G1 AND G2	171
FIGURE 5.7 (A) FLUORESCENCE INTENSITY OF G2 AND (B) ANISOTROPY OF G2 AT EXCITATION OF 377NM	173
FIGURE 5.8 ILLUSTRATION OF ENERGY TRANSFER PROCESS IN G2.....	174
FIGURE 5.9 (A)TRANSIENT ABSORPTION SPECTRA AND 3-D SPECTRUM (INSERTED) OF COMPOUNDS G0 WITH AN EXCITATION OF 550NM. (B)TRANSIENT ABSORPTION KINETICS OF G0 AT 714NM.	176

FIGURE 5.10 (A) TRANSIENT ABSORPTION SPECTRA AND 3-D SPECTRUM (INSERTED) OF COMPOUNDS G1 WITH AN EXCITATION OF 550NM. (B) TRANSIENT ABSORPTION KINETICS OF G1 AT 710NM.	177
FIGURE 5.11 (A), (B) AND (C) TRANSIENT ABSORPTION SPECTRA OF G2 OF AT DIFFERENT TIME. INSERTED IN (A) 3-D SPECTRUM OF COMPOUNDS G2 WITH AN EXCITATION OF 550NM. (D) TRANSIENT ABSORPTION KINETICS OF G2 AT 704NM.	178
FIGURE 6.1 SCHEMATIC OF OPTICAL TRANSITIONS IN INTERMEDIATE BAND SOLAR CELLS (CB: CONDUCTION BAND; IB: INTERMEDIATE BAND; VB: VALENCE BAND) ³	194
FIGURE 6.2 NON-OVERLAPPING BAND CONDITION: (A) OPTIMAL CONDITION, (B) SPATIAL SEPARATION CONDITION ²⁰	195
FIGURE 6.3 SCHEMATICS OF POSSIBLE OXYGEN SITES IN ZNTE CRYSTAL ³⁶	197
FIGURE 6.4 ABSORPTION COEFFICIENTS OF ZNTE AND ZNTEO ⁴⁴	198
FIGURE 6.5 PHOTOLUMINESCENCE SPECTRA OF ZNTE AND ZNTEO	199
FIGURE 6.6 PHOTOLUMINESCENCE SPECTRA OF ZNTEO AND ZNTE (LOG SCALE) ^{19, 44}	199
FIGURE 6.7 SCHEMATIC DIAGRAM OF TWO PHOTON EXCITATION OF ZNTEO	200
FIGURE 6.8 SCHEMATIC DRAWING OF REFLECTION AND TRANSMISSION PARAMETERS OF TWO-LAYER ZNTEO	200
FIGURE 6.9 PLOT OF ZNTEO SAMPLE : INPUT POWER I_0 VERSES $1/T$	203
FIGURE 7.1 PROPOSED SUBSTITUTED CHROMOPHORES	215
FIGURE 7.2 A MODEL OF THE 2-D CRYSTALLIZATION OF THE POSS MACROMERS ³	216
FIGURE 7.3 SCHEMATIC DRAWINGS OF (A) SILSESQUIOXANE WITH π -STACKING CHROMOPHORES (B) SILSESQUIOXANE POLYMER	216

LIST OF TABLES

TABLE 3.1 CHARACTERIZATION DATA FOR R-VINYLSILBENEOS.	86
TABLE 3.2 SPECTRAL DATA OF R-STYRENYLOS AND R-VINYLSILBENEOS.	90
TABLE 3.3 SPECTRAL DATA OF R-STYRENYLOS AND R-VINYLSILBENEOS AS A FUNCTION OF SOLVENT AND TWO PHOTON CROSS-SECTIONS OF SELECTED COMPOUNDS	90
TABLE 3.4 MOLECULAR SPECIES PRESENT IN MESTYR _x OPS	94
TABLE 3.5 MOLECULAR SPECIES PRESENT IN NH ₂ STYR _x OPS.....	95
TABLE 3.6 MOLECULAR SPECIES PRESENT IN ACESTYR _x OPS	95
TABLE 3.7 PHOTOPHYSICAL DATA FOR RSTYR _x OPS (THF, CH ₂ CL ₂ PEAK POSITIONS ARE IDENTICAL.....	97
TABLE 3.8 TPA PROPERTIES OF OF O-NBOCSTIL ₈ OS, NBOCSTIL ₁₆ OS, NBOCSTIL ₂₃ OS, O-ACESTIL ₈ OS, O- ACESTIL ₁₆ OS AND O-ACESTIL ₂₃ OS.....	106
TABLE 4.1 STEADY-STATE PROPERTIES OF SILSESQUIOXANE DERIVATIVES IN THF.....	117
TABLE 4.2 SUMMARY OF TWO-PHOTON CROSS-SECTION OF SILSESQUIOXANE DERIVATIVES	120
TABLE 4.3. FLUORESCENCE LIFETIMES OF CORNER, HALF AND CUBE SQ SYSTEMS.....	123
TABLE 4.4. RADIATIVE AND NONRADIATIVE DECAY RATE CONSTANTS FOR CORNER, HALF AND CUBE IN THF	123
TABLE 4.5 TRANSIENT ABSORPTION KINETICS LIFETIME AT 550 NM	135
TABLE 4.6 TRANSIENT ABSORPTION KINETICS LIFETIME COMPONENTS AT PROBE WAVELENGTH 467 NM	140
TABLE 4.7 DETAILS OF THE TIME DEPENDENT DYNAMIC ESA BLUE SHIFT ESA BAND IN 470 TO 650 NM REGION. ESA MAXIMA OF CORNER, HALF AND CUBE AT DIFFERENT DELAY TIME	141

TABLE 5.1 STEADY-STATE PROPERTIES OF INVESTIGATED DENDRIMER FUNCTIONALIZED PERYLENE BISIMIDES.	161
TABLE 5.2 TPA PROPERTIES OF SILSESQUIOXANE DERIVATIVES	163
TABLE 5.3 FLUORESCENCE LIFETIME OF G0, G1 AND G2 AT DIFFERENT EXCITATION WAVELENGTHS	164
TABLE 5.4 SUMMARY OF TRANSIENT LIFETIMES OF G0, G1 AND G2	181
TABLE 6.1 BASIC CHARACTERISTICS OF SINGLE CRYSTAL ZNTE ^{27, 36}	196

LIST OF APPENDICES

APPENDIX I: MAITAI LASER CLEANING PROCEDURE	219
APPENDIX II: RESET MAITAI PZTs POSITION	220
APPENDIX III: OPERATION PROCEDURE OF FEMTOSECOND SYNCHRONOUSLY PUMPED OPTICAL PARAMETERIC OSCILLATOR (OPAL)	222
APPENDIX IV: OPAL ALIGNMENT PROCEDURE.....	224

ABSTRACT

PROBING STRUCTURE FUNCTION RELATIONSHIPS IN NOVEL SILICON CONTAINING MACROMOLECULES WITH NONLINEAR OPTICAL AND ULTRA-FAST SPECTROSCOPY

by

Jin Zhang

Chair: Theodore G. Goodson III

Organic photovoltaics (OPVs) as a relatively novel technology have drawn significant attentions to many scientists during the past few years because of their potential low mass production costs, simple fabrication processes, mechanical flexibility, and light weight. Countless efforts have been devoted to overcoming technological and material barriers for high power conversion efficiencies. Understanding the photophysical properties and energy transfer processes of the potential candidates as well as the mechanisms of charge generation, recombination and transportation are crucial to improving overall OPV device efficiencies and guiding new research of designing novel OPV materials. In this dissertation, nonlinear optical and time resolved methods such as two-photon absorption, time-resolved transient absorption, and fluorescence emission are used to study the nature of charge transfer character, energy transfer processes and charge transfer mechanisms in OPV materials. Two groups of organic macromolecules were investigated:

1) Three sets of chromophore substituted silsesquioxane derivatives were investigated to determine structure function relationships on a molecule basis.

Exceptional red shift in emission and large two-photon cross-section found in $[\text{NH}_2\text{vinylStilbeneSiO}_{1.5}]_8$ suggest that charge transfer character could be dramatically enhanced by introducing strong electron donating group to the substituted chromophores. Both steady state photophysical and two-photon absorption study of polyfunctional phenylsilsesquioxanes ($[\text{o-RPhSiO}_{1.5}]_8$, $[\text{2,5-R}_2\text{PhSiO}_{1.5}]_8$ and $[\text{R}_3\text{PhSiO}_{1.5}]_8$) indicate that adding additional chromophores in a nanostructure could strengthen the electronic coupling among substituted chromophores and enhance charge transfer character of the entire molecule. Time resolved absorption and emission spectroscopy reveal the excited state dynamics of corner and half ($[\textit{p}\text{-Me}_2\text{NStilSi(OSiMe)}_3]$, $[\textit{p}\text{-Me}_2\text{NStilSi(OSiMe)}_4]$), as well as cube ($[\textit{p}\text{-Me}_2\text{NStil}_8\text{SiO}_{1.5}]_8$). Ultrafast depolarization of the fluorescence in the half and cube systems was observed indicating strong electronic coupling between the chromophores and excitation energy delocalization taking place between the chromophores within the molecules. Time-resolved transient absorption studies on a femtosecond time scale were used to monitor the earliest events in the excited-state relaxation process. Blue shifts in the excited state absorption correlate with solvent stabilized intramolecular charge transfer processes. The transient dynamics revealed ultrafast delocalization of charge in the half and cube systems. An increase in charge transfer character of the excited state is found in half and cube with an increase in the number of chromophores, and this explains the increase of two-photon cross-sections.

2) A series of novel oligothiophene-perylene bisimide hybrid (DOTPBI) dendrimers (G0, G1, and G2) were investigated. Results revealed the ability of these molecules to undergo intramolecular fluorescence resonance energy transfer (FRET) from the dendritic oligothiophenes (DOT) to the perylene bismide (PBI) moiety. The delocalization length and the photoinduced electron transfer (PET) rates were investigated as a function of dendrimer generation. An ultra-fast (~ 200 fs) energy transfer process from the DOT dendron to the PBI core was observed. In the case of the G2 dendrimer, with relatively larger oligothiophene dendrons attached to the bay area of the perylene bisimide, the PBI core is highly twisted and thus loses its electron trapping ability. As a result, among the three generations studied, G1, which has the best two-

photon cross section and the most efficient energy transfer, is the best light harvesting material among three samples.

CHAPTER 1

INTRODUCTION AND BACKGROUND

1.1 Motivation and Background

The energy challenges we face are severe.¹ The worldwide industry and daily necessities currently rely heavily on non-renewable energy supplies such as coal, oil, and natural gas, which will eventually diminish and cannot be renewed. Continuously consuming these materials will cause environmental consequences and break down the ecosystem of our planet. In contrast, the many types of renewable energy resources such as wind and solar energy are constantly replenished and will never run out. As shown in Figure 1.1, in 2011, renewable sources such as solar, geothermal, waste, wind, biofuels, wood and hydroelectric power hold only 9 % share of the United States national energy supply. This number is probably much lower throughout the world. Therefore, seeking alternative and renewable energy supply is one of the crucial elements to maintaining long-term sustainable development for our human society.

U.S. Department of Energy has a comprehensive plan to promote renewable energy production, reduce the dependence on foreign oil and solve the global warming crisis.¹⁻³ To achieve this, solar energy is used as one of the key renewable energy sources without greenhouse gas emissions. The amount of solar radiation reaching the surface of the earth is about 164 PW with an average energy density of about 1270 W/m².⁴ In one year, the total energy of solar radiation is about twice amount of the energy that will ever be obtained from all of the other Earth's non-renewable resources, such as coal, oil and

natural gas.⁴ In addition, solar energy can be harvested around the planet, mostly depending on latitude and average local cloud cover. Therefore, solar, as one of the cleanest types and the most abundant energy sources, has obtained quite amount interests and became the key approach to the next generation energy supply. The consumption of solar energy will be increased dramatically in the next few decades, as indicated in Figure 1.2.

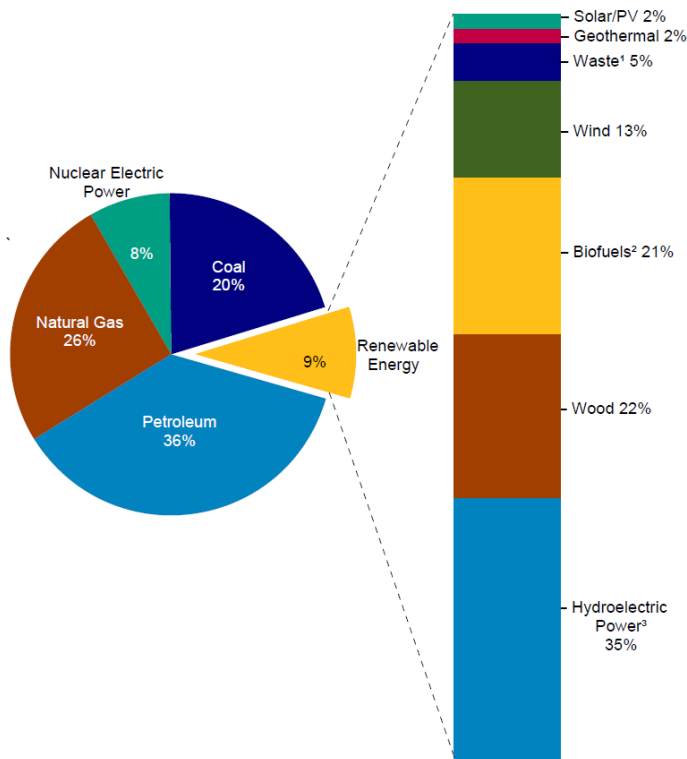


Figure 1.1 Energy consumption, 2011⁵

Although solar energy is an ideal alternative energy, it only provided 2% of the US's renewable energy in 2011, as shown in Figure 1.2. Currently, commercial photovoltaic cells are inorganic with efficiencies between 12-25 %.⁶ However, there are some drawbacks of current photovoltaic techniques. First of all, fabrication processes are very complex and involve a number of steps that make commercial solar panels very

expensive. Secondly, inorganic solar cells are made by rigid materials which are unable to be manufactured into large scale mass production because of the limitation of current industrial fabrication technology. Thirdly, the amount of energy produced is still uncompetitive to traditional non-renewable sources.

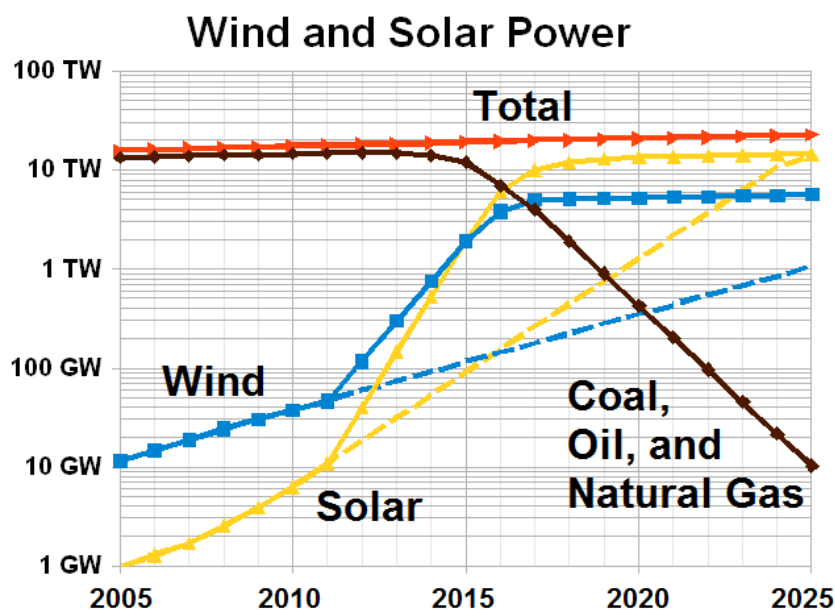


Figure 1.2 Energy consumption prediction to 2025⁵

Organic photovoltaics (OPV) as relatively novel technology, in contrast, have efficiencies of ~8 %, but can be potentially produced at a much lower cost.⁷⁻⁸ OPV materials also provide other advantages, such as good solubility,⁹⁻¹⁰ light weight,¹¹ and mechanical flexibility.¹¹ Most importantly, OPV provide the possibility of cheap production, such as simple roll-to-roll printing processes,¹²⁻¹⁵ drives the development of organic photovoltaic devices further in a dynamic way. An example of flexible organic solar cell¹⁶ is illustrated in Figure 1.3. In a word, the biggest challenge is how to improve the power conversion efficiency of organic photovoltaics to exceed the 10% mark for large scale commercialization.¹⁶



Figure 1.3 Flexible organic solar cell¹⁶

1.2 Photovoltaic Techniques

Photovoltaic cells are specialized semiconductor diodes that convert visible light into direct current electricity. Common materials used for photovoltaics are inorganic, with 12-25 % efficiency,⁶ while most of organic photovoltaics have efficiency about 8 %.^{7, 16-17} In order to understand the basic idea of enhancing the efficiency of organic photovoltaics, a brief introduction to the physics of the solar cell efficiency and background of current organic photovoltaic materials are presented in the following section.

1.2.1. Basic Physical Principles

Generally, the *power conversion efficiency* (PCE) is used to evaluate the performance of a solar cell as an industrial standard. It is defined as the ratio of the maximum electrical power produced by a solar cell per unit area in watts, divided by the incident radiant energy in watts per unit area under "Standard Test Conditions" (STC). STC represents a series condition that: (1). Light intensity of 1000 Watts/m². (2). Air Mass 1.5 solar reference spectrum, corresponding to a solar zenith angle of 48.19 °, as shown in Figure 1.4. (3). Solar cell temperature during measurement of 25 °C.

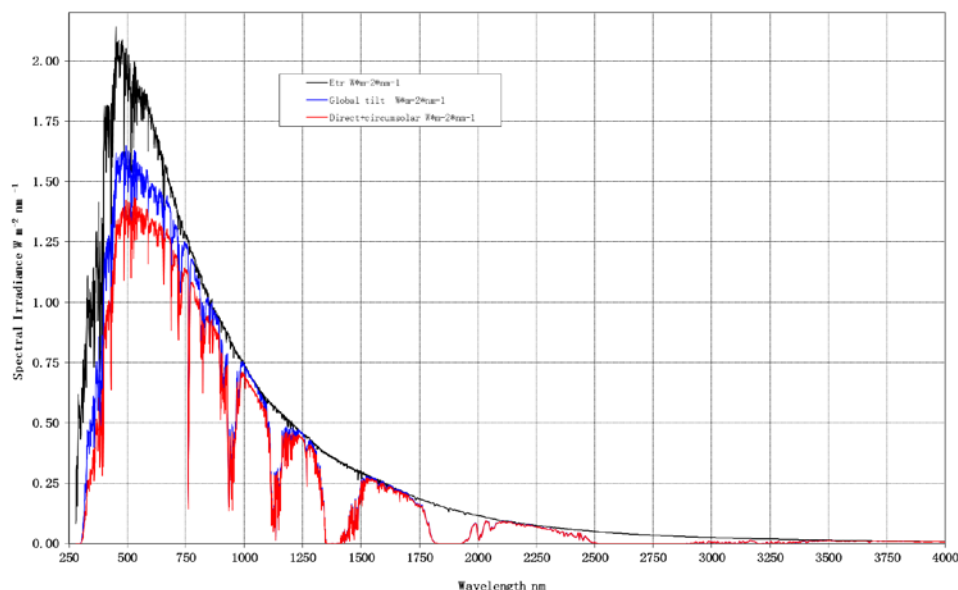


Figure 1.4 American Society for Testing and Materials (ASTM) Terrestrial Reference Spectra for Photovoltaic Performance Evaluation¹⁸

The power conversion efficiency, which is used to evaluate the performance of a photovoltaic device, can be represented by the amount of optical power of light (P_{light}) converted into the electrical power of a solar cell ($P_{solar\ cell}$):

Equation 1.1
$$PCE = \frac{P_{solar\ cell}}{P_{light}} = \frac{I_{SC}U_{OC}FF}{P_{light}}$$

In the above equation, I_{SC} is the short circuit current in ampere, which is defined as the current produced by solar cells under illumination without application of any external resistance. In other words, it is the maximum electrical current that can be generated by a solar cell device. In organic semiconductors, I_{SC} is determined by both the photoinduced charge carrier density and the charge carrier mobility. U_{OC} is the open circuit voltage in volt, which is the maximum possible voltage between two electrodes of solar cells under illumination when no current is flowing through terminals. It depends on the saturation current of the solar cell, photo-generated current and recombination process of the charge

carriers. Particularly, in organic photovoltaics, it is determined by the energy difference between the highest occupied molecular orbital (HOMO) of the donor (p-type semiconductor) and the lowest unoccupied molecular orbital (LUMO) of the acceptor (n-type semiconductor). A linear relationship has been found between the HOMO level of the conjugated polymer and the open circuit voltage.¹⁹ FF is the fill factor, which is defined by the ratio of actual maximum output power generated by a solar cell to its theoretical output power under the condition when both open circuit voltage and short circuit current conditions are achieved:

$$\text{Equation 1.2} \quad FF = \frac{U_{mmp}I_{mmp}}{U_{oc}I_{oc}}$$

Where, V_{mmp} and I_{mmp} are the voltage and current, respectively, at maximum power point (MMP). At this point, the power output is the largest and used to compare with the incident light intensity in order to evaluate the efficiency of a solar cell. An increase of FF could directly lead to an improvement of overall PCE. There are two important factors needs to be aware of in order to obtain a high FF . First, the shunt resistance (R_{SH}) needs to be very large in order to prevent leakage current. Second, the series resistance (R_S) needs to be very low in order to get a sharp rise in the forward current. The corresponding equivalent circuit is shown in Figure 1.5. FF can be significant different based on the materials. Currently, for polymer based semiconductors, FF over 70% can be achieved.²⁰

According to Equation 1.1, the PCE can be improved by improving I_{SC} which can be presented by the equation below:

$$\text{Equation 1.3} \quad I_{SC} = \varphi\eta_{EQE}qA$$

Where, φ is photon flux per second per square meter, A is area of device, η_{EQE} is external quantum efficiency, and q is electron charge in coulomb. External quantum efficiency (EQE) is the number of charge carriers collected by a solar cell divided by the number of

incident photons. It includes energy losses caused by reflection and transmission. EQE is related with other efficiencies, as shown in the following:

Equation 1.4
$$\eta_{EQE} = \eta_o \eta_{IQE}$$

Where, η_o is the optical efficiency and η_{IQE} is the internal quantum efficiency (IOE). IOE only involves the percentage of absorbed photons and factors out the energy losses due to reflection and transmission.

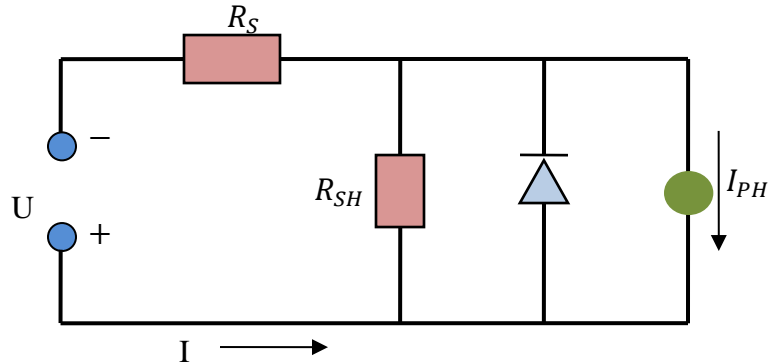


Figure 1.5 Equivalent circuit for a solar cell¹⁷

Figure 1.6 illustrates the typical the current-voltage characteristics of a solar cell in the dark and under illumination conditions. In the dark condition, no current flows until forward bias for voltages at the contact is much greater than the open circuit voltage. Under illumination condition, the current flows following the direction opposite to the injected currents. In Figure 1.6, the open circuit voltage (V_{OC}) and the short-circuit current (I_{SC}) are marked as the intersections with x and y axis, respectively. Under closed circuit condition, the photo generated current is maximum, whereas under flat band or open circuit condition, it becomes zero. The largest power output is obtained at the maximum power point (MPP) where the product of voltage and current is maximized.

Generally, the I-V characteristics of a photovoltaic device after the Shockley equation can be expressed as following:

$$\text{Equation 1.5} \quad I = I_0 \cdot \left\{ \exp\left(\frac{e}{nkT}(U - IR_S)\right) - 1 \right\} + \frac{U - IR_S}{R_{SH}} - I_{PH}$$

Where, I_0 is the reverse saturated dark current, e is the elementary charge in coulombs, n is the ideality factor of the device, U is the applied voltage, R_S is the series resistance, R_{SH} is the shunt resistance, I_{PH} is the photocurrent generated, and k is the Boltzmann constant.

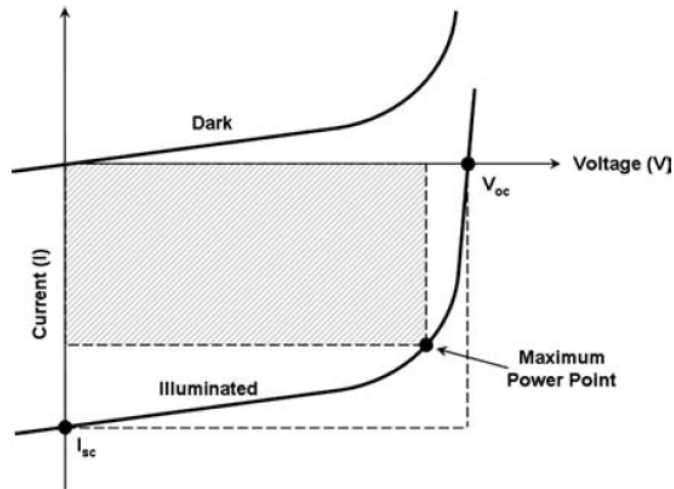


Figure 1.6 Current density-voltage (*J-V*) characteristics for a generic photovoltaic devices²¹

In organic photovoltaics, there are five consecutive steps to accomplish in order to convert light into electric current electricity: (1) absorption of a photon to generate an electron-hole pair (exciton); (2) exciton diffusion; (3) exciton dissociation; (4) charge carrier generation and separation at the donor/acceptor interface and charge transportation through the organic layers; (5) charge collection at electrodes to generate a direct current.

Each of these five steps has some associated efficiency. Thus, EQE can be re-expressed as:

$$\text{Equation 1.6} \quad \eta_{EQE} = \eta_{abs} \times \eta_{diff} \times \eta_{diss} \times \eta_{tr} \times \eta_{cc}$$

Where, η_{abs} is the efficiency of absorption, η_{diff} is the efficiency of exciton diffusion, η_{diss} is the exciton dissociation yield, η_{tr} is the efficiency of charge carrier transport throughout the device and η_{cc} is the efficiency of charge collection at the electrodes. The basic operating process of p-n heterojunction photovoltaics are illustrated in Figure 1.7.

Organic solar cells consist of donor and acceptor moieties to construct donor-acceptor heterojunction structures. Two different heterojunction designs are shown in Figure 1.8. When a photon with sufficient energy is absorbed in donor, the electron hops into the LUMO level, leaving a hole in the HOMO level, and thus a bound state of electron/hole pair (exciton) is generated, as shown in Figure 1.7. The electron-hole pairs must then be further separated into free charge carriers and transported to the electrodes to generate direct current. During this step, exciton recombination (usually $\sim\mu\text{s}$) could happen unless it is quickly dissociated and followed by a long-lived charge separation state (usually $\sim\text{ns}$).²² In order to dissociate the exciton, the acceptor materials have to overcome the exciton binding energy of the donor. The binding energy of OPV materials is usually between 0.5-1.0 eV.²³ For donor-acceptor type heterojunction materials, a decrease in exciton binding energy could result to a more efficient photocurrent generation.²⁴ The following condition describes the requirement for the charge transfer process taking place at an interface:

$$\text{Equation 1.7} \quad E_A^A - E_A^D > U_D$$

Where, E_A^A and E_A^D are electron affinity of acceptor and donor, respectively, and U_D is the binding energy of exciton in donor.

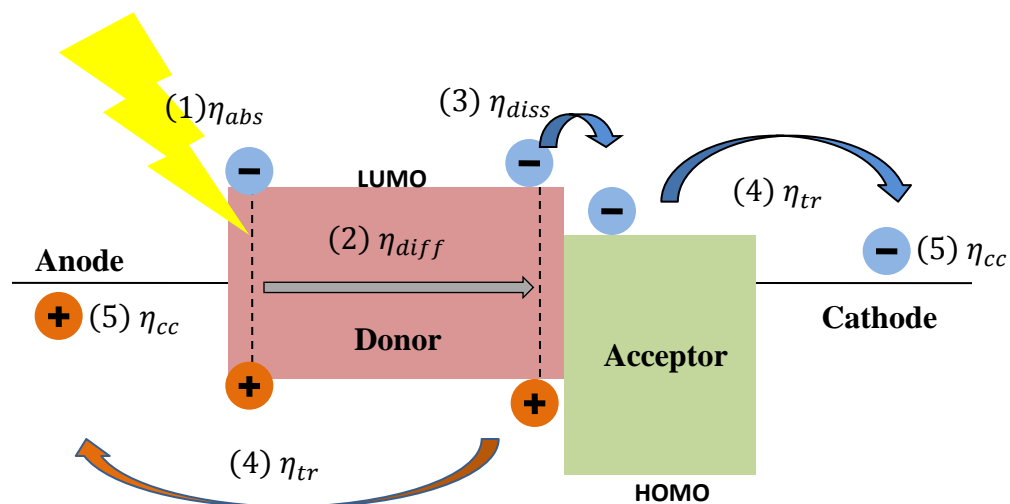


Figure 1.7 Energy band diagram illustrating the five consecutive steps and HOMO /LUMO levels in a hybrid solar cell²⁵

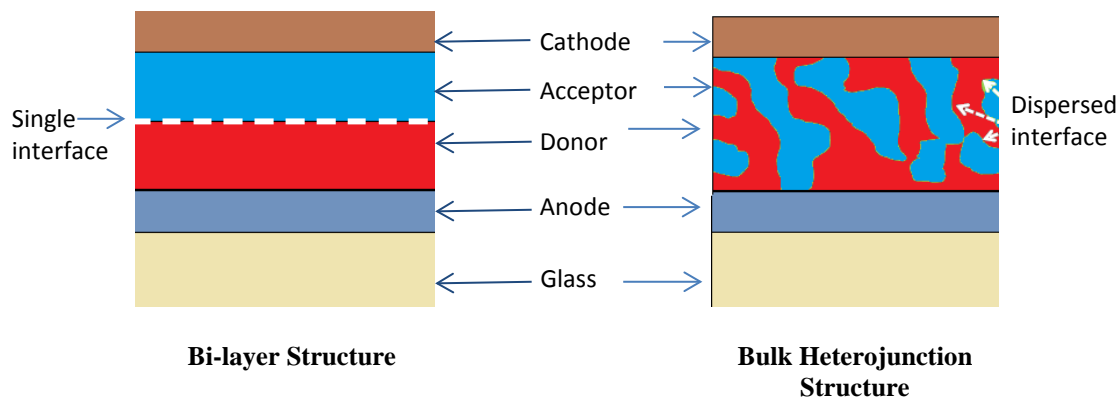


Figure 1.8 Schematic diagram of bi-layer and bulk heterojunction structure photoactive layers²⁵

In order to increase the overall efficiency PCE, there are many approaches have been focused on. First of all, increasing η_{abs} is the most effective way to increase η_{EQE} and thus improve I_{SC} .²⁶⁻²⁷ The absorption spectrum of the material is affected by both the band gap and absorption extinction coefficient. Organic semiconductor thin films may have high absorption extinction coefficients exceeding 10^5 cm^{-1} . The thickness of the active layer is also essential to the absorption intensity. Material such as P3HT polymer with high charge-carrier mobility and long lifetime allows the capability of increasing the layer thickness (up to 500 nm) and substantially increasing the solar absorption yield.²⁸ Another important factor is the efficiency of exciton diffusion, which depends on the both exciton diffusion length, and the distance between excitation and the nearest interface. The maximum exciton diffusion length is around 10nm in disordered and semi-crystalline polymers and small molecules.^{23,28} Exciton dissociation happens near the junction (usually less than 20nm) between donor and acceptor, and therefore, the distribution and morphology of the interface throughout the active layer are also critical to the overall efficiency of the solar cell. Charge transportation occurs via hopping process between energy states, which is greatly depending on the charge mobility of the semiconducting material. There is a competition between charge recombination and transportation. The charge carriers drift length (d) is determined by the product of charge carrier mobility (μ), carrier lifetime (τ) and applied electrical field (E). The lifetime of exciton (usually \sim ps) is typically very short. It has been found that introducing intermediate layers between the photoactive layer and electrodes could enhance the injection of charge carriers energetically. η_{cc} is influenced by the electronic composition of the device.

1.2.2. Organic Photovoltaic Materials

Organic materials with delocalized π electron systems can absorb sunlight, create photogenerated charge carriers, and transport these charge carriers to electrodes to generate direct current electricity. Tremendous efforts have been made to develop organic solar cells within the last few decades.^{17, 21, 25-27, 29-39} The first generation of organic photovoltaic solar cells was based on single active layers made of organic material,

sandwiched between two electrodes.^{29, 40} Unfortunately, their power conversion efficiencies reported were generally poor (far below 1%), because the charge recombination occurs readily when exciton diffusion length is much shorter than the sample thickness. Introducing a second organic semiconductor layer to form bilayer heterojunction solar cell was a huge breakthrough to improve the overall power conversion efficiency of OPV cells. There are two specific types of semiconducting materials commonly used in heterojunction solar cells. For instance, phthalocyanine, as a p-type, hole conducting material, behaves like an electron donor.^{34, 40-47} In contrast, perylene and its derivatives show an n-type, electron conducting behavior and serve as electron acceptor.⁴⁸⁻⁵³ The first organic heterojunction solar cell reported by Tang in 1986 is a huge milestone in this field, which provides about 1% power conversion efficiency with a phtalocyanine derivative as p-type semiconductor and a perylene derivative as n-type semiconductor.⁵⁴ However, this heterojunction concept has requirements on both the low exciton diffusion length and the thickness for a sufficient absorption in order to achieve a better efficiency.

Later on, bulk heterojunction solar cell was introduced to overcome these limitations, by blending two different donor and acceptor materials in solution and then utilizing spin coating or evaporation methods to obtain solid state mixture.⁵⁵⁻⁵⁶ In 1995, Yu *et al.*⁵⁷ made the first polymer/polymer bulk heterojunction photovoltaic device based on a mixture of phenylene-vinylene derivative and fullerene. In contrast to the bilayer heterojunction, this novel concept features both distributed junction and increased interface area between the donor and acceptor. The advantage is that it is very efficient to dissociate exciton and generate charge carriers over the whole extent of the thin film. However, separation of these charge carrier pairs is very difficult because of the strong Coulomb bound between them, and recombination process between the trapped charge carriers and the mobile ones. Despite of the drawbacks, solar cell under this concept provides much higher power conversion efficiency than the bilayer system. Currently, state of the art OPV cell reported by a German company, Heliatek, offers power conversion efficiency ~12 %.⁵⁸

The choice of materials used in solar cells is crucial to the overall efficiency, and thus the success of OPV cell device. Research on organic photovoltaics cells has been focused on solution processable low band gap semiconducting polymers, small molecules and hybrid materials.^{37-39, 59-60} Examples of current popular OPV materials are shown in Figure 1.9. Materials with low ionization potentials and low electron affinities usually behave as hole-transporting materials, while materials with high ionization potentials and high electron affinities behave as electron-transporting materials. The valence band edge is identified by the ionization energy required to remove a HOMO electron and to obtain a LUMO electron. The band gap of most organic photovoltaic materials is usually around 2eV.²⁸ The optimum band gap for harvesting the solar spectrum is approximately 1.4eV according to the detailed balance limit.⁶¹ Decreasing the band gap could actually enhance absorption yield by increasing the total amount of photons absorbed from the solar spectrum. However, lowering of the band gap will cause a decrease in open circuit voltage and eventually lower the overall power conversion efficiency. Other than that, the probability of charge dissociation can be increased when the potential difference between the LUMO of donor and the LUMO of acceptor is increased. The large difference between the LUMO levels can provide large offset energy, high built-in potential (V_{BI}) and thus results large open-circuit voltage.⁶² Theoretically, V_{BI} is given by the following equation⁶³:

$$\text{Equation 1.8} \quad V_{BI} = \frac{1}{e} (|E_{HOMO}(\text{donor})| - |E_{LUMO}(\text{Acceptor})|)$$

In which, e is the elementary charge in Coulomb. In addition, V_{oc} is empirically suggested that $\sim 0.3V$ less than the built-in potential.⁶³

Quite amount of low band gap polymers were studied in the literature.^{28, 64-73} There are several factors that influence the band gap of conjugated polymer materials: (1) charge transfer from one part of the molecule to another/intra-chain charge transfer, (2) bond-length alternation, (3) aromaticity, (4) substituents effects, (5) intermolecular interaction, (6) π -conjugation length.

Thiophene, as one of the most promising OPV material, has gained strong interested in current research.⁷⁴⁻⁷⁶ The structure of polythiophene is shown in Figure 1.11. It can be incorporated as polymer backbone in a copolymer or as part of a fused ring systems. Different orientations of thiophene monomers are illustrated in Figure 1.10. The band gap of polythiophene is 2 eV.⁷⁷

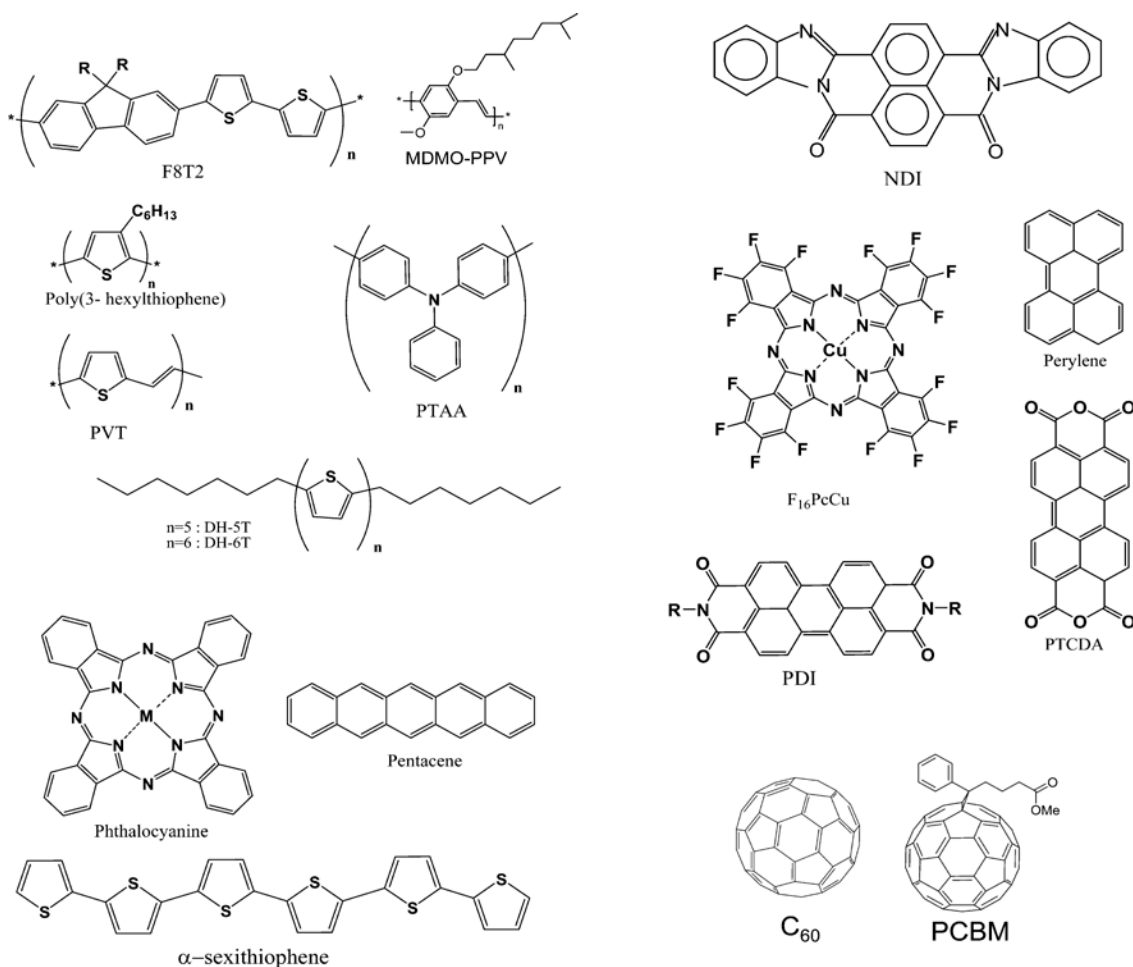


Figure 1.9 Organic semiconductor materials in organic solar cells⁴⁷

Poly(3-hexylthiophene), P3HT, is one of the most studied conjugated polymers based on polythiophene, as an electron donor. The structure is shown in Figure 1.8. The band gap of P3HT is around 1.9 eV, with absorbance below a wavelength of 650nm.^{28, 78} There are many methods to optimize its band gap. First of all, the absorption maximum

of P3HT is related with the percentage of head-to-tail coupling, and thus, the synthetic approach methods, such as the solvent used for spin coating, the annealing temperature and additive added to the active layer are essential to the photo physical properties of the thin film.⁷⁹⁻⁸³ In addition, it has been noted that the molecular weight also has strong influence on the absorption spectrum of P3HT.⁸⁴ An increase in molecular weight results in a red shift and broadening of absorption maximum, and provides better photovoltaic performance.⁸⁴ The regioregularity is another important factor which affects the characteristics of the P3HT such as conductivity and charge carrier mobility and transport. Several studies have been reported on the regioregularity and its effect on packing of the polymer.^{81-82, 84-88} It has been found that the P3HT could stack in lamella structure and improve charge transport.^{82, 88-91} The dimension of lamella thickness is affected by the length of the substituted side chains.⁸⁹ However, the main disadvantage of this polymer is that its absorption spectrum doesn't match well with the solar cell spectra.

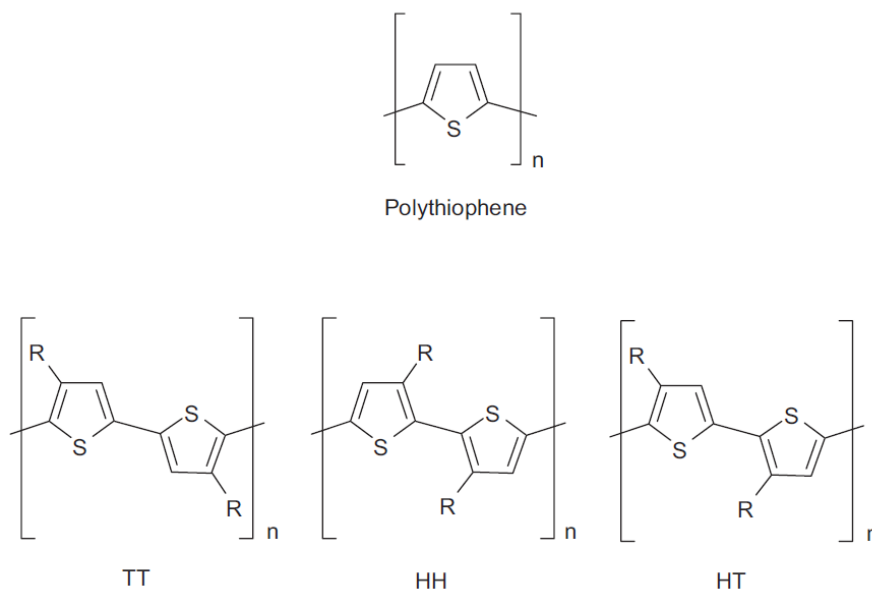


Figure 1.10 Structure of polythiophene and substituted derivatives of polythiophene in HH, HT and TT couplings⁷⁸

Another state-of-the-art organic photovoltaics is based on the fullerene derivative [6,6]-phenyl-C61-butyric acid methyl ester (PCBM).^{26, 70, 72, 92-95} The structures of fullerene and PCBM are presented in Figure 1.9. Numerous studies have been aimed at designing optimal donor polymers for PCBM.⁹⁶⁻⁹⁷ The HOMO and LUMO energy levels of P3HT, MDMO-PPV and an ideal donor with respect to the band structure of PCBM is presented in Figure 1.11. Two possible mechanisms have been raised of the fundamental photo-conversion process. The first one follows the general accepted mechanism for photo energy conversion in excitonic solar cells. Exciton is created in donor material after excitation. The electron in the LUMO level of donor exciton transfers to the LUMO level of the acceptor directly. Another possible mechanism involves a Förster resonance energy transfer (FRET) from the donor to the acceptor after excitation, thus generating an exciton in the acceptor. This process has recently been observed for fullerenes in both solution⁹⁸ and solid state.⁹⁹

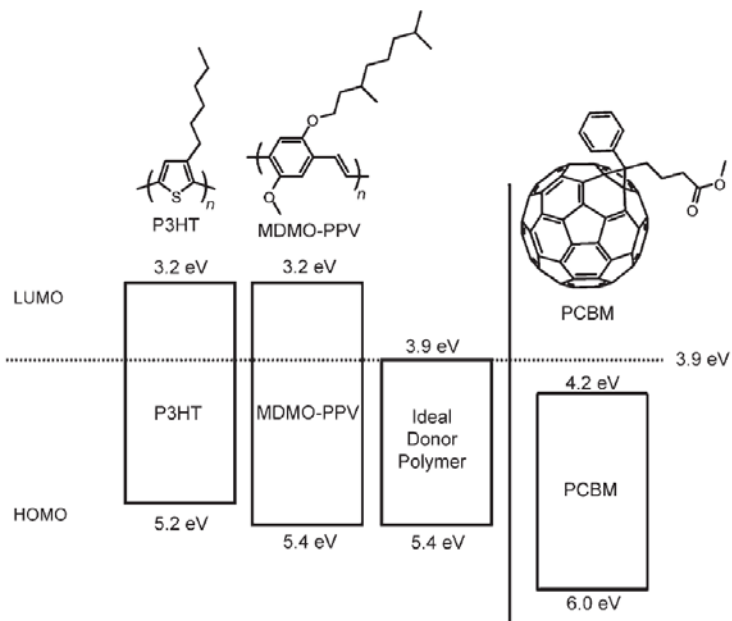


Figure 1.11 Band structure diagram illustrating the HOMO and LUMO energies of P3HT, MDMO-PPV and an ideal donor with respect to the band structure of PCBM³⁶

Many other OPV materials such as perylene bisimides (PDI),^{49, 100-101} phthalocyanine,¹⁰¹⁻¹⁰⁴ 1,5-naphthalene diisocyanate (NDI)¹⁰⁵ and poly(triarylamine) (PTAA)¹⁰⁶ have been widely studied. The structures are presented in Figure 1.9.

The fabrication techniques are very simple and cost-effective, such as vacuum deposite,¹⁰⁷ spin-coating,¹⁰⁸⁻¹⁰⁹ spray deposition,¹¹⁰⁻¹¹¹ doctor blading,¹¹²⁻¹¹³ screen printing^{8, 112} and inkjet printing.¹¹⁴⁻¹¹⁶ Most polymer-based photovoltaic elements are solution processed at low temperatures. Vacuum evaporation and solution processing techniques are the most commonly used thin film preparation methods in the production of organic solar cells. In addition, vacuum evaporation/sublimation is a very clean choice for the deposition of thin films based on small molecules.¹¹⁷ The printing/coating techniques are usually used to deposit conjugated semiconducting polymers.¹¹⁷ Large scale printing/coating techniques uncover the possibility for large scale cost-effective manufacturing with low energy consumption.

Understanding the mechanisms of charge generation, recombination and transportation is crucial to making significant improvement in the overall OPV device efficiency. Transient absorption spectroscopy has been widely used to study the nature of excited states in solar cells.^{24, 118-121} It is a pump-probe technique which can be used to characterize all steps of device operation, such as absorption, exciton diffusion and dissociation, charge transport and charge collection. Ultrafast spectroscopic technique can monitor the photoinduced charge transfer process in real time (less than 50 fs).¹²²⁻¹²³ It also provides the evidence and significance of the charge transfer state. Ohkita et al.¹¹⁸ utilized transient absorption spectroscopy to examine the correlation between polaron yield for a series of polythiophenes blended with fullerene (5 wt %) and the activation energy of charge separation. The results imply that charge carrier dissociation efficiency is dependent on the free energy of the starting exciton. High activation energy provides the initially formed CT state with sufficient excess thermal energy to overcome the binding energy and thus leads to efficient charge dissociation into fully charge separated state. The energy diagram of the carrier formation in polythiophene/fullerene blend films is shown in Figure 1.12. Similar trends also found in other alternative blends.¹²⁴⁻¹²⁶ In this

dissertation, time-resolved transient absorption technique is used to study charge transfer process of the silsesquioxane and oligothiophene-peryene bisimides.

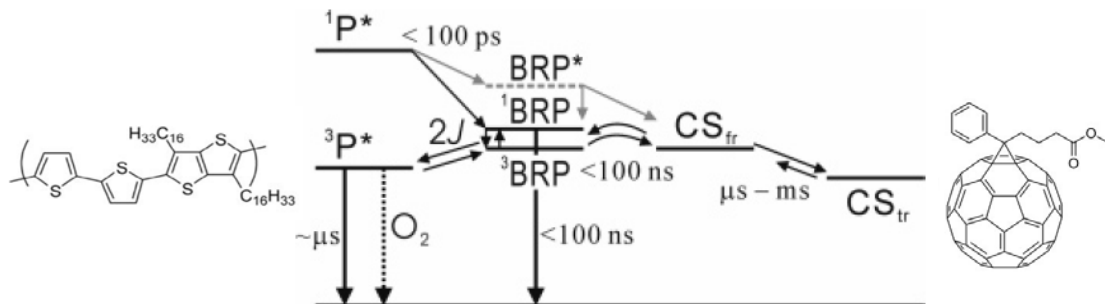


Figure 1.12 Charge photogeneration diagram in polythiophene:PCBM blend films¹¹⁸

1.3 Two-Photon Absorption

1.3.1. The Main Concepts of Two-Photon Absorption

Two-photon absorption is a nonlinear optical process, in which two photons are absorbed simultaneously. The energy of the excited atom or molecule is equal to the sum of the energy of the two photons:

Equation 1.9
$$h\nu_1 + h\nu_2 = E$$

Where, h is the Plank constant, ν_1 and ν_2 are the frequencies of the absorbed photon in wavenumber and E is the energy difference between the upper and lower energy level. In two photon process, molecule absorbs photons simultaneously, mediated by a so called “virtual state”, according to quantum mechanics. A schematic representation of TPA process is provided in Figure 1.13.

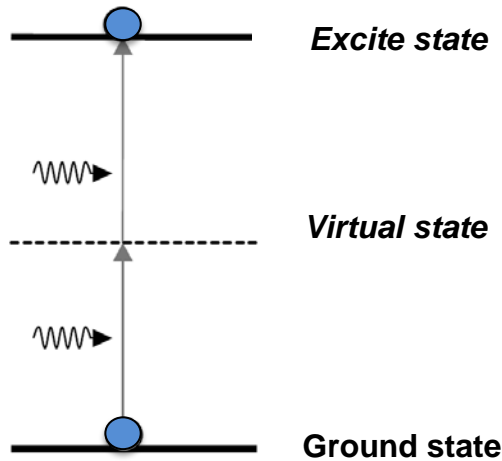


Figure 1.13 Schematic representation of simultaneous TPA process

The TPA theory was first developed by Göppert-Mayer in 1931.¹²⁷ In 1961, Kaiser and Garrett¹²⁸ reported the first experimental evidence for TPA process. The advent of high peak power laser made the first experimental evidence of this non-linear phenomenon when performed two-photon excitation in a $\text{CaF}_2:\text{Eu}^{2+}$ crystal. A quadratic dependent relationship between the observed fluorescence intensity and the incident beam intensity was observed in this experiment. It was the historical moment of demonstrating the existence of two-photon excited fluorescence process. Later on, Prasad *et al.*¹²⁹⁻¹³⁰ and Marder *et al.*¹³¹⁻¹³² opened the research area of designing novel TPA materials with enhanced two photon cross-sections.

The probability of multiphoton absorption process follows the power law. In the case of just one light source for excitation, the probability can be expressed as:

Equation 1.10
$$P = \frac{1}{n} \sigma_n I^n$$

Where, P is the probability of multiphoton excitation, n is the number of photon, σ_n is the n -photon absorption cross-section, and I is the intensity of the incident light.

Therefore, in the case of two photon cross absorption, the absorption rate is quadratically depending on the input light intensity, as shown in Figure 1.14.

TPA offers low scattering when compared to one photon process. According to Rayleigh's law, the scattering can be expressed as:

Equation 1.11
$$\text{scattering} \propto \frac{1}{\lambda^4}$$

The excitation wavelength of two-photon process is about twice of that of the one-photon process, and thus the Rayleigh scattering is reduced by a factor of 16.

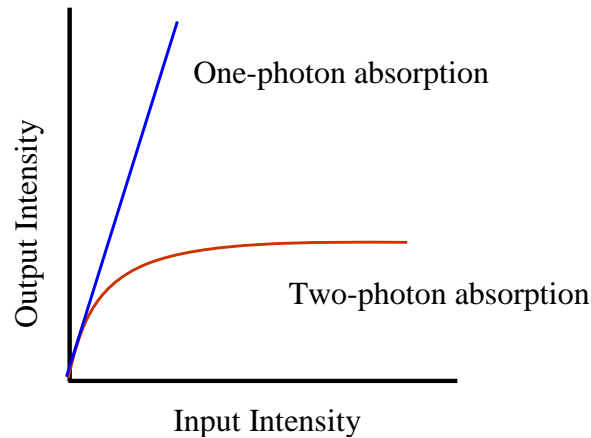


Figure 1.14 Output intensity with respect to input excitation intensity in one-photon and two-photon process

There are many applications on the basis of unique features of two-photon absorption phenomenon. First of all, TPA is the quadratic dependence on the excitation light intensity and it provides instantaneous response time even on femtosecond time scale. Therefore it can be used for optical power limiting application which is very useful for protecting human eyes and sensors exposed to hazardous sources of light.¹³³⁻¹³⁵ An

ideal power limiter allows low intensity input light to transmit, whereas high intensity light, such as laser beams, is blocked.

In addition, by focusing laser light in a two-photon absorbing medium, the two-photon excitation is localized in a three dimensional (3D) focal volume $\sim \lambda^3$, as shown in Figure 1.15. This unique property provides a method for the direct laser writing on 3D structures. It allows patterning materials with true 3D spatial resolution. This is particularly important for applications such as high-density 3D optical data storage,¹³⁶⁻¹³⁸ 3D photopolymerization,¹³⁹⁻¹⁴⁰ 3D microfabrication¹³⁹⁻¹⁴³ and *etc.* For example, SEM images of woodpile-type photonic crystal (PC) structures by 3D multiphoton lithography (MPL) method are shown Figure 1.15. In this example, woodpile-type face-centered tetragonal PC structures were fabricated by multiphoton photoinduced polymerization method using the 4,4'-bis(di-n-butylamino)biphenyl (DABP)-triacyrylate resin system.

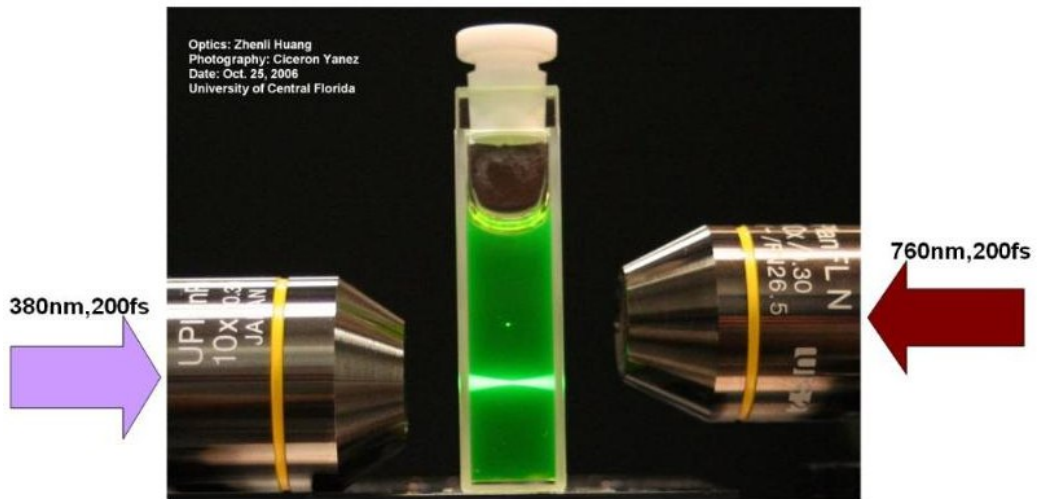


Figure 1.15 Demonstration of one-photon excitation process (left) and two-photon process (right)¹⁴⁴

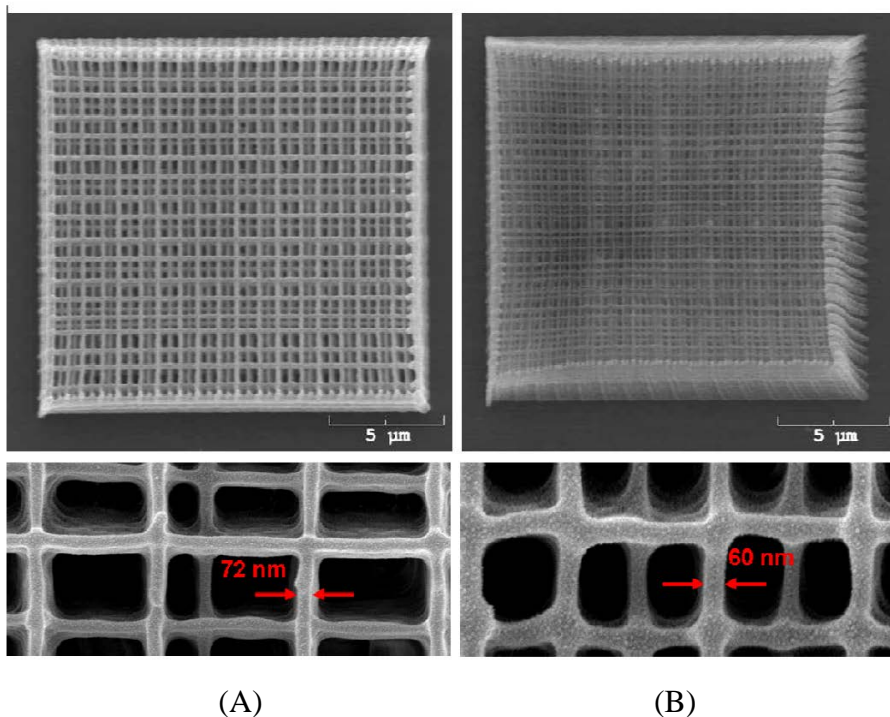


Figure 1.16 SEM images of woodpile-type photonic crystal (PC) structures fabricated with 520 nm excitation at (A) $0.60 \mu\text{W}$ and at (B) $0.45 \mu\text{W}$ using the 4,4'-bis(di-n-butylamino)biphenyl(DABP)-triacrylate resin.¹⁴⁵

Two-photon photo polymerization is also based on this TPA feature that it is possible to selectively excite molecules in a tiny volume. Kawata *et al.*¹⁴⁶ utilized two-photon photo polymerization to fabricate three dimensional microdevices. These microdevices are featured with sizes even close to the diffraction limit. They reported the scanning electron micrographs of “micro-bull” sculptures, fabricated by two-photon polymerization process with an accuracy of about 150nm, as shown in Figure 1.17. The size of these 3D sculptures is about $10\mu\text{m} \times 7\mu\text{m}$, which is about the size of a red blood cell. Their small volume feature allows us to send them, or any actually microdevice of this size, to any location inside the human body through blood micro-vessels to make clinical treatments.

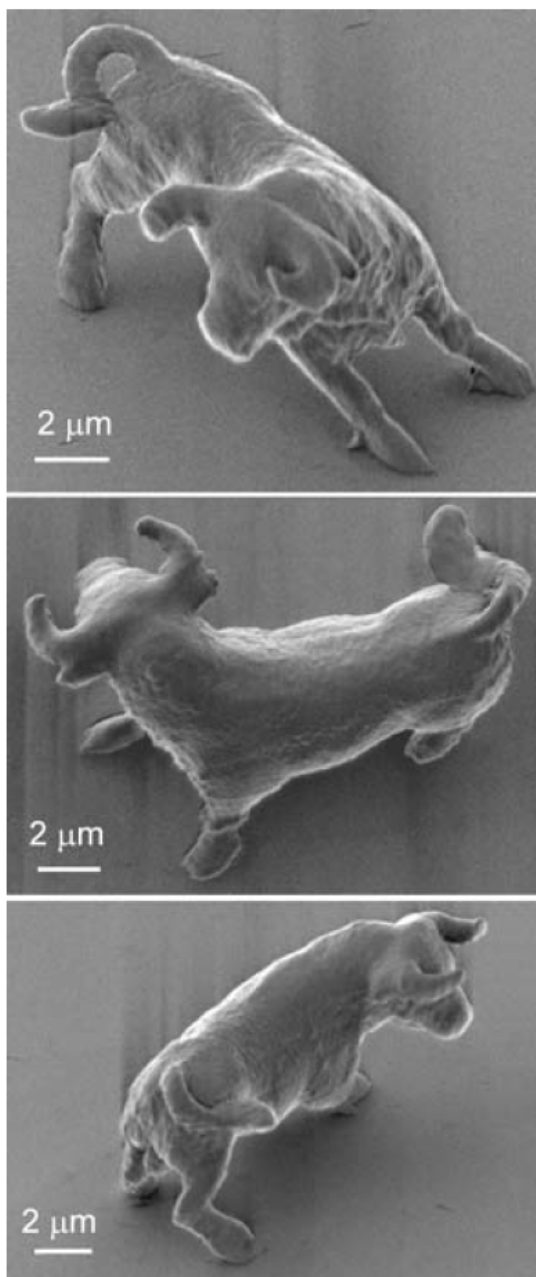


Figure 1.17 Different view-angle SEM images of a micro-bull sculpture that was two-photon photopolymerized with sub-diffraction-limit accuracy^{140, 146}

Most importantly, in a TPA process, the excitation wavelength is usually in the longer wavelength and can be easily separated from the wavelength of the resulting fluorescence. In addition, the longer wavelength excitation, especially the near-IR light

provides less damage, less absorption and scattering, and deeper penetration depth into tissues than visible light. These advantages make two-photon fluorescence microscopy¹⁴⁷⁻¹⁴⁸ of great importance to the current biomedical imaging techniques. Example of *in vivo* two-photon imaging in mouse neocortex is shown in Figure 1.17. There are three different types of brain access, as illustrated on the left side of the figure. Almost the entire depth of the neocortex was imaged, as shown on the right side. The experiment utilized Ti:sapphire oscillator with 40×, NA 0.8 water-immersion lens (Zeiss).

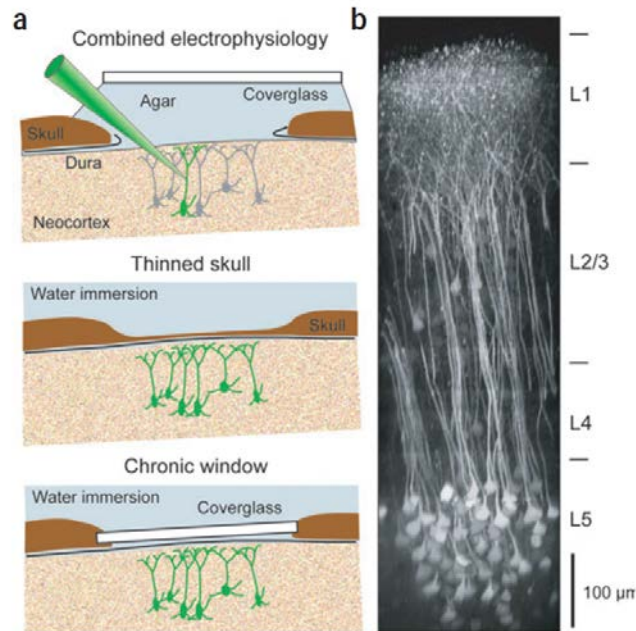


Figure 1.18 *In vivo* two-photon imaging in the intact neocortex. (a) Different types of brain access. (b) Example of deep two-photon imaging in mouse neocortex¹⁴⁷

Other examples of applications utilizing TPA phenomenon include two-photon photodynamic therapy,¹⁴⁹⁻¹⁵⁰ *in vivo* multiphoton tomography,¹⁵¹⁻¹⁵² drug delivery¹⁵³⁻¹⁵⁴, sensors¹⁵⁵, and two photon polymerization.^{142, 148}

Several techniques have been used to determine two-photon excitation cross sections of various materials for more than two decades, such as two-photon excited

fluorescence method,¹⁵⁶ nonlinear transmission method,¹⁵⁷ Z-scan method,¹⁵⁸⁻¹⁶⁰ and non-degenerate pump probe method.¹⁶¹

1.3.2. Theoretical Consideration

When an organic molecule is excited by an electrical or optical field, the resulting induced dipole moment (μ_{ind}) can be expressed by:

$$\text{Equation 1.12} \quad \mu_{ind} = -er$$

Where, e is the elementary charge and r is the field-induced displacement. Under bulk material condition, the induced dipole moment can be re-expressed as polarization (P_{ind}), which is given by:

$$\text{Equation 1.13} \quad P_{ind} = -Ner$$

Where, N is the electron density in the material. When the strength of applied electrical or optical field is relatively low, the induced polarization $P_{ind}(E)$ is proportional to the applied field (E):

$$\text{Equation 1.14} \quad P_{ind}(E) = \chi^{(1)} E$$

Where, $\chi^{(1)}$ is so called linear susceptibility. It relates to the dielectric constant (ϵ) as:

$$\text{Equation 1.15} \quad \epsilon = 1 + 4\pi\chi^{(1)}$$

However, under two-photon excitation, the external optical field is generated by a high power laser with relatively high output power. Therefore, the linear relationship between the induced polarization and the applied field isn't applicable under this

condition. Higher order susceptibility terms must take into account. According to the anharmonic oscillator model, the polarizability of a material can be expressed as a power series in the strength of applied field, as the following:¹⁶²

$$\text{Equation 1.16} \quad P_{ind}(\mathbf{E}) = \chi^{(1)}\mathbf{E} + \chi^{(2)}\mathbf{E}^2 + \chi^{(3)}\mathbf{E}^3 + \chi^{(4)}\mathbf{E}^4 + \dots$$

Where, $\chi^{(2)}$, $\chi^{(3)}$, and $\chi^{(4)}$ are the second, third and fourth order susceptibilities respectively. According to the Maxwell's equations and electromagnetic wave equations, the wave equation in a nonlinear optical media is derived as:¹⁶³

$$\text{Equation 1.17} \quad \nabla^2 \mathbf{E} - \frac{n^2}{c^2} \frac{\partial^2 \mathbf{E}}{\partial t^2} = \frac{4\pi}{c} \frac{\partial^2 \mathbf{P}}{\partial t^2}$$

Where, ∇^2 is the Laplace operator and c is the speed of light in this medium which is related with permeability and permittivity.

In an isotropic nonlinear optical medium, the two-photon cross section δ is theoretically described by the second-order hyperpolarizability (γ) via the following equation:¹⁶⁴

$$\text{Equation 1.18} \quad \delta = \frac{4\pi^2 \hbar \omega^2}{n^2 c^2} L^4 \text{Im}\langle \gamma \rangle$$

Where, n is the refractive index of the medium, c is the speed of light, \hbar is Planck's constant divided by 2π , L is the local field factor, and Im is the imaginary part of the complex quantity $\langle \gamma \rangle$, the orientational average of γ . Assuming that there are only two excited electronic states and the γ tensor is mainly along the chain axis, Butcher and Cotter¹⁶² reported the sum-over-states expression for γ . Its simplified expression is below:¹⁶⁵⁻¹⁶⁸

Equation 1.19

$$Im\langle\gamma\rangle = \frac{4}{5} Im \frac{M_{ge}^2 M_{ee'}^2}{(E_{ge} - \hbar\omega - i\Gamma_{ge})^2 (E_{ge'} - 2\hbar\omega - i\Gamma_{ge'})}$$

Where, g represents the ground state (IA_g), e represents the one-photon allowed excited state (IB_u), e' represents the two-photon allowed excited state ($2A_g$ or nA_g), M is the transition dipole moment of the two involved states, E is the energy difference between the two involved electronic states, and Γ is the corresponding damping factor (half width at half maximum). Assuming that the energy difference ($E_{ge'}$) between IA_g and $2A_g$ states is close to the twice of the excitation photon energy ($2\hbar\omega$), and the damping factor (Γ_{ge}) is significantly smaller than the one-photon detuning energy ($\Delta E = E_{ge} - \hbar\omega = E_{ge} - \frac{1}{2}E_{ge'}$), an approximation of the above equation is obtained.¹⁶⁵

Equation 1.20

$$Im\langle\gamma\rangle \approx \frac{4}{5} \frac{M_{ge}^2 M_{ee'}^2}{(E_{ge} - \hbar\omega)^2 \Gamma_{ge'}}$$

According to Equation 1.18 and Equation 1.20, the following expression for the transition dipole moment $M_{ee'}$ is obtained:

Equation 1.21

$$M_{ee'} = \frac{nc(E_{ge} - \hbar\omega)}{4\pi\omega L^2 M_{ge}} \left(\frac{5\Gamma_{ge'} \delta_{max}}{\hbar} \right)^{\frac{1}{2}}$$

Where, δ_{max} is the peak absorptivity of two-photon absorption. After rearrangement of Equation 1.21, the following expression can be obtained:

Equation 1.22

$$\delta_{max} \propto \frac{M_{ee'}^2 M_{ge}^2}{(E_{ge} - \hbar\omega)^2 \Gamma_{ge'}}$$

Furthermore, for a two-state model:¹⁶⁹

Equation 1.23

$$\delta_{2-state} \propto \frac{M_{ge}^2 \Delta\mu_{ge}^2}{\frac{E_{ge}^2}{4} \Gamma_{ge'}}$$

And for a three-state model:¹⁶⁹

Equation 1.24

$$\delta_{3-state} \propto \frac{M_{ge''}^2 M_{ee'}^2}{\left(E_{ge} - \frac{E_{ge'}}{2}\right)^2 \Gamma_{ge'}}$$

Where, $\Delta\mu_{ge}$ is the dipole moment difference between the g and e states. Therefore, the key parameters affecting δ are the ground and excited state transition dipole moments, change in dipole moment term ($M_{ee'}$) and the energy differences ($E_{ee'}$) between the states involved, as shown in Figure 1.19. In order to obtain large two-photon cross section, it is important to maximize the transition dipole moments ($M_{ee'}$). In addition, the peak wavelengths of one-photon ($\lambda_{max}^{(1)}$) and two-photon absorption ($\lambda_{max}^{(2)}$) are determined by the energy of the electronic transitions $e \rightarrow g$ and $e' \rightarrow g$. In contrast to one-photon absorption, two-photon absorption requires excitation involving an electron changing its molecular orbital angular momentum of +2, 0, or -2.

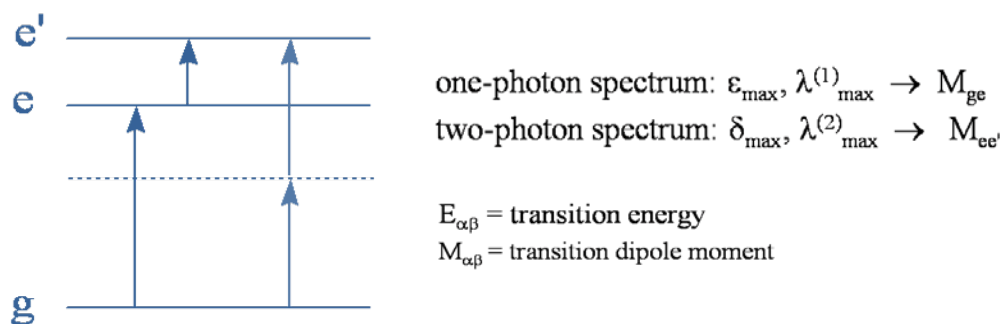


Figure 1.19 Schematic diagram of transition dipole moment difference in one-photon absorption and two-photon absorption process

1.4 Silsesquioxanes

Silsesquioxanes represent a group of materials with the empirical formula $(\text{RSiO}_{1.5})_n$, where R can be selected from a range of functional groups such as hydrogen or any alkyl, alkylene, aryl, arylene, or their derivatives. These compounds are usually considered as hybrids since their formulas are between inorganic silica and organic silicone polymers. Shown in Figure 1.20 are a variety of polymeric structures based on the $\text{RSiO}_{1.5}$ backbone, including random, full cage and partial cage structures.

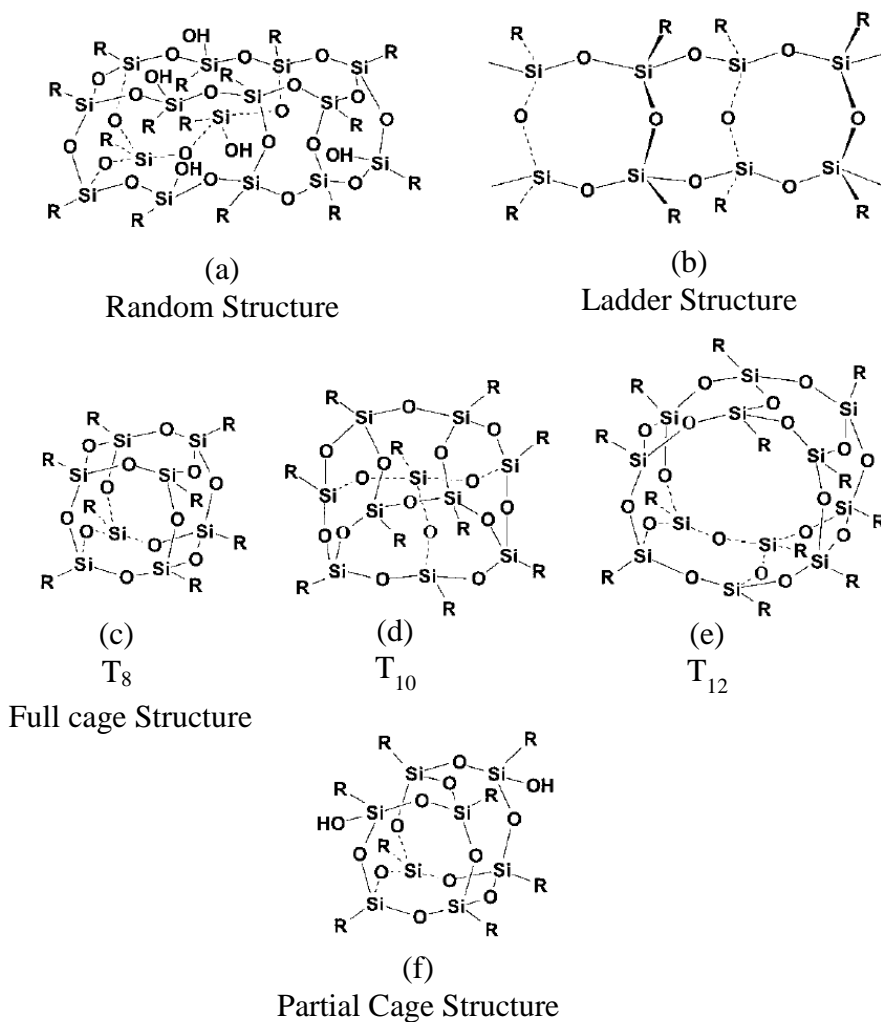


Figure 1.20 Structures of silsesquioxanes¹⁷⁰

The structure of a polyhedral oligomeric silsesquioxane (SQ) molecule is shown in Figure 1.21. The central core T_8 is functionalized with 8 organic substituents (R) at each Si atom. The cubic SQ core, with sizes of 0.53 nm in diameter, can be considered as the smallest possible particles of silica.¹⁷¹ Single crystal structure of $[p\text{-IC}_6\text{H}_4\text{SiO}_{1.5}]_8$ is presented in Figure 1.22. Cubic SQs have a 3-dimensional symmetrical cubic structure. Because of this structural feature, it is expected to provide distinctly characteristics different from planar molecules. Furthermore, the silsesquioxane core offers an increased

glass transition temperature, better mechanical properties, and enhanced thermal stability. Because its property and conformation may vary depending on its substituents, SQ is widely used as a building block to design functional nanomaterials. Based on these characteristics, a large number of high-performance materials have been developed.^{3, 172-178} Silsesquioxane based materials have drawn great interests in a variety of applications, such as dental materials,¹⁷⁹⁻¹⁸⁰ catalysts,¹⁸¹⁻¹⁸⁴ dielectric materials,¹⁸⁵⁻¹⁸⁸ light emitting materials,¹⁸⁹⁻¹⁹³ coating materials¹⁹⁴⁻¹⁹⁵ and organic transistors.¹⁹⁶

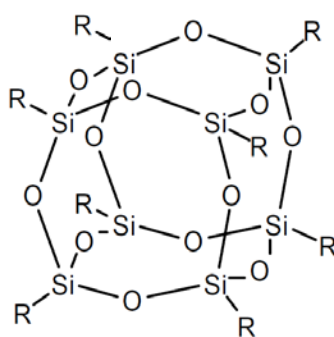


Figure 1.21 Structure example of cubic T₈ SQ

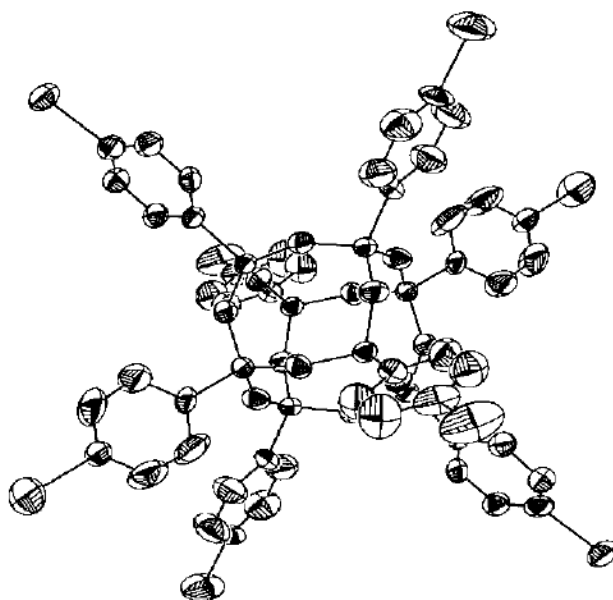
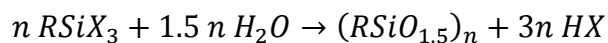


Figure 1.22 Single-crystal structure of recrystallized $[p\text{-IC}_6\text{H}_4\text{SiO}_{1.5}]_8$ ¹⁹⁷

The oligomeric organosilsesquioxanes, $(\text{CH}_3\text{SiO}_{1.5})_n$, were first isolated by Scott¹⁹⁸ in 1946 via thermal rearrangement of methylpolysiloxanes. Generally, the hydrolytic condensation reaction of RSiX_3 is used to produce silsesquioxanes:¹⁹⁹



Where, R is a chemically stable substituent, such as CH_3 , and X is a highly reactive substituent, such as Br. These reactions can be influenced by different experimental conditions such as concentration, solvent, characters of R and X groups, catalyst, water addition, and solubility of the condensation products. However, this synthetic approach is a complex, time-consuming, multistep process.

In 1958, Olsson¹⁷¹ first synthesized octaphenylsilsesquioxane (OPS) with a 9% yield from a hydrolysis reaction. This preferential formation of cubic structure is likely due to the stability introduced by the Si_4O_4 ring. Since then, tremendous efforts have been

made to optimize the synthetic approach to OPS based materials.²⁰⁰⁻²⁰⁷ However, how to improve the production yield was one of the biggest challenges in the hydrolysis/condensation synthetic methods. The synthesis reactions in these methods always result a mixture of products, including non-polyhedral silsesquioxane, and other oligomers, such as the T₁₀ and T₁₂ derivatives. In order to avoid byproducts and improve the product yields, many attempts have been made, such as modifying the solvent, changing hydrolysis process, and adding other compounds to the reaction. Laine's group²⁰⁸ has developed the synthesis methods of OPS to achieve greater than 90% yield. The synthesis pathways are illustrated in Figure 1.23. They used commercially available PhSiCl₃ as starting material, followed by reaction with ethanol to form either phenyltriethoxysilane, PhSi(OEt)₃, or its hydrolyzed oligomers depending on the reaction conditions. After the optimization of synthesis methods, separation of the desired cubic SQs from the byproduct is crucial to obtain good yields.

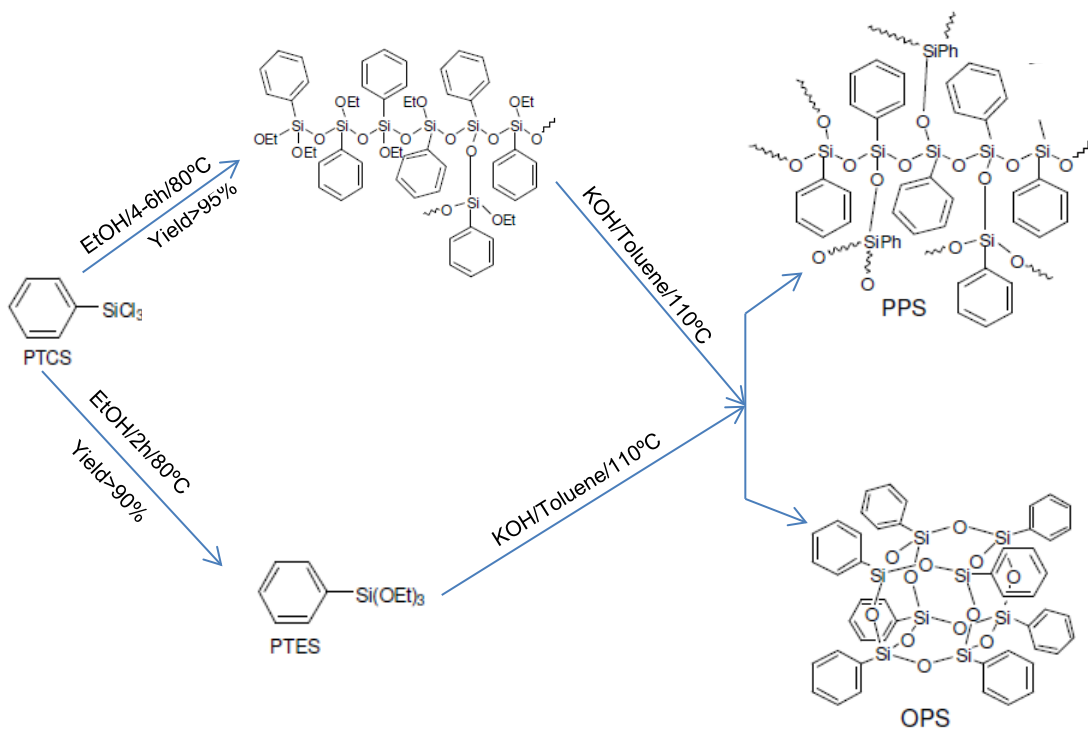


Figure 1.23 Experimental procedure for synthesis OPS²⁰⁸

There are also a lot efforts of developing nanobuilding blocks base on octavinylsilsesquioxane (OVS, $[\text{vinylSiO}_{1.5}]_8$).^{191, 209-210} Because this type of SQ gives the possibility of synthesizing cubic SQs with different functional group with perfect 3-D structures. Later, octa(*p*-bromostyrenyl)silsesquioxanes is further functionalized via Heck reactions using first generation crubbs as catalyst with versatile functionalized styrenes to generate octa-(R'vinylstilbene)silsesquioxanes, as shown in Figure 1.24.²¹¹ Octaphenylsilsesquioxane derivatives also provide opportunities to be further functionalized with stronger π -conjugation systems.²¹¹

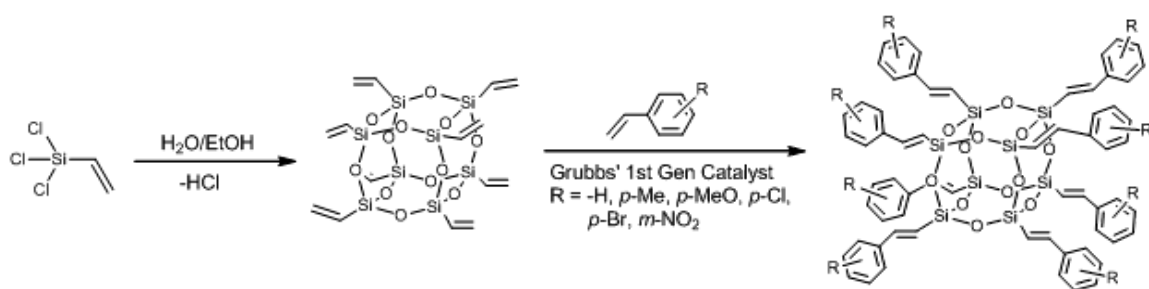


Figure 1.24 Synthesis of octavinylsilsesquioxane and octa(styrenyl)silsesquioxanes derivatives²¹¹

The UV-Vis absorption spectrum of SQ T8 is presented in Figure 1.25, with absorption maximum at 224 nm. It should be noted that the SQ cage doesn't have significant effect on the absorption properties of substituted chromophores. However, the photoluminescence spectrum may exhibit a significant shift with respect to that of the single chromophore.²¹²⁻²¹⁵ It has also been reported that luminescence stabilities could be significantly enhanced when SQs incorporated into π -conjugated polymers due to the steric effect of the rigid SQ units.²¹⁶⁻²¹⁷

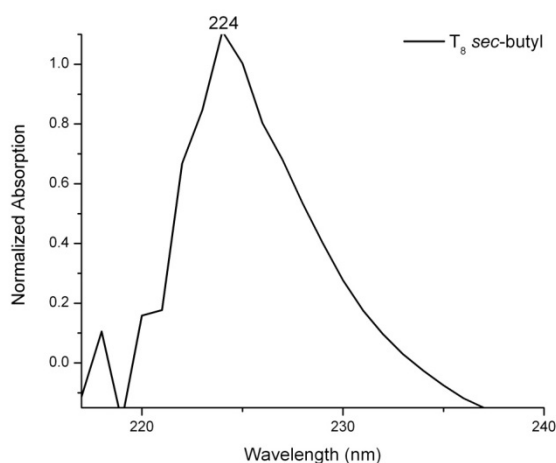


Figure 1.25 The absorption of the T_8 cage without chromophores. The absorption band is due to excitation of an electron from the non-bonding n orbital to the antibonding σ^* orbital¹³²

Numerous examples of the application of cubic SQs have been published in the fields of optics and electronics. Most importantly, silsesquioxanes derivatives as photoluminescent materials in organic light emitting diodes (OLEDs) are well studied.^{189, 193, 218} In 2003, Xiao *et al.*²¹⁹ reported the higher brightness (1320 cd m^{-2} at 3.5V) and external quantum efficiency ($\eta_{\text{ext}} = 2.2 \%$ photons per electron) of covalently anchored POSS at the chain-terminal of poly (phenylene vinylene), compared to poly(2-methoxy-5-(2-ethhexyloxy)-1,4-phenylenevinylene) which offers 230 cd m^{-2} at 3.5V and 1.5% efficiency. As shown in Figure 1.26, this material was the first introduction of silsesquioxane materials to the OLEDs application. It also demonstrated that when photo- and electro- active π conjugated chromophores are incorporated into SQ frameworks, their photoluminescence quantum efficiencies and thermal stabilities can be significantly improved.²¹⁹ To this effect, the electronic spectra of T_8 SQ derivative have been widely studied, including photoluminescent and fluorescent studies.^{211, 220-224} Most reported materials with OLEDs applications have core-shell structures with fluorescence chromophores as the shell attached to SQ cage center core. For example, a series of

polyaromatic substituted SQs, were prepared from octavinyl SQs through Heck coupling reactions.^{190, 218} Both of them are photoluminescent and have charge transport abilities.

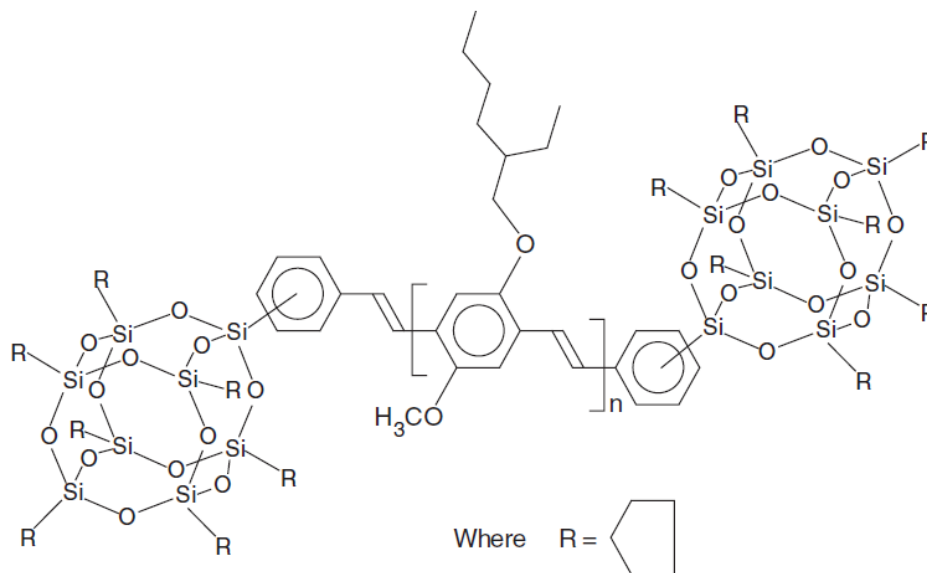


Figure 1.26 Structure of POSS anchored poly(2-methoxy-5-(2-ethhexyloxy)-1,4-phenylenevinylene)

There are extensive computational studies on electronic structure, electronic spectra, optical properties and reactivity of T_8 octahedral SQs over the past two decades.²²⁵⁻²²⁷ Computational modeling has been used to predict the electronic structure of the simplest cubic silsesquioxane (H_8T_8).^{227, 230-231} As shown in Figure 1.27, the results indicate that the LUMO is located in the center of the silsesquioxane core, whereas the HOMO involves the silicon, oxygen and hydrogen atoms on the SQ cage. The predicted band gap between the HOMO and LUMO is as high as 6~7 eV,^{227, 230} which suggest the SQ core can be considered as an insulator. However, when chromophores are attached to the SQ cage, its band gap could be dramatically lowered. Shown in Figure 1.28 are the HOMO and LUMO states of octastilbene-functionalized systems. In contrast to H_8T_8 , both the HOMO and LUMO this system are localized on the stilbene chromophores with a smaller band gap about 4.79 eV.²²⁸ In addition, Phillips *et al.*²²⁶ found out that the

excitations are mainly localized on the chromophores, except for vinylsilsesquioxane based on time-dependent density functional theory.²²⁶ Zheng *et al.*²²⁷ suggest that the emissive state of these octahedral silsesquioxanes is ligand-to-ligand, rather than ligand-to-silsesquioxane.²²⁷

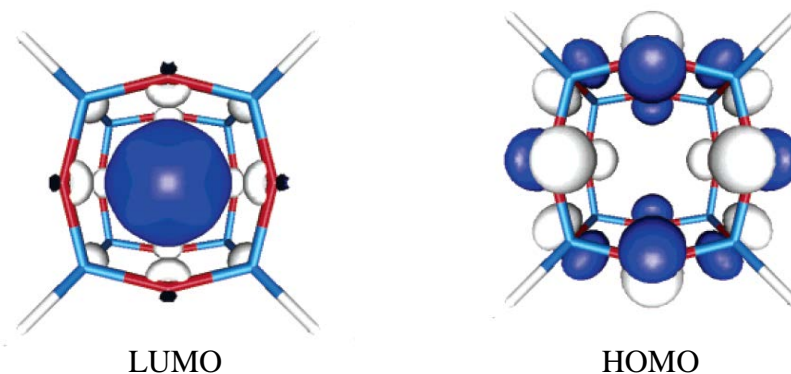


Figure 1.27 Isosurfaces (dark, positive; light, negative values) for HOMO and LUMO states of cubic silsesquioxanes ($\text{HSiO}_{1.5}$)₈²²⁹

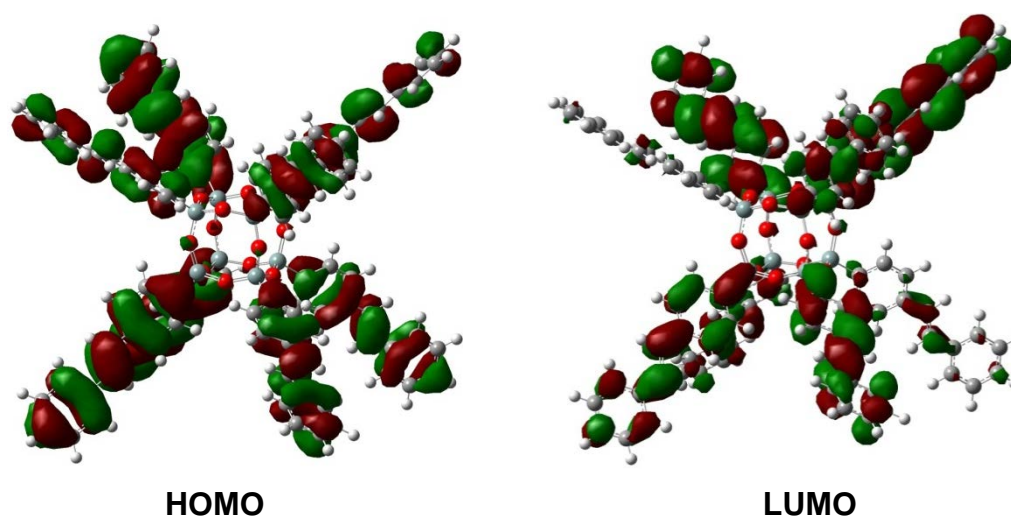


Figure 1.28 HOMO and LUMO states of octastilbene-functionalized OS, residing on the stilbene tethers²²⁸

1.5 Organization of Thesis

The remaining body of this dissertation is organized as following:

Chapter 2: Relevant experimental techniques utilized in this dissertation will be presented, including steady-state spectroscopy, quantum yield measurement and two-photon excited fluorescence excitation measurement, time-resolved fluorescence up-conversion spectroscopy, ultrafast transient absorption and two-photon measurement for solid thin film.

Chapter 3: In order to study the structure and charge transfer character relationship, steady state and two photon absorption properties of two sets of silsesquioxanes systems will be addressed. The investigated systems are: (1) cubic octavinylstilbenesilsesquioxanes derivatives, (2) polyfunctional phenylsilsesquioxanes: $[o\text{-RPhSiO}_{1.5}]_8$ (8mer), $[2,5\text{-R}_2\text{PhSiO}_{1.5}]_8$ (16mer), and $[\text{R}_3\text{PhSiO}_{1.5}]_8$ (23mer) compounds. Change in dipole moment term is one of the key parameters affecting two-photon cross-section. Therefore, investigating two-photon cross-section is of great importance to understand of intramolecular charge transfer properties with respect to different organic tethers as well as different of SQ core.

Chapter 4: Steady state and excited state properties of SQs with partial and full cages is completely discussed. The materials investigated are $\text{Me}_2\text{NStilbeneSi}(\text{OSiMe}_3)_3$ (corner), $\text{Me}_2\text{NStilbeneSi}(\text{O})(\text{OSiMe}_3)_4$ (half), and $[\text{Me}_2\text{NStilbeneSi}(\text{OSiMe}_3)\text{O}_{1.5}]_8$ (cube). Energy transfer process and excited state dynamics is address under the study of time-resolved fluorescence up-conversion spectroscopy and ultrafast transient absorption. The manuscript is prepared for the submission to Journal of Physical Chemistry. The ultrafast fluorescence dynamics and excited state charge transfer properties are investigated through ultrafast nonlinear optical spectroscopy methods.

Chapter 5: Other photovoltaic materials: energy migration processes in dendritic oligothiophene-perylene bisimides (G0, G1 and G2) are thoroughly presented. This work

is published in the Journal of Physical Chemistry B. Optical measurements carried out include nonlinear optical and time-resolved spectroscopy, including two-photon absorption, fluorescence upconversion, and excited state transient absorption. The ability of these molecules to undergo intramolecular fluorescence resonance energy transfer (FRET) from the dendritic oligothiophenes (DOT) to the perylene bisimide (PBI) moiety is discussed. In this study, it has been found out that the size of the bay area substitutes on the perylene bisimide plays a very essential role in affecting the electron accepting ability of the PBI core. When the size of the substitute is relatively large, the PBI core is highly twisted and its ability to self-assemble into π - π stacked aggregates and trap electrons is destroyed. This result is very useful for guiding new research on designing novel perylene base OPV materials.

Chapter 6: Two photon absorption investigation of ZnTeO photovoltaic thin films with intermediate band is discussed. Backgrounds including the basic concepts of intermediate band solar cells, introduction to ZnTe and ZnTeO photovoltaic thin film, and optical properties of ZnTeO is provided. A two-photon nonlinear transmission experiment is designed to confirm sub-band absorption and the proposed energy conversion mechanism for intermediated band ZnTeO.

Chapter 7: An overall summary of the research is presented for the purpose of synopsis. Future research is also suggested.

Appendix I-IV: Operation and troubleshooting details of Mai Tai and OPAL laser systems are presented in details.

References

- [1]. Singh, C.; Ghosh, R.; Mondal, J. A.; Palit, D. K., Excited State Dynamics of a Push-Pull Stilbene: A Femtosecond Transient Absorption Spectroscopic Study. *Journal of Photochemistry and Photobiology a-Chemistry* **2013**, 263, 50-60.

- [2]. Kopelman, R.; Shortreed, M.; Shi, Z. Y.; Tan, W. H.; Xu, Z. F.; Moore, J. S.; BarHaim, A.; Klafter, J., Spectroscopic Evidence for Excitonic Localization in Fractal Antenna Supermolecules. *Physical Review Letters* **1997**, 78 (7), 1239-1242.
- [3]. Cordes, D. B.; Lickiss, P. D.; Rataboul, F., Recent Developments in the Chemistry of Cubic Polyhedral Oligosilsesquioxanes. *Chemical Reviews* **2010**, 110 (4), 2081-2173.
- [4]. Hermann, W. A., Quantifying Global Exergy Resources. *Energy* **2006**, 31 (12), 1685-1702.
- [5]. Westenhoff, S.; Beenken, W. J. D.; Friend, R. H.; Greenham, N. C.; Yartsev, A.; Sundstrom, V., Anomalous Energy Transfer Dynamics Due to Torsional Relaxation in a Conjugated Polymer. *Physical Review Letters* **2006**, 97 (16).
- [6]. Szlufcik, J.; Sivoththaman, S.; Nijs, J. F.; Mertens, R. P.; VanOverstraeten, R., Low Cost Industrial Technologies of Crystalline Silicon Solar Cells. *Proceedings of the Ieee* **1997**, 85 (5), 711-730.
- [7]. Dou, L. T.; You, J. B.; Yang, J.; Chen, C. C.; He, Y. J.; Murase, S.; Moriarty, T.; Emery, K.; Li, G.; Yang, Y., Tandem Polymer Solar Cells Featuring a Spectrally Matched Low-Bandgap Polymer. *Nature Photonics* **2012**, 6 (3), 180-185.
- [8]. Krebs, F. C.; Tromholt, T.; Jorgensen, M., Upscaling of Polymer Solar Cell Fabrication Using Full Roll-to-Roll Processing. *Nanoscale* **2010**, 2 (6), 873-886.
- [9]. Troshin, P. A.; Susarova, D. K.; Khakina, E. A.; Goryachev, A. A.; Borshchev, O. V.; Ponomarenko, S. A.; Razumov, V. F.; Sariciftci, N. S., Material Solubility and Molecular Compatibility Effects in the Design of Fullerene/Polymer Composites for Organic Bulk Heterojunction Solar Cells. *Journal of Materials Chemistry* **2012**, 22 (35), 18433-18441.
- [10]. Brabec, C. J.; Nann, T.; Shaheen, S. E., Nanostructured P-N Junctions for Printable Photovoltaics. *Mrs Bulletin* **2004**, 29 (1), 43-47.
- [11]. Kaltenbrunner, M.; White, M. S.; Glowacki, E. D.; Sekitani, T.; Someya, T.; Sariciftci, N. S.; Bauer, S., Ultrathin and Lightweight Organic Solar Cells with High Flexibility. *Nature Communications* **2012**, 3.
- [12]. Logothetidis, S.; Georgiou, D.; Laskarakis, A.; Koidis, C.; Kalfagiannis, N., In-Line Spectroscopic Ellipsometry for the Monitoring of the Optical Properties and Quality of Roll-to-Roll Printed Nanolayers for Organic Photovoltaics. *Solar Energy Materials and Solar Cells* **2013**, 112, 144-156.

- [13]. Liu, Y.; Larsen-Olsen, T. T.; Zhao, X. G.; Andreasen, B.; Sondergaard, R. R.; Helgesen, M.; Norrman, K.; Jorgensen, M.; Krebs, F. C.; Zhan, X. W., All Polymer Photovoltaics: From Small Inverted Devices to Large Roll-to-Roll Coated and Printed Solar Cells. *Solar Energy Materials and Solar Cells* **2013**, *112*, 157-162.
- [14]. Koidis, C.; Logothetidis, S.; Kassavetis, S.; Kapnopoulos, C.; Karagiannidis, P. G.; Georgiou, D.; Laskarakis, A., Effect of Process Parameters on the Morphology and Nanostructure of Roll-to-Roll Printed P3ht:Pcbm Thin Films for Organic Photovoltaics. *Solar Energy Materials and Solar Cells* **2013**, *112*, 36-46.
- [15]. Koidis, C.; Logothetidis, S.; Ioakeimidis, A.; Laskarakis, A.; Kapnopoulos, C., Key Factors to Improve the Efficiency of Roll-to-Roll Printed Organic Photovoltaics. *Organic Electronics* **2013**, *14* (7), 1744-1748.
- [16]. Abdulrazzaq, O. A.; Saini, V.; Bourdo, S.; Dervishi, E.; Biris, A. S., Organic Solar Cells: A Review of Materials, Limitations, and Possibilities for Improvement. *Particulate Science and Technology* **2013**, *31* (5), 427-442.
- [17]. Ameri, T.; Dennler, G.; Lungenschmied, C.; Brabec, C. J., Organic Tandem Solar Cells: A Review. *Energy & Environmental Science* **2009**, *2* (4), 347-363.
- [18]. National Renewable Energy Laboratory.
<http://rredc.nrel.gov/solar/spectra/am1.5/S>.
- [19]. Goodman, A. M.; Rose, A., Double Extraction of Uniformly Generated Electron-Hole Pairs from Insulators with Noninjecting Contacts. *Journal of Applied Physics* **1971**, *42* (7), 2823-&.
- [20]. Murphy, L.; Hong, W.; Aziz, H.; Li, Y. N., Influences of Using a High Mobility Donor Polymer on Solar Cell Performance. *Organic Electronics* **2013**, *14* (12), 3484-3492.
- [21]. Hoppe, H.; Sariciftci, N. S., Organic Solar Cells: An Overview. *Journal of Materials Research* **2004**, *19* (7), 1924-1945.
- [22]. Mandal, G.; Bhattacharya, S.; Das, S.; Ganguly, T., The Rates of Charge Separation and Energy Destructive Charge Recombination Processes within an Organic Dyad in Presence of Metal-Semiconductor Core Shell Nanocomposites. *Journal of Nanoscience and Nanotechnology* **2012**, *12* (1), 187-194.
- [23]. Dennler, G.; Scharber, M. C.; Brabec, C. J., Polymer-Fullerene Bulk-Heterojunction Solar Cells. *Advanced Materials* **2009**, *21* (13), 1323-1338.

- [24]. Clarke, T. M.; Jamieson, F. C.; Durrant, J. R., Transient Absorption Studies of Bimolecular Recombination Dynamics in Polythiophene/Fullerene Blend Films. *Journal of Physical Chemistry C* **2009**, *113* (49), 20934-20941.
- [25]. Wright, M.; Uddin, A., Organic-Inorganic Hybrid Solar Cells: A Comparative Review. *Solar Energy Materials and Solar Cells* **2012**, *107*, 87-111.
- [26]. Spanggaard, H.; Krebs, F. C., A Brief History of the Development of Organic and Polymeric Photovoltaics. *Solar Energy Materials and Solar Cells* **2004**, *83* (2-3), 125-146.
- [27]. Bundgaard, E.; Krebs, F. C., Low Band Gap Polymers for Organic Photovoltaics. *Solar Energy Materials and Solar Cells* **2007**, *91* (11), 954-985.
- [28]. Kroon, R.; Lenes, M.; Hummelen, J. C.; Blom, P. W. M.; De Boer, B., Small Bandgap Polymers for Organic Solar Cells (Polymer Material Development in the Last 5 Years). *Polymer Reviews* **2008**, *48* (3), 531-582.
- [29]. Chamberlain, G. A., Organic Solar-Cells - a Review. *Solar Cells* **1983**, *8* (1), 47-83.
- [30]. Qian, X. M.; Liu, H. B.; Li, Y. L., Self-Assembly Low Dimensional Inorganic/Organic Heterojunction Nanomaterials. *Chinese Science Bulletin* **2013**, *58* (22), 2686-2697.
- [31]. Brabec, C. J.; Shaheen, S. E.; Fromherz, T.; Padinger, F.; Hummelen, J. C.; Dhanabalan, A.; Janssen, R. A. J.; Sariciftci, N. S., Organic Photovoltaic Devices Produced from Conjugated Polymer/Methanofullerene Bulk Heterojunctions. *Synthetic Metals* **2001**, *121* (1-3), 1517-1520.
- [32]. Pivrikas, A.; Sariciftci, N. S.; Juska, G.; Osterbacka, R., A Review of Charge Transport and Recombination in Polymer/Fullerene Organic Solar Cells. *Progress in Photovoltaics* **2007**, *15* (8), 677-696.
- [33]. Benten, H.; Ogawa, M.; Ohkita, H.; Ito, S., Design of Multilayered Nanostructures and Donor-Acceptor Interfaces in Solution-Processed Thin-Film Organic Solar Cells. *Advanced Functional Materials* **2008**, *18* (10), 1563-1572.
- [34]. Shirota, Y., Organic Materials for Electronic and Optoelectronic Devices. *Journal of Materials Chemistry* **2000**, *10* (1), 1-25.
- [35]. Brabec, C. J.; Durrant, J. R., Solution-Processed Organic Solar Cells. *Mrs Bulletin* **2008**, *33* (7), 670-675.

- [36]. Thompson, B. C.; Frechet, J. M. J., Organic Photovoltaics - Polymer-Fullerene Composite Solar Cells. *Angewandte Chemie-International Edition* **2008**, *47* (1), 58-77.
- [37]. Liu, Z. Y.; Ojima, H.; Hong, Z. R.; Kido, J. J.; Tian, W. J.; Wang, X. F., Solution-Processed Organic Photovoltaics Based on Indoline Dye Molecules Developed in Dye-Sensitized Solar Cells. *Molecules* **2013**, *18* (3), 3107-3117.
- [38]. Wan, X. J.; Liu, Y. S.; Wang, F.; Zhou, J. Y.; Long, G. K.; Chen, Y. S., Improved Efficiency of Solution Processed Small Molecules Organic Solar Cells Using Thermal Annealing. *Organic Electronics* **2013**, *14* (6), 1562-1569.
- [39]. Zhou, J. Y.; Zuo, Y.; Wan, X. J.; Long, G. K.; Zhang, Q.; Ni, W.; Liu, Y. S.; Li, Z.; He, G. R.; Li, C. X.; Kan, B.; Li, M. M.; Chen, Y. S., Solution-Processed and High-Performance Organic Solar Cells Using Small Molecules with a Benzodithiophene Unit. *Journal of the American Chemical Society* **2013**, *135* (23), 8484-8487.
- [40]. Wohrle, D.; Meissner, D., Organic Solar-Cells. *Advanced Materials* **1991**, *3* (3), 129-138.
- [41]. Peumans, P.; Uchida, S.; Forrest, S. R., Efficient Bulk Heterojunction Photovoltaic Cells Using Small-Molecular-Weight Organic Thin Films. *Nature* **2003**, *425* (6954), 158-162.
- [42]. Peumans, P.; Yakimov, A.; Forrest, S. R., Small Molecular Weight Organic Thin-Film Photodetectors and Solar Cells. *Journal of Applied Physics* **2003**, *93* (7), 3693-3723.
- [43]. Xue, J. G.; Rand, B. P.; Uchida, S.; Forrest, S. R., A Hybrid Planar-Mixed Molecular Heterojunction Photovoltaic Cell. *Advanced Materials* **2005**, *17* (1), 66-+.
- [44]. Pulgdollers, J.; Voz, C.; Fonrodona, M.; Cheylan, S.; Stella, M.; Andreu, J.; Vetter, M.; Alcubilla, R., Copper Phthalocyanine Thin-Film Transistors with Polymeric Gate Dielectric. *Journal of Non-Crystalline Solids* **2006**, *352* (9-20), 1778-1782.
- [45]. Signerski, R., The Photovoltaic Effect in a Heterojunction of Molybdenyl Phthalocyanine and Perylene Dye. *Journal of Non-Crystalline Solids* **2006**, *352* (40-41), 4319-4324.

- [46]. Vertsimakha, Y.; Mamykin, S.; Lutsyk, P., Substitution of Phthalocyanines Affecting the Properties of Their Films and Heterostructures. *Chemical Physics* **2012**, *404*, 16-21.
- [47]. Gunes, S.; Neugebauer, H.; Sariciftci, N. S., Conjugated Polymer-Based Organic Solar Cells. *Chemical Reviews* **2007**, *107* (4), 1324-1338.
- [48]. Brunetti, F. G.; Kumar, R.; Wudl, F., Organic Electronics from Perylene to Organic Photovoltaics: Painting a Brief History with a Broad Brush. *Journal of Materials Chemistry* **2010**, *20* (15), 2934-2948.
- [49]. Li, C.; Wonneberger, H., Perylene Imides for Organic Photovoltaics: Yesterday, Today, and Tomorrow. *Advanced Materials* **2012**, *24* (5), 613-636.
- [50]. Fuller, M. J.; Sinks, L. E.; Rybtehinski, B.; Giaimo, J. M.; Li, X. Y.; Wasielewski, M. R., Ultrafast Photoinduced Charge Separation Resulting from Self-Assembly of a Green Perylene-Based Dye into Pi-Stacked Arrays. *Journal of Physical Chemistry A* **2005**, *109* (6), 970-975.
- [51]. Fortage, J.; Severac, M.; Houarner-Rassin, C.; Pellegrin, Y.; Blart, E.; Odobel, F., Synthesis of New Perylene Imide Dyes and Their Photovoltaic Performances in Nanocrystalline TiO₂ Dye-Sensitized Solar Cells. *Journal of Photochemistry and Photobiology a-Chemistry* **2008**, *197* (2-3), 156-169.
- [52]. Howard, I. A.; Laquai, F.; Keivanidis, P. E.; Friend, R. H.; Greenham, N. C., Perylene Tetracarboxydiimide as an Electron Acceptor in Organic Solar Cells: A Study of Charge Generation and Recombination. *Journal of Physical Chemistry C* **2009**, *113* (50), 21225-21232.
- [53]. Sharma, G. D.; Suresh, P.; Mikroyannidis, J. A.; Stylianakis, M. M., Efficient Bulk Heterojunction Devices Based on Phenylenevinylene Small Molecule and Perylene-Pyrene Bisimide. *Journal of Materials Chemistry* **2010**, *20* (3), 561-567.
- [54]. Tang, C. W., 2-Layer Organic Photovoltaic Cell. *Applied Physics Letters* **1986**, *48* (2), 183-185.
- [55]. Yu, G.; Heeger, A. J., Charge Separation and Photovoltaic Conversion in Polymer Composites with Internal Donor-Acceptor Heterojunctions. *Journal of Applied Physics* **1995**, *78* (7), 4510-4515.
- [56]. Halls, J. J. M.; Walsh, C. A.; Greenham, N. C.; Marseglia, E. A.; Friend, R. H.; Moratti, S. C.; Holmes, A. B., Efficient Photodiodes from Interpenetrating Polymer Networks. *Nature* **1995**, *376* (6540), 498-500.

- [57]. Yu, G.; Gao, J.; Hummelen, J. C.; Wudl, F.; Heeger, A. J., Polymer Photovoltaic Cells - Enhanced Efficiencies Via a Network of Internal Donor-Acceptor Heterojunctions. *Science* **1995**, *270* (5243), 1789-1791.
- [58]. Tamaki, R.; Tanaka, Y.; Asuncion, M. Z.; Choi, J. W.; Laine, R. M., Octa(Aminophenyl)Silsesquioxane as a Nanoconstruction Site. *Journal of the American Chemical Society* **2001**, *123* (49), 12416-12417.
- [59]. Hadipour, A.; Muller, R.; Heremans, P., Room Temperature Solution-Processed Electron Transport Layer for Organic Solar Cells. *Organic Electronics* **2013**, *14* (10), 2379-2386.
- [60]. Lee, J. K.; Lee, S.; Yun, S. J., Effects of Fused Thiophene Bridges in Organic Semiconductors for Solution-Processed Small-Molecule Organic Solar Cells. *Bulletin of the Korean Chemical Society* **2013**, *34* (7), 2148-2154.
- [61]. Shockley, W.; Queisser, H. J., Detailed Balance Limit of Efficiency of P-N Junction Solar Cells. *Journal of Applied Physics* **1961**, *32* (3), 510-&.
- [62]. Fonash, S., *Solar Cell Device Physics*. Wiley: New York, 1981.
- [63]. Scharber, M. C.; Wuhlbacher, D.; Koppe, M.; Denk, P.; Waldauf, C.; Heeger, A. J.; Brabec, C. L., Design Rules for Donors in Bulk-Heterojunction Solar Cells - Towards 10 % Energy-Conversion Efficiency. *Advanced Materials* **2006**, *18* (6), 789-+.
- [64]. Do, T. T.; Ha, Y. E.; Kim, J. H., Effect of the Number of Thiophene Rings in Polymers with 2,1,3-Benzooxadiazole Core on the Photovoltaic Properties. *Organic Electronics* **2013**, *14* (10), 2673-2681.
- [65]. Song, H. S.; Ahn, S. K.; Karthikeyan, N. S.; Gal, Y. S.; Jin, S. H.; Lee, J. W., Study on Low-Band Gap Polymers Based on Diketopyrrolopyrrole for Organic Photovoltaic Applications. *Molecular Crystals and Liquid Crystals* **2013**, *578* (1), 55-62.
- [66]. Park, O. Y.; Kim, H. U.; Kim, J. H.; Park, J. B.; Kwak, J.; Shin, W. S.; Yoon, S. C.; Hwang, D. H., Tetrafluorene-9,9'-Bifluorenylidene as a Non-Fullerene Type Electron Acceptor for P3ht-Based Bulk-Heterojunction Polymer Solar Cells. *Solar Energy Materials and Solar Cells* **2013**, *116*, 275-282.
- [67]. Campos, L. M.; Tontcheva, A.; Gunes, S.; Sonmez, G.; Neugebauer, H.; Sariciftci, N. S.; Wudl, F., Extended Photocurrent Spectrum of a Low Band Gap Polymer in a Bulk Heterojunction Solar Cell. *Chemistry of Materials* **2005**, *17* (16), 4031-4033.

- [68]. Tamayo, A. B.; Dang, X. D.; Walker, B.; Seo, J.; Kent, T.; Nguyen, T. Q., A Low Band Gap, Solution Processable Oligothiophene with a Dialkylated Diketopyrrolopyrrole Chromophore for Use in Bulk Heterojunction Solar Cells. *Applied Physics Letters* **2009**, *94* (10).
- [69]. Velusamy, M.; Thomas, K. R. J.; Lin, J. T.; Hsu, Y. C.; Ho, K. C., Organic Dyes Incorporating Low-Band-Gap Chromophores for Dye-Sensitized Solar Cells. *Organic Letters* **2005**, *7* (10), 1899-1902.
- [70]. Brabec, C. J.; Gowrisanker, S.; Halls, J. J. M.; Laird, D.; Jia, S. J.; Williams, S. P., Polymer-Fullerene Bulk-Heterojunction Solar Cells. *Advanced Materials* **2010**, *22* (34), 3839-3856.
- [71]. Vandewal, K.; Gadisa, A.; Oosterbaan, W. D.; Bertho, S.; Banishoeib, F.; Van Severen, I.; Lutsen, L.; Cleij, T. J.; Vanderzande, D.; Manca, J. V., The Relation between Open-Circuit Voltage and the Onset of Photocurrent Generation by Charge-Transfer Absorption in Polymer: Fullerene Bulk Heterojunction Solar Cells. *Advanced Functional Materials* **2008**, *18* (14), 2064-2070.
- [72]. Walker, B.; Kim, C.; Nguyen, T. Q., Small Molecule Solution-Processed Bulk Heterojunction Solar Cells. *Chemistry of Materials* **2011**, *23* (3), 470-482.
- [73]. Zhou, E. J.; Nakamura, M.; Nishizawa, T.; Zhang, Y.; Wei, Q. S.; Tajima, K.; Yang, C. H.; Hashimoto, K., Synthesis and Photovoltaic Properties of a Novel Low Band Gap Polymer Based on N-Substituted Dithieno 3,2-B:2',3'-D Pyrrole. *Macromolecules* **2008**, *41* (22), 8302-8305.
- [74]. Bredas, J. L.; Heeger, A. J.; Wudl, F., Towards Organic Polymers with Very Small Intrinsic Band-Gaps .1. Electronic-Structure of Polyisothianaphthene and Derivatives. *Journal of Chemical Physics* **1986**, *85* (8), 4673-4678.
- [75]. Karikomi, M.; Kitamura, C.; Tanaka, S.; Yamashita, Y., New Narrow-Bandgap Polymer Composed of Benzobis(1,2,5-Thiadiazole) and Thiophenes. *Journal of the American Chemical Society* **1995**, *117* (25), 6791-6792.
- [76]. Yamamoto, T.; Sanechika, K.; Yamamoto, A., Preparation of Thermostable and Electric-Conducting Poly(2,5-Thienylene). *Journal of Polymer Science Part C-Polymer Letters* **1980**, *18* (1), 9-12.
- [77]. Salzner, U.; Lagowski, J. B.; Pickup, P. G.; Poirier, R. A., Comparison of Geometries and Electronic Structures of Polyacetylene, Polyborole, Polycyclopentadiene, Polypyrrole, Polyfuran, Polysilole, Polyphosphole,

Polythiophene, Polyselenophene and Polytellurophene. *Synthetic Metals* **1998**, *96* (3), 177-189.

- [78]. Andersson, M. R.; Thomas, O.; Mammo, W.; Svensson, M.; Theander, M.; Inganäs, O., Substituted Polythiophenes Designed for Optoelectronic Devices and Conductors. *Journal of Materials Chemistry* **1999**, *9* (9), 1933-1940.
- [79]. McCullough, R. D., The Chemistry of Conducting Polythiophenes. *Advanced Materials* **1998**, *10* (2), 93-+.
- [80]. Chen, J. W.; Cao, Y., Development of Novel Conjugated Donor Polymers for High-Efficiency Bulk-Heterojunction Photovoltaic Devices. *Accounts of Chemical Research* **2009**, *42* (11), 1709-1718.
- [81]. Aasmundtveit, K. E.; Samuelsen, E. J.; Guldstein, M.; Steinsland, C.; Flornes, O.; Fagermo, C.; Seeberg, T. M.; Pettersson, L. A. A.; Inganäs, O.; Feidenhans'l, R.; Ferrer, S., Structural Anisotropy of Poly(Alkylthiophene) Films. *Macromolecules* **2000**, *33* (8), 3120-3127.
- [82]. Breiby, D. W.; Samuelsen, E. J.; Groenendaal, L.; Struth, B., Smectic Structures in Electrochemically Prepared Poly(3,4-Ethylenedioxythiophene) Films. *Journal of Polymer Science Part B-Polymer Physics* **2003**, *41* (9), 945-952.
- [83]. Fell, H. J.; Samuelsen, E. J.; Mardalen, J.; Andersson, M. R., X-Ray-Diffraction Study of Octylphenyl-Substituted Polythiophene. *Synthetic Metals* **1995**, *69* (1-3), 283-284.
- [84]. Schilinsky, P.; Asawapirom, U.; Scherf, U.; Biele, M.; Brabec, C. J., Influence of the Molecular Weight of Poly(3-Hexylthiophene) on the Performance of Bulk Heterojunction Solar Cells. *Chemistry of Materials* **2005**, *17* (8), 2175-2180.
- [85]. Breiby, D. W.; Samuelsen, E. J.; Konovalov, O., The Drying Behaviour of Conjugated Polymer Solutions. *Synthetic Metals* **2003**, *139* (2), 361-369.
- [86]. Aasmundtveit, K. E.; Samuelsen, E. J.; Hoffmann, K.; Bakken, E.; Carlsen, P. H. J., Structural Studies of Polyalkylthiophenes with Alternating Sidechain Positioning. *Synthetic Metals* **2000**, *113* (1-2), 7-18.
- [87]. Aasmundtveit, K. E.; Samuelsen, E. J.; Inganäs, O.; Pettersson, L. A. A.; Johansson, T.; Ferrer, S., Structural Aspects of Electrochemical Doping and Dedoping of Poly(3,4-Ethylenedioxythiophene). *Synthetic Metals* **2000**, *113* (1-2), 93-97.

- [88]. Aasmundtveit, K. E.; Samuelsen, E. J.; Mammo, W.; Svensson, M.; Andersson, M. R.; Pettersson, L. A. A.; Inganas, O., Structural Ordering in Phenyl-Substituted Polythiophenes. *Macromolecules* **2000**, *33* (15), 5481-5489.
- [89]. Mardalen, J.; Samuelsen, E. J.; Gautun, O. R.; Carlsen, P. H., X-Ray-Scattering from Oriented Poly(3-Alkylthiophenes). *Synthetic Metals* **1992**, *48* (3), 363-380.
- [90]. Fell, H. J.; Samuelsen, E. J.; Andersson, M. R.; Alsnielsen, J.; Grubel, G.; Mardalen, J., Structural Aspects of Oriented Poly(Octylphenylthiophene) Studied in Bulk and Submicron Layers by X-Ray-Diffraction. *Synthetic Metals* **1995**, *73* (3), 279-283.
- [91]. Prosa, T. J.; Winokur, M. J.; Moulton, J.; Smith, P.; Heeger, A. J., X-Ray Structural Studies of Poly(3-Alkylthiophenes) - an Example of an Inverse Comb. *Macromolecules* **1992**, *25* (17), 4364-4372.
- [92]. Sun, Y. M.; Welch, G. C.; Leong, W. L.; Takacs, C. J.; Bazan, G. C.; Heeger, A. J., Solution-Processed Small-Molecule Solar Cells with 6.7% Efficiency. *Nature Materials* **2012**, *11* (1), 44-48.
- [93]. Bredas, J. L.; Norton, J. E.; Cornil, J.; Coropceanu, V., Molecular Understanding of Organic Solar Cells: The Challenges. *Accounts of Chemical Research* **2009**, *42* (11), 1691-1699.
- [94]. He, Y. J.; Chen, H. Y.; Hou, J. H.; Li, Y. F., Indene-C-60 Bisadduct: A New Acceptor for High-Performance Polymer Solar Cells. *Journal of the American Chemical Society* **2010**, *132* (4), 1377-1382.
- [95]. Lungenschmied, C.; Dennler, G.; Neugebauer, H.; Sariciftci, S. N.; Glatthaar, M.; Meyer, T.; Meyer, A., Flexible, Long-Lived, Large-Area, Organic Solar Cells. *Solar Energy Materials and Solar Cells* **2007**, *91* (5), 379-384.
- [96]. Koster, L. J. A.; Mihailitchi, V. D.; Blom, P. W. M., Bimolecular Recombination in Polymer/Fullerene Bulk Heterojunction Solar Cells. *Applied Physics Letters* **2006**, *88* (5).
- [97]. Koster, L. J. A.; Mihailitchi, V. D.; Blom, P. W. M., Ultimate Efficiency of Polymer/Fullerene Bulk Heterojunction Solar Cells. *Applied Physics Letters* **2006**, *88* (9).
- [98]. van Hal, P. A.; Meskers, S. C. J.; Janssen, R. A. J., Photoinduced Energy and Electron Transfer in Oligo(P-Phenylene Vinylene)-Fullerene Dyads. *Applied Physics a-Materials Science & Processing* **2004**, *79* (1), 41-46.

- [99]. Liu, Y. X.; Summers, M. A.; Scully, S. R.; McGehee, M. D., Resonance Energy Transfer from Organic Chromophores to Fullerene Molecules. *Journal of Applied Physics* **2006**, *99* (9).
- [100]. Bhavsar, G. A.; Asha, S. K., Pentadecyl Phenol- and Cardanol-Functionalized Fluorescent, Room-Temperature Liquid-Crystalline Perylene Bisimides: Effect of Pendant Chain Unsaturation on Self-Assembly. *Chemistry-a European Journal* **2011**, *17* (45), 12646-12658.
- [101]. Chen, Z. J.; Lohr, A.; Saha-Moller, C. R.; Wurthner, F., Self-Assembled Pi-Stacks of Functional Dyes in Solution: Structural and Thermodynamic Features. *Chemical Society Reviews* **2009**, *38* (2), 564-584.
- [102]. Bottari, G.; de la Torre, G.; Guldi, D. M.; Torres, T., Covalent and Noncovalent Phthalocyanine-Carbon Nanostructure Systems: Synthesis, Photoinduced Electron Transfer, and Application to Molecular Photovoltaics. *Chemical Reviews* **2010**, *110* (11), 6768-6816.
- [103]. De Arco, L. G.; Zhang, Y.; Schlenker, C. W.; Ryu, K.; Thompson, M. E.; Zhou, C. W., Continuous, Highly Flexible, and Transparent Graphene Films by Chemical Vapor Deposition for Organic Photovoltaics. *Acs Nano* **2010**, *4* (5), 2865-2873.
- [104]. Martinez-Diaz, M. V.; de la Torre, G.; Torres, T., Lighting Porphyrins and Phthalocyanines for Molecular Photovoltaics. *Chemical Communications* **2010**, *46* (38), 7090-7108.
- [105]. Sennbro, C. J.; Lindh, C. H.; Tinnerberg, H.; Gustavsson, C.; Littorin, M.; Welinder, H.; Jonsson, B. A. G., Development, Validation and Characterization of an Analytical Method for the Quantification of Hydrolysable Urinary Metabolites and Plasma Protein Adducts of 2,4- and 2,6-Toluene Diisocyanate, 1,5-Naphthalene Diisocyanate and 4,4'-Methylenediphenyl Diisocyanate. *Biomarkers* **2003**, *8* (3-4), 204-217.
- [106]. Yasuda, T.; Shinohara, Y.; Ishi-i, T.; Han, L. Y., Use of Benzothiadiazole-Triphenylamine Amorphous Polymer for Reproducible Performance of Polymer-Fullerene Bulk-Heterojunction Solar Cells. *Organic Electronics* **2012**, *13* (10), 1802-1808.
- [107]. Schulze, K.; Uhrich, C.; Schuppel, R.; Leo, K.; Pfeiffer, M.; Brier, E.; Reinold, E.; Bauerle, P., Efficient Vacuum-Deposited Organic Solar Cells Based on a New Low-Bandgap Oligothiophene and Fullerene C-60. *Advanced Materials* **2006**, *18* (21), 2872-+.
- [108]. Ayzner, A. L.; Tassone, C. J.; Tolbert, S. H.; Schwartz, B. J., Reappraising the Need for Bulk Heterojunctions in Polymer-Fullerene Photovoltaics: The Role of

Carrier Transport in All-Solution-Processed P3ht/Pcbm Bilayer Solar Cells. *Journal of Physical Chemistry C* **2009**, *113* (46), 20050-20060.

- [109]. Irwin, M. D.; Buchholz, B.; Hains, A. W.; Chang, R. P. H.; Marks, T. J., P-Type Semiconducting Nickel Oxide as an Efficiency-Enhancing Anode Interfacial Layer in Polymer Bulk-Heterojunction Solar Cells. *Proceedings of the National Academy of Sciences of the United States of America* **2008**, *105* (8), 2783-2787.
- [110]. Girotto, C.; Rand, B. P.; Genoe, J.; Heremans, P., Exploring Spray Coating as a Deposition Technique for the Fabrication of Solution-Processed Solar Cells. *Solar Energy Materials and Solar Cells* **2009**, *93* (4), 454-458.
- [111]. Na, S. I.; Yu, B. K.; Kim, S. S.; Vak, D.; Kim, T. S.; Yeo, J. S.; Kim, D. Y., Fully Spray-Coated Ito-Free Organic Solar Cells for Low-Cost Power Generation. *Solar Energy Materials and Solar Cells* **2010**, *94* (8), 1333-1337.
- [112]. Krebs, F. C., Fabrication and Processing of Polymer Solar Cells: A Review of Printing and Coating Techniques. *Solar Energy Materials and Solar Cells* **2009**, *93* (4), 394-412.
- [113]. Kunz, D. A.; Schmid, J.; Feicht, P.; Erath, J.; Fery, A.; Breut, J., Clay-Based Nanocomposite Coating for Flexible Optoelectronics Applying Commercial Polymers. *Acs Nano* **2013**, *7* (5), 4275-4280.
- [114]. Egbe, D. A. M.; Carbonnier, B.; Birckner, E.; Grummt, U. W., Arylene-Ethynylene/Arylene-Vinylene Copolymers: Synthesis and Structure-Property Relationships. *Progress in Polymer Science* **2009**, *34* (10), 1023-1067.
- [115]. Hoth, C. N.; Choulis, S. A.; Schilinsky, P.; Brabec, C. J., High Photovoltaic Performance of Inkjet Printed Polymer: Fullerene Blends. *Advanced Materials* **2007**, *19* (22), 3973-+.
- [116]. Lange, A.; Wegener, M.; Boeffel, C.; Fischer, B.; Wedel, A.; Neher, D., A New Approach to the Solvent System for Inkjet-Printed P3ht:Pcbm Solar Cells and Its Use in Devices with Printed Passive and Active Layers. *Solar Energy Materials and Solar Cells* **2010**, *94* (10), 1816-1821.
- [117]. Kallmann, H.; Pope, M., Photovoltaic Effect in Organic Crystals. *Journal of Chemical Physics* **1959**, *30* (2), 585-586.
- [118]. Ohkita, H.; Cook, S.; Astuti, Y.; Duffy, W.; Tierney, S.; Zhang, W.; Heeney, M.; McCulloch, I.; Nelson, J.; Bradley, D. D. C.; Durrant, J. R., Charge Carrier Formation in Polythiophene/Fullerene Blend Films Studied by Transient

Absorption Spectroscopy. *Journal of the American Chemical Society* **2008**, *130* (10), 3030-3042.

- [119]. Mihailetschi, V. D.; Koster, L. J. A.; Blom, P. W. M.; Melzer, C.; de Boer, B.; van Duren, J. K. J.; Janssen, R. A. J., Compositional Dependence of the Performance of Poly(P-Phenylene Vinylene): Methanofullerene Bulk-Heterojunction Solar Cells. *Advanced Functional Materials* **2005**, *15* (5), 795-801.
- [120]. Cook, S.; Katoh, R.; Furube, A., Ultrafast Studies of Charge Generation in Pcbm:P3ht Blend Films Following Excitation of the Fullerene Pcbm. *Journal of Physical Chemistry C* **2009**, *113* (6), 2547-2552.
- [121]. Howard, I. A.; Laquai, F., Optical Probes of Charge Generation and Recombination in Bulk Heterojunction Organic Solar Cells. *Macromolecular Chemistry and Physics* **2010**, *211* (19), 2063-2070.
- [122]. Brabec, C. J.; Zerza, G.; Cerullo, G.; De Silvestri, S.; Luzzati, S.; Hummelen, J. C.; Sariciftci, S., Tracing Photoinduced Electron Transfer Process in Conjugated Polymer/Fullerene Bulk Heterojunctions in Real Time. *Chemical Physics Letters* **2001**, *340* (3-4), 232-236.
- [123]. Nogueira, A. F.; Montanari, I.; Nelson, J.; Durrant, J. R.; Winder, C.; Sariciftci, N. S., Charge Recombination in Conjugated Polymer/Fullerene Blended Films Studied by Transient Absorption Spectroscopy. *Journal of Physical Chemistry B* **2003**, *107* (7), 1567-1573.
- [124]. Clarke, T. M.; Ballantyne, A.; Shoaee, S.; Soon, Y. W.; Duffy, W.; Heeney, M.; McCulloch, I.; Nelson, J.; Durrant, J. R., Analysis of Charge Photogeneration as a Key Determinant of Photocurrent Density in Polymer: Fullerene Solar Cells. *Advanced Materials* **2010**, *22* (46), 5287-5291.
- [125]. Clarke, T. M.; Ballantyne, A. M.; Nelson, J.; Bradley, D. D. C.; Durrant, J. R., Free Energy Control of Charge Photogeneration in Polythiophene/Fullerene Solar Cells: The Influence of Thermal Annealing on P3ht/Pcbm Blends. *Advanced Functional Materials* **2008**, *18* (24), 4029-4035.
- [126]. Clarke, T.; Ballantyne, A.; Jamieson, F.; Brabec, C.; Nelson, J.; Durrant, J., Transient Absorption Spectroscopy of Charge Photogeneration Yields and Lifetimes in a Low Bandgap Polymer/Fullerene Film. *Chemical Communications* **2009**, (1), 89-91.
- [127]. Goppert-Mayer, M., Elementary File with Two Quantum Fissures. *Annalen Der Physik* **1931**, *9* (3), 273-294.

- [128]. Kaiser, W.; Garrett, C. G. B., 2-Photon Excitation in $\text{CaF}_2 - \text{Eu}^{2+}$. *Physical Review Letters* **1961**, 7 (6), 229-&.
- [129]. He, G. S.; Xu, G. C.; Prasad, P. N.; Reinhardt, B. A.; Bhatt, J. C.; Dillard, A. G., 2-Photon Absorption and Optical-Limiting Properties of Novel Organic-Compounds. *Optics Letters* **1995**, 20 (5), 435-437.
- [130]. Narang, U.; Zhao, C. F.; Bhawalkar, J. D.; Bright, F. V.; Prasad, P. N., Characterization of a New Solvent-Sensitive Two-Photon-Induced Fluorescent (Aminostyryl)Pyridinium Salt Dye. *Journal of Physical Chemistry* **1996**, 100 (11), 4521-4525.
- [131]. Albota, M.; Beljonne, D.; Bredas, J. L.; Ehrlich, J. E.; Fu, J. Y.; Heikal, A. A.; Hess, S. E.; Kogej, T.; Levin, M. D.; Marder, S. R.; McCord-Maughon, D.; Perry, J. W.; Rockel, H.; Rumi, M.; Subramaniam, C.; Webb, W. W.; Wu, X. L.; Xu, C., Design of Organic Molecules with Large Two-Photon Absorption Cross Sections. *Science* **1998**, 281 (5383), 1653-1656.
- [132]. Kogej, T.; Beljonne, D.; Meyers, F.; Perry, J. W.; Marder, S. R.; Bredas, J. L., Mechanisms for Enhancement of Two-Photon Absorption in Donor-Acceptor Conjugated Chromophores. *Chemical Physics Letters* **1998**, 298 (1-3), 1-6.
- [133]. Lin, T.-C.; Guo, F.-L.; Li, M.-H.; Liu, C.-Y., Degenerate Two-Photon Absorption and Effective Optical-Power-Limiting Properties of Multipolar Chromophores Derived from 2,3,8-Trisubstituted Indenoquinoxaline. *Chemistry, an Asian journal* **2013**, 8 (9), 2102-2110.
- [134]. Pawlicki, M.; Collins, H. A.; Denning, R. G.; Anderson, H. L., Two-Photon Absorption and the Design of Two-Photon Dyes. *Angewandte Chemie-International Edition* **2009**, 48 (18), 3244-3266.
- [135]. Spangler, C. W., Recent Development in the Design of Organic Materials for Optical Power Limiting. *Journal of Materials Chemistry* **1999**, 9 (9), 2013-2020.
- [136]. Corredor, C. C.; Huang, Z. L.; Belfield, K. D., Two-Photon 3d Optical Data Storage Via Fluorescence Modulation of an Efficient Fluorene Dye by a Photochromic Diarylethene. *Advanced Materials* **2006**, 18 (21), 2910-+.
- [137]. Corredor, C. C.; Huang, Z. L.; Belfield, K. D.; Morales, A. R.; Bondar, M. V., Photochromic Polymer Composites for Two-Photon 3d Optical Data Storage. *Chemistry of Materials* **2007**, 19 (21), 5165-5173.
- [138]. Yamasaki, K.; Juodkazis, S.; Watanabe, M.; Sun, H. B.; Matsuo, S.; Misawa, H., Recording by Microexplosion and Two-Photon Reading of Three-Dimensional

Optical Memory in Polymethylmethacrylate Films. *Applied Physics Letters* **2000**, 76 (8), 1000-1002.

- [139]. Lee, K. S.; Kim, R. H.; Yang, D. Y.; Park, S. H., Advances in 3d Nano/Microfabrication Using Two-Photon Initiated Polymerization. *Progress in Polymer Science* **2008**, 33 (6), 631-681.
- [140]. Sun, H. B.; Kawata, S., Two-Photon Photopolymerization and 3d Lithographic Microfabrication. *Nmr - 3d Analysis - Photopolymerization* **2004**, 170, 169-273.
- [141]. Miwa, M.; Juodkazis, S.; Kawakami, T.; Matsuo, S.; Misawa, H., Femtosecond Two-Photon Stereo-Lithography. *Applied Physics a-Materials Science & Processing* **2001**, 73 (5), 561-566.
- [142]. Nguyen, L. H.; Straub, M.; Gu, M., Acrylate-Based Photopolymer for Two-Photon Microfabrication and Photonic Applications. *Advanced Functional Materials* **2005**, 15 (2), 209-216.
- [143]. Zhou, W. H.; Kuebler, S. M.; Braun, K. L.; Yu, T. Y.; Cammack, J. K.; Ober, C. K.; Perry, J. W.; Marder, S. R., An Efficient Two-Photon-Generated Photoacid Applied to Positive-Tone 3d Microfabrication. *Science* **2002**, 296 (5570), 1106-1109.
- [144]. Belfield, K. D.; Yao, S.; Bondar, M. V., Two-Photon Absorbing Photonic Materials: From Fundamentals to Applications. In *Photoresponsive Polymers I*, Marder, S. R.; Lee, K. S., Eds. Springer-Verlag Berlin: Berlin, 2008; Vol. 213, pp 97-156.
- [145]. Haske, W.; Chen, V. W.; Hales, J. M.; Dong, W. T.; Barlow, S.; Marder, S. R.; Perry, J. W., 65 Nm Feature Sizes Using Visible Wavelength 3-D Multiphoton Lithography. *Optics Express* **2007**, 15 (6), 3426-3436.
- [146]. Kawata, S.; Sun, H. B.; Tanaka, T.; Takada, K., Finer Features for Functional Microdevices - Micromachines Can Be Created with Higher Resolution Using Two-Photon Absorption. *Nature* **2001**, 412 (6848), 697-698.
- [147]. Helmchen, F.; Denk, W., Deep Tissue Two-Photon Microscopy. *Nature Methods* **2005**, 2 (12), 932-940.
- [148]. Larson, D. R.; Zipfel, W. R.; Williams, R. M.; Clark, S. W.; Bruchez, M. P.; Wise, F. W.; Webb, W. W., Water-Soluble Quantum Dots for Multiphoton Fluorescence Imaging in Vivo. *Science* **2003**, 300 (5624), 1434-1436.

- [149]. Fisher, A. M. R.; Murphree, A. L.; Gomer, C. J., Clinical and Preclinical Photodynamic Therapy. *Lasers in Surgery and Medicine* **1995**, *17* (1), 2-31.
- [150]. Mongin, O.; Sankar, M.; Charlot, M.; Mir, Y.; Blanchard-Desce, M., Strong Enhancement of Two-Photon Absorption Properties in Synergic 'Semi-Disconnected' Multiporphyrin Assemblies Designed for Combined Imaging and Photodynamic Therapy. *Tetrahedron Letters* **2013**, *54* (48), 6474-6478.
- [151]. Wang, B. G.; Konig, K.; Halbhuber, K. J., Two-Photon Microscopy of Deep Intravital Tissues and Its Merits in Clinical Research. *Journal of Microscopy-Oxford* **2010**, *238* (1), 1-20.
- [152]. Balu, M.; Mazhar, A.; Hayakawa, C. K.; Mittal, R.; Krasieva, T. B.; Konig, K.; Venugopalan, V.; Tromberg, B. J., In Vivo Multiphoton NADH Fluorescence Reveals Depth-Dependent Keratinocyte Metabolism in Human Skin. *Biophysical Journal* **2013**, *104* (1), 258-267.
- [153]. Liu, G.; Liu, W.; Dong, C. M., Uv- and Nir-Responsive Polymeric Nanomedicines for on-Demand Drug Delivery. *Polymer Chemistry* **2013**, *4* (12), 3431-3443.
- [154]. Kehrlöesser, D.; Behrendt, P. J.; Hampp, N., Two-Photon Absorption Triggered Drug Delivery from a Polymer for Intraocular Lenses in Presence of an Uv-Absorber. *Journal of Photochemistry and Photobiology a-Chemistry* **2012**, *248*, 8-14.
- [155]. Ma, H. Y.; Gao, R.; Yan, D. P.; Zhao, J. W.; Wei, M., Organic-Inorganic Hybrid Fluorescent Ultrathin Films and Their Sensor Application for Nitroaromatic Explosives. *Journal of Materials Chemistry C* **2013**, *1* (26), 4128-4137.
- [156]. Xu, C.; Webb, W. W., Measurement of Two-Photon Excitation Cross Sections of Molecular Fluorophores with Data from 690 to 1050 Nm. *Journal of the Optical Society of America B-Optical Physics* **1996**, *13* (3), 481-491.
- [157]. Townsend, P. D.; Jackel, J. L.; Baker, G. L.; Shelburne, J. A.; Etemad, S., Observation of Nonlinear Optical-Transmission and Switching Phenomena in Polydiacetylene-Based Directional-Couplers. *Applied Physics Letters* **1989**, *55* (18), 1829-1831.
- [158]. Sheikbaha, M.; Said, A. A.; Vanstryland, E. W., High-Sensitivity, Single-Beam N₂ Measurements. *Optics Letters* **1989**, *14* (17), 955-957.

- [159]. Sheikbahae, M.; Said, A. A.; Wei, T. H.; Hagan, D. J.; Vanstryland, E. W., Sensitive Measurement of Optical Nonlinearities Using a Single Beam. *Ieee Journal of Quantum Electronics* **1990**, *26* (4), 760-769.
- [160]. Lin, T. C.; Chung, S. J.; Kim, K. S.; Wang, X. P.; He, G. S.; Swiatkiewicz, J.; Pudavar, H. E.; Prasad, P. N., Organics and Polymers with High Two-Photon Activities and Their Applications. *Polymers for Photonics Applications Ii* **2003**, *161*, 157-193.
- [161]. Yamaguchi, S.; Tahara, T., Observation of an Optically Forbidden State of C-60 by Nondegenerate Two-Photon Absorption Spectroscopy. *Chemical Physics Letters* **2004**, *390* (1-3), 136-139.
- [162]. Butcher, P. N.; Cotter, D. A., *The Elements of Nonlinear Optics*. Cambridge University press: 1990.
- [163]. Boyd, R. W., *Nonlinear Optics*. Academic Press Inc.: 1992.
- [164]. Sutherland, R. L., *Handbook of Nonlinear Optics*. Marcel Dekker: New York, 1996.
- [165]. Rumi, M.; Ehrlich, J. E.; Heikal, A. A.; Perry, J. W.; Barlow, S.; Hu, Z. Y.; McCord-Maughon, D.; Parker, T. C.; Rockel, H.; Thayumanavan, S.; Marder, S. R.; Beljonne, D.; Bredas, J. L., Structure-Property Relationships for Two-Photon Absorbing Chromophores: Bis-Donor Diphenylpolyene and Bis(Styryl)Benzene Derivatives. *Journal of the American Chemical Society* **2000**, *122* (39), 9500-9510.
- [166]. Birge, R. R., *Ultrasensitive Laser Spectroscopy*. Academic Press: New York, 1983.
- [167]. Herzberg, G., *Molecular Spectra and Molecular Structure*. Van Nostrand Reinhold Company: New York, 1950.
- [168]. Mulliken, R. S., Intensities of Electronic Transitions in Molecular Spectra I. Introduction. *Journal of Chemical Physics* **1939**, *7* (1), 14-20.
- [169]. Beljonne, D.; Wenseleers, W.; Zojer, E.; Shuai, Z. G.; Vogel, H.; Pond, S. J. K.; Perry, J. W.; Marder, S. R.; Bredas, J. L., Role of Dimensionality on the Two-Photon Absorption Response of Conjugated Molecules: The Case of Octupolar Compounds. *Advanced Functional Materials* **2002**, *12* (9), 631-641.

- [170]. Li, G. Z.; Wang, L. C.; Ni, H. L.; Pittman, C. U., Polyhedral Oligomeric Silsesquioxane (Poss) Polymers and Copolymers: A Review. *Journal of Inorganic and Organometallic Polymers* **2001**, *11* (3), 123-154.
- [171]. Osslon, K., Improved Preparation of Octakis(Alkylsilsesquioxanes). *Ark. Kemi* **1958**, *37*, 367-379.
- [172]. Choi, J.; Harcup, J.; Yee, A. F.; Zhu, Q.; Laine, R. M., Organic/Inorganic Hybrid Composites from Cubic Silsesquioxanes. *Journal of the American Chemical Society* **2001**, *123* (46), 11420-11430.
- [173]. Choi, J.; Kim, S. G.; Laine, R. M., Organic/Inorganic Hybrid Epoxy Nanocomposites from Aminophenylsilsesquioxanes. *Macromolecules* **2004**, *37* (1), 99-109.
- [174]. Choi, J.; Yee, A. F.; Laine, R. M., Organic/Inorganic Hybrid Composites from Cubic Silsesquioxanes. Epoxy Resins of Octa(Dimethylsiloxyethylcyclohexylepoxyde) Silsesquioxane. *Macromolecules* **2003**, *36* (15), 5666-5682.
- [175]. Choi, J. W.; Tamaki, R.; Kim, S. G.; Laine, R. M., Organic/Inorganic Imide Nanocomposites from Aminophenylsilsesquioxanes. *Chemistry of Materials* **2003**, *15* (17), 3365-3375.
- [176]. Laine, R. M.; Choi, J. W.; Lee, I., Organic-Inorganic Nanocomposites with Completely Defined Interfacial Interactions. *Advanced Materials* **2001**, *13* (11), 800-+.
- [177]. Liu, H. Z.; Zheng, S. X.; Nie, K. M., Morphology and Thermomechanical Properties of Organic-Inorganic Hybrid Composites Involving Epoxy Resin and an Incompletely Condensed Polyhedral Oligomeric Silsesquioxane. *Macromolecules* **2005**, *38* (12), 5088-5097.
- [178]. Sellinger, A.; Laine, R. M., Silsesquioxanes as Synthetic Platforms .3. Photocurable, Liquid Epoxides as Inorganic/Organic Hybrid Precursors. *Chemistry of Materials* **1996**, *8* (8), 1592-&.
- [179]. Soh, M. S.; Sellinger, A.; Yap, A. U. J., Dental Nanocomposites. *Current Nanoscience* **2006**, *2* (4), 373-381.
- [180]. Soh, M. S.; Yap, A. U. J.; Sellinger, A., Methacrylate and Epoxy Functionalized Nanocomposites Based on Silsesquioxane Cores for Use in Dental Applications. *European Polymer Journal* **2007**, *43* (2), 315-327.

- [181]. Pescarmona, P. P.; van der Waal, J. C.; Maschmeyer, T., Application of Combinatorial Chemistry and High-Speed Experimentation Concepts to the Study of Titanium-Silsesquioxane Catalysts. *Catalysis Today* **2003**, *81* (3), 347-357.
- [182]. Duchateau, R.; Cremer, U.; Harmsen, R. J.; Mohamud, S. I.; Abbenhuis, H. C. L.; van Santen, R. A.; Meetsma, A.; Thiele, S. K. H.; van Tol, M. F. H.; Kranenburg, M., Half-Sandwich Group 4 Metal Siloxy and Silsesquioxane Complexes: Soluble Model Systems for Silica-Grafted Olefin Polymerization Catalysts. *Organometallics* **1999**, *18* (26), 5447-5459.
- [183]. Pescarmona, P. P.; Van der Waal, J. C.; Maschmeyer, T., Silsesquioxane-Based Homogeneous and Heterogeneous Epoxidation Catalysts Developed by Using High-Speed Experimentation. *Chemistry-a European Journal* **2004**, *10* (7), 1657-1665.
- [184]. Aish, E. H.; Crocker, M.; Ladipo, F. T., Tripodal Titanium Silsesquioxane Complexes Immobilized in Polydimethylsiloxane (Pdms) Membrane: Selective Catalysts for Epoxidation of Cyclohexene and 1-Octene with Aqueous Hydrogen Peroxide. *Journal of Catalysis* **2010**, *273* (1), 66-72.
- [185]. Hwang, S. W.; Lee, G. R.; Min, J. H.; Moon, S. H.; Kim, Y. C.; Ryu, H. K.; Cho, Y. S.; Kim, J. W., Etch Characteristics of Silsesquioxane-Based Low Dielectric Constant Material in Fluorocarbon Plasma. *Japanese Journal of Applied Physics Part 1-Regular Papers Brief Communications & Review Papers* **2002**, *41* (9), 5782-5786.
- [186]. Zhang, Z. P.; Pei, J. Z.; Liang, G. Z.; Yuan, L., Methyl Silsesquioxane/Cyanate Ester Resin Organic-Inorganic Hybrids with Low Dielectric Constant. *Journal of Applied Polymer Science* **2011**, *121* (2), 1004-1012.
- [187]. Liu, W. C.; Yu, Y. Y.; Chen, W. C., Structural Control and Properties of Low-Dielectric-Constant Poly(Hydrogen Silsesquioxane) Precursors and Their Thin Films. *Journal of Applied Polymer Science* **2004**, *91* (4), 2653-2660.
- [188]. Costescu, R. M.; Bullen, A. J.; Matamis, G.; O'Hara, K. E.; Cahill, D. G., Thermal Conductivity and Sound Velocities of Hydrogen-Silsesquioxane Low-K Dielectrics. *Physical Review B* **2002**, *65* (9).
- [189]. Chan, K. L.; Sonar, P.; Sellinger, A., Cubic Silsesquioxanes for Use in Solution Processable Organic Light Emitting Diodes (Oled). *Journal of Materials Chemistry* **2009**, *19* (48), 9103-9120.
- [190]. Lo, M. Y.; Zhen, C. G.; Lauters, M.; Jabbour, G. E.; Sellinger, A., Organic-Inorganic Hybrids Based on Pyrene Functionalized Octavinylsilsesquioxane

Cores for Application in Oleds. *Journal of the American Chemical Society* **2007**, 129 (18), 5808-+.

- [191]. Sellinger, A.; Tamaki, R.; Laine, R. M.; Ueno, K.; Tanabe, H.; Williams, E.; Jabbour, G. E., Heck Coupling of Haloaromatics with Octavinylsilsesquioxane: Solution Processable Nanocomposites for Application in Electroluminescent Devices. *Chemical Communications* **2005**, (29), 3700-3702.
- [192]. Renaud, C.; Josse, Y.; Lee, C. W.; Nguyen, T. P., Investigation of Defects in Polyhedral Oligomeric Silsesquioxanes Based Organic Light Emitting Diodes. *Journal of Materials Science-Materials in Electronics* **2008**, 19, S87-S91.
- [193]. Ervithayasuporn, V.; Abe, J.; Wang, X.; Matsushima, T.; Murata, H.; Kawakami, Y., Synthesis, Characterization, and Oled Application of Oligo(P-Phenylene Ethynylene)S with Polyhedral Oligomeric Silsesquioxanes (Poss) as Pendant Groups. *Tetrahedron* **2010**, 66 (48), 9348-9355.
- [194]. Zhang, X. Z.; Huang, Y. D.; Wang, T. Y.; Liu, L., Influence of Fibre Surface Oxidation-Reduction Followed by Silsesquioxane Coating Treatment on Interfacial Mechanical Properties of Carbon Fibre/Polyarylacetylene Composites. *Composites Part a-Applied Science and Manufacturing* **2007**, 38 (3), 936-944.
- [195]. Ghaderi, S.; Ramesh, B.; Seifalian, A. M., Synthesis of Mercaptosuccinic Acid/Mercaptopolyhedral Oligomeric Silsesquioxane Coated Cadmium Telluride Quantum Dots in Cell Labeling Applications. *Journal of Nanoscience and Nanotechnology* **2012**, 12 (6), 4928-4935.
- [196]. Bao, Z. N.; Kuck, V.; Rogers, J. A.; Paczkowski, M. A., Silsesquioxane Resins as High-Performance Solution Processible Dielectric Materials for Organic Transistor Applications. *Advanced Functional Materials* **2002**, 12 (8), 526-531.
- [197]. Roll, M. F.; Asuncion, M. Z.; Kampf, J.; Laine, R. M., Para-Octaiodophenylsilsesquioxane, P-Ic6h4sio1.5 (8), a Nearly Perfect Nano-Building Block. *Acs Nano* **2008**, 2 (2), 320-326.
- [198]. Scott, D. W., Thermal Rearrangement of Branched-Chain Methylpolysiloxanes. *Journal of the American Chemical Society* **1946**, 68 (3), 356-358.
- [199]. Voronkov, M. G.; Lavrentyev, V. I., Polyhedral Oligosilsesquioxanes and Their Homo Derivatives. *Topics in Current Chemistry* **1982**, 102, 199-236.
- [200]. Olsson, K.; Groenwal.C, On Octa-(Arylsilsesquioxanes), (ArSi)8O12 .1. Phenyl, 4-Tolyl, and 1-Naphthyl Compounds. *Arkiv for Kemi* **1961**, 17 (6), 529-&.

- [201]. Brown, J. F.; Vogt, L. H.; Prescott, P. I., Preparation + Characterization of Lower Equilibrated Phenylsilsesquioxanes. *Journal of the American Chemical Society* **1964**, 86 (6), 1120-&.
- [202]. Dare, E. O.; Liu, L. K.; Peng, J., Modified Procedure for Improved Synthesis of Some Octameric Silsesquioxanes Via Hydrolytic Polycondensation in the Presence of Amberlite Ion-Exchange Resins. *Dalton Transactions* **2006**, (30), 3668-3671.
- [203]. Ito, H.; Truong, H. D.; Burns, S. D.; Pfeiffer, D.; Medeiros, D. R., Bilayer Resists for 193 Nm Lithography: Ssq and Poss. *Journal of Photopolymer Science and Technology* **2006**, 19 (3), 305-311.
- [204]. Hoque, M. A.; Cho, Y. H.; Kawakami, Y., High Performance Holographic Gratings Formed with Novel Photopolymer Films Containing Hyper-Branched Silsesquioxane. *Reactive & Functional Polymers* **2007**, 67 (11), 1192-1199.
- [205]. Chen, H. J.; Fu, M., Core-Shell-Shaped Organic-Inorganic Hybrid as Pore Generator for Imprinting Nanopores in Organosilicate Dielectric Films. *Macromolecules* **2007**, 40 (6), 2079-2085.
- [206]. Ni, Y.; Zheng, S. X.; Nie, K. M., Morphology and Thermal Properties of Inorganic-Organic Hybrids Involving Epoxy Resin and Polyhedral Oligomeric Silsesquioxanes. *Polymer* **2004**, 45 (16), 5557-5568.
- [207]. Jothibas, S.; Premkumar, S.; Alagar, M., Synthesis and Characterization of a Poss-Maleimide Precursor for Hybrid Nanocomposites. *High Performance Polymers* **2008**, 20 (1), 67-85.
- [208]. Kim, S. G.; Sulaiman, S.; Fargier, D.; Laine, R. M., Octaphenyloctasilsesquioxane and Polyphenylsilsesquioxane for Nanocomposites. In *Materials Syntheses*, Schubert, U.; Hüsing, N.; Laine, R., Eds. Springer Vienna: 2008; pp 179-191.
- [209]. Marciniak, B.; Pietraszuk, C., Synthesis of Unsaturated Organosilicon Compounds Via Alkene Metathesis and Metathesis Polymerization. *Current Organic Chemistry* **2003**, 7 (8), 691-735.
- [210]. Kujawa-Welten, M.; Pietraszuk, C.; Marciniak, B., Cross-Metathesis of Vinylsilanes with Allyl Alkyl Ethers Catalyzed by Ruthenium-Carbene Complexes. *Organometallics* **2002**, 21 (5), 840-845.
- [211]. Sulaiman, S.; Bhaskar, A.; Zhang, J.; Guda, R.; Goodson, T.; Laine, R. M., Molecules with Perfect Cubic Symmetry as Nanobuilding Blocks for 3-D

Assemblies. Elaboration of Octavinylsilsesquioxane. Unusual Luminescence Shifts May Indicate Extended Conjugation Involving the Silsesquioxane Core. *Chemistry of Materials* **2008**, 20 (17), 5563-5573.

- [212]. Bao, C. Y.; Lu, R.; Jin, M.; Xue, P. C.; Tan, C. H.; Xu, T. H.; Liu, G. F.; Zhao, Y. Y., Triphenyl Benzene-Bridged Fluorescent Silsesquioxane: Shape-Controlled Hybrid Silicas by Hydrolytic Conditions. *Journal of Nanoscience and Nanotechnology* **2006**, 6 (8), 2560-2565.
- [213]. Bordianu, I.; Olaru, M.; Cotofana, C.; Ursu, L., Synthesis and Characterization of a Silsesquioxane Nanocomposite with Photoluminescence Properties. *Journal of Optoelectronics and Advanced Materials* **2011**, 13 (5-6), 635-637.
- [214]. Cheng, C. C.; Chien, C. H.; Yen, Y. C.; Ye, Y. S.; Ko, F. H.; Lin, C. H.; Chang, F. C., A New Organic/Inorganic Electroluminescent Material with a Silsesquioxane Core. *Acta Materialia* **2009**, 57 (6), 1938-1946.
- [215]. Li, Q.; Dong, L. J.; Wang, X.; Huang, J.; Xie, H. A.; Xiong, C. X., Self-Assembled Quantum Dots-Polyhedral Oligomeric Silsesquioxane Nanohybrids with Enhanced Photoluminescence. *Scripta Materialia* **2012**, 66 (9), 646-649.
- [216]. Miyake, J.; Chujo, Y., Thermally Stabilized Blue Luminescent Poly(P-Phenylene)S Covered with Polyhedral Oligomeric Silsesquioxanes. *Macromolecular Rapid Communications* **2008**, 29 (1), 86-92.
- [217]. Miyake, J.; Chujo, Y., A Hybrid-Type, Chiral Pi-Conjugated Polymer Wrapped with Polyhedral Oligomeric Silsesquioxanes. *Journal of Polymer Science Part a-Polymer Chemistry* **2008**, 46 (18), 6035-6040.
- [218]. Lo, M. Y.; Ueno, K.; Tanabe, H.; Sellinger, A., Silsesquioxane-Based Nanocomposite Dendrimers with Photo-Luminescent and Charge Transport Properties. *Chemical Record* **2006**, 6 (3), 157-168.
- [219]. Xiao, S.; Nguyen, M.; Gong, X.; Cao, Y.; Wu, H. B.; Moses, D.; Heeger, A. J., Stabilization of Semiconducting Polymers with Silsesquioxane. *Advanced Functional Materials* **2003**, 13 (1), 25-29.
- [220]. Iacono, S. T.; Budy, S. M.; Mabry, J. M.; Smith, D. W., Synthesis, Characterization, and Properties of Chain Terminated Polyhedral Oligomeric Silsesquioxane-Functionalized Perfluorocyclobutyl Aryl Ether Copolymers. *Polymer* **2007**, 48 (16), 4637-4645.

- [221]. Froehlich, J. D.; Young, R.; Nakamura, T.; Ohmori, Y.; Li, S.; Mochizuki, A.; Lauters, M.; Jabbour, G. E., Synthesis of Multi-Functional Poss Emitters for OLED Applications. *Chemistry of Materials* **2007**, *19* (20), 4991-4997.
- [222]. Grimsdale, A. C.; Mullen, K.; Springer, V., Polyphenylene-Type Emissive Materials: Poly(Para-Phenylene)S, Polyfluorenes, and Ladder Polymers. In *Emissive Materials: Nanomaterials*, Springer-Verlag Berlin: Berlin, 2006; Vol. 199, pp 1-82.
- [223]. Imae, I.; Kawakami, Y., Unique Photoluminescence Property of a Novel Perfectly Carbazole-Substituted Poss. *Journal of Materials Chemistry* **2005**, *15* (43), 4581-4583.
- [224]. Lin, W. J.; Chen, W. C.; Wu, W. C.; Niu, Y. H.; Jen, A. K. Y., Synthesis and Optoelectronic Properties of Starlike Polyfluorenes with a Silsesquioxane Core. *Macromolecules* **2004**, *37* (7), 2335-2341.
- [225]. Xiang, K. H.; Pandey, R.; Pernisz, U. C.; Freeman, C., Theoretical Study of Structural and Electronic Properties of H-Silsesquioxanes. *Journal of Physical Chemistry B* **1998**, *102* (44), 8704-8711.
- [226]. Phillips, H.; Zheng, S. H.; Hyla, A.; Laine, R.; Goodson, T.; Geva, E.; Dunietz, B. D., Ab Initio Calculation of the Electronic Absorption of Functionalized Octahedral Silsesquioxanes Via Time-Dependent Density Functional Theory with Range-Separated Hybrid Functionals. *Journal of Physical Chemistry A* **2012**, *116* (4), 1137-1145.
- [227]. Zheng, S. H.; Phillips, H.; Geva, E.; Dunietz, B. D., Ab Initio Study of the Emissive Charge-Transfer States of Solvated Chromophore-Functionalized Silsesquioxanes. *Journal of the American Chemical Society* **2012**, *134* (16), 6944-6947.
- [228]. Laine, R. M.; Sulaiman, S.; Brick, C.; Roll, M.; Tamaki, R.; Asuncion, M. Z.; Neurock, M.; Filhol, J. S.; Lee, C. Y.; Zhang, J.; Goodson, T.; Ronchi, M.; Pizzotti, M.; Rand, S. C.; Li, Y., Synthesis and Photophysical Properties of Stilbeneoctasilsesquioxanes. Emission Behavior Coupled with Theoretical Modeling Studies Suggest a 3-D Excited State Involving the Silica Core. *Journal of the American Chemical Society* **2010**, *132* (11), 3708-3722.
- [229]. Park, S. S.; Xiao, C. Y.; Hagelberg, F.; Hossain, D.; Pittman, C. U.; Saebo, S., Endohedral and Exohedral Complexes of Polyhedral Double Four-Membered-Ring (D_{4r}) Units with Atomic and Ionic Impurities. *Journal of Physical Chemistry A* **2004**, *108* (51), 11260-11272.

CHAPTER 2

EXPERIMENTAL TECHNIQUES

2.1 Overview

The various optical techniques are utilized in order to reveal the characteristics of investigated systems in this dissertation. In this chapter, a general introduction of each experimental technique and instrument operation details are provided. These steady state measurements and nonlinear optical techniques are generally utilized in the research of chapter 3, 4 and 5. The ultrafast absorption and emission measurements are applied in the research of chapter 4 and 5. The two-photon nonlinear transmission measurement is utilized in the research of chapter 6.

2.2 Optical Absorption and Emission Measurement

Absorption spectroscopy refers to spectroscopic techniques that measure the absorption of radiation energy, such as photons. The intensity of the absorption is measured as a function of frequency or wavelength. Ultra Violet and Visible (UV/Vis) absorption follows the principle of the Beer-Lambert law.¹

Equation 2.1

$$A = -\log \frac{I}{I_0} = \epsilon \times c \times l$$

Where, I_0 and I are the intensity (or power per unit area) of the incident light and the transmitted light, respectively, ϵ is the molar extinction coefficient ($M^{-1}cm^{-1}$), c is the concentration of the absorber (mol/L), l is the path length (cm). The experiment is usually performed in the solution phase in a quartz cuvette. The absorbance at a selected wavelength is the so called optical density of a material, which is a logarithmic ratio of the radiation incident into a material, to the radiation transmitted through a material. Usually, in our experiment, this equation is used to determine the molar extinction coefficient of a sample with a known concentration, or the concentration of a solution with known extinction coefficient. The wavelength of light absorbed provides the information of different types electronic transitions, as shown in Figure 2.1.

Fluorescence is a luminescence process, in which a substance absorbs electromagnetic radiation, and then emits light after vibrational relaxation process. Fluorescence emission is a radiative relaxation process in which the excited molecules emit photons from higher electronic states after excitation. In our experiment, number of photons emitted at different wavelength is measured. It also can be used to measure the quantum yield as presented in section 2.3.

Both absorption and fluorescence emission process are often visualized with a Jablonski energy diagram, as shown in Figure 2.2.

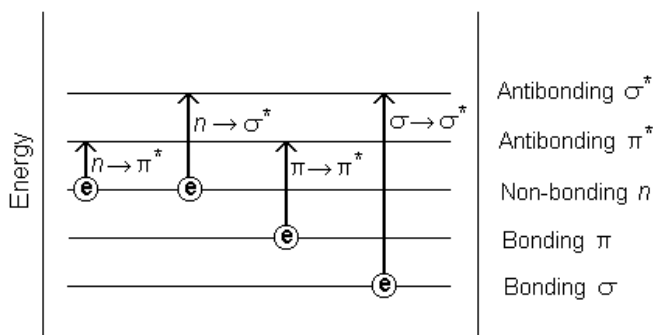


Figure 2.1 Types of electronic transitions

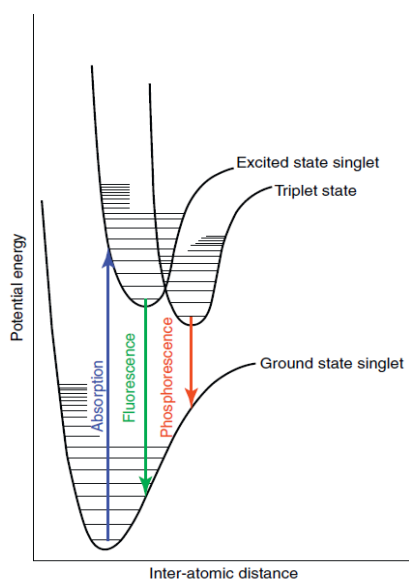


Figure 2.2 Illustration of absorption and fluorescence process using Jablonski energy Diagrams

The absorption spectra of the molecules were measured using an Agilent (Model#8341) spectrophotometer. The light sources used for UV/Vis incident light generation in this spectrophotometer are two sets of lamps. They are deuterium and tungsten with spectra ranging from 200-1100 nm. The samples were dissolved in solution with solvent, such as THF, and held in a quartz cuvette manufactured by Starna. The optical path length of the quartz cuvette is 0.5 cm. A reference spectrum was taken with the same cuvette containing the same solvent used in the sample measurements. This will eliminate the possibility of contaminations of the absorption data from the environment. The collected blank spectrum was then automatically subtracted from the product spectrums. The solution is stored in a dark and low temp environment to protect against possible photo and thermal degradation. In order to measure molar extinction coefficients, the original stock solutions were diluted to 10^{-6} M. The absorption spectrum was checked before and after any other nonlinear optical experiments to monitor the possible degradation processes.

The steady state emission spectra were measured using a SPEX Fluoromax-2 fluorimeter. The main excitation light source of this fluorimeter is xenon lamp. A diffraction grating is used for single wavelength selection. A photomultiplier tube is used to collect the number of fluorescence counts with excellent sensitivity from 300 nm to about 750 nm. The sample in dilute solution ($\sim 10^{-6}$ M) is hold in the same quartz cuvettes used for absorption measurements. The fluorescence counts are collected at 90° to the incident beam. Besides the fluorescence emission spectrum, the SPEX Fluoromax-2 is designed for excitation spectrum measurement as well. An excitation spectrum is measuring the emission light at a constant wavelength via a monochromator, while wavelength of excitation light is scanned over a range.

2.3 Fluorescence Quantum Yield Measurement

The fluorescence quantum yield (Φ) is determined by the ratio of the number of photons emitted to the number of photons absorbed:

Equation 2.2

$$\Phi = \frac{\text{\# of photon emitted}}{\text{\# of photon absorbed}}$$

Fluorescence quantum yield is an effective indication of the fluorescence emission strength. In our lab, the quantum yields of the molecules were measured using a known procedure.² This measurement utilizes a standard dye with known quantum yield. The dyes used in this dissertation are Coumarin 307, Bis-MSB, Rhodamine B and Rhodamine 6G. The standard dye is prepared with the optical density that is similar to the sample at the same excitation wavelength. The following equation was used to determine the quantum yield:

Equation 2.3

$$\phi_{sample} = \phi_{std} \frac{\int J_{sample}(\bar{\nu})d\bar{\nu}}{\int J_{std}(\bar{\nu})d\bar{\nu}} \frac{(J_{abs})_{std}}{(J_{abs})_{sample}} \frac{n_{sample}^2}{n_{std}^2}$$

Where, ϕ is the quantum yield at a selected wavelength, $\int J(\bar{\nu})d\bar{\nu}$ is the integrated area under the fluorescence emission spectrum with units of wavenumber, J_{abs} is the absorbance at the selected excitation wavelength, and n is the refractive index of the solvent used for each sample/standard preparation. “Sample” and “std” represent sample and standard, respectively. There might be some errors due to the sensitivity of detection apparatus and environmental conditions. Usually, the selective wavelength of this measurement is close to the wavelength of emission maximum.

2.4 Two-Photon Excited Fluorescence Method

The background of Two-photon absorption was presented in Chapter 1. There are two different two-photon excited fluorescence (TPEF) setup used in our lab:

(1) The TPEF setup I utilizes a Kapteyn Murnane (KM) Laboratories diode-pumped modelocked Ti:sapphire laser which is tunable from 770 to 830 nm, with peak output powers of ~250-320 mW and ~40 nm pulse widths. The optical diagram is illustrated in Figure 2.3.

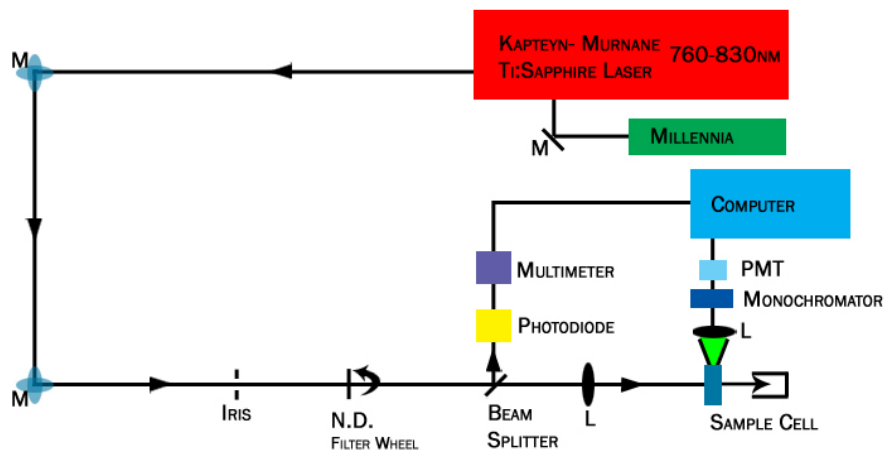


Figure 2.3 Optical diagram of two-photon setup I with KM laser with wavelength range from 770-830nm

(2) The TPEF setup utilized a Spectra-Physics Mai-Tai Diode-pumped Mode-Locked Ti:Sapphire laser which is tunable from 700 to 980 nm with average output power upto 2 W, repetition rate 80 MHz, noise less than 0.15 %, stability less than ± 1 % and polarization ratio large than 500:1 horizontal. The optical diagram of this setup is presented in Figure 2.4. A femtosecond synchronously pumped parametric oscillator (OPAL) laser can be selectively involved into the beam path and pumped by the Mai-Tai. This OPAL laser provides wide continuous spectral coverage: synchronized signal and idler outputs deliver wavelengths from 1.1 to 2.25 μm with mode-locked output pulses less than 130 femtoseconds, repetition rate 80 MHz and high output power (more than 200 mW at 1.3 μm and 1.5 μm). The optical cavity layout is presented in Figure 2.5. Although it is a menu driven electronics and the operation procedure is simple, open cavity alignment is an important fulfillment in this dissertation. The details of operation and alignment of Opal system are presented in Appledix III & IV. Different range of excitation wavelength can be obtained by choosing different beam paths and selecting different involved apparatus: (a)Mai-Tai (700 – 980 nm), (b)Mai-Tai and OPAL (1200 – 2250 nm), (c) Mai-Tai, OPAL and the first beam frequency doubler (BBO1) (600 – 1125 nm) , and (d) Mai-Tai, OPAL and both the first and the second BBO crystal (300 – 550

nm). The total wavelength range for the second TPA setup is 300 – 2200 nm. Two-photon measurement apparatus are displayed in Figure 2.6.

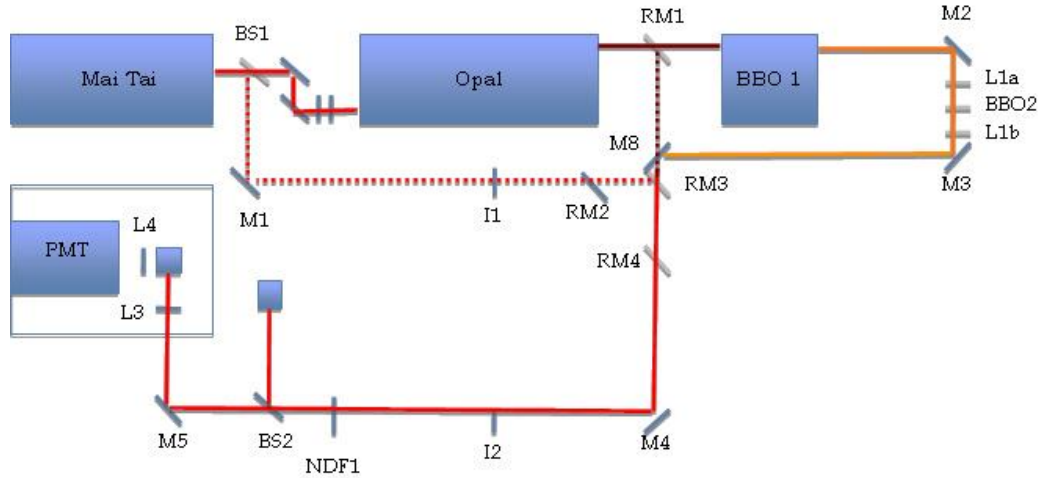


Figure 2.4 Optical diagram of two-photon setup II with selective pathways involving Mai-Tai and OPAL laser. Wavelength range from 250 to 2250nm can be achieved by selecting different optical pathways.

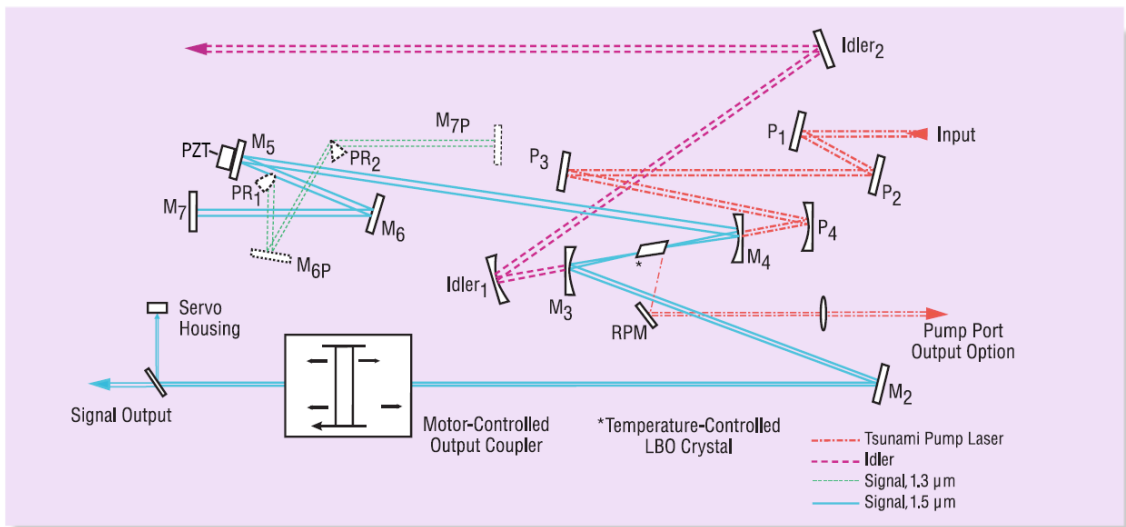


Figure 2.5 The Opal cavity layout

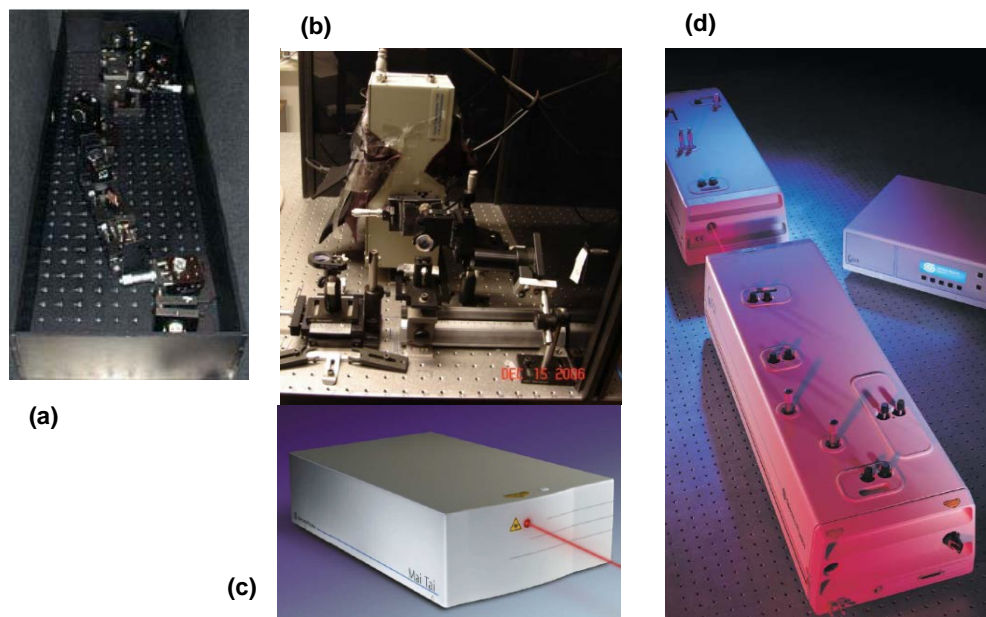


Figure 2.6 Photo illustration of (a) Kapteyn Murnane laser, (b) sample holder and PMT, (c) Mai-Tai laser and (d) OPAL laser

In order to measure the two-photon absorption cross sections, we followed the two-photon excited fluorescence (TPEF) method.³ A standard with known TPA cross-section at measurement wavelength was used as the reference. The standard is prepared with a known concentration that provides the similar optical density to the sample at the measurement wavelength. In all setups and pathways, an iris is used to ensure a circular incident beam. A neutral density filter is used to control the input beam intensity. A beam splitter is used to reflect partial beam to the photodiode which is used to monitor the intensity of the input beam. A focal optical lens is placed prior to the sample in order to focus the laser beam onto a quartz cuvette. The path length of the quartz cuvette cell is 0.5 cm. The fluorescence from the cuvette cell is collected in a direction that is perpendicular to the incident beam. It should be noted that the excitation beam is focused close to the edge of the sample cell towards the direction of collection rather than center. In this way, the path length of the fluorescence travelling in the sample cell before collection is reduced. Therefore the self-absorption of the fluorescence can be minimized. A 1" focal length plano-convex lens was used to direct the collected fluorescence into a

monochromator. The output from the monochromator was coupled to a photomultiplier tube (PMT). The fluorescence signal was converted into photon counts by a photon counting unit. The collected fluorescence counts and input intensity follows:

Equation 2.4

$$F(t) = \frac{1}{2} \eta \delta c \frac{g_p}{\pi \lambda f \tau} \phi \langle P(t) \rangle^2$$

Where, $F(t)$ is the number of fluorescence photons collected per second, η is the fluorescence quantum yield of the measured sample, δ is the TPA cross section in GM, c is the concentration of the sample in molarity, n is the refractive index of the solvent, g_p is the shape factor (usually 0.664 for Gaussian pulses), λ is the wavelength of the excitation beam, f is the frequency of the laser pulse, τ is the pulse duration of the laser source, ϕ is the efficiency of collecting system, and $\langle P(t) \rangle$ is the input intensity of excitation beam.

After taking log on both side of the equation above, a logarithmic plot can be drawn base on the following equation **Error! Bookmark not defined.:**

Equation 2.5

$$\log(F(t)) = 2\log\langle P(t) \rangle + \log\left(\frac{1}{2} \eta \delta c n \frac{g_p}{\pi \lambda f \tau} \phi\right)$$

This linear plot gave a slope of two, ensuring a quadratic dependence between the fluorescence photons and input intensity. By comparing with intercept at $y=0$ of the standard under the same experimental condition, the following equation can be derived to calculate the two-photon cross-section:

Equation 2.6

$$\delta_{sample} = \frac{10^{b_{sample} - b_{std}} \eta_{std} \delta_{std} c_{std} n_{std}}{\eta_{sample} c_{sample} n_{sample}}$$

Where, std and sample represent for standard and investigated sample, respectively, b is the intercept at $y=0$, η is the quantum yield, c is concentration in molarity and n is the reflective index. The calculated two-photon cross-section is in Göppert-Mayer (GM) with $1 \text{ GM} = 10^{-50} \text{ cm}^4 \text{ s photon}^{-1}$.

2.5 Fluorescence Up-Conversion

Fluorescence up-conversion is based on the principle that fluorescence from the sample and probe laser pulse is up-converted by a nonlinear optical crystal, such as β -barium borate (BBO) crystal. The time resolution mechanism of the up-conversion technique is illustrated in Figure 2.7. This measurement is based on a cross-correlation process between the fluorescence and the excitation pulse. A second or third harmonic probe laser pulse is used to excite the sample at time $t=0$. At time $t = \tau$, both the fluorescence from the sample and the excitation probe pulse arrive at a nonlinear crystal simultaneously. A special magic angle between the fluorescence and probe beam is required to generate sum frequency. The sum frequency (ω_s) is the sum of frequency of the collected incoherent fluorescence (ω_F) and the probe beam (ω_p). Therefore, the time resolution of up-conversion experiment is the pulse width of the excitation beam. The fluorescence can be monitored at each delay time of the probe beam. The time delay is controlled by an optical delay line. The fluorescence intensity is correlated with the intensity of the sum frequency.

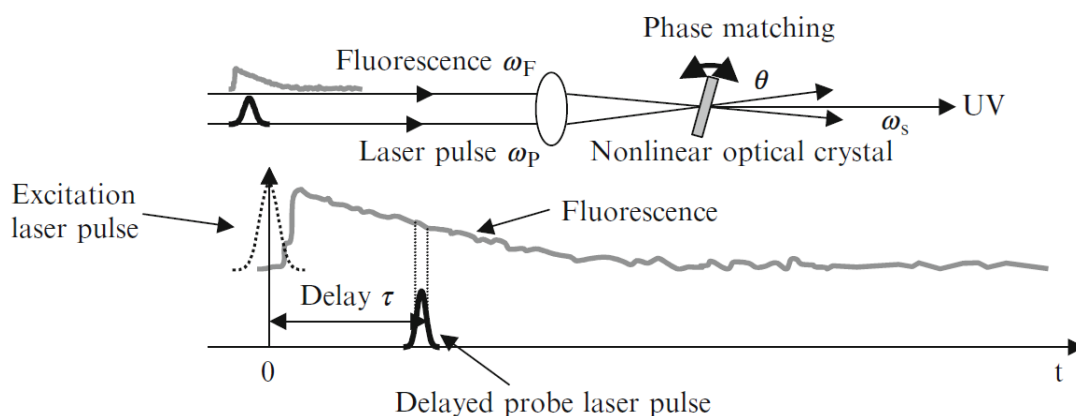


Figure 2.7 Schematic diagram of fluorescence upconversion mechanism⁴

The up-conversion system used in our lab has been previously described.⁵⁻⁶ The optical diagram of the fluorescence up-conversion setup is illustrated in Figure 2.8. Figure 2.9 shows the fluorescence setup under operation. The primary light source is from a mode-locked Ti-sapphire laser (Tsunami, Spectra Physics), which produces pulses of approximately 100 fs duration in the wavelength range of 770-830 nm. This laser is pumped by Millennia with output power ~ 5 W. A frequency-doubled light is generated after a BBO crystal (NC1) with wavelength 335-415 nm. Besides the second harmonic generation, the system also provides third harmonic (around 266 nm) excitation light source from fundamental beam directly. In order to produce the third harmonic light, the second harmonic was mixed with the fundamental one using an additional BBO crystal which is able to generate the sum frequency beam with the wavelength around 266 nm and the intensity up to 15 mW. Under this third harmonic generation mode, the second harmonic unit is simply removed. The third harmonic Instrument Response Function (IRF) of this experiment system was determined and reported and the pulse width is 350fs.⁷ And the second harmonic IRF was obtained from the Raman signal of water and it was found to be around 110fs.⁸ The average power for excitation is typically less than 3 mW, in order to ensure the excitation pulse energy well below 0.1 nJ. Under this

excitation energy, the fluorescence dynamics and the excitation power are independent of the each other.

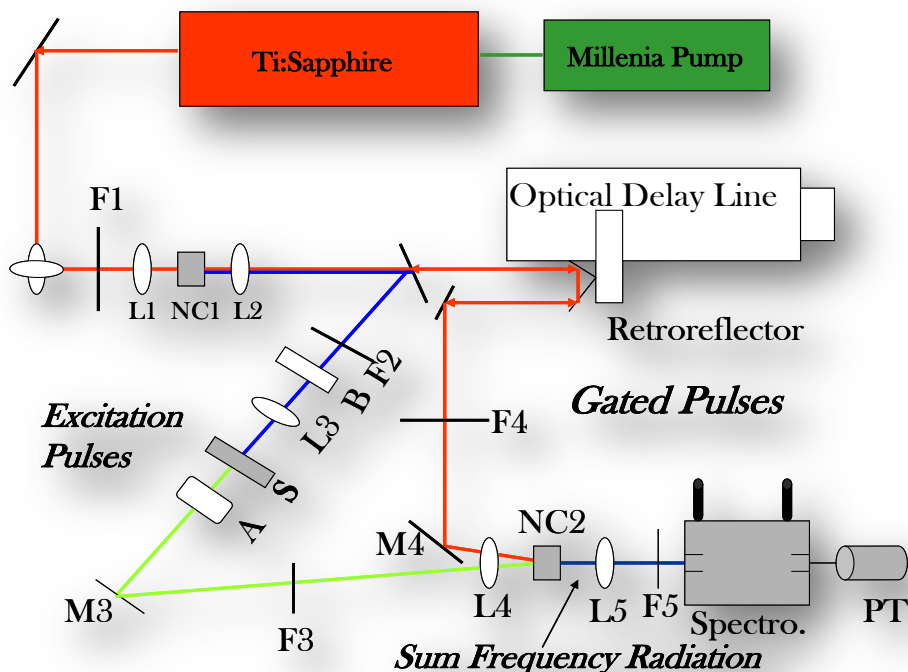


Figure 2.8 Optical diagram for time resolve fluorescence up-conversion measurements

In both second and third harmonic excitation, a beam splitter is used to separate the excitation pulse with the fundamental beam. A filter (F2) is installed prior to the sample cell in order to ensure the monochromaticity of excitation beam. A Berek compensator (B) is placed prior to the sample to control the polarization of the excitation beam. The sample cuvette (S) is made with quartz, 1mm thick and held in a rotating holder to prevent photo-degradation. An acromat (A) is placed after the sample cell to select the horizontally polarized fluorescence component emitted from the sample. On the other hand, the fundamental beam (red line in Figure 2.8) travels through a variable optical delay line which is controlled by FOG-100 system. This process serves as an optical gate and provides an observation time window from 200 fs to 1ns. The step size in

this system is 6.25 fs. Both transmitted fluorescence and the fundamental beam reach the second BBO crystal (NC2). The up-converted signal is detected by a photo-multiplier tube (PT), Hamamatsu R1527P, coupled with a monochromator.



Figure 2.9 Femtosecond fluorescence upconversion set-up under operation

In this experiment, both parallel emissions from parallel excitation (I_{\parallel}) and from perpendicular excitation (I_{\perp}) can be measured. Given that there are one parallel direction and two perpendicular directions to the propagated wave, the total (rotation-free) intensity as a function of time is given by:

Equation 2.7
$$I(t) = I_{\parallel}(t) + 2I_{\perp}(t)$$

Anisotropy is defined by the fluorescence intensity difference in parallel and perpendicular directions. The following relationship describes the anisotropy as a function of time:

Equation 2.8
$$r(t) = \frac{I_{\parallel}(t) - I_{\perp}(t)}{I_{\parallel}(t) + 2I_{\perp}(t)}$$

Coumarin 30 is a standard dye commonly used in fluorescence up-conversion and anisotropy measurements. In our system, the g-factor is 0.95, which is a correction factor for the difference in sensitivity of the detection system for the vertically and horizontally polarized light. A deconvolution process is performed using Surface Explorer software with a minimum resolution about 30fs. Longer lifetimes are fitted by Origin 8 software.

The lifetime components of anisotropy decay provide substantial information on energy migration process. For example, a fast decay component (\sim fs) suggests a coherent type of energy migration, whereas existence of a long time component (\sim ns) indicates Förster type of energy hopping mechanism.⁶ In addition, it also provides information about rotational orientation of a molecular. For molecule with a planar geometry, the value of residual anisotropy is expected to be 0.1.⁹

2.6 Ultrafast Transient Absorption Spectroscopy

Transient Absorption¹⁰ (TA) is a pump probe technique for investigating the excited state dynamics of investigated materials such as electron and/or proton transfer processes. It also provides the information of the intersystem crossing process to the non-emissive dark states. A schematic illustrating the principle of TA is shown in Figure 2.10.

The ultrafast tunable lasers systems provide femtosecond resolution and allow us to monitor the earliest events occur within a light-harvesting system. The Figure 2.11 illustrates the pump-probe process of TA. The wavelength of the probe beam is lower than the absorption maximum of the investigated molecules. After excitation, a fraction of the molecules (0.1 % \sim 10 %) is excited to higher electronically excited state at time $t=0$. A white light continuum (WLC) with low intensity arrives the sample at the delay time $t= \tau$. Only the WLC passes through the iris and reaches the detector.

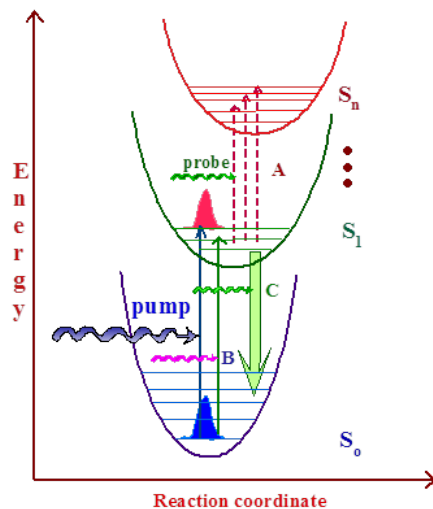


Figure 2.10 Basic principle of transient absorption spectroscopy

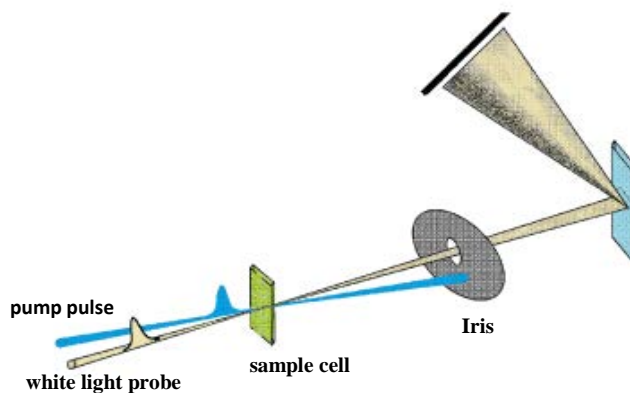


Figure 2.11 Schematic illustration of the transient absorption pump-probe process¹¹

Figure 2.12 illustrate the schematic diagram of transient absorption setup in our lab. The light source is a Regenerative Amplifier (Spitfire Pro, Spectra Physics) with 1 mJ/pulse at 800 nm, pulse duration ~100 fs, repetition rate 1 kHz and average power 1 W. This Regenerative Amplifier is pumped by a Nd: YLF pulse laser (Empower, Spectra Physics) at 532 nm. The seed pulse is generated by a Ti: Sapphire system (Tsunami, Spectra Physics) with output power 370 mW at 800 nm, repetition rate ~80 MHz, pulse

duration ~ 20 fs and energy 1 nJ/pulse. This Tsunami system is pumped by a Nd:YVO₂ continuous wave laser (Millennia, Spectra-Physics) with output power 3.75W at 532 nm. The seed pulses inside the regenerative amplifier is amplified in three stages: pulse stretching, regenerative amplification and pulse compression.

The output beam of this amplifier is split to generate pump (80%) and probe beam (20%) pulses using a beam splitter. The pump beam goes into an Optical Parametric Amplifier (OPA-800C, Spectra Physics). It is a nonlinear conversion process to generate wavelength between 300-1000 nm with pulse duration ~ 100 fs. The output from the OPA-800C constitutes the pump beam.

On the other hand, the probe pulse after the splitter is delayed by an optical delay line and then focused onto a sapphire plate to generate a WLC. Both probe beam and white light pump are focused on a sample cuvette with 2mm path length. A rotating magnetic stirrer is used in the cuvette cell to avoid photo degradation. The white light after the sample, which contains the information of change in absorbance, was detected by a charge-coupled device (CCD) detector (Ocean optics). Data was collected by specialized software from Ultrafast Systems Inc. The data acquired is further analyzed by Surface Xplore software. Excited state absorption change is obtained by the absorption spectrum of the sample in the excited state subtracting the absorption spectrum in the ground state. The TA spectrum contains three dimensions of data: changes in absorbance, wavelength and time.

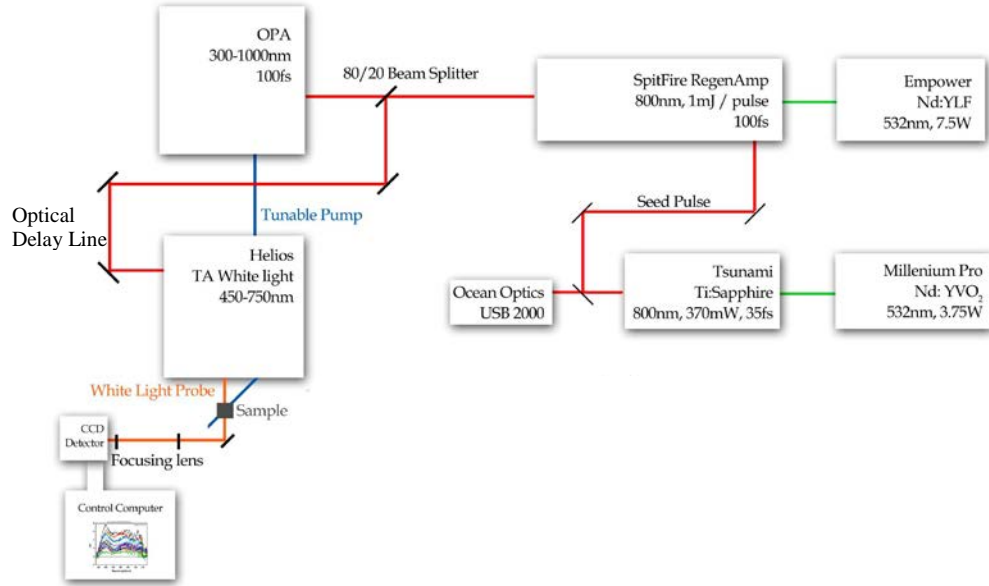


Figure 2.12 Optical diagram of transient absorption experimental setup in our lab

2.7 Two Photon Nonlinear Transmission

Two-photon transmission is a method to quantitatively measure two-photon cross-section by measuring the relationship between input and output intensity after absorption. This method is used to measure the two-photon cross section of ZnTeO thin film in Chapter 6. A schematic diagram of nonlinear transmission setup in our lab is shown in Figure 2.13. The laser source is a femtosecond synchronously pumped parametric oscillator (OPAL) laser pumped by the Mai-Tai laser. This OPAL laser provides wide continuous spectral coverage: synchronized signal and idler outputs deliver wavelengths from 1.1 to 2.25 μm with mode-locked output pulses less than 130 femtoseconds, repetition rate 80 MHz and high output power (more than 200 mW at 1.3 μm and 1.5 μm). The wavelength used in this measurement is 1380 nm. The pump wavelength from MaiTai is 775nm. An iris is used before the neutral density filter to ensure a circular beam. The neutral density filter is used to control the input intensity. In order to monitor the input intensity, a beam splitter used to split partial of the beam into a photo diode. A

focal lens is placed before the sample to focus the incident beam onto the sample film. The transmitted signal is monitored by a spectrometer. The spectrometer is Spectra Physics NIRQuest512-2.2 with Hamamatsu G9204-512W InGaAs linear array as detector, detection range 900-2200 nm, optical resolution ~ 4.6 nm w/25 μ m slit and noise to signal ratio $>10000:1$. Before measuring the sample, a relationship between the photo diode signal and spectrometer counts without the existence of sample is obtained by varying the input intensity. Then under the same experimental condition, the film sample is carefully placed into the sample holder perpendicular to the input beam.

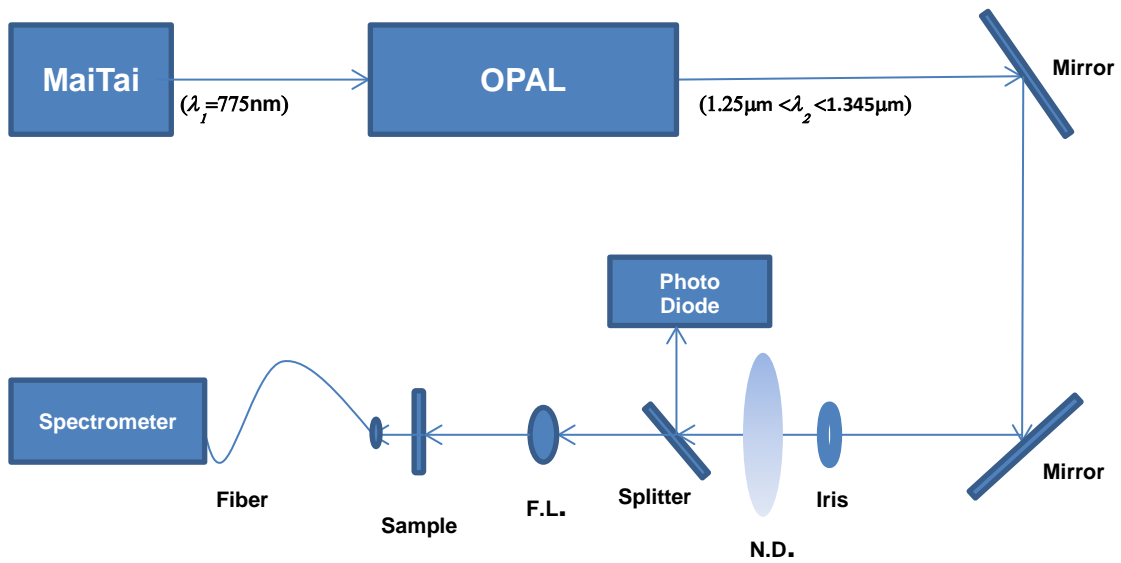


Figure 2.13 Schematic diagram of two-photon transmission measurement setup

Theoretically, if the nonlinear transmission change is only due to the two-photon absorption process, the transmitted intensity I' can be expressed as:

Equation 2.9

$$I' = \frac{I_0}{1 + I_0 L \beta}$$

Here, I_0 is the incident beam intensity, L is the thickness of the given sample, β is two-photon absorption coefficient of the given material in m/W . This equation can be rearranged as following:

Equation 2.10

$$1 + I_0 L \beta = \frac{I_0}{I'} = \frac{1}{T}$$

Where, T is the percentage of transmission. According to the equation above, a linear plot of $\frac{1}{T}$ with respect to I_0 should give us a linear relationship, and the resulting slope $b = L\beta$ is used to further calculate two-photon absorption coefficient:

Equation 2.11

$$\beta = b/L$$

If the nonlinear absorption coefficient β is experimentally measured, we can determine the two-photon cross section σ_2 using the following expression:

Equation 2.12

$$\beta = \sigma_2 N_0 = \sigma_2 N_A c \times 10^{-3}$$

Here, N_0 is the molecular density of the TPA compound, N_A is the Avogadro constant, $6.022 \times 10^{23} mol^{-1}$ and c is the concentration of the TPA compound in units of mol/L.

References

- [1]. Lakowicz, J. R., *Principles of Fluorescence Spectroscopy*. Springer: New York, 2006.
- [2]. Maciejewski, A.; Steer, R. P., Spectral and Photophysical Properties of 9,10-Diphenylanthracene in Perfluoro-Normal-Hexane - the Influence of Solute Solvent Interactions. *Journal of Photochemistry* **1986**, 35 (1), 59-69.

- [3]. Xu, C.; Webb, W. W., Measurement of Two-Photon Excitation Cross Sections of Molecular Fluorophores with Data from 690 to 1050 Nm. *Journal of the Optical Society of America B-Optical Physics* **1996**, *13* (3), 481-491.
- [4]. Xu, J. H.; Knutson, J. R., Ultrafast Fluorescence Spectroscopy Via Upconversion: Applications to Biophysics. In *Fluorescence Spectroscopy*, Brand, L.; Johnson, M. L., Eds. Elsevier Academic Press Inc: San Diego, 2008; Vol. 450, pp 159-183.
- [5]. Varnavski, O.; Yan, X. Z.; Mongin, O.; Blanchard-Desce, M.; Goodson, T., Strongly Interacting Organic Conjugated Dendrimers with Enhanced Two-Photon Absorption. *Journal of Physical Chemistry C* **2007**, *111* (1), 149-162.
- [6]. Varnavski, O.; Samuel, I. D. W.; Palsson, L. O.; Beavington, R.; Burn, P. L.; Goodson, T., Investigations of Excitation Energy Transfer and Intramolecular Interactions in a Nitrogen Corded Distyrylbenzene Dendrimer System. *Journal of Chemical Physics* **2002**, *116* (20), 8893-8903.
- [7]. Ramakrishna, G.; Goodson, T.; Rogers-Haley, J. E.; Cooper, T. M.; McLean, D. G.; Urbas, A., Ultrafast Intersystem Crossing: Excited State Dynamics of Platinum Acetylide Complexes. *Journal of Physical Chemistry C* **2009**, *113* (3), 1060-1066.
- [8]. Marconnet, A. M.; David, M. P.; Rogacs, A.; Flynn, R. D.; Goodson, K. E.; Asme, *Temperature-Dependent Permeability of Microporous Membranes for Vapor Venting Heat Exchangers*. 2009; p 1005-1012.
- [9]. Varnavski, O. P.; Ranasinghe, M.; Yan, X.; Bauer, C. A.; Chung, S. J.; Perry, J. W.; Marder, S. R.; Goodson, T., Ultrafast Energy Migration in Chromophore Shell-Metal Nanoparticle Assemblies. *Journal of the American Chemical Society* **2006**, *128* (34), 10988-10989.
- [10]. Ohsako, Y.; Thorne, J. R. G.; Phillips, C. M.; Zeigler, J. M.; Hochstrasser, R. M., Picosecond Transient Absorption-Spectroscopy of Polysilanes. *Journal of Physical Chemistry* **1989**, *93* (11), 4408-4411.
- [11]. Berera, R.; van Grondelle, R.; Kennis, J. T. M., Ultrafast Transient Absorption Spectroscopy: Principles and Application to Photosynthetic Systems. *Photosynthesis Research* **2009**, *101* (2-3), 105-118.

CHAPTER 3

BASIC CHARACTERIZATIONS AND TWO-PHOTON ABSORPTION OF T₈ SILSESQUIOXANES

The work in this chapter was published in two separate publications:

“Molecules with Perfect Cubic Symmetry as Nanobuilding Blocks for 3-D Assemblies. Elaboration of Octavinylsilsesquioxane. Unusual Luminescence Shifts May Indicate Extended Conjugation Involving the Silsesquioxane Core” Santy Sulaiman, Ajit Bhaskar, Jin Zhang, Guda Ramakrishna, Theodore Goodson III and Richard M. Laine *Chemistry of Materials* 2008, 20, pp 5563–5573.

“Synthesis, Characterization and Photophysical Properties of Polyfunctional Phenylsilsesquioxanes: [o-RPhSiO_{1.5}]₈, [2,5-R₂PhSiO_{1.5}]₈, and [R₃PhSiO_{1.5}]₈ Compounds with the Highest Number of Functional Units/Unit Volume” Santy Sulaiman, Jin Zhang, Theodore Goodson III and Richard M. Laine *Journal of Materials Chemistry* 2011, 21, pp 11177–11187.

This work is with contributions from Dr. Santy Sulaiman and Professor Richard M. Laine (Macromolecular Science and Engineering Center, University of Michigan). The work presented in this chapter was also published in Dr. Santy Sulaiman’s dissertation: “Synthesis and Characterization of Polyfunctional Polyhedral Silsesquioxane Cages”.

3.1 Overview

Polyhedral silsesquioxanes (SQs) and hybrid materials based on SQs offer advantages including enhanced thermal stability, good solubility, improved mechanical properties and low flammability. Shown in Figure 3.1 are the structure examples of the silsesquioxanes with different generation, symmetry and substitution. Molecular components assembled in a well-defined three dimensional geometry potentially lead to novel electronic, optical and nonlinear optical properties. Among nonlinear optical properties, two-photon absorption (TPA, a third order optical nonlinearity) has received tremendous research attention in recent years because of their applications in different areas of science.¹ Several molecular architectures such as branched,²⁻⁶ dendritic,⁷⁻⁸ macrocyclic topologies⁹⁻¹¹ have shown enhanced TPA cross-sections over their linear counterparts. It has also been shown that when the chromophores are decorated on silver and gold nanoparticle, there is a strong electronic coupling between the chromophores and thereby enhancing the nonlinear optical properties.¹²⁻¹⁵ However when the chromophores are adsorbed on a nanoparticle it is difficult to judge the orientation and geometry of chromophore on the nanoparticle. If the chromophores are covalently attached to a known three dimensional geometry, it is easy to understand the influence of the molecular orientation as well as charge transfer character on the two-photon absorption properties. Additional interests include the possibility of introducing 8, 16 or even up to 24 functional groups to the core molecular structures providing potential access to novel star, dendrimer and hyperbranched compounds. Understanding electronic coupling between the π -conjugated chromophores is also crucial to design 3-D SQ materials and make them suitable for electronic and photonic applications. To these effects, three sets of silsesquioxane derivatives have been studied, including octavinylstilbenesilsesquioxane ($[\text{RStyrenylSiO}_{1.5}]_8$, R= NH_2 , MeO, or H), polyfunctional phenylsilsesquioxanes ($[\text{o-RPhSiO}_{1.5}]_8$, $[\text{2,5-R}_2\text{PhSiO}_{1.5}]_8$ and $[\text{R}_3\text{PhSiO}_{1.5}]_8$, R= NBocStilbene , AceStilbene , MeStilbene), and partial and full cage dimethylaminostilbene silsesquioxane derivatives ($[\text{p-Me}_2\text{NStilSi}(\text{OSiMe})_3]$, $[\text{p-Me}_2\text{NStilSi}(\text{OSiMe})_4]$, and $[\text{p-Me}_2\text{NStil}_8\text{SiO}_{1.5}]_8$).

This chapter mainly focuses on the steady state measurement and two-photon absorption measurement of octavinylstilbenesilsesquioxane and polyfunctional phenylsilsesquioxanes derivatives are presented. In order to better understand the materials, synthesis, basic characterizations and theoretical studies regarding investigated systems are also provided.

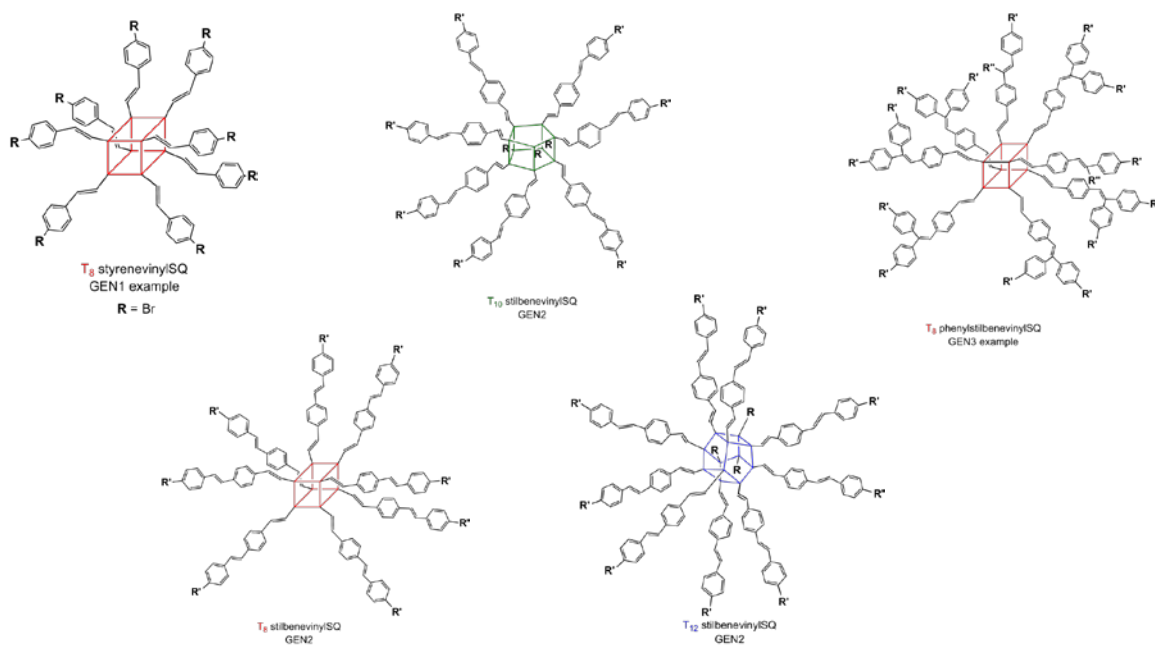


Figure 3.1 Structure examples of silsesquioxanes with different core, symmetry, chromophores and generation

3.2 Octavinylstilbenesilsesquioxane Derivatives (GEN2 T₈)

In this section, a set of R-vinylStilbeneSiO_{1.5}]₈ compounds with perfect 3-D or cubic symmetry were investigated. The Structures are shown in Figure 3.2. The synthesis procedure is present in Figure 3.3. Study on the UV-Vis, emission and two-photon absorption properties of the R-vinylStilbeneSiO_{1.5}]₈ compounds especially where R =

NH₂ reveals exceptional red shifts (120 nm), and excellent two photon absorption properties suggest excellent charge transfer character in the system.

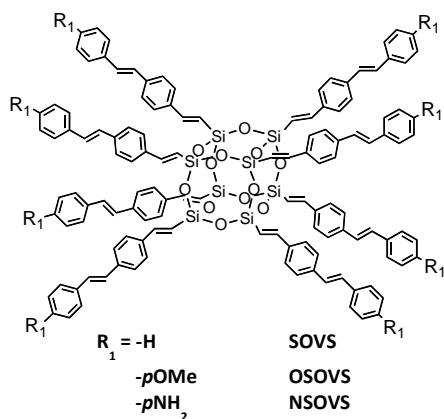


Figure 3.2 Molecular structure of *R*-vinylstilbeneOS.

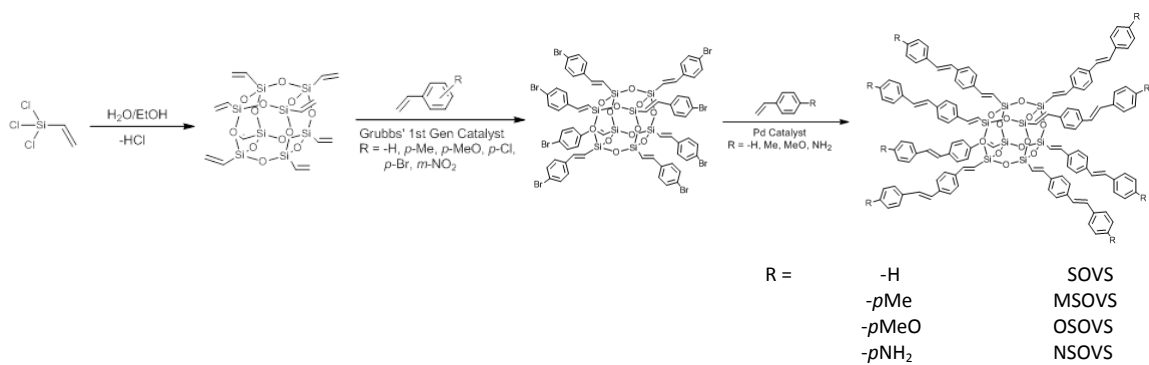


Figure 3.3 Synthesis of *R*-vinylstilbeneOS.

3.2.1. Basic Characterization

MALDI-TOF and Gel-permeation chromatographic analyses data for first and second generation stars are given in Table 3.1. These materials exhibit narrow molecular weight distributions, indicating that they retain their silica cube structures. The values of M_n and M_w as measured by GPC are smaller than the molecular weight measured by MALDI-TOF, but expected from GPC characterization of rigid, spherical molecules using flexible, linear standards, based on previous results.¹⁶

Table 3.1 Characterization data for R-vinylstilbeneOS.

Compound	m/z (Ag^+ adduct)		GPC			Ceramic yield (%)		$T_{d5\%}$ (°C)
	MALDI	calc	M_n	M_w	PDI	Calculated	Actual	
SOVS	2162.7	2166.7	1511	1597	1.06	23.4	23.8	400
MSOVS	2279.9	2279.0	1775	1876	1.06	22.1	21.1	390
OSOVS	2404.6	2406.9	1880	2096	1.12	20.9	22.6	315
NSOVS	2287.6	2286.9	1374	1549	1.13	22.1	20.1	345

UV-Vis absorption and photoluminescence (PL) of R-vinylstilbeneOS in THF are shown below (Figure 3.4). Both the absorption and emission spectra show red-shifts from the corresponding small molecule analogues (styrene and *p*-vinylstilbene) untethered to the silsesquioxane core. R-styrenylOS compounds show smaller red-shifts than R-vinylstilbeneOS compounds (10-40 nm shifts vs 30-80 nm shifts). This is expected because the conjugation lengths for the R-vinylstilbeneOS compounds are twice those of the R-styrenylOS compounds. Within both series of compounds, the red-shifts from the small molecules become larger as the functional groups at the silsesquioxane's vertex become more electron-donating. The photoluminescence from NSOVS is quenched on reaction with 3,5-difunctional benzoyl chlorides.

The silsesquioxane core, with a silicon atom attached to three oxygen atoms, has been suggested to act as an electron-withdrawing substituent equivalent to a CF_3 group.¹⁷ Therefore, one would normally expect to observe a blue-shift for both UV-Vis and PL spectra. One possible reason for this shift is considered below.

The Figure 3.5 absorption and emission spectra of POVS and SOVS allow us to compare the photophysical properties of the first and second generation materials. The two sets of materials demonstrate similar Stokes shifts of ~ 50 nm. Both absorption and emission spectra for the second generation materials are red-shifted ~ 70 nm from those for the first generation materials. The spectra show normal 0-0 transitions typical for conjugated aromatic compounds suggesting that the silica core has little influence other than the slight red shifts compared with the organic compounds alone.

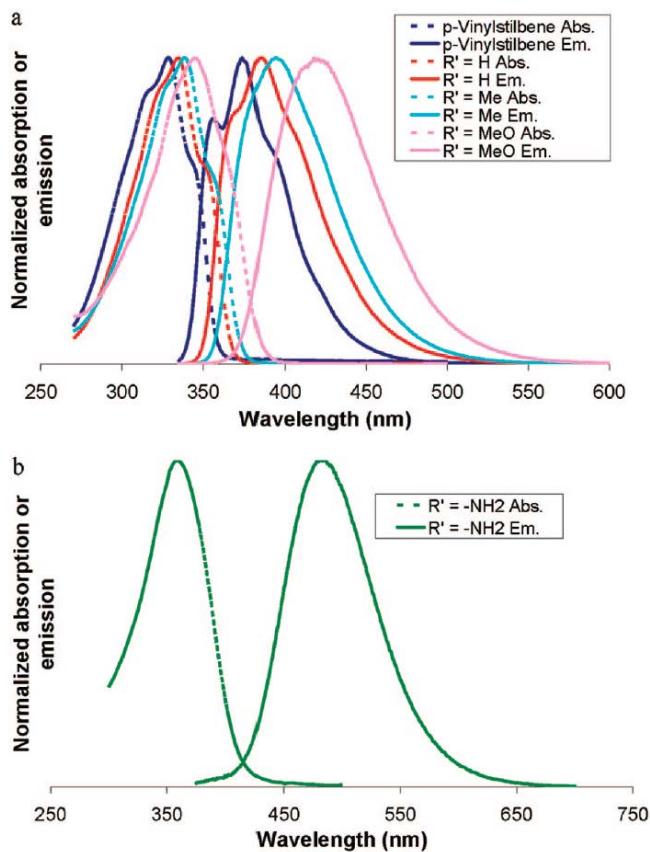


Figure 3.4 UV-Vis and PL spectra of R' VinylStilbeneOS (a: $R' = -H, -Me, \text{ and } -MeO$; b: $R' = -NH_2$) in THF

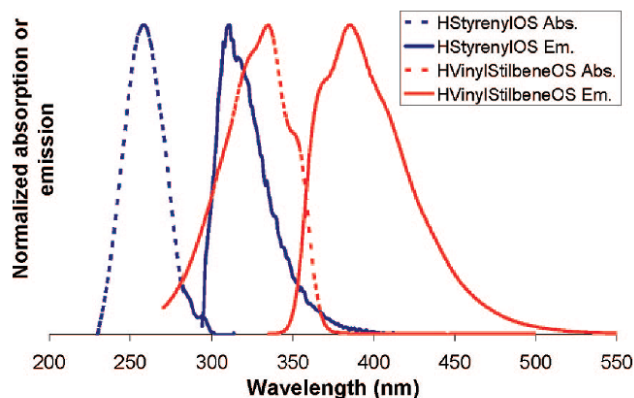


Figure 3.5 UV-Vis and PL spectra of HStyrenylOS and HVinylStilbeneOS

The PL quantum yields for R-styrenylOS are very low, as observed from the need to characterize their PL behavior using samples from UV-Vis absorption measurements without dilution. The PL quantum yields for R-vinylstilbeneOS were measured at 320 nm at high dilution to avoid the formation of aggregates in solution. The PL quantum yields were calculated using anthracene and 9,10-diphenylanthracene as standards.¹⁸⁻²⁰ Their values are shown in Table 3.2. The observed Φ_{PL} for SOVS is 36%, which is comparable to that measured for the corresponding small molecule, *p*-vinylstilbene. The measured Φ_{PL} for NSOVS is six times lower as a result of charge transfer (CT) effects in the solution, which partially funnel the energy away from luminescence but greatly improve the two-photon cross-section (see Table 3.2 and Figure 3.9) which led to the two photon studies as follows.

3.2.2. Steady-State Measurements

As noted above the absorption and emission spectra of the investigated systems dissolved in THF are shown in Figure 3.6 and Figure 3.7. The corresponding optical properties are summarized in Table 3.2. It can be noted from the figure that the absorption spectrum of the more polar derivative (NSOVS) has shown structureless and

red-shifted absorption when compared to the less polar ones (SOVS and OSOVS) suggesting the involvement of a charge transfer transition.

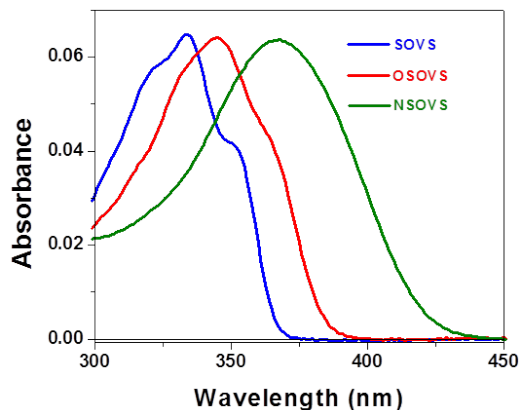


Figure 3.6 Steady state absorption spectra of SOVS, OSOVS and NSOVS

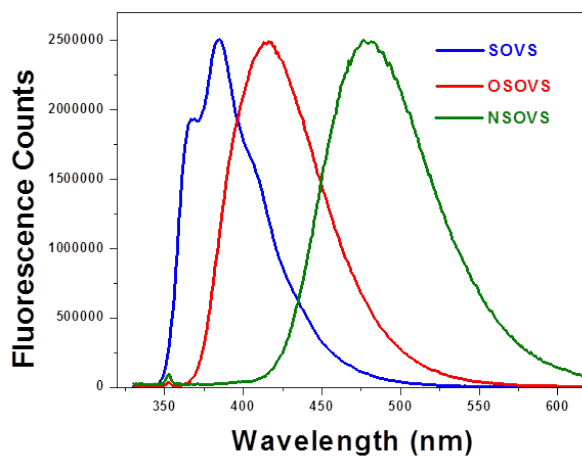


Figure 3.7 Steady state fluorescence emission spectra of SOVS, OSOVS and NSOVS

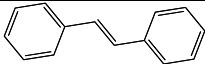
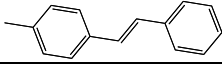
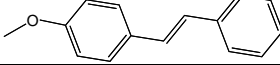
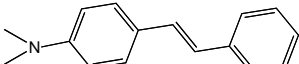
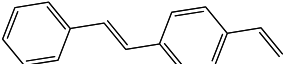
It can also be observed from Figure 3.9 and Table 3.2 that the Stoke's shift increases with increases in the strength of donor (from SOVS to NSOVS) suggesting an increased charge transfer character. The reduction of the quantum yield from SOVS to NSOVS is also in accordance with the increased charge transfer character of the

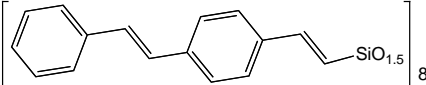
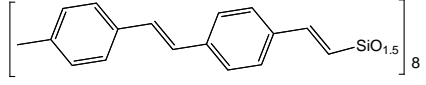
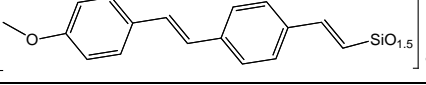
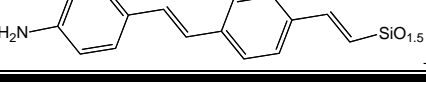
chromophores. It will be interesting to observe how the arrangement of chromophores and the charge transfer character influence the two-photon absorption properties as will be explored at a later date.

Table 3.2 Spectral data of R-styrenylOS and R-vinylstilbeneOS.

Compound	UV λ_{\max} (nm)	PL λ_{\max} (nm)	Φ_{PL} (%)	Stokes shift $\Delta\nu$ (cm^{-1})	δ (GM) 780 nm	δ/group (GM)
POVS	260	311	n.a.			
MPOVS	265	315	n.a.			
OPOVS	275	326	n.a.			
Styrene	251	304	n.a.			
SOVS	335	385	36	3966	25	3.1
MSOVS	338	394	22			
OSOVS	345	418	16	4947	110	13.8
NSOVS	358	482	6			
<i>p</i> -Vinylstilbene	329	374	24	6458	810	101

Table 3.3 Spectral data of R-styrenylOS and R-vinylstilbeneOS as a function of solvent and two photon cross-sections of selected compounds

Compound	Absorption Max (nm)	Emission Max (nm)	Solvent	Q_f %	Ref
	307	350	CH ₃ CN		21
	311	354	CH ₃ CN		21
	318	375	CH ₃ CN		21
	347	379	Hexane,		22
	349	407	Et ₂ O,		22
	352	418	BuCl,		22
	348	433	EtOH		22
	351	440	CH ₃ CN		22
	324	370	hexane		
	329	374	CH ₂ Cl ₂	24	

	325	369	CH ₃ CN	
	329	375	hexane	
	335	385	CH ₂ Cl ₂	36
	331	388	CH ₃ CN	
	335	384	hexane	
	338	394	CH ₂ Cl ₂	22
	334	398	CH ₃ CN	
	339	378	hexane	
	345	418	CH ₂ Cl ₂	12
	343	431	CH ₃ CN	
	358	482	CH ₂ Cl ₂	6
	361	507	CH ₃ CN	

3.2.3. Two-Photon Cross-Section Measurements

Molecular components assembled in a well-defined three dimensional geometry can potentially lead to novel electronic, optical and nonlinear optical properties. Among nonlinear optical properties, two-photon absorption (TPA, a third order optical nonlinearity) has received tremendous research attention in recent years because of their applications in different areas of science.¹ Several molecular architectures such as branched^{2-6, 23}, dendritic⁷⁻⁸, macrocyclic topologies¹⁰⁻¹¹ have shown enhanced TPA cross-sections over their linear counterparts. It has also been shown that when the chromophores are decorated on silver nanoparticles, there is a strong electronic coupling between the chromophores and thereby enhancing the nonlinear optical properties.¹² However when the chromophores are adsorbed on a nanoparticle it is difficult to judge the orientation and geometry of chromophore on the nanoparticle. If the chromophores are covalently attached to a known three dimensional geometry, it is easy to understand the influence of the molecular orientation as well as charge transfer character on the two-photon absorption properties. To this effect, we have investigated the two-photon absorption properties of the donor-acceptor derivatives of selected vinyl stilbenes shown in Figure 3.2 using methods described in the experimental section.

The relationship between input intensity and fluorescence is plotted in Figure 3.8. TPA cross-sections as a function of wavelength are plotted in Figure 3.9 for all the investigated chromophores. It is clear from the TPA cross-sections that the cross-section

increases with the increases in donor-strength on the chromophore. It can also be noted that the cross-section per molecule has also increased (Table 3.2) and it is increased by 35 times when the donor is changed from SOVS to NSOVS. This 35 fold increase of TPA cross-section can be explained by increased change in dipole-moment term (major factor responsible in sum-over states formalism).⁴⁻⁶

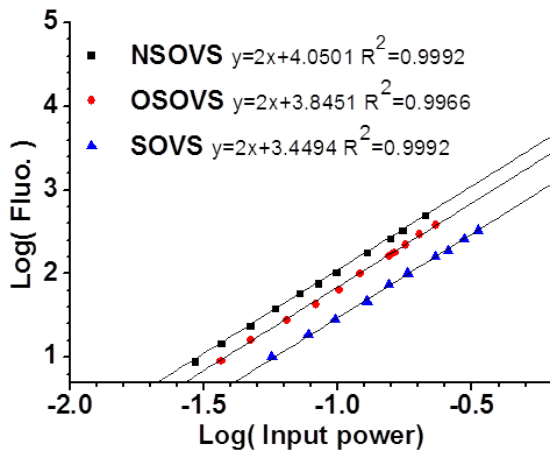


Figure 3.8 Two photon absorption cross-section measurement calculation of NSOVS, OSOVS and SOVS

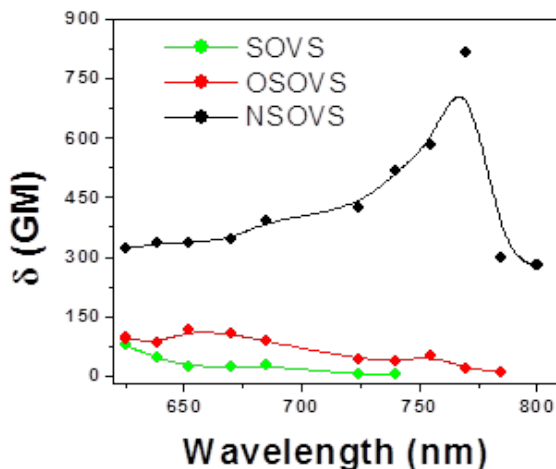
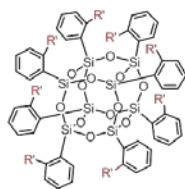


Figure 3.9 Two-photon absorption cross-section spectra for SOVS, OSOVS and NSOVS

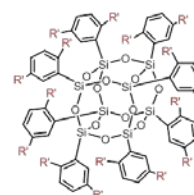
3.3 Polyfunctional Phenylsilsesquioxanes: $[o\text{-RPhSiO}_{1.5}]_8$, $[2,5\text{-R}_2\text{PhSiO}_{1.5}]_8$ and $[\text{R}_3\text{PhSiO}_{1.5}]_8$

The steady state and two photon absorption results of polyfunctional phenylsilsesquioxanes: $o\text{-RStyr}_8\text{OPS}$, $\text{RStyr}_{16}\text{OPS}$, and $\text{RStyr}_{24}\text{OPS}$ where R = 4-methyl (Me), Boc-protected 4-amino (NBoc), or 4-acetoxy (Ace) are presented in this section. The molecular structures are shown in Figure 3.10. These derivatives show unique UV-Vis absorption and photoluminescent behavior that point to interesting interactions between the organic tethers. $\text{RStyr}_{16}\text{OPS}$ exhibit absorption and emission spectra as well as Φ_{PL} similar to 1,4-distyrylbenzene, pointing to disruption in conjugation with the silsesquioxane cage because of steric interactions. $\text{RStyr}_{24}\text{OPS}$ offer absorption maxima that are blue-shifted and emission maxima that are red-shifted relative to $\text{RStyr}_{16}\text{OPS}$. $\text{NBocStyr}_{24}\text{OPS}$ and $\text{AceStyr}_{24}\text{OPS}$ show moderate Φ_{PL} and high two photon cross-section values, leading us to conclude that they offer better charge transfer character than the 16mers.

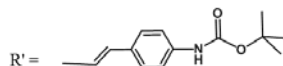
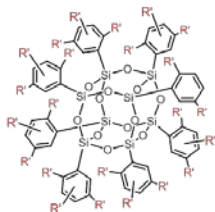
**$o\text{-RStil}_8\text{OS}$:
(8mer)**



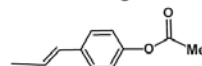
**$\text{RStil}_{16}\text{OS}$:
(16mer)**



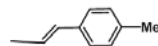
**$\text{RStil}_{23}\text{OS}$:
(23mer)**



$o\text{-NBocStil}_8\text{OS}$, $\text{NBocStil}_{16}\text{OS}$, $\text{NBocStil}_{23}\text{OS}$



$o\text{-AceStil}_8\text{OS}$, $\text{AceStil}_{16}\text{OS}$, $\text{AceStil}_{23}\text{OS}$



$o\text{-MeStil}_8\text{OS}$, $\text{MeStil}_{16}\text{OS}$, $\text{MeStil}_{23}\text{OS}$

Figure 3.10 Molecular structures of investigated systems: $o\text{-NBocStil}_8\text{OS}$, $\text{NBocStil}_{16}\text{OS}$, $\text{NBocStil}_{23}\text{OS}$, $o\text{-AceStil}_8\text{OS}$, $o\text{-AceStil}_{16}\text{OS}$ and $o\text{-AceStil}_{23}\text{OS}$

3.3.1. Basic Characterization

Table 3.4, Table 3.5 and Table 3.6 detail the different molecular species present in RStyr_xOPS and their percentages based on MALDI-ToF data. Even though each set of compounds (o-RStyr₈OPS, RStyr₁₆OPS, and RStyr₂₄OPS) was synthesized using starting material from the same batch, their MALDI-ToF data show different compositions of molecular species. For example, MALDI-ToF data for o-MeStyr₈OPS and o-AceStyr₈OS show different percentages for the 7-mer and the 8-mer, and o-NH₂Styr₈OS show the presence of the 9-mer, which is not present in the other two compounds. We attribute these results to differences in ionization potentials of the compounds rather than substitutional variations.

Table 3.4 Molecular species present in MeStyr_xOPS

<i>o</i> -MeStyr ₈ OPS		MeStyr ₁₆ OPS		MeStyr ₂₄ OPS	
Species present	%	Species present	%	Species present	%
<i>o</i> -MeStyr ₇ OPS	5	MeStyr ₁₄ OPS	2.4	MeStyr ₂₂ OPS	18.5
<i>o</i> -MeStyr ₈ OPS	95	MeStyr ₁₅ OPS	30.5	MeStyr ₂₂ BrPh ₁ OPS	5.1
		MeStyr ₁₆ OPS	62.2	MeStyr ₂₃ OPS	47.0
		MeStyr ₁₇ OPS	4.9	MeStyr ₂₃ BrOPS	5.8
				MeStyrenyl ₂₄ OPS	23.6
Average: 7.95		Average: 15.7			

Complete conversion of the –Br groups is observed in the MALDI-ToF spectra for almost all the compounds, with the exception of MeStyr₂₄OPS, which shows small amounts of unreacted –Br groups. This is not completely unexpected, considering the steric hindrance associated with having three –Br groups on a phenyl ring attached to the SQ core, especially for *o*-Br groups.

The MALDI-ToF data of NBocStyr_xOPS show a series of low intensity peaks close to the mass of the deprotected species. We were able to collect MALDI-ToF data for two of the deprotected compounds: *o*-NH₂Styr₈OS and NH₂Styr₁₆OPS. No MALDI-ToF data were obtained for NH₂Styr₂₄OPS and AceStyr₂₄OPS, most probably due to their

complex structures, which makes them unstable under the UV laser of MALDI-ToF such that they fragment. GPC and ceramic yield data for these two compounds suggest that nearly all of the –Br groups were converted to the organic derivatives.

Table 3.5 Molecular species present in NH₂Styr_xOPS

<i>o</i> -NH ₂ Styr ₈ OPS		NH ₂ Styr ₁₆ OPS	
Species present	%	Species present	%
<i>o</i> -NH ₂ Styr ₈ OPS	89.6	NH ₂ Styr ₁₆ OPS	100
<i>o</i> -NH ₂ Styr ₉ OPS	10.4		
Average: 8.1		Average: 16.0	

Table 3.6 Molecular species present in AceStyr_xOPS

<i>o</i> -AceStyr ₈ OPS		AceStyr ₁₆ OPS	
Species present	%	Species present	%
<i>o</i> -AceStyr ₇ OPS	23.6	AceStyr ₁₅ OPS	10.6
<i>o</i> -AceStyr ₈ OPS	76.4	AceStyr ₁₆ OPS	74.4
		AceStyr ₁₇ OPS	15.1
Average: 8.1		Average: 16.05	

3.3.2. Steady-State Measurements

The UV-Vis absorption and photoluminescence spectra for RStyr_xOPS are shown in Figure 3.11, Figure 3.12 and Figure 3.13. The photophysical data is summarized in Table 3.8. Within each series of compounds with the same R group, we observed the same trends as discussed below. While consistent in their trends, there are still some important surprises.

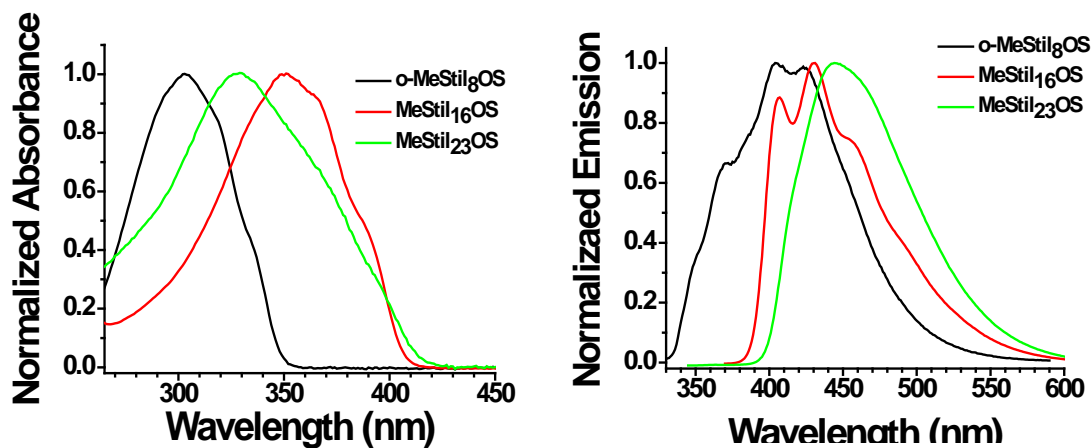


Figure 3.11 Absorption and emission spectra for MeStyr_xOPS

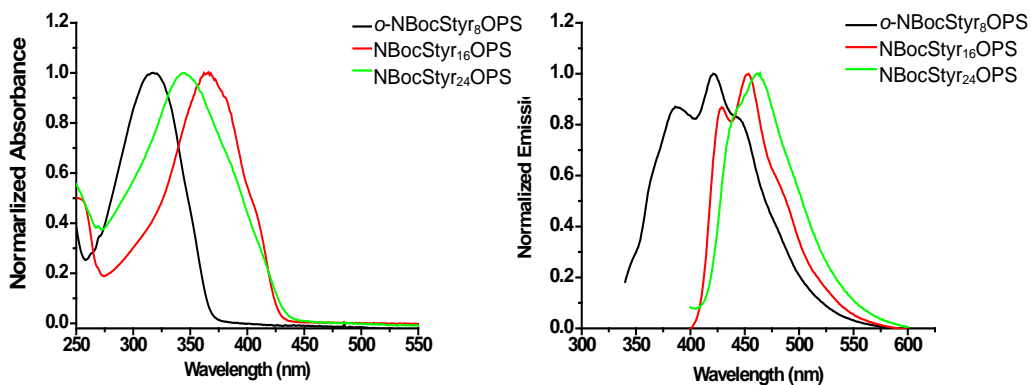


Figure 3.12 Absorption and emission spectra for NBocStyr_xOPS

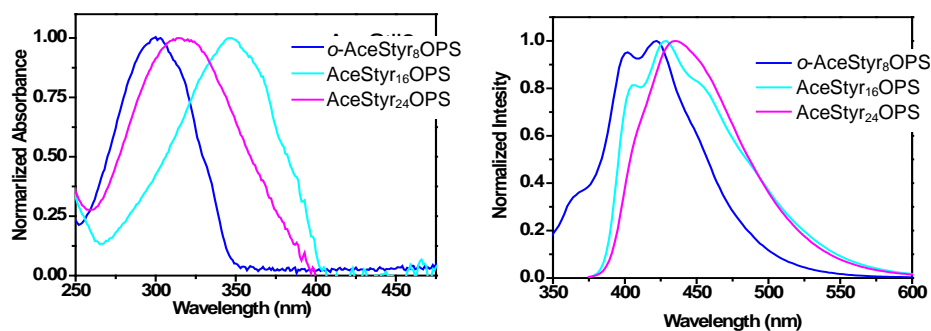


Figure 3.13 Absorption and emission spectra for AceStyr_xOS

First, the absorption and emission spectra for RStyr₁₆OPS are red-shifted from those for *o*-RStyr₈OPS as expected because of the longer conjugation length. However, the absorption spectra for RStyr₂₄OPS are blue-shifted from those for RStyr₁₆OPS, whereas the emission spectra are red-shifted. Furthermore, for RStyr₈OPS Φ_{PL} are typical of those seen previously at ca. 0.04 whereas for the RStyr₁₆OPS Φ_{PL} are an order of magnitude higher at 0.40-0.60. Unexpectedly the Φ_{PL} for RStyr₂₄OPS are 0.10-0.30 lower than RStyr₁₆OPS. This is surprising because it might be anticipated that RStyr₂₄OPS would exhibit more extensive conjugation resulting in red-shifts in both the absorption and emission spectra relative to those of RStyr₁₆OPS. This should lead to more stabilization in the excited state leading to higher Φ_{PL} values.

Table 3.7 Photophysical data for RStyr_xOPS (THF, CH₂Cl₂ peak positions are identical)

<i>R</i> group	<i>x</i>	Absorption λ_{max} (nm)	Emission λ_{max} (nm)	Φ_{PL} %	Stoke's shift $\lambda_{max}(\lambda_{max})$ (cm ⁻¹)
<i>p</i> -MeStilbene ²⁴		298, 311	355	9	
1,4-Distyrylbenzene ²⁵		353	385, 408	62	
1,2,4-TriStyrenylbenzene ²⁶		320, 355 ^b			
1,3,5-Tristyrenylbenzene ²⁷		297	412 (toluene) 384 (<i>n</i> -hexane)		
<i>p</i> -MeStyr ₈ OPS ^a		320	400, 422	4	

<i>Me</i>	<i>o</i> -8	303	<u>405</u>	4	8312 ^c
	16	349	407, <u>431</u> , 457	57	5451 ^c
	24	329	<u>444</u>	39	7873 ^c
<i>NBoc</i>	<i>o</i> -8	317	386, <u>422</u> , 445 ^b	5	7849 ^c
	16	364	429, <u>453</u>	43	5398 ^c
	24	346	440, ^b <u>461</u>	8	7210 ^c
<i>Acetoxy</i>	<i>o</i> -8	300	402, <u>422</u>	4	9637 ^c
	16	347	407, <u>429</u> , 451	45	5508 ^c
	24	317	<u>435</u> , 453 ^b	19	8557 ^c

^a*p*-MeStyr₈OPS synthesized from *p*-I₈OPS. ^bShoulder. ^cThere are several emission bands; the emission maximum (underlined) is used to calculate the Stoke's shift.

In order to explain these results we must first compare the observed behavior with their organic analogs.²⁵⁻²⁷ The comparative data are also provided in Table 3.7. Thus, the absorption spectrum of *o*-MeStyr₈OPS has the same λ_{\max} as *p*-methylstilbene. This is \approx 20 nm blue-shifted from the absorption λ_{\max} of *p*-MeStyr₈OPS synthesized from *p*-I₈OPS.²⁸ In contrast, the emission λ_{\max} for *p*-methylstilbene is 355 nm compared to 400 nm and 420 nm for *p*-Metyr₈OPS and 405 nm for *o*-MeStyr₈OPS.

A comparison of 1,4-distyrenylbenzene with MeStyr₁₆OPS shows similar absorption λ_{\max} of 353 nm and 349 nm suggesting similar ground states. The emitting λ_{\max} are 408 nm vs 431 nm, which may be accounted for in part by the methyl substituent. In addition, the Φ_{PL} values are quite similar at 62 % and 57 % (ethanol vs THF).

Finally, comparing 1,2,4-tristyrenylbenzene, 1,3,5-tristyrenylbenzene and MeStyr₂₄OPS, we see that the all *meta* 1,3,5-tristyrenylbenzene has an absorption λ_{\max} at \approx 300 nm whereas the 1,2,4-isomer has an absorption λ_{\max} at \approx 320 nm. The emission λ_{\max} for the 1,2,4-isomer is not reported but that for the 1,3,5-isomer is 412 nm in toluene. The data suggest that the absorption and emission max for MeStyr₂₄OPS are quite red-shifted from the 1,3,5-tristyrenylbenzene analog but may be similar to or red-shifted from the 1,2,4-isomer as well. Thus, the blue shift for MeStyr₂₄OPS seems explainable in terms of the organic analogs. However, the Φ_{PL} values remain difficult to explain.

Multiple theoretical calculations suggest that the cage is highly electrophilic,²⁹ which is supported by the fact that it auto-catalyzes bromination as discussed in the accompanying paper.³⁰ Further support for this comes from our recent studies offering considerable evidence for charge transfer transitions in the excited state leading, for example, to quite high two photon absorption cross sections as discussed below.^{28, 31} As also noted in the accompanying paper, the cage interacts with aromatic ring substituents as if it were an electron withdrawing substituent equivalent to a CF₃ or NO₂ group.¹⁷

Consequently, one might expect to see such an electron withdrawing effect on the stilbene substituents prepared here (RStyr₈OPS) whether they are *ortho*- or *para*-substituents. The implication is that the cages should cause considerable blue shifts in both the absorption and emission maxima. This is contrary to what is seen. Therefore this argument cannot be used to explain the blue shift in the absorption data for the *ortho*-stilbene (*o*-MeStyr₈OPS). The only other possible explanation that seems valid is that the styrenyl group in the *ortho* position is forced to spend some of its time above the cage face. The crystal structure of the starting [*o*-BrPhSiO_{1.5}] indicates that the bromo group sits over the face of the very electrophilic cage.³⁰ Indeed, this interaction might actually be stabilized if the cage is considered to be highly electrophilic. In fact, Bowers et al calculate that the highly electrophilic behavior extends beyond the cage,²⁹ supporting the suggestion that the cage face polarizes Br₂ promoting *ortho*-substitution and the possibility that the styrenyl group prefers to sit above the electrophilic cage face.³⁰ This latter interaction could explain the blue shift relative to the *para* analog (*p*-MeStyr₈OPS).

However, the emission spectrum of *o*-MeStyr₈OPS is clearly red-shifted from that of *p*-methylstilbene and similar to that of *p*-MeStyr₈OPS. The quantum yield of *o*-MeStyr₈OPS is also similar to *p*-MeStyr₈OPS. In our previous work, we attributed the red-shifts in the absorption and emission spectra of *p*-MeStyr₈OPS compared to molecular stilbene to 3-D conjugation as involving the LUMO of the SQ cage.²⁸ It appears that the excited states of both *o*- and *p*-MeStyr₈OPS are quite similar allowing for the argument that both excited states access the same LUMO inside the SQ cage.

The absorption and emission spectra of NBocStyr_xOPS are only slightly red-shifted from those of MeStyr_xOPS and AceStyr_xOPS. This is expected given that the amino groups are masked by the Boc protecting groups, which are electron withdrawing. We would expect much larger red-shifts from free amino groups due to their strong donor characteristics, as seen previously.^{28, 31} Normally, *para*-alkoxy substituents exhibit good-to-excellent electron donating properties; however, the AceStyr_xOS absorption and emission spectra are similar to MeStyr_xOS suggesting roughly equivalent electron-donating abilities. Thus the electron-withdrawing characteristics of the acyl group seems to balance the normal electron donating properties of a *para* oxygen substituent, but the TPA data suggest this is not quite a correct assessment (see below).

The absorption and emission spectra of RStyr₁₆OPS are both red-shifted from those of *o*-RStyr₈OPS as expected considering the longer conjugation lengths. The absorption maxima and quantum yields for RStyr₁₆OPS are comparable to those for the small molecule analog, 1,4-distyrylbenzene, while the emission spectra are red-shifted from 1,4-distyrylbenzene (20-45 nm depending on the R-group). The emission spectra of RStyr₁₆OPS exhibit structured bands typical for conjugated aromatic compounds. These compounds also have low two-photon cross-sections (GM values, see below). All of these observations, as briefly noted above, suggest that the HOMO and LUMO of RStyr₁₆OS are similar to those of 1,4-distyrylbenzene without any contributions from the SQ cage.²⁶ The simplest explanation for this behavior is that the presence of the second styrenyl group on each corner of the cage causes overcrowding around the cage, forcing the distyrenylphenyl groups away from the cage face. It also may interrupt the 3-D interaction with the cage in the excited state. Thus we observe photophysical behavior expected for an electronically isolated organic fragment. This contrasts with the RStyr₂₄OPS compounds.

The blue-shifts in the RStyr₂₄OPS absorption spectra compared to those of RStyr₁₆OPS likely arise from the *meta*-styrenyl groups present on each central phenyl ring (see Figure 3.14). As discussed in the accompanying paper on the polybromination of OPS,³⁰ Br substitution starts at the *ortho*-position (position 1 in Figure 3.14). The

second Br- adds (almost exclusively) *para*- to the first Br- (position 5 in Figure 3.32). We believe that at this point, the steric hindrance will prevent addition of a third Br to the other *ortho*-position (position 6, Figure 3.14). Therefore, addition of a third Br would be expected to occur at either of the two other positions on the phenyl rings (positions 3 and 4 in Figure 3.14), as supported by the X-ray single crystal data from the accompanying paper, which shows partial occupancy at both positions. This means that there will always be two styrenyl groups *meta* to each other in RStyr₂₄OPS.

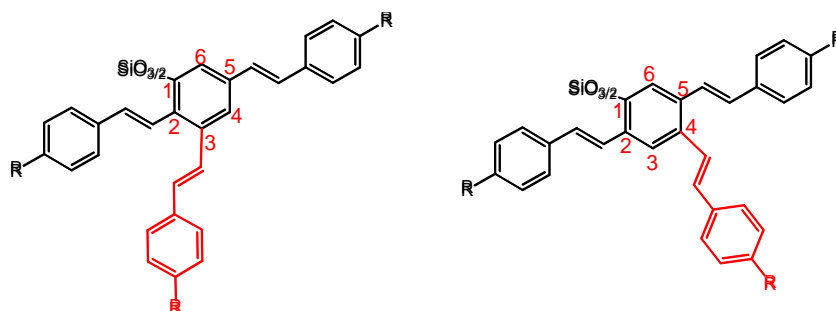


Figure 3.14 Two possible configurations of RStilbene₂₄OS corner

Previous work on 1,2,4-tristyrylbenzene²⁶ suggests that its absorption spectrum can be considered as a summation of the 1,3-distyrylbenzene and 1,4-distyrylbenzenespectra, with a maximum (320 nm) in between the maxima of the two distyrylbenzenes (300 nm and 355 nm) and a shoulder corresponding to the absorption maximum of 1,4-distyrylbenzene (355 nm). The authors attribute this phenomenon to interactions between the two conjugated distyrylbenzene “fragments” of the molecule. However, no rationalization as to what these interactions might be is available in the literature.

Related work suggests that *meta*-substituted phenylenevinylene units in *meta*-distyrylbenzene and oligo(phenylenevinylene) can be considered “conjugative insulators” that disrupt the interaction between phenylenevinylene units.²⁵⁻²⁶ The 1,3,5-

tristyrylbenzene absorption λ_{\max} , where all phenylenevinylene units are *meta*-, is 297 nm (toluene or *n*-hexane) and the emission λ_{\max} at 412 nm in toluene.²⁵

In comparison, we begin by considering the widths of the absorption bands for RStyr₂₄OPS. For each series of R-groups, the absorption spectrum of RStyr₂₄OPS has an onset similar to that for *o*-RStyr₈OPS that tails into the absorption spectrum for RStyr₁₆OPS. Each has a λ_{\max} in between the maxima of *o*-RStyr₈OPS and RStyr₁₆OPS. This implies that the absorption spectra for each RStyr₂₄OPS actually consist of contributions from all “fragments” of the tristyrenylphenyl groups. Basically we observe a sum of the interaction between the *ortho*-stilbenes with the face of the SQ cage (Figure 3.33a) with the longer conjugation of the distyrylbenzene units (Figure 3.33b) coupled with the disruption in overall conjugation caused by the *meta*-positioned styrenyl (a.k.a. phenylenevinylene) units (Figure 3.33c). The presence of the third styrenyl group on each corner of the cage causes even more crowding around the cage and some of the organic groups are forced to approach the face of the cage, thus giving rise to an interaction (blue shift) between the cage face and the organic groups observed in the absorption spectra.

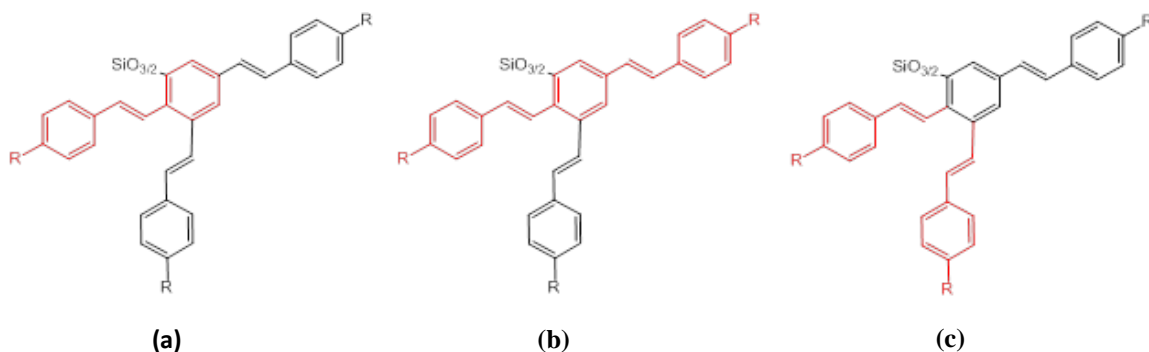


Figure 3.15 Interactions of “fragments” of tristyrenylphenyl groups on each corner of RStyr₂₄OS

The emission spectra for RStyr₂₄OPS are red-shifted from their respective RStyr₁₆OPS and show no band structure. Their quantum yields are slightly lower, but the two-photon cross-section values are much higher for the NBoc and Acetoxy groups, see

below. The data suggest that there are actually two pathways for the transition from the excited to the ground state: charge transfer (CT) and normal radiative emission from a π^* state.

The CT effects explain the lack of structure in their emission spectra and the two high TPA values (see below). Normally CT funnels energy away from luminescence and gives rise to low quantum yields. However, in the case of RStilbene₂₄OS, the Φ_{PL} values are not as low as expected if CT is the only mechanism for excited-to-ground state transition. The normal π^* radiative emission provides another option, and explains the Φ_{PL} values of RSyr₂₄OS. For both mechanisms to be active, both processes must have roughly equivalent decay rates and energies otherwise one would dominate over the other. Indeed, this suggests that one might promote the CT transition by using a more polar solvent to stabilize the CT transition state and perhaps improve the TPA values at the expense of the Φ_{PL} values. Such studies are planned in the future.

One final comment about these results should be made. Because of the very high density of functional groups, it is possible that some form of 3-D through space interactions are also involved in their absorption and emission behavior. At this point, this is still a matter of intense discussion and research regarding the possibility that as higher densities of functional groups affect absorption and emission behavior in cyclic polystyrenes albeit mostly causing blue shifts.³²

3.3.3. Two-Photon Cross-Section Measurements

The interaction of the functional groups at the corners of the cage can be very strong and it has been shown previously that this interaction can lead to new optical properties.²⁸ The possibility of enhancement of the cage macromolecule's two-photon absorption cross-section may result in possible applications in not only optical limiting and sensor protection but the enhanced transition moment of these systems may also lead to enhanced solar energy harvesting devices. In this section we discuss the linear and

nonlinear optical properties of this new class of SQs and probe their two-photon absorption properties both in magnitude and spectral width.

Two-photon excited-state fluorescence (TPEF) measurements with a femtosecond laser were used to measure TPA cross-sections as a function of wavelength. Figure 3.16 illustrate the quadratic dependence between the input power and fluorescence counts. It is clear from Figure 3.17 that the NBocStyr_xOPS compounds offer superior TPA cross-sections when compared with the AceStyr_xOPS compounds for RStyr₁₆OPS and RStyr₂₄OPS. This can be explained by the greater strength of the donor group and by changes in the dipole-moment.⁵⁻⁶ It was also noted that TPA cross sections increase with an increase in the number of chromophores attached to the phenyl group. As seen in Table 3.8, the cross-sections “per chromophore” in RStyr₂₄OPS are also enhanced by the additional chromophores in comparison with RStyr₁₆OPS and *o*-RStyr₈OPS systems.

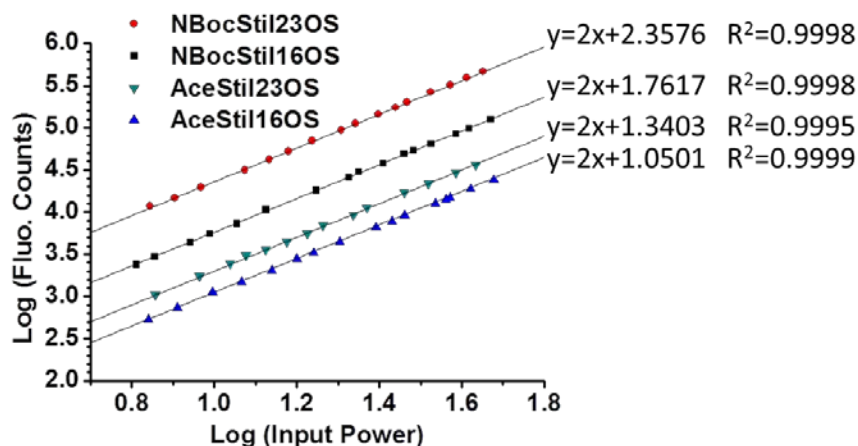


Figure 3.16 TPA cross-section measurements of *o*-NBocStil₈OS, NBocStil₁₆OS, NBocStil₂₃OS, *o*-AceStil₈OS, *o*-AceStil₁₆OS and *o*-AceStil₂₃OS

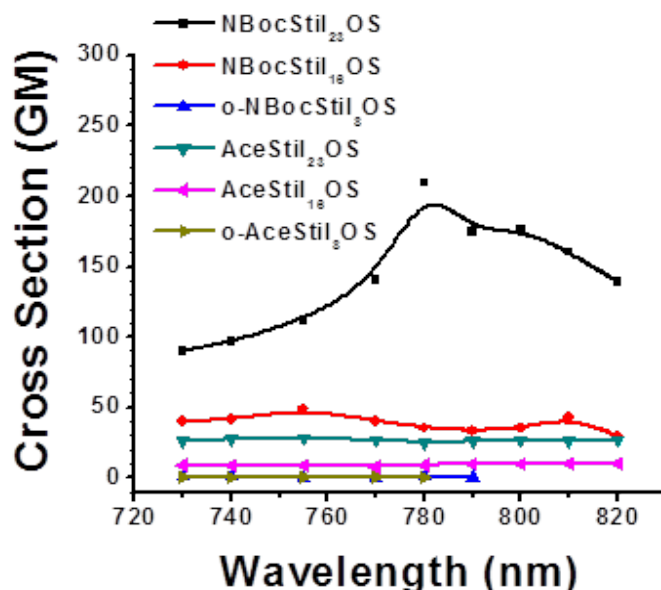


Figure 3.17 TPA cross section measurements of *o*-NBocStil₈OS, NBocStil₁₆OS, NBocStil₂₃OS, *o*-AceStil₈OS, *o*-AceStil₁₆OS and *o*-AceStil₂₃OS

For NBocStyr₂₄OPS and NBocStyr₁₆OPS, the cross-section increases by a factor of 4.4, while the cross-section increase per chromophore is by a factor of 3. This seems to correlate well with the increase of the cross-section per chromophore, which seems to correlate well with the steady-state measurements of Table 3.7. In the case of RStyr₁₆OPS, although the absorption measurements showed a red shift, the fluorescence emissions and quantum yields suggest that the system possesses less charge transfer character. The literature suggests that molecular systems with symmetric charge transfer from the ends of a conjugation to the middle gives enhanced TPAs¹, such as found here for RStyr₁₆OPS and RStyr₂₄OPS. Similar trends are observed in AceStyr_xOPS systems as well. Note that *o*-NBocStyr₈OPS and *o*-AceStyr₈OPS with cross-sections below 1 GM, do not appear to be promising two photon materials, but it may be that on deprotection they will offer TPAs equivalent to the *para* systems we have studied before.³³ Finally, time-resolved measurements are underway in order to understand the actual mechanism of the charge transfer character of these systems.

Table 3.8 TPA properties of of *o*-NBocStil₈OS, NBocStil₁₆OS, NBocStil₂₃OS, *o*-AceStil₈OS, *o*-AceStil₁₆OS and *o*-AceStil₂₃OS

Sample	δ (GM)	δ /molecule (GM)
NBocStil ₂₃ OS	209	9
NBocStil ₁₆ OS	48	3
<i>o</i> -NBocStil ₈ OS	<1	0
AceStil ₂₃ OS	28	1.3
AceStil ₁₆ OS	10	0.6
<i>o</i> -AceStil ₈ OS	<1	0

3.4 Summary

The current work suggests that cubic silsesquioxanes offer unique opportunities to build new types of 3-D molecular structures around a nanometer size octafunctional core with cubic symmetry. From SOVS to NSOVS, we observed red shifts in both absorption and emission spectra with respect to the single chromophore, indicating electronic coupling taking place among the chromophores. In addition, when compared with OSOVS and SOVS, a decrease in quantum yield, an increase in stokes shift and an increase in charge transfer character of NSOVS suggests it exhibits the best charge transfer character among the three systems. By introducing strong electron donating group into the chromophore, one could dramatically enhance the charge transfer character and eventually lead to a high power conversion efficiency of organic solar cell.

Other than that, a series of stilbene-SQs (RStyr_xOPS, x = 8, 16, 24; R = 4-methylstyrenyl, 4-acetoxystyrenyl, Boc-protected 4-aminostyrenyl) have also been characterized and investigated. These molecules have the highest densities of functional groups/unit volume of any molecules even when compared to silsesquioxane dendrimers.

However, separation of different molecular species is extremely difficult but necessary. A mixture of different molecular species could cause broad and multiple peaks in both absorption and emission spectra. Higher chromophore densities (23mer) per cage provides special characters including blue shift (upto 30 nm) with respect to 16 mer, disruption of conjugation due to meta-substitution and steric hindrance effect, a decrease in quantum yield in comparison with 16mer (NBocStil23OS, 0.08 vs NBocStil16OS,0.43), enhanced TPA cross-section (NBocStil23OS: 209GM, 4.4 X NBocStil16OS) and enhanced TPA cross-section per chromophore (NBocStil23OS: 9GM, 3 X NBocStil16OS). These results suggest 23mer offer enhanced charge transfer character compared to 16mer. Therefore, high chromophore density per nanostructure could enhance the charge transfer character of the material.

References

- [1]. Albota, M.; Beljonne, D.; Bredas, J. L.; Ehrlich, J. E.; Fu, J. Y.; Heikal, A. A.; Hess, S. E.; Kogej, T.; Levin, M. D.; Marder, S. R.; McCord-Maughon, D.; Perry, J. W.; Rockel, H.; Rumi, M.; Subramaniam, C.; Webb, W. W.; Wu, X. L.; Xu, C., Design of Organic Molecules with Large Two-Photon Absorption Cross Sections. *Science* **1998**, *281* (5383), 1653-1656.
- [2]. Chung, S. J.; Kim, K. S.; Lin, T. H.; He, G. S.; Swiatkiewicz, J.; Prasad, P. N., Cooperative Enhancement of Two-Photon Absorption in Multi-Branched Structures. *Journal of Physical Chemistry B* **1999**, *103* (49), 10741-10745.
- [3]. Wang, Y.; He, G. S.; Prasad, P. N.; Goodson, T., Ultrafast Dynamics in Multibranch Structures with Enhanced Two-Photon Absorption. *Journal of the American Chemical Society* **2005**, *127* (29), 10128-10129.
- [4]. Bhaskar, A.; Ramakrishna, G.; Lu, Z. K.; Twieg, R.; Hales, J. M.; Hagan, D. J.; Van Stryland, E.; Goodson, T., Investigation of Two-Photon Absorption Properties in Branched Alkene and Alkyne Chromophores. *Journal of the American Chemical Society* **2006**, *128* (36), 11840-11849.
- [5]. Ramakrishna, G.; Bhaskar, A.; Goodson, T., Ultrafast Excited State Relaxation Dynamics of Branched Donor-Pi-Acceptor Chromophore: Evidence of a Charge-Delocalized State. *Journal of Physical Chemistry B* **2006**, *110* (42), 20872-20878.

- [6]. Ramakrishna, G.; Goodson, T., Excited-State Deactivation of Branched Two-Photon Absorbing Chromophores: A Femtosecond Transient Absorption Investigation. *Journal of Physical Chemistry A* **2007**, *111* (6), 993-1000.
- [7]. Ramakrishna, G.; Bhaskar, A.; Bauerle, P.; Goodson, T., Oligothiophene Dendrimers as New Building Blocks for Optical Applications. *Journal of Physical Chemistry A* **2008**, *112* (10), 2018-2026.
- [8]. Varnavski, O.; Yan, X. Z.; Mongin, O.; Blanchard-Desce, M.; Goodson, T., Strongly Interacting Organic Conjugated Dendrimers with Enhanced Two-Photon Absorption. *Journal of Physical Chemistry C* **2007**, *111* (1), 149-162.
- [9]. Varnavski, O.; Bauerle, P.; Goodson, T., Strong Coupling in Macrocyclic Thiophene Investigated by Time-Resolved Two-Photon Excited Fluorescence. *Optics Letters* **2007**, *32* (21), 3083-3085.
- [10]. Bhaskar, A.; Ramakrishna, G.; Hagedorn, K.; Varnavski, O.; Mena-Osteritz, E.; Bauerle, P.; Goodson, T., Enhancement of Two-Photon Absorption Cross-Section in Macrocyclic Thiophenes with Cavities in the Nanometer Regime. *Journal of Physical Chemistry B* **2007**, *111* (5), 946-954.
- [11]. Williams-Harry, M.; Bhaskar, A.; Ramakrishna, G.; Goodson, T.; Imamura, M.; Mawatari, A.; Nakao, K.; Enozawa, H.; Nishinaga, T.; Iyoda, M., Giant Thienylene-Acetylene-Ethylene Macrocycles with Large Two-Photon Absorption Cross Section and Semishape-Persistence. *Journal of the American Chemical Society* **2008**, *130* (11), 3252-+.
- [12]. Varnavski, O. P.; Ranasinghe, M.; Yan, X.; Bauer, C. A.; Chung, S. J.; Perry, J. W.; Marder, S. R.; Goodson, T., Ultrafast Energy Migration in Chromophore Shell-Metal Nanoparticle Assemblies. *Journal of the American Chemical Society* **2006**, *128* (34), 10988-10989.
- [13]. Yau, S. H.; Abeyasinghe, N.; Orr, M.; Upton, L.; Varnavski, O.; Werner, J. H.; Yeh, H. C.; Sharma, J.; Shreve, A. P.; Martinez, J. S.; Goodson, T., Bright Two-Photon Emission and Ultra-Fast Relaxation Dynamics in a DNA-Templated Nanocluster Investigated by Ultra-Fast Spectroscopy. *Nanoscale* **2012**, *4* (14), 4247-4254.
- [14]. Yau, S. H.; Varnavski, O.; Gilbertson, J. D.; Chandler, B.; Ramakrishna, G.; Goodson, T., Ultrafast Optical Study of Small Gold Monolayer Protected Clusters: A Closer Look at Emission. *Journal of Physical Chemistry C* **2010**, *114* (38), 15979-15985.

- [15]. Yau, S. H.; Varnavski, O.; Goodson, T., An Ultrafast Look at Au Nanoclusters. *Accounts of Chemical Research* **2013**, *46* (7), 1506-1516.
- [16]. Brick, C. M.; Tamaki, R.; Kim, S. G.; Asuncion, M. Z.; Roll, M.; Nemoto, T.; Ouchi, Y.; Chujo, Y.; Laine, R. A., Spherical, Polyfunctional Molecules Using Poly(Bromophenylsilsequioxane)S as Nanoconstruction Sites. *Macromolecules* **2005**, *38* (11), 4655-4660.
- [17]. Feher, F. J.; Budzichowski, T. A., Syntheses of Highly-Functionalized Polyhedral Oligosilsequioxanes. *Journal of Organometallic Chemistry* **1989**, *379* (1-2), 33-40.
- [18]. Hamai, S.; Hirayama, F., Actinometric Determination of Absolute Fluorescence Quantum Yields. *Journal of Physical Chemistry* **1983**, *87* (1), 83-89.
- [19]. Demas, J. N.; Crosby, G. A., Measurement of Photoluminescence Quantum Yields - Review. *Journal of Physical Chemistry* **1971**, *75* (8), 991-&.
- [20]. Miller, J. N., *Standards for Fluorescence Spectrometry*. Chapman and Hall: London, 1981.
- [21]. Samori, S.; Hara, M.; Tojo, S.; Fujitsuka, M.; Majima, T., Important Factors for the Formation of Radical Cation of Stilbene and Substituted Stilbenes During Resonant Two-Photon Ionization with a 266-or 355-Nm Laser. *Journal of Photochemistry and Photobiology a-Chemistry* **2006**, *179* (1-2), 115-124.
- [22]. Letard, J. F.; Lapouyade, R.; Rettig, W., Structure Photophysics Correlations in a Series of 4-(Dialkylamino)Stilbenes - Intramolecular Charge-Transfer in the Excited-State as Related to the Twist around the Single Bonds. *Journal of the American Chemical Society* **1993**, *115* (6), 2441-2447.
- [23]. Ramakrishna, G.; Bhaskar, A.; Bauerle, P.; Ma, C. Q.; Goodson, T. G., Oligothiophene Dendrimers as New Building Blocks for Optical Applications (Vol 112, Pg 2018, 2008). *Journal of Physical Chemistry A* **2008**, *112* (27), 6235-6235.
- [24]. Samsonova, L. G.; Kopylova, T. N.; Svetlichnaya, N. N.; Andrienko, O. S., The Phototransformations of Trans-Stilbene and Its Derivatives on Laser Excitation. *High Energy Chemistry* **2002**, *36* (4), 276-279.
- [25]. Meier, H., The Photochemistry of Stilbenoid Compounds and Their Role in Materials Technology. *Angewandte Chemie-International Edition in English* **1992**, *31* (11), 1399-1420.

- [26]. Dmitriev.Vn; Kheifets, L. Y.; Dmitriev.Li; Malkes, L. Y.; Boronenk.Tp, Polarography of Styryl-Benzenes. *Zhurnal Obshchei Khimii* **1974**, *44* (2), 352-358.
- [27]. Meier, H.; Zertani, R.; Noller, K.; Oelkrug, D.; Krabichler, G., Investigations on the Fluorescence of Styryl-Substituted Benzenes. *Chemische Berichte-Recueil* **1986**, *119* (5), 1716-1724.
- [28]. Laine, R. M.; Sulaiman, S.; Brick, C.; Roll, M.; Tamaki, R.; Asuncion, M. Z.; Neurock, M.; Filhol, J. S.; Lee, C. Y.; Zhang, J.; Goodson, T.; Ronchi, M.; Pizzotti, M.; Rand, S. C.; Li, Y., Synthesis and Photophysical Properties of Stilbeneoctasilsesquioxanes. Emission Behavior Coupled with Theoretical Modeling Studies Suggest a 3-D Excited State Involving the Silica Core. *Journal of the American Chemical Society* **2010**, *132* (11), 3708-3722.
- [29]. Anderson, S. E.; Bodzin, D. J.; Haddad, T. S.; Boatz, J. A.; Mabry, J. M.; Mitchell, C.; Bowers, M. T., Structural Investigation of Encapsulated Fluoride in Polyhedral Oligomeric Silsesquioxane Cages Using Ion Mobility Mass Spectrometry and Molecular Mechanics. *Chemistry of Materials* **2008**, *20* (13), 4299-4309.
- [30]. Roll, M. F.; Mathur, P.; Takahashi, K.; Kampf, J. W.; Laine, R. M., Phsio1.5 (8) Promotes Self-Bromination to Produce O-Brphsio1.5 (8): Further Bromination Gives Crystalline 2,5-Br₂phsio1.5 (8) with a Density of 2.32 G Cm⁻³ and a Calculated Refractive Index of 1.7 or the Tetraicosa Bromo Compound Br₃phsio1.5 (8). *Journal of Materials Chemistry* **2011**, *21* (30), 11167-11176.
- [31]. Sulaiman, S.; Bhaskar, A.; Zhang, J.; Guda, R.; Goodson, T.; Laine, R. M., Molecules with Perfect Cubic Symmetry as Nanobuilding Blocks for 3-D Assemblies. Elaboration of Octavinylsilsesquioxane. Unusual Luminescence Shifts May Indicate Extended Conjugation Involving the Silsesquioxane Core. *Chemistry of Materials* **2008**, *20* (17), 5563-5573.
- [32]. Hogen-Esch, T. E., Synthesis and Characterization of Macrocyclic Vinyl Aromatic Polymers. *Journal of Polymer Science Part a-Polymer Chemistry* **2006**, *44* (7), 2139-2155.
- [33]. Sellinger, A.; Tamaki, R.; Laine, R. M.; Ueno, K.; Tanabe, H.; Williams, E.; Jabbour, G. E., Heck Coupling of Haloaromatics with Octavinylsilsesquioxane: Solution Processable Nanocomposites for Application in Electroluminescent Devices. *Chemical Communications* **2005**, (29), 3700-3702.

CHAPTER 4

ULTRAFAST FLUORESCENCE DYNAMICS AND EXCITED STATE CHARGE TRANSFER PROCESS OF FUNCTIONALIZED SILSESQUIOXANES INVESTIGATED BY TIME-RESOLVED ABSORPTION AND EMISSION SPECTROSCOPY

The work in this chapter includes two separate publications:

“Synthesis and Photophysical Properties of Stilbeneoctasilsesquioxanes. Emission Behavior Coupled with Theoretical Modeling Studies Suggest a 3-D Excited State Involving the Silica Core” Laine, R. M. ; Sulaiman, S.; Brick, C.; Roll, M.; Tamaki, R.; Asuncion, M. Z.; Neurock, M.; Filhol, J. S.; Lee, C.Y.; Zhang, J.; Goodson, T.; Ronchi, M.; Pizzotti, M.; Rand, S. C.; Li, Y. *Journal of the American Chemical Society* 2010, 132(11), pp 3708-3722

“Ultrafast Fluorescence Dynamics and Excited State charge Transfer Process of Functionalized Silsesquioxanes Investigated by Time-Resolved Absorption and Emission Spectroscopy” Jin Zhang, Santy Sulaiman, Richard M. Laine, Theodore Goodson III Manuscript prepared for a submission to *Journal of Physical Chemistry*

Some of the work presented in this chapter was also published in our collaborator, Dr. Santy Sulaiman’s dissertation: “Synthesis and Characterization of Polyfunctional Polyhedral Silsesquioxane Cages” (Macromolecular Science and Engineering Center, University of Michigan).

Abstract

A set of model compounds were investigated including the corner, half and cube cages: [*p*-Me₂NStilSi(OSiMe)₃], [*p*-Me₂N-StilSi(OSiMe)]₄ and [*p*-MeStil₈SiO_{1.5}]₈. The full and partial cages all show Uv-Vis absorption spectra (THF) identical to trans-stilbene, except for [*o*-MeStil₈SiO_{1.5}]₈ which exhibits absorption spectra expected for cis-stilbene. However, the partial cages show emissions that are red-shifted by approximately 20 nm as found for stilbene-siloxane macrocycles, suggesting some interaction of the silicon center(s) with the stilbene π^* orbital in both the corner and half cages. These materials were also investigated by ultrafast fluorescence up-conversion and femtosecond transient spectroscopy in order to study the mechanism of excitation energy transport and excited state dynamics. The fluorescence decay lifetimes are 146, 73, and 75 ps, for corner, half and cube respectively. Fluorescent, twisted intramolecular charge transfer (TICT) states are found in all three systems. Ultrafast depolarization of the fluorescence in the half and cube systems was observed indicating excitation energy delocalization between the chromophores by strong electronic coupling. Transient absorption dynamics reveal the presence of ultrafast delocalization of charge in the half and cube systems. Blue shifts in the excited state absorption (ESA) of all three systems correlate with solvation process and reveal a solvent stabilized TICT state. The amount of ESA blue shift indicates an increase in charge-transfer character of the excited state in the case of half and cube. This explains their enhanced two-photon cross-sections.

4.1 Introduction

From the time of the original thermal rearrangement by Scott in 1946¹, polyhedral silsesquioxanes (SQs) have shown significant promise for a number of applications, as nanocomposite materials used in dentistry,²⁻³ catalyst,⁴⁻⁵ coating,⁶ electret filter⁷, nano-imprinting lithography⁸ and biomedical device⁹. Cubic SQs, (RSiO_{1.5})₈, having 3-dimensional structure with a diameter of 0.53 nm, provides eight or even more possible sites for functionalization with organic chromophores.¹⁰ Their electronic and photonic properties can be tuned by tailoring the structures of the chromophores. For this reason,

SQ materials incorporating a silica cage as the core and with versatile conjugated chromophores as the shell have drawn extensive attention as candidates for photovoltaic materials.¹¹⁻¹³ Besides that, SQ hybrids offer special features that make them attractive as organic electronic materials. First, SQ hybrids are exceptional candidates for developing well-defined, molecular nanobuilding blocks with perfect cubic symmetry. In addition, they exhibit excellent solubility in various organic solvents (such as THF, toluene, dioxane, CH₂Cl₂ and CHCl₃), and therefore they can be easily purified by standard methods.¹⁴ Moreover, the single crystal silica core provides the heat capacity making these materials exceptional robust.¹⁵ Most importantly, with eight or even more chromophores in a single molecule, potential electronic coupling among the chromophores could possibly enhance the charge transfer character of the entire system, and therefore may increase the overall solar capture efficiency.

In the past few years, several sets of cubic SQ derivatives with different degrees of functionalization have been synthesized by Laine *et al.*¹⁶⁻²⁰ The UV-vis absorption, photoluminescence and two-photon absorption properties of these compounds were investigated. The emission spectrum of [NH₂VinylStilbeneSiO_{1.5}]₈ shows exceptional red-shifts up to 120 nm.¹⁵ Its excellent two-photon absorption cross-section (up to 810 GM) reveals strong interactions between each substituent chromophore, and may suggest that the silica core serves as an electron acceptor in the system.¹⁵ The photophysical properties and two-photon properties of corner and half cage systems, were also studied and compared with the full cage. The results suggest that full cages with perfect symmetry offer better nonlinear properties with the largest two-photon cross sections per chromophore.¹⁹

There have also been extensive computational studies carried out on the electronic structure, electronic spectra, optical properties and reactivity of T₈ octahedral SQs over the past two decades.²¹⁻²⁶ Phillips *et al.*²³ investigated the absorption excitation energy of functionalized octahedral SQs via time-dependent density functional theory. Using B3LYP and RSH functional, they find that the excitations are mainly localized on the chromophores, except for vinylsilsesquioxane.²³ Zheng *et al.*²⁴ reproduced the

experimental results of the absorption and emission spectra of stilbene-functionalized octahedral silsesquioxane, by combining time-dependent density functional theory and the Tamm-Dancoff approximation with range-separated hybrid functional of Baer-Neuhauser-Livshits. They also report that their modeling studies suggest that the emissive state of these octahedral silsesquioxanes is ligand-to-ligand, rather than ligand-to-silsesquioxane.²⁴

Although there are many theoretical studies on this class of materials, we are not aware of any experimental results that examine the excited state absorption and excited charge transfer processes of chromophore substituted SQs. In this paper, we use nonlinear ultrafast spectroscopy to investigate the excited state dynamics of SQs, and to reveal the unstudied area: whether there is an interaction between the substituted chromophores and the silica core in the excited state. In addition, we investigate the fluorescence emission dynamics to study the energy transfer process and fluorescence lifetimes of SQ systems.

Time-resolved fluorescence up-conversion and transient absorption are very powerful experimental tools for the purpose of our study. The time-resolved spectroscopic methods have been applied extensively to study the excited state behavior of many kind of materials including organic macromolecules,²⁷⁻²⁹ peptides,³⁰⁻³¹ nanoclusters,³²⁻³⁵ metallacycles.³⁶⁻³⁹ Maya *et al.*⁴⁰ studied the nonlinear absorption properties of lead phthalocyanines substituted with siloxane chains using picosecond time-resolved transient absorption. The results suggest that the charge transfer through the polysiloxane chain did not observed. Cohen *et al.*⁴¹ reported the femtosecond fluorescence dynamics of a proton-transfer chromophore covalently bonded to the inner surface of amorphous silica nanoparticles. In these studies, it was reported that an excited state intermolecular proton-transfer process occurs from the chromophore to the silica surface, suggesting the development of nanophotonic devices based on mesoporous silica nano materials.

Understanding the mechanism of energy transfer and excited state charge transfer processes in the silica cage materials, as well as the extent of intramolecular interactions

among the chromophores is crucial to make significant improvement of photophysical properties as organic optoelectronic materials. For this purpose, corner and half cage systems and full cubic cages are investigated using ultrafast absorption and emission spectroscopy. The structures of these materials are shown in Figure 4.1. Investigations have revealed interesting features in relation to the excited-state dynamics and amount of ICT character of the excited state with increase in branching, which are very important in elucidating the mechanism behind the TPA cross sections of the branched systems.

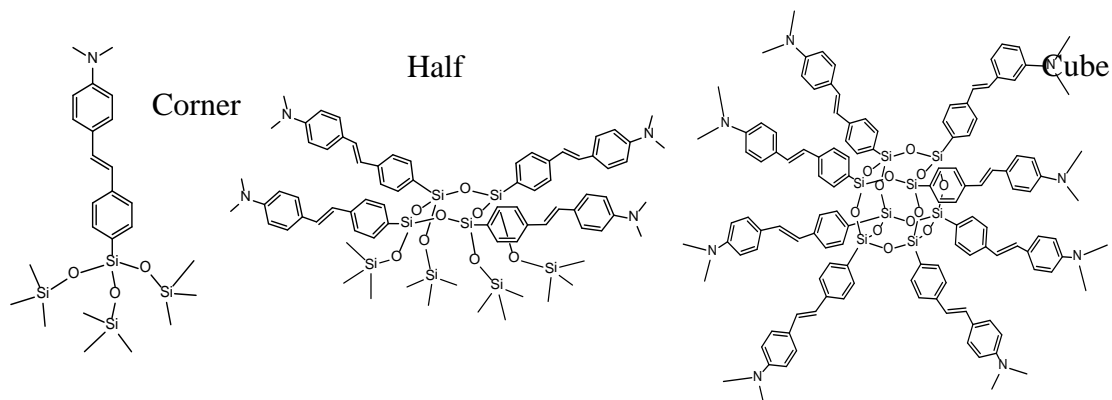


Figure 4.1 Molecular structure of investigated Corner, Half and Cube silsesquioxane systems.

4.2 Results and Discussion

4.2.1. Steady-State Measurements

The measured optical absorption and fluorescence spectra of the investigated systems dissolved in THF are shown in Figure 4.2 and Figure 4.3. A summary of the corresponding optical properties are shown in Table 4.1, in addition we have added data on the MeStil₈OS compound and the [*p*-NH₂PhCH=CHPhCH=CH₂SiO_{1.5}]₈ NH₂StilOVS compound from our previous paper.¹⁹

It can be observed from the figure and table that the absorption of the Me₂NStil-half is red-shifted in comparison to the Me₂NStil-corner and the full cage is red-shifted still further. This might follow the expected trend in increasing wavelength of absorption with length of interaction and conjugation in these particular compounds. However, the emissions of these derivatives show an interesting effect in the Stokes shift. The Me₂NStil-corner emission is red-shifted in comparison to the Me₂NStil-half; furthermore, it also exhibits a greater shift than the full cage. This is contrary to what might be expected and at this moment we have no explanation for these results.

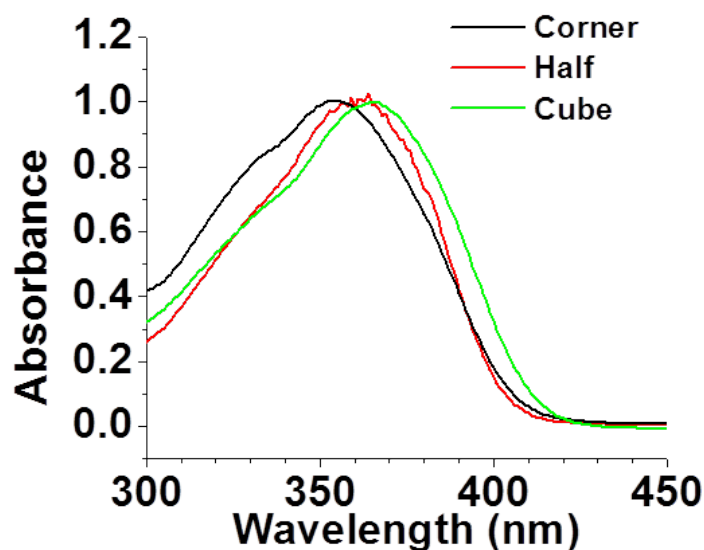


Figure 4.2 Steady state absorption spectrum of Corner, Half and Cube

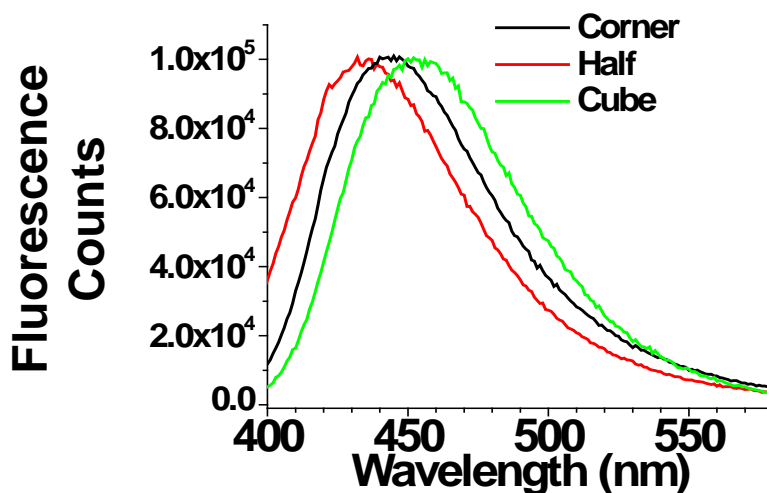


Figure 4.3 Steady state fluorescence emission spectra of Corner, Half and Cube

Table 4.1 Steady-state properties of silsesquioxane derivatives in THF.

Sample	λ_{abs} (nm)	λ_{em} (nm)	Φ_f	Stoke's shift $\Delta\nu$ (cm ⁻¹)
MeStil ₈ OS	317	365	0.06	--:--
Me ₂ NStil-corner	355	445	0.08	5700
Me ₂ NStil-half	361	436	0.09	4760
Me ₂ NStil ₈ OS	365	454	0.03	5370
NH ₂ StilOVS ⁶⁷	367	481	0.05	--:--

The fluorescence quantum yield (Φ_f) measurements are also unexpected. First the Me₂NStil-corner is smaller than that found for Me₂NStil-half, which might be expected; however, the full cage has the lowest Φ_f of all. A number of similar organic chromophoric systems have been investigated in the past. In particular, it was found that the extent of charge separation or transfer in these systems has a dramatic effect on the Stokes shift. This has also been connected to the extent of disorder or conformational rearrangement in the system. The reduction of the quantum yield from Me₂NStil-half to Me₂NStil-corner is also in accordance with the increased charge transfer character of the chromophores. In this case, for the case of Me₂NStil-corner the extent of charge transfer is reduced by the fact that the system becomes unsymmetrical at the joining points and the charge

correlation is lost. This same argument can be used to explain the lowest Φ_f observed for the full cage suggesting that CT effects dominate the photophysics of this compound. Consequently, we carried out two-photon measurements on these systems in order to probe the varying extent of charge correlation in these novel systems.

4.2.2. Two-Photon Cross-Section Measurements

TPA cross-section measurements of corner, half and cube are plotted in Figure 4.4. TPA cross-sections as a function of wavelength are plotted in Figure 4.5 for the Me₂N chromophores. The data are presented in Table 4.2 including data from our recent paper where conjugation at the cage begins with vinyl rather than phenyl groups. It is clear from the TPA cross-sections that the cross-section increases with increasing numbers of chromophores. However, the cross-section “per chromophore” in these systems is not enhanced by the additional chromophores in the case of Me₂NStil-half. The cross-section increases by a factor of 2.5 while the number of chromophores increases by 4. This seems to correlate well with the steady-state measurements described above. In the case of Me₂NStil-half; while the absorption measurements suggest a red shift and longer range interaction, the fluorescence and quantum yields suggest a system with lower charge transfer character.

The two-photon absorption (and resulting fluorescence) appear to also follow this trend as the increase in the cross-section is found for Me₂NStil-half but the enhancement factor observed in a number of different donor-acceptor charge transfer systems is not present here.⁴²⁻⁴³ The degree of conformational flexibility is an effect that we have previously observed to change the long range nonlinear optical properties in a number of systems. While it appears that these systems could have considerable rigidity across the junctions of the building blocks, small vibrations and conformational changes are just enough to cause disruption of the charge correlation. Further investigations of these effects are underway with time-resolved measurements such as transient absorption and fluorescence up-conversion.

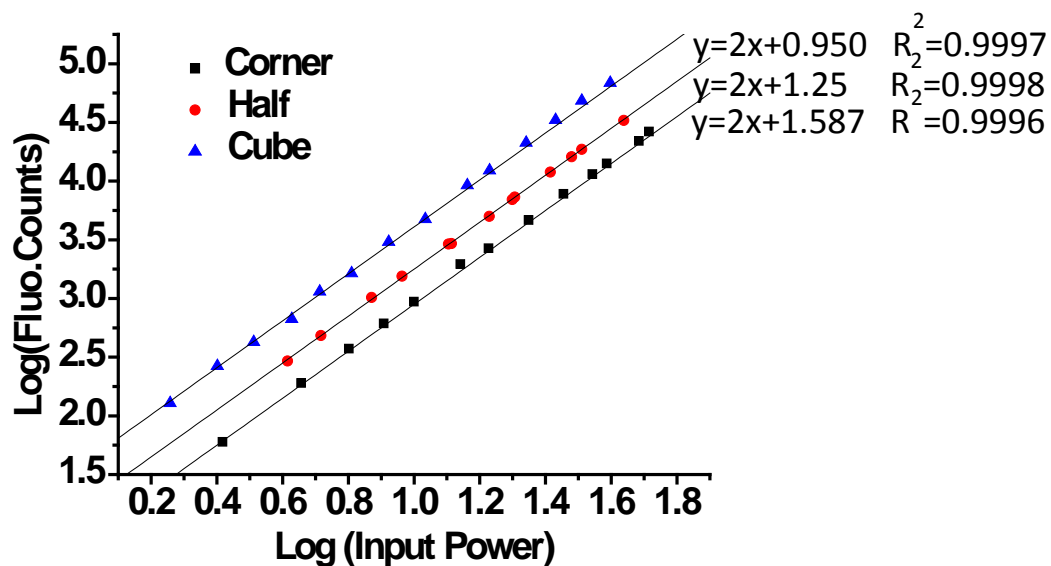


Figure 4.4 Two-photon cross section measurements of Corner, Half and Cube

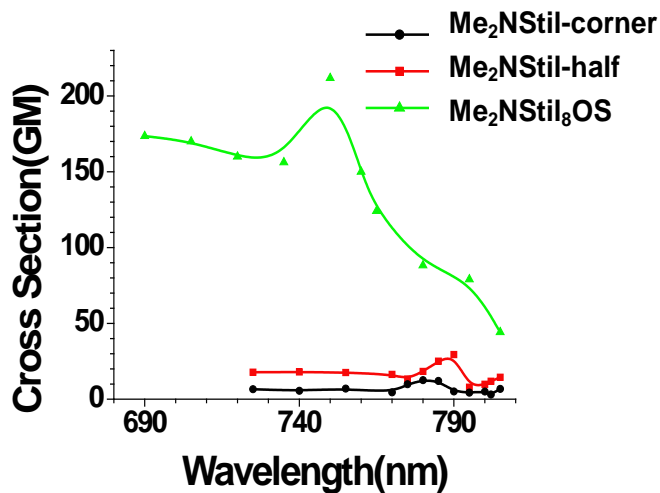


Figure 4.5 Two-photon absorption cross-section spectra for the investigated chromophores.

Perhaps the most important observations from these studies are the fact that the GM value for the full cage is 26/moiety whereas the half cage is 8/moiety and the corner is 12/moiety. The fact that the full cage offers 2-3 times the TPA of the fragments combined with the lowest Φ_f suggests that this system offers much higher C-T than the fragments. This type of behavior is more pronounced in the OVS systems studies earlier which have longer conjugation lengths, as seen in Table 4.2.¹⁹ However, the data continue to support our contention that in the excited state, the cage seems to influence the photophysics more than would be expected if each corner served solely as a SiO₃ fragment. It is important to add at this point that the effect of a simple SiO₃ fragment on the Uv-Vis and emission behavior of methylstilbene is also much less than seen in the complete cage in Table 4.2.

Table 4.2 Summary of two-photon cross-section of silsesquioxane derivatives

Sample	δ (GM)	δ /moiety (GM)	λ_{\max} nm
MeStil ₈ OS	11	1.2	735
Me ₂ NStil-corner	12	12	780
Me ₂ NStil-half	30	7.5	790
Me ₂ NStil ₈ OS	211	26	755
StilOVS ⁶⁷	25	3	705
MeOStilOVS ⁶⁷	110	14	705
NH ₂ StilOVS ⁶⁷	810	101	720

According to previous studies, steady state absorption and emission data of corner, half and cube systems are listed in Table 4.1.¹⁹ It should be noted that the SQ cage without chromophores has absorption maximum near 224 nm.⁴⁴ In comparison with that, the cube sample, with 8 conjugated chromophores attached to the SQ cage, has an absorption maximum at 365 nm. The absorption maximum of corner ($\lambda_{\text{abs}}=355$ nm in THF) is blue shifted with respect to the 4-dimethylaminostilbene (DAS) chromophore ($\lambda_{\text{abs}}=365$ nm in THF).⁴⁵⁻⁴⁷ This can be explained by the negative mesomeric effect⁴⁸ that there is no lone pair electron available from a saturated Si atom. This steady state absorption result corresponds well with the fluorescence decay results discussed below. In the corner molecule, DAS chromophore is attached with a relatively large group, -Si(OSiMe₃)₃, through a single bond. The steric hindrance effect reduces the electron

mobility through the π conjugation and therefore the photoisomerization process is retarded. The absorption maxima of half and cube are shifted to the longer wavelength with respect to the corner. It may suggest that this shift is due to either mesomeric effect from half/full cage and /or the dipole-dipole interaction between DAS chromophores. The emission results of these systems are also listed in Table 4.1. The emission maxima of corner, half and cube are at 445 nm, 436 nm and 454 nm, respectively. The emission spectra of the three systems are dramatically red-shifted with respect to that of single chromophore, 4-dimethylaminostilbene (emission wavelength maximum at 407 nm), due to non-radioactive decay processes.

Studies regarding $\sigma^*-\pi^*$ conjugation between the σ^* orbital of the silicon and the π^* orbital of the conjugating moiety have been reported.⁴⁹⁻⁵³ Based on their ab initio calculations, it has been found that the other substituents on the silicon atom could largely affect the resulting low-lying LUMO level as well as the HOMO level not because of perturbation through the $\sigma^*-\pi^*$ conjugation but by an inductive effect.⁴⁹ An increase in electronegativity of substituents on the silicon could induce the bathochromic shift of the absorption maxima to the longer wavelength.⁴⁹ According to these previous reports, the red shifts of half and cube with respect to corner might be an indication that cyclotetrasiloxane (half SQ) and full cubic SQ cage have better electronegativity in comparison with $-\text{Si}(\text{OSiMe}_3)_3$ group.

With eight chromophores attached, the cube has the largest two-photon cross-section (211GM) among these three systems. When considering the two-photon cross-section per chromophores, the cube system also has the highest value (26 GM) among the three. The enhanced two-photon cross-section found in cube sample suggests a complex interplay between intramolecular interactions and the improvement of charge-transfer character. As a result, the SQ cage plays an important role in affecting the overall photophysical properties of attached conjugated chromophores. In order to understand the fundamental process, it would be very interesting to study energy transfer and the excited state charge transfer processes via the time-resolved spectroscopy measurements. In the

following sections, we present and discuss the time-resolved fluorescence and excited state dynamics data.

4.2.3. Fluorescence Up-Conversion Measurements

Fluorescence Life Time Features

The time-resolved fluorescence up-conversion technique was applied to measure the fluorescence lifetime of the three systems. The fluorescence up-conversion results under an excitation of 380 nm are shown in Figure 4.6. Figure 4.6A presents the fluorescence decay curve of the three investigated systems. The corresponding mono-exponential lifetime result is described by the following equation:

$$\text{Equation 4.1} \quad y = a \exp(-t/\tau)$$

Where y is the fluorescence intensity (counts per second), a is the amplitude and τ is the fluorescence decay time. The fluorescence decay time or as commonly used lifetime is the average time a chromophore remains in the excited state after excitation, and it is defined as

$$\text{Equation 4.2} \quad \tau = \frac{1}{k_r + k_{nr}}$$

where k_r is the radiative rate constant, and k_{nr} is the non-radiative rate constant.

$$\text{Equation 4.3} \quad \tau_0 = k_r^{-1}$$

where τ_0 is the natural or radiative lifetime which is related to the fluorescence lifetime τ via the fluorescence quantum yield Φ :

Equation 4.4
$$\Phi = \frac{\tau}{\tau_0} = \frac{k_r}{k_r + k_{nr}}$$

Mono-exponential decay fitting was performed on time-resolved fluorescence curves for corner, half and cube systems and their lifetimes (τ) are 146, 73 and 75 ps, respectively, as summarized in Table 4.3. Given the quantum yield are 0.08, 0.09 and 0.03 for corner, half and cube systems respectively,²⁰ the estimated radiative and nonradiative rate constants can be calculated from the fluorescence decay time, based on Eq.4.2, Eq.4.3 and Eq.4.4. The results are listed in Table 4.4.

Table 4.3. Fluorescence lifetimes of Corner, Half and Cube SQ systems

	Lifetime
Corner	1.3ps, 146ps
Half	650fs, 73ps
Cube	850fs, 75ps

Table 4.4. Radiative and nonradiative decay rate constants for Corner, Half and Cube in THF

Sample	k_r ($10^7 s^{-1}$)	k_{nr} ($10^8 s^{-1}$)
Corner	54	68
Half	120	124
Cube	40	126

Fluorescence process of substituted trans-stilbene needs to be taken into consideration. According to the previous experimental and theoretical fluorescence dynamics of trans-stilbene and its derivatives, the fluorescence dynamics of trans-stilbene and its derivatives have been studied experimentally and theoretically.⁵⁴⁻⁶³ Similar to donor-acceptor-type trans-stilbene derivatives, possible twisting around single and double bonds are illustrated in Figure 4.7. The main fluorescence state of the donor/acceptor substituted trans-stilbene is T* state, so called “twisted intramolecular charge transfer” (TICT) state, in which the phenyl ring twists by $\Phi_s=90^\circ$ around the single bond starting from a fully planar geometry.⁶⁴ The electronic structure of T* corresponds to a fully charge transfer state from the donor to the acceptor. The kinetic scheme according to a three-state model⁶⁵⁻⁶⁷ is presented in Figure 4.8. Here, E* is the primary excited state, and P* is excited state with a geometry having the phenyl ring twists by 90° around the double bond. There is a competition between the formation of T* and P*. In the trans-planar configuration, an intense intramolecular charge-resonance transition to the S₁ state may cause the existence of the energy barrier on the S₁ potential energy surface for the trans- to cis- isomerization process.⁶⁴ Under this condition, ultrafast excited state deactivation through the S₁ photochemical funnel is expected. Given that fluorescence quantum yields of both corner and trans-stilbene at room temperature are very small, an assumption can be made that $k_{ET} \ll k_{EP}$. Therefore k_{nr} mainly corresponds to a transition from E*→S₀. At room temperature, the typical fluorescence lifetime of trans-stilbene is ~108 ps involving bond twisting, and the quantum yield is about 0.05.^{56, 63} According to these results, the radiative and non-radiative rate constant of trans-stilbene can be calculated as $k_r(\text{stil}) = 46 \times 10^7 \text{ s}^{-1}$, and $k_{nr}(\text{stil})=93 \times 10^8 \text{ s}^{-1}$.

In the case of corner, it shows a longer fluorescence lifetime (146ps) and a slightly slower k_{nr} rate ($68 \times 10^8 \text{ s}^{-1}$) than those of the pure trans-stilbene. This is expected if the formation of main fluorescence state T* in the corner is retarded by steric hindrance caused by the large substitution (-Si(OSiMe₃)₃) on the trans-stilbene, as shown in Figure 4.9. This result corresponds well with the observed blue shift in steady state absorption spectrum of corner with respect to the DAS chromophore. In addition, it has been found out that the donor/acceptor substitutions with a large dipole moment on trans-stilbene

could further stabilize the T* state with respect to P* since the dipole moment of T* is larger than that of P*.^{56, 63} The strongly different dipole moments expected for T* and P* states are consistent with observed anomalous solvent polarity dependence of the absorption wavelength maxima in the previous study of these samples.¹⁸⁻¹⁹ In the case of corner, comparing kinetic rates with trans-stilbene, the slower k_{nr} and similar k_r value suggest that the dipole moment is somewhat in favor of and increasing T* fluorescence state and decreasing P* state. This also corresponds well with quantum yield results of Corner (0.08) and trans-stilbene (0.05). In the previous study, the corner and half systems were investigated as push-pull nonlinear optical chromophores substituted by $-NMe_2$ and $[-Si(-O-)_3]$ interacting through a π -conjugated trans stilbene.⁶⁸ Ronchi *et al.*⁶⁸ found that the $-Si(OSiMe_3)_3$ group behaves as an electron withdrawing group equal to that of a nitro group by theoretical study. Although $-NMe_2$ is a good electron donating group, the donor/acceptor substitution pair on corner didn't provide remarkable dipole moment. Therefore, it can be concluded that the electronegativity of $-Si(OSiMe_3)_3$ group is very weak.

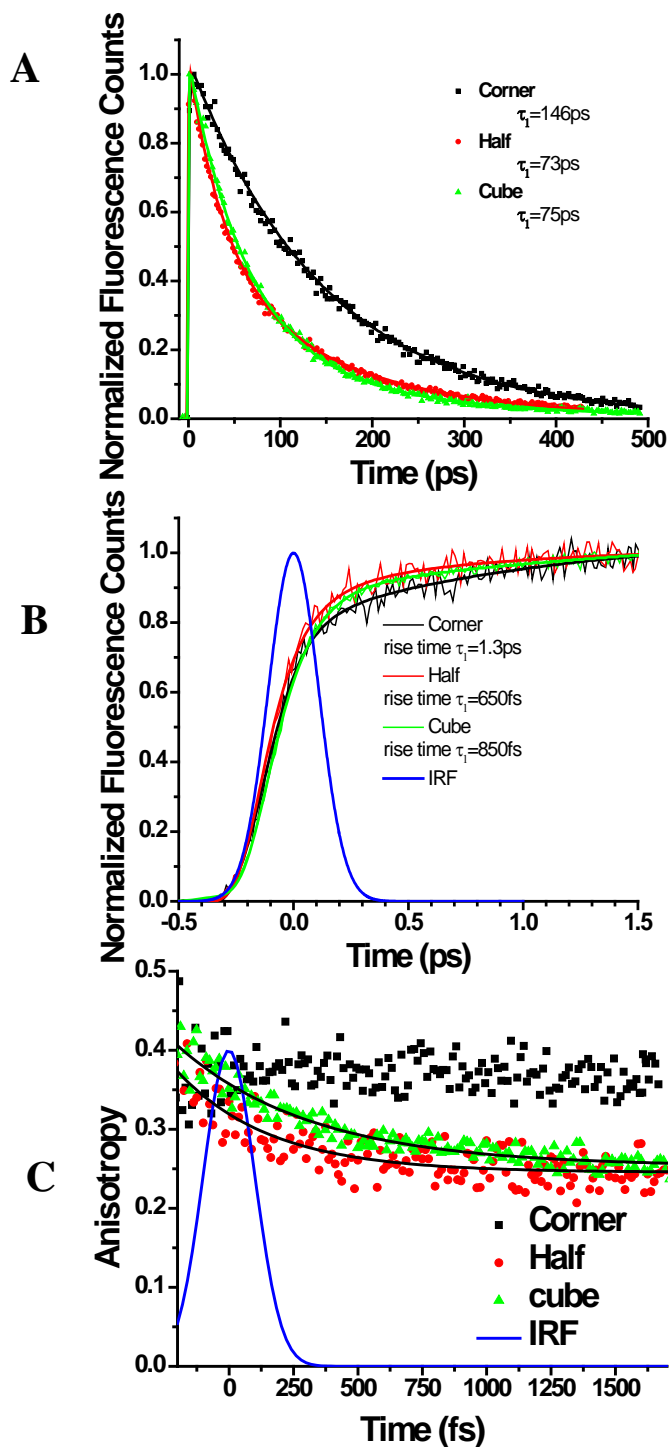


Figure 4.6 (A) Fluorescence decay, (B) fluorescence risetime, (C) fluorescence anisotropy for the investigated systems

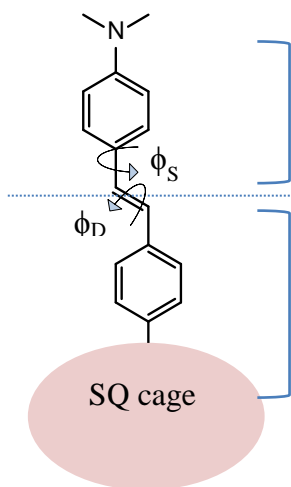


Figure 4.7 Schematic illustration of twisted single-bond (T^*) and twisted double-bond (P^*) conformation of corner. Starting from a fully planar geometry, the T^* and P^* geometries were driven by twisting by 90° around the respective single or double bond.

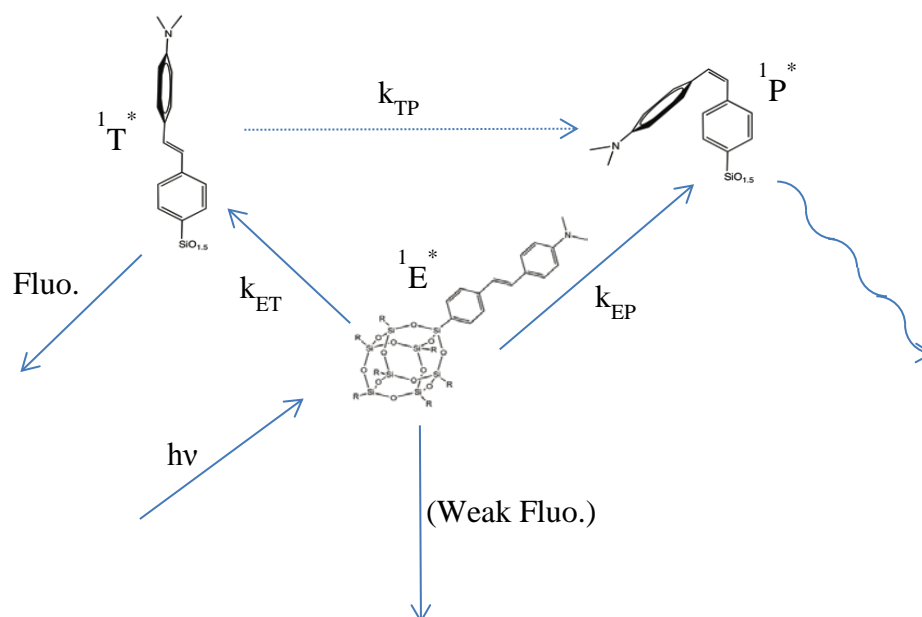


Figure 4.8 Three-state kinetic scheme proposed for the interpretation of the photophysical behavior of donor-acceptor substituted stilbenes.

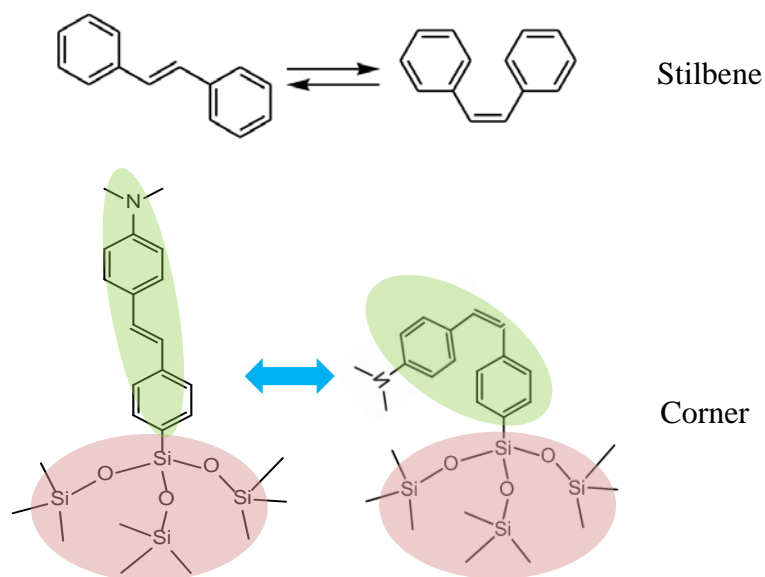


Figure 4.9 Photoisomerization processes in stilbene and corner system.

As observed, the fluorescence lifetime of the half (73 ps) and cube (75 ps) systems are about one half of that of the corner system (146 ps). The fluorescence lifetime of corner (146ps) is much longer than that of trans-stilbene (~108ps). This can be explained by the steric hindrance effect caused by the $-\text{Si}(\text{OSiMe}_3)_3$ group. However, because the half and full SQ cage are even bulkier than the $-\text{Si}(\text{OSiMe}_3)_3$ group, twisting around both the single bond (ϕ_S) and double bond (ϕ_D) are considered much more difficult. The fluorescence lifetime of the half and cube are expected to be longer than that of corner. In addition, in the case of half, both k_r and k_{nr} are faster than those of corner, which means the conformational transition to T^* and P^* states are easier in spite of the steric hindrance effect. It has been found out that when a bigger group substituted on one side of stilbene, the twisting inside may occur mainly around the single bond which is near the other side, dimethylamino group.⁶⁹ Theoretically, in the case of twisting of the N,N-dimethylamino group, the barrier height is as high as about 0.303eV.⁷⁰ Therefore it would be expected to see that both half and cube offer slower radiative and non-radiative rates, as well as longer fluorescence lifetime than those of corner. However, this argument doesn't correspond with our experimental results.

These results might be due the possibility that a stronger dipole moment is formed after excitation to facilitate the twisting processes,^{56, 63} and the possible $\sigma^*-\pi^*$ conjugation between Si atom and DAS chromophore might be stronger in the excited state.⁴⁹⁻⁵³ In the case of half and cube, steady state absorption wavelength maxima are shifted to the red with respect to that of the corner and this observation suggests the electronic transitions are perturbed by the chromophore-chromophore interactions. With more than one chromophore attached to a single macrostructure, the possibility of dipole-dipole coupling between the chromophore increased dramatically. This inter-chromophore interaction and the possible formation of delocalized/localized state under the optical excitation are discussed below in the fluorescence anisotropy section. The cube has larger number of chromophores attached and thus allows higher probability to undergo excitation energy redistribution. The slower radiative rate found in cube corresponds well with the quantum yield (Φ) result that the Φ of cube is one third of half. Based on the fluorescence decay results, the following conclusion can be drawn that both cyclotetrasiloxane (half SQ) and full cubic SQ cage exhibit stronger electronegativity in the excited state than ground state.

Figure 4.6(B) presents the initial fluorescence rise-time curve for each investigated systems within 1.5ps. Fluorescence rise time data are listed in Table 4.3. The corner, half and cube have the fluorescence rise-time component as 1.3 ps, 650 fs and 850 fs with instrument response function of 110 fs. The corner, half and cube have the fluorescence rise-time component as 1.3 ps, 650 fs and 850 fs with instrument response function of 110 fs. The fluorescence rise-time components reveal the initial energy redistribution process to the fluorescence state right after the excitation. According to the discussion above, it corresponds well to the proposed transition from the primary excited state (E^*) to the main fluorescent TICT state (T^*) in these three systems.

Fluorescence Anisotropy Decay Features.

The decay of the fluorescence anisotropy is used to characterize the electronic interaction strength and excitation energy transfer (exciton or hopping dynamics) among

chromophores, which are mainly reflecting the first few steps of energy transfer.⁷¹⁻⁷³ Exciton migration via intermolecular excitation transfer in macromolecules with high degree of symmetry has been studied both experimentally and theoretically.⁷⁴⁻⁷⁸ Kopelman *et al.*⁷⁷⁻⁷⁸ have demonstrated the correlation between the molecular geometry and the electronic properties on a series of dendrimer based on phenylacetylene chromophores. The efficient and unidirectional energy transfer from an initially excited state on a phenylacetylene dendrimer to a trap located at its core has been found. Our group has reported the study on excitation energy transfer in different dendritic core branched structures.⁷⁵⁻⁷⁶ In these systems, both Förster-type hopping and excitonic-type coherent transport mechanism are observed depending on the different architectures.⁷⁶ Wynne and Hochstrasser⁷⁹ examined the coherent type energy transfer between identical molecules by the anisotropy associated with degenerate intermediate states. The chromophore-chromophore coupling causes the excitation energy transferred between the two chromophores by the Coulomb interaction of the electrons of the two molecules. Theoretically, the efficiency can be determined by transition density, orientation, and spatial location of the two chromophores.⁸⁰

The fluorescence anisotropy decay curves are illustrated in Figure 4.2C. The initial anisotropy before rotational diffusion was studied. The decay dynamics of the half and cube systems are different than what is observed for the corner (as monomer). The corner shows no significant anisotropy decay during this experimental time window. A depolarization of fluorescence in half and cube as compared to the corner indicating that electronic energy transfer takes place between the chromophores within the molecule. The initial dynamics of fluorescence anisotropy of half and cube systems are very fast and completing with the instrument response function. Therefore, a deconvolution process is performed in order to estimate the fluorescence anisotropy decay time.⁸¹ The anisotropy decay of half can be fitted by a monoexponential decay with the decay time constant of 420fs. The anisotropy decay time was found to be 525fs for cube. In the case of the half and cube, the fast fluorescence anisotropy decay provides clear evidence of the interactions among the DAS chromophores.⁷⁶ This is denoted as exciton limit in which the interaction (J) between the chromophores is much larger than the homogeneous line

width (Γ). Under this condition, nonequilibrium initial preparation effects must be applied with inhomogeneous broadening terms.⁷³ As a result, the weak interaction limit (Föster limit), in which was used for interpretation a small perturbation, could not be applicable for the intramolecular chromophores energy migration.^{73, 82} Therefore, in our case, the presence of ultra-fast decay time components in both half (420fs) and cube (525fs) systems suggest the substantial contribution of coherent type energy migration.^{27, 75} The excitation energy transfer process is accompanied by the reorientation of the transition dipole moment.

The residual value of the fluorescence anisotropy before rotational diffusion also contains information of the arrangement of transition dipole moments and gives the molecular geometry information. In general, the initial anisotropy value is 0.4 for a randomly oriented single chromophore. For some symmetrical molecular systems, the initial anisotropy is larger than 0.4.^{79, 83} The cube system with perfect symmetry can be considered as a spherical-like structure before excitation with the initial anisotropy value 0.4, which means molecules are more randomly orientated in the solution. The residual anisotropy for the equilibrated system is another important parameter related to the geometry of the molecular system. The cube and half structures make the average angle between absorption and emission transition dipoles of the chromophores different from that of corner. And hence, it alters the residual value of the fluorescence anisotropy before rotational diffusion.

4.2.4. Ultrafast Transient Absorption Measurements

Many of the molecular photochemical and photophysical properties depend on the kinetics of excited-state processes that occur after the absorption of a photon. Therefore, femtosecond transient absorption measurements have been carried out under an excitation of 330 nm in order to understand the fundamental mechanism of the excitation delocalization, charge localization process and the extent of charge transfer character in these systems. The detection window of our apparatus is from 450 to 750 nm.

Shown in Figure 4.10-4.12 are the transient absorption spectra at different time delays for the corner, half, and cube in THF, respectively. The transient absorption features of the corner, half, and cube look similar in the region of 450 nm to 750 nm with a positive absorption below 650 nm and a maximum around 525 nm. The positive absorption is due to the excited singlet state ($S_n \leftarrow S_1$) absorption (ESA). The spectra also show very weak negative absorptions below 475 nm. The steady state of these samples absorb below 365 nm but the fluorescence spectrum has strong emission band with the emission maxima at 445 nm, 436 nm, and 454 nm for corner, half, and cube, respectively. According to the steady state photophysical properties and previous ultrafast pump-probe studies on push-pull stilbene, these negative absorptions can be ascribed to the simulated emission (SE) originated from the S_1 state.⁷⁰ Due to the limitations of our apparatus, only the shoulder of the bleach in each spectrum was observed. The spectra of these three systems also show a broad but relatively weak ESA band in the 675-750 nm region, as presented in Figure 4.10B, 4.11B and 4.12B. Since both the decreasing of SE band population below 475 nm region and the increasing of ESA band population in the 675-750 nm region are observed, the ESA band with the maximum at about 735 nm is assigned to the excited triplet state transition $T_n(\pi\pi^*) \leftarrow T_1(\pi\pi^*)$, according to previous reports.^{70, 84-85} Another interesting finding from the Figure 4.10B, 4.11B and 4.12B is that the maxima of the ESA band in the 470 to 650 nm region shows a blue shift mainly within the first 7ps delay time. This time dependence of dynamic shift of the maxima of the ESA band suggests the transition between two distinctly different excited states. The resulting state is ascribed to the twisted intramolecular charge transfer (TICT) state, accompanied by which is the twisting around a σ bond in the trans-stilbene close to either the electron donating or the withdrawing substitutes, to populate a TICT state.^{69-70, 84}

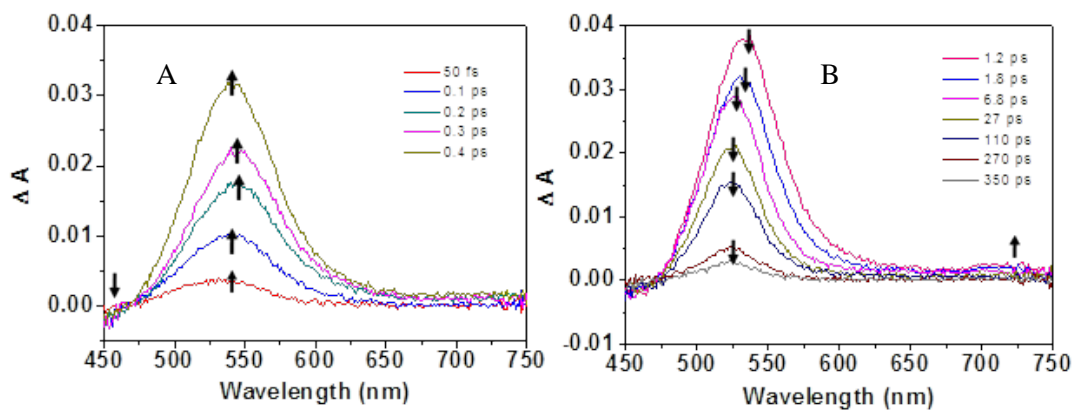


Figure 4.10 Femtosecond Transient absorption spectra of Corner sample (A) at time delays before 1.2ps and (B) at time delays between 1.2ps to 350ps

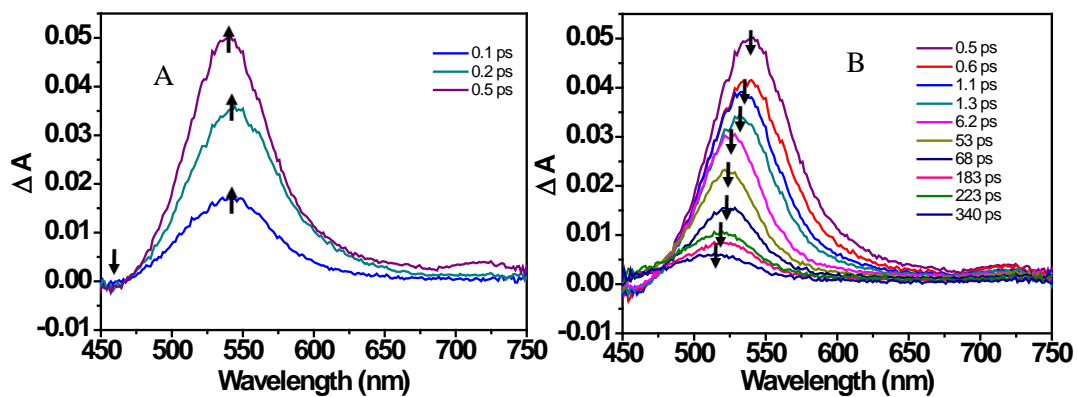


Figure 4.11 Femtosecond transient absorption spectra of Half sample (A) at time delays before 0.5ps and (B) at time delays between 0.5ps to 340ps

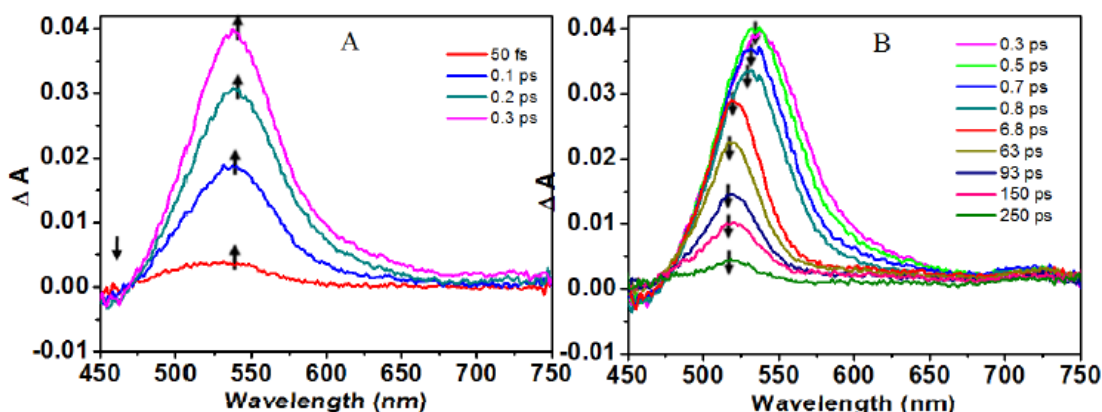


Figure 4.12 Femtosecond transient absorption spectra of Cube sample (A) at time delays before 0.3ps and (B) at time delays between 0.3ps to 250ps

The transient dynamics at the ESA peak maxima are plotted in Figure 4.13. In order to quantitatively estimate the lifetimes associated with the different relaxation processes, exponential fitting functions were used to fit the kinetic curves at the probe wavelength of 550 nm. Different lifetime components are listed in Table 4.5. Trifluoroaminostilbene ($\text{CF}_3\text{stilbeneNH}_2$) is also measured as a model compound for comparison. The first components are 1.4ps for the corner, 2.5ps for the half, 1.6ps for the cube, and 2ps for the model compound, respectively. They are assigned to the vibrational relaxation in a locally excited singlet (S_1) state, which is the $\text{LE}(S_1)$ state. The second lifetime components, 166ps for corner, 58ps for half, 75ps for cube, and 32ps for model compound are ascribed to the conformational relaxation process of stilbene involving the rotation around the single bond, as suggested by the previous reports.^{70, 86} In the case of the corner, the lifetime component 166ps is larger than that of trans-stilbene $\sim 100\text{ps}$,^{56, 63} and even larger than the push-pull stilbene model compound (32ps). This is due to the retardation of the cis-trans isomerization process caused by the steric hindrance effect of the large substituted group in corner. It is worth noting that the transient lifetime components are in accordance with the fluorescence lifetime results. As a result, these evidences suggest the conversion from the vibrationally relaxed $\text{LE}(S_1)$ to another lower energy S_1 state $A^*(S_1)$ which is the TICT state (T^* as shown earlier). Similar excited

states transitions of push-pull stilbenes have been reported recently.⁷⁰ In addition, this transition is also associated with the blue shift of the absorption maxima of the ESA band from 475 to 650 nm.

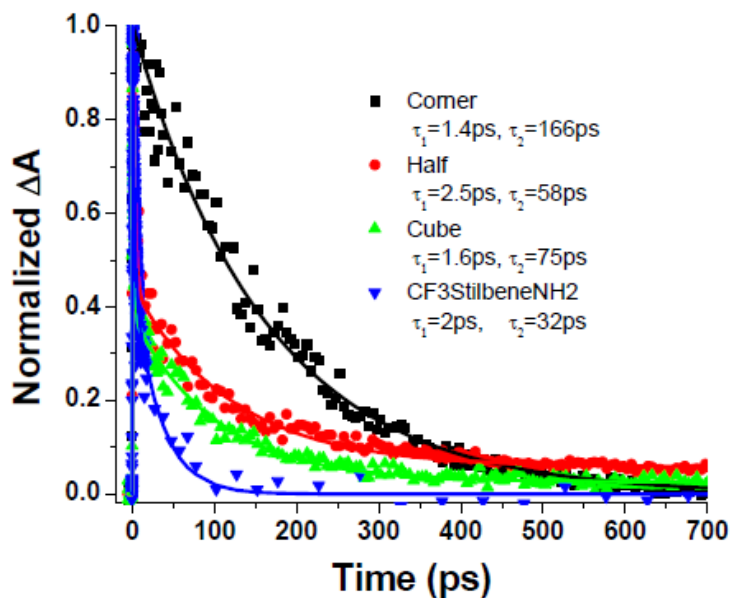


Figure 4.13 Transient absorption kinetics of Corner, Half and Cube and model compound CF₃StilbeneNH₂

Table 4.5 Transient absorption kinetics lifetime at 550 nm

SQs	Lifetime Components
Corner	1.4ps , 166ps
Half	2.5ps , 58ps
Cube	1.6ps , 75ps
CF ₃ -Stilbene-NH ₂	2ps , 32ps

Further examination on the charge transfer state (TICT) is performed. Figure 4.14 presents the dynamics providing evidence for the formation of the TICT state of each system. The probe wavelengths are 467 nm for the corner, 470 nm for the half, and 467 nm for the cube, respectively, which are at the left shoulder of the ESA band assigned to the $S_n(n\pi^*) \leftarrow S_1(n\pi^*)$ transition of the solvent stabilized TICT state of the push-pull stilbene system (TICT').⁸⁵ It is very clear that the excited dynamics of the corner is under a different mechanism in comparison with the half and cube. The fitted lifetime components are listed in Table 4.6. In the case of corner, the ESA undergoes a decay process with a life time of 170ps after an ultrafast transition within the initial 350fs. This decay process indicates a non-radiative relaxation process back to the ground state. In contrast to the corner, a growth in the amplitude is observed after the formation of this TICT' state in both the half and cube, within 16ps and 3.5ps, respectively. It suggests that a solvent stabilized long-lived charge transfer state is favored in the case of half and cube. Upon photoexcitation, transient absorption measurements have shown the presence of a charge-transfer (TICT) state depending on the number of chromophores. The results point to the ultrafast delocalization of charge in this particular system.

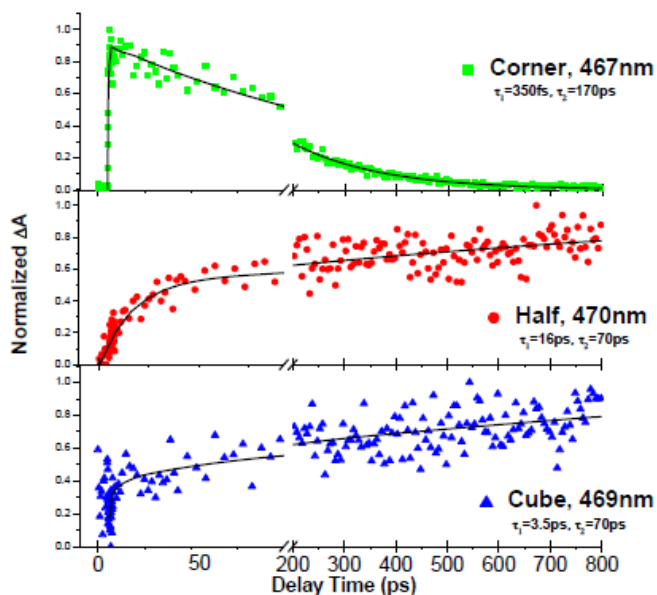


Figure 4.14 Transient absorption kinetics of Corner at 467 nm, Half at 470 nm and Cube at 467 nm.

As mentioned earlier, the time dependent dynamic blue shift of the maximum of the ESA band in the 470 to 650 nm region was observed within the initial several picoseconds. The ESA maxima shifts for each sample at different time delay are listed in Table 4.7. It has been reported that in the non-substituted trans-stilbene, the ultrafast transient shifts to the blue in a few picoseconds, and this is interpreted as the formation of an intermediate state before isomerization.⁸⁷⁻⁸⁹ This blue shift is also related with the solvation process.⁷⁰ In addition, a red shift as a result of solvation effect was observed from time-resolved emission spectra of push-pull stilbene derivatives,⁴⁷ indicating the excited state energy level is lowered by vibrational coupling. The shift of maximum wavelength of emission spectra of 15–20 nm is observed within the first few hundred picoseconds delay time after the excitation. In our case, a spectral blue-shift in transient absorption is more likely a combination of solvation and conformational relaxation along the potential energy surface associated with the charge transfer process. Because the conversion from LE(S₁) to TICT (A* (S₁)) state upon excitation is extremely fast, there is no significant change in the geometry of the central double bond in the DAS chromophore. In this charge transfer state, the character of the stilbene central double bond becomes to be more like a single bond character which facilitates the torsional motion and results a stronger dipole moment.⁹⁰ As a result, this conformation could assist the charge transfer process so as to reinforce the electrostatic interaction. Another process between solvent and chromophores is required to further stabilize the twisting geometry. The interactions between the chromophore and the surrounding solvent molecules are different in each excited electronic state. This change in interaction can originate due to different dipole moments in these two states. A solvent stabilized relaxed intramolecular charge transfer state (TICT') is reached after the solvation shell is in thermodynamic equilibrium with the molecule. In order to further study the solvation process, femtosecond transient absorption measurements of cube in DMSO polar solvent were carried out. Non-polar solvent environment wasn't studied because of the poor solubility of these systems in non-polar solvents. The transient absorption spectrum of cube in DMSO is plotted in Figure 4.15. The time dependent dynamic blue shift of the ESA maxima is from 540 nm to 511 nm, which is 7 nm more than the result using THF as solvent. In addition, a new transient was observed from 600 nm to 675 nm. This transient

is assigned to conversion from the vibrationally relaxed LE S₁ state to the S_n state.⁷⁰ In the transient absorption spectrum of the cube in THF, this ESA band was overlapped with the ESA band from 450 nm and 600 nm, as shown in Figure 4.12B. These evidences are in support of that the time dependent dynamics is due to solvation processes. It is also observed from Figure 4.15 that the SE negative absorption band below 480 nm region was vanishing along with the formation of TICT'. It gives the evidence supporting that the resulting solvent stabilized TICT' is a non-emissive state. In the theoretical consideration, the solvent-controlled charge transfer rate is expressed by the following equation:⁹¹

Equation 4.5

$$k_A = \frac{1}{\tau_s} \left(\frac{\lambda_s}{16\pi k_B T} \right)^{1/2} \exp\left(-\frac{\Delta G^*}{k_B T}\right)$$

Where, τ_s is the characteristic time for solvation dynamics, λ_s is the solvent reorganization energy, k_B is the Boltzmann constant and ΔG^* is the free energy of activation. According to the Born-Hush equation.⁹²⁻⁹³

Equation 4.6

$$\lambda_s = \frac{e^2}{4\pi\epsilon_0} \left[\frac{1}{2} \left(\frac{1}{r^+} + \frac{1}{r^-} \right) - \frac{1}{R_{cc}} \right] \left(\frac{1}{n^2} - \frac{1}{\epsilon_s} \right)$$

Here, n is the refractive index of the solvent r^+ and r^- are the radii of the charged molecules, R_{cc} is the center-to-center distance of the photogenerated charges and ϵ_s is the relative dielectric constant of the solvent. According to the Marcus theory, the barrier of charge transfer process ΔG^* is related to change in free energy for charge transfer state via the following expression:⁹⁴

Equation 4.7

$$\Delta G^* = \frac{(\Delta G_0 + \lambda_s)^2}{4\lambda_s}$$

Here, ΔG_0 is the energy gap between the reactant and product states. In our cases, ΔG_0 is attributed to the blue shift observed in the transient absorption ESA band. Stronger charge transfer character in the product states could actually decrease the energy gap ΔG_0 (more negative), and this leads to a decrease of the activation energy barrier. Therefore, the charge transfer rate rises until the reorganization energy equals the change of free energy ($\lambda_s = -\Delta G_0$). According to Eq.4.6, λ_s is dependent on the geometry of the molecule and the distance between the chromophore and the center core.

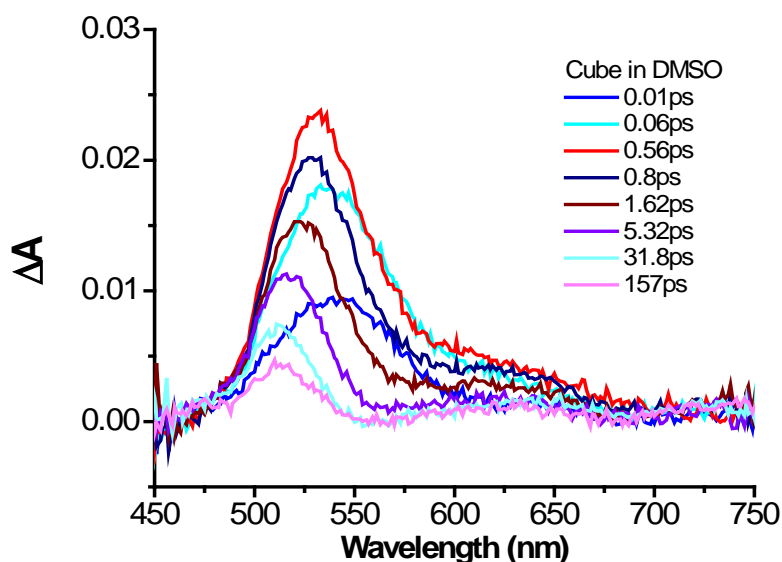


Figure 4.15 Femtosecond transient absorption spectrum of Cube in DMSO

It has been well established that photoexcitation drives the linear push pull stilbene derivatives into the charge transfer (CT) state.^{70, 90} Fully charge separated TICT states have been found in the push-pull type stilbene derivatives.⁹⁵ The formation of the

photoinduced charge transfer state of a similar chromophore, 4-dimethylamino, 4'-cyanostilbene has been investigated theoretically by the free energy decomposition analysis.⁹⁰ Two important factors affecting the stable CT geometry of push-pull stilbenes have been found: (1) the torsional motion of the single bond linkage between the stilbene and its substituted functional groups, and (2) the electrostatic interaction, which is enhanced by twisting geometrically assisted charge separation process.⁹⁰ The photoexcitation process of branched multi-chromophore shell-core systems have been investigated both experimentally and theoretically.^{75, 96-98} It has been found that the photoexcitation produces a charge-transfer state and the excitation is actually localized on one of the chromophores.^{75, 96-98} In our systems, Table 4.7 lists the amount of shifts of the ESA peak in wavenumber ($\Delta\nu$) for each system. This value is a strong indication of the extent of the charge transfer character. A greater amount of charge transfer observed in the case of cube (720 cm^{-1}) and half (750 cm^{-1}) when compared to the corner (250 cm^{-1}) suggests that the charge is more in favor of the entire molecule than localized on one arm of the chromophore. This result is in accordance with the dynamics presented in Figure 4.10. Similar increase (by more than a factor of 2) in the donor to acceptor charge transfer with increasing number of chromophores has been found in the core-branched systems.⁹⁹⁻

100

Table 4.6 Transient absorption kinetics lifetime components at probe wavelength 467 nm

SQs	Lifetime Components
Corner	350 fs , 170 ps
Half	16 ps , 70 ps, long
Cube	3.5 ps , 70 ps, long

Therefore, the strength of the non-emissive TICT' in the excited state has increased with an increasing number of the chromophores, which was not predicted by

the steady-state stokes shift measurements. These results correspond well with the two-photon absorption results that the TPA cross-section is enhanced with an increasing number of chromophores in the half and cube systems in comparison with the corner. In addition, the acceptor strength is also crucial in affecting the population of the CT state. Mattori *et al.*¹⁰¹ reported computational results on the trapping and the release transition states (TS) of the atomic hydrogen in an octasilsesquioxane cage. The stronger charge transfer state found in half and cube might be an indication that half and full SQ cages have better electron accepting ability than the corner as an electron trapper.

Table 4.7 Details of the time dependent dynamic ESA blue shift ESA band in 470 to 650 nm region. ESA maxima of corner, half and cube at different delay time

Sample	ESA peak maximum		ESA peak maximum		Shift $\Delta\nu(\text{cm}^{-1})$
	Wavelength	Delay time	Wavelength	Delay time	
Corner	532 nm	1.2 ps	525 nm	6.8 ps	250
Half	540 nm	500 fs	519 nm	6.2 ps	750
Cube	538 nm	300 fs	518 nm	6.8 ps	720

Based on the observations above, a simplified energy diagram of our investigated system is drawn in Figure 4.16. After photoexcitation, the molecule reaches the main emissive TICT state within subpicosecond (about 1.3ps for corner, 650fs for half and 850fs for cube). The fluorescence emission process takes about 146ps, 73ps, and 75ps for corner, half, and cube, respectively. A further solvent stabilized charge transfer TICT' state is reached with long lived life time for half and cube. Intersystem crossing to the dark state is observed after few tens of picoseconds time delay.

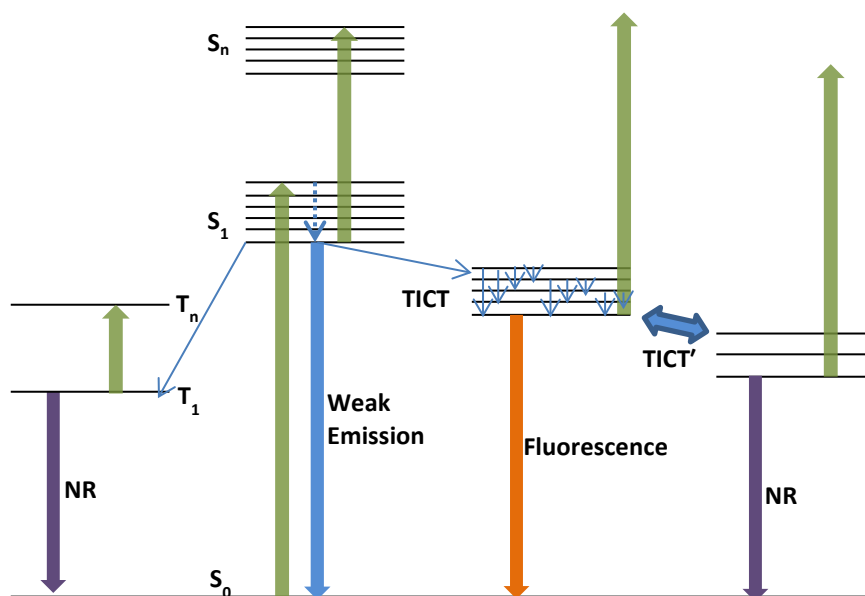


Figure 4.16 Simplified schematic energy diagram of investigated systems

4.3 Conclusion

In summary, a series of dimethylaminostilbene substituted silsesquioxanes with partial and full cages has been investigated by fluorescence up-conversion and femtosecond transient absorption measurements. Fluorescence up-conversion measurements provide an insight into the energy transfer process in these three systems. The kinetics results indicate that the twisting around the double bond of the substituted stilbene is more sensitive to the degree of its dipole moment than the size of its substitutes. In the case of corner, the twisting is retarded by the steric hindrance effect compared to stilbene free dye. In the case of half and cube, strong dipole moments are induced by the substitution which could facilitate the twisting process, overcome the steric hindrance effect and decrease the fluorescence lifetime. The dynamics of the transient absorption show significant differences between the corner and the half and cube. The pump-probe measurements have shown the presence of TICT state in 500-600 nm region. The lifetimes of this emissive TICT state corresponds well with fluorescence

lifetimes for each system respectively. The transient absorption results also reveal a combination of charge transfer dynamics and solvation process associated with excited-state absorption blue shifts, and a resulting solvent stabilized non-emissive TICT' state. Ultrafast transient measurements have shown an interesting trend with respect to the amount charge-transfer character with increasing number of chromophores. Both half and cube show enhanced charge transfer character compared to the corner. In addition, this explains the enhanced two-photon cross-sections found in the half and cube systems. Upon photoexcitation, transient absorption measurements have shown the presence of a charge-transfer (TICT) state depending on the number of chromophores, suggesting the ultrafast delocalization of charge in half and cube systems.

References

- [1]. Scott, D. W., Thermal Rearrangement of Branched-Chain Methylpolysiloxanes. *Journal of the American Chemical Society* **1946**, 68 (3), 356-358.
- [2]. Gao, F.; Tong, Y. H.; Schrickler, S. R.; Culbertson, B. M., Evaluation of Neat Resins Based on Methacrylates Modified with Methacryl-Poss, as Potential Organic-Inorganic Hybrids for Formulating Dental Restoratives. *Polymers for Advanced Technologies* **2001**, 12 (6), 355-360.
- [3]. Fong, H.; Dickens, S. H.; Flaim, G. M., Evaluation of Dental Restorative Composites Containing Polyhedral Oligomeric Silsesquioxane Methacrylate. *Dental Materials* **2005**, 21 (6), 520-529.
- [4]. Pescarmona, P. P.; van der Waal, J. C.; Maxwell, I. E.; Maschmeyer, T., A New, Efficient Route to Titanium-Silsesquioxane Epoxidation Catalysts Developed by Using High-Speed Experimentation Techniques. *Angewandte Chemie-International Edition* **2001**, 40 (4), 740-743.
- [5]. Carniato, F.; Bisio, C.; Boccaleri, E.; Guidotti, M.; Gavrilova, E.; Marchese, L., Titanosilsesquioxane Anchored on Mesoporous Silicas: A Novel Approach for the Preparation of Heterogeneous Catalysts for Selective Oxidations. *Chemistry-a European Journal* **2008**, 14 (27), 8098-8101.

- [6]. Devaux, E.; Rochery, M.; Bourbigot, S., Polyurethane/Clay and Polyurethane/Poss Nanocomposites as Flame Retarded Coating for Polyester and Cotton Fabrics. *Fire and Materials* **2002**, *26* (4-5), 149-154.
- [7]. Ellsworth, M. W.; Gin, D. L., Recent Advances in the Design and Synthesis Of. Polymer Inorganic Nanocomposites. *Polym. News* **1999**, *24*, 331-341.
- [8]. Ro, H. W.; Popova, V.; Chen, L.; Forster, A. M.; Ding, Y. F.; Alvine, K. J.; Krug, D. J.; Laine, R. M.; Soles, C. L., Cubic Silsesquioxanes as a Green, High-Performance Mold Material for Nanoimprint Lithography. *Advanced Materials* **2011**, *23* (3), 414-420.
- [9]. Kannan, R. Y.; Salacinski, H. J.; Butler, P. E.; Seifalian, A. M., Polyhedral Oligomeric Silsesquioxane Nanocomposites: The Next Generation Material for Biomedical Applications. *Accounts of Chemical Research* **2005**, *38* (11), 879-884.
- [10]. Osslon, K., Improved Preparation of Octakis(Alkylsilsesquioxanes). *Ark. Kemi* **1958**, *37*, 367-379.
- [11]. Chan, K. L.; Sonar, P.; Sellinger, A., Cubic Silsesquioxanes for Use in Solution Processable Organic Light Emitting Diodes (Oled). *Journal of Materials Chemistry* **2009**, *19* (48), 9103-9120.
- [12]. Lo, M. Y.; Ueno, K.; Tanabe, H.; Sellinger, A., Silsesquioxane-Based Nanocomposite Dendrimers with Photo-Luminescent and Charge Transport Properties. *Chemical Record* **2006**, *6* (3), 157-168.
- [13]. Laine, R. M., Nanobuilding Blocks Based on the Osio1.5 (X) (X=6, 8, 10) Octasilsesquioxanes. *Journal of Materials Chemistry* **2005**, *15* (35-36), 3725-3744.
- [14]. Furgal, J. C.; Abeyasinghe, N.; Jung, J. H.; Yi, E. Y.; Goodson, T.; Laine, R. M., Analyzing Structure-Photophysical Property Pelationships of T8, T10, T12, and Oligomeric Stilbenevinyl Silsesquioxanes. *Abstracts of Papers of the American Chemical Society* **2013**, 245.
- [15]. Brick, C. M.; Tamaki, R.; Kim, S. G.; Asuncion, M. Z.; Roll, M.; Nemoto, T.; Ouchi, Y.; Chujo, Y.; Laine, R. A., Spherical, Polyfunctional Molecules Using Poly(Bromophenylsilsesquioxane)S as Nanoconstruction Sites. *Macromolecules* **2005**, *38* (11), 4655-4660.
- [16]. Asuncion, M. Z.; Laine, R. M., Fluoride Rearrangement Reactions of Polyphenyl- and Polyvinylsilsesquioxanes as a Facile Route to Mixed Functional Phenyl,

Vinyl T-10 and T-12 Silsesquioxanes. *Journal of the American Chemical Society* **2010**, *132* (11), 3723-3736.

- [17]. Jung, J. H.; Furgal, J. C.; Goodson, T.; Mizumo, T.; Schwartz, M.; Chou, K. L.; Vonet, J. F.; Laine, R. M., 3-D Molecular Mixtures of Catalytically Functionalized Vinylsio(1.5) (10)/ Vinylsio(1.5) (12). Photophysical Characterization of Second Generation Derivatives. *Chemistry of Materials* **2012**, *24* (10), 1883-1895.
- [18]. Laine, R. M.; Sulaiman, S.; Brick, C.; Roll, M.; Tamaki, R.; Asuncion, M. Z.; Neurock, M.; Filhol, J. S.; Lee, C. Y.; Zhang, J.; Goodson, T.; Ronchi, M.; Pizzotti, M.; Rand, S. C.; Li, Y., Synthesis and Photophysical Properties of Stilbeneoctasilsesquioxanes. Emission Behavior Coupled with Theoretical Modeling Studies Suggest a 3-D Excited State Involving the Silica Core. *Journal of the American Chemical Society* **2010**, *132* (11), 3708-3722.
- [19]. Sulaiman, S.; Bhaskar, A.; Zhang, J.; Guda, R.; Goodson, T.; Laine, R. M., Molecules with Perfect Cubic Symmetry as Nanobuilding Blocks for 3-D Assemblies. Elaboration of Octavinylsilsesquioxane. Unusual Luminescence Shifts May Indicate Extended Conjugation Involving the Silsesquioxane Core. *Chemistry of Materials* **2008**, *20* (17), 5563-5573.
- [20]. Sulaiman, S.; Zhang, J.; Goodson, T.; Laine, R. M., Synthesis, Characterization and Photophysical Properties of Polyfunctional Phenylsilsesquioxanes: O-Rphsio1.5 (8), 2,5-R2phsio1.5 (8), and R3phsio1.5 (8). Compounds with the Highest Number of Functional Units/Unit Volume. *Journal of Materials Chemistry* **2011**, *21* (30), 11177-11187.
- [21]. Lin, T. T.; He, C. B.; Xiao, Y., Theoretical Studies of Monosubstituted and Higher Phenyl-Substituted Octahydrosilsesquioxanes. *Journal of Physical Chemistry B* **2003**, *107* (50), 13788-13792.
- [22]. Xiang, K. H.; Pandey, R.; Pernisz, U. C.; Freeman, C., Theoretical Study of Structural and Electronic Properties of H-Silsesquioxanes. *Journal of Physical Chemistry B* **1998**, *102* (44), 8704-8711.
- [23]. Phillips, H.; Zheng, S. H.; Hyla, A.; Laine, R.; Goodson, T.; Geva, E.; Dunietz, B. D., Ab Initio Calculation of the Electronic Absorption of Functionalized Octahedral Silsesquioxanes Via Time-Dependent Density Functional Theory with Range-Separated Hybrid Functionals. *Journal of Physical Chemistry A* **2012**, *116* (4), 1137-1145.
- [24]. Zheng, S. H.; Phillips, H.; Geva, E.; Dunietz, B. D., Ab Initio Study of the Emissive Charge-Transfer States of Solvated Chromophore-Functionalized

- Silsesquioxanes. *Journal of the American Chemical Society* **2012**, *134* (16), 6944-6947.
- [25]. Zhen, C. G.; Becker, U.; Kieffer, J., Tuning Electronic Properties of Functionalized Polyhedral Oligomeric Silsesquioxanes: A Dft and Tddft Study. *Journal of Physical Chemistry A* **2009**, *113* (35), 9707-9714.
- [26]. Shen, J.; Cheng, W. D.; Wu, D. S.; Li, X. D.; Lan, Y. Z.; Zhang, H.; Gong, Y. J.; Li, F. F.; Huang, S. P., Modeling of Configurations and Third-Order Nonlinear Optical Properties of Methyl Silsesquioxanes. *Journal of Chemical Physics* **2005**, *122* (20).
- [27]. Zhang, J.; Fischer, M. K. R.; Bauerle, P.; Goodson, T., Energy Migration in Dendritic Oligothiophene-Perylene Bisimides. *Journal of Physical Chemistry B* **2013**, *117* (16), 4204-4215.
- [28]. Raymond, J. E.; Casado, J.; Navarrete, J. T. L.; Takimiya, K.; Goodson, T., Two-Photon Mediated Three-Photon Fluorescence: Lessons from a Quinoidal Oligothiophene Dimer. *Journal of Physical Chemistry Letters* **2011**, *2* (17), 2179-2183.
- [29]. Oliva, M. M.; Casado, J.; Navarrete, J. T. L.; Patchkovskii, S.; Goodson, T.; Harpham, M. R.; de Melo, J. S. S.; Amir, E.; Rozen, S., Do All -S,S '-Dioxide Oligothiophenes Show Electronic and Optical Properties of Oligoenes and/or of Oligothiophenes? *Journal of the American Chemical Society* **2010**, *132* (17), 6231-6242.
- [30]. Clark, T. B.; Goodson, T., Two-Photon Absorbing Gfp-Type Chromophores: Synthetic Design and Spectroscopic Characterization. *Abstracts of Papers of the American Chemical Society* **2010**, 240.
- [31]. Clark, T. B.; Orr, M. E.; Goodson, T., Nonlinear and Time-Resolved Spectroscopic Studies of Gfp-Type Chromophore as a Probe for Amyloid-B Folding Dynamics. *Abstracts of Papers of the American Chemical Society* **2011**, 242.
- [32]. Varnavski, O.; Ramakrishna, G.; Kim, J.; Lee, D.; Goodson, T., Optically Excited Acoustic Vibrations in Quantum-Sized Monolayer-Protected Gold Clusters. *Acs Nano* **2010**, *4* (6), 3406-3412.
- [33]. Yau, S. H.; Abeyasinghe, N.; Orr, M.; Upton, L.; Varnavski, O.; Werner, J. H.; Yeh, H. C.; Sharma, J.; Shreve, A. P.; Martinez, J. S.; Goodson, T., Bright Two-Photon Emission and Ultra-Fast Relaxation Dynamics in a DNA-Templated Nanocluster Investigated by Ultra-Fast Spectroscopy. *Nanoscale* **2012**, *4* (14), 4247-4254.

- [34]. Yau, S. H.; Varnavski, O.; Gilbertson, J. D.; Chandler, B.; Ramakrishna, G.; Goodson, T., Ultrafast Optical Study of Small Gold Monolayer Protected Clusters: A Closer Look at Emission. *Journal of Physical Chemistry C* **2010**, *114* (38), 15979-15985.
- [35]. Devadas, M. S.; Kim, J.; Sinn, E.; Lee, D.; Goodson, T.; Ramakrishna, G., Unique Ultrafast Visible Luminescence in Monolayer-Protected Au-25 Clusters. *Journal of Physical Chemistry C* **2010**, *114* (51), 22417-22423.
- [36]. Flynn, D.; Goodson, T., Light Harvesting Mechanisms: Exciton-Phonon Coupling in Thiophene Macrocycles at Low Temperature. *Abstracts of Papers of the American Chemical Society* **2010**, *240*.
- [37]. Yoon, Z. S.; Chan, Y. T.; Li, S. N.; Newkome, G. R.; Goodson, T., Ultrafast Time-Resolved Spectroscopy of Self-Assembled Cyclic Fe(II)-Bisterpyridine Complexes. *Journal of Physical Chemistry B* **2010**, *114* (36), 11731-11736.
- [38]. Flynn, D. C.; Ramakrishna, G.; Yang, H. B.; Northrop, B. H.; Stang, P. J.; Goodson, T., Ultrafast Optical Excitations in Supramolecular Metallacycles with Charge Transfer Properties. *Journal of the American Chemical Society* **2010**, *132* (4), 1348-1358.
- [39]. Ramakrishna, G.; Goodson, T.; Rogers-Haley, J. E.; Cooper, T. M.; McLean, D. G.; Urbas, A., Ultrafast Intersystem Crossing: Excited State Dynamics of Platinum Acetylide Complexes. *Journal of Physical Chemistry C* **2009**, *113* (3), 1060-1066.
- [40]. Maya, E. M.; Snow, A. W.; Shirk, J. S.; Pong, R. G. S.; Flom, S. R.; Roberts, G. L., Synthesis, Aggregation Behavior and Nonlinear Absorption Properties of Lead Phthalocyanines Substituted with Siloxane Chains. *Journal of Materials Chemistry* **2003**, *13* (7), 1603-1613.
- [41]. Cohen, B.; Wang, S. F.; Organero, J. A.; Campo, L. F.; Sanchez, F.; Douhal, A., Femtosecond Fluorescence Dynamics of a Proton-Transfer Dye Interacting with Silica-Based Nanomaterials. *Journal of Physical Chemistry C* **2010**, *114* (14), 6281-6289.
- [42]. Ramakrishna, G.; Bhaskar, A.; Goodson, T., Ultrafast Excited State Relaxation Dynamics of Branched Donor-Pi-Acceptor Chromophore: Evidence of a Charge-Delocalized State. *Journal of Physical Chemistry B* **2006**, *110* (42), 20872-20878.

- [43]. Goodson, T. G., Optical Excitations in Organic Dendrimers Investigated by Time-Resolved and Nonlinear Optical Spectroscopy. *Accounts of Chemical Research* **2005**, 38 (2), 99-107.
- [44]. Furgal, J.; Goodson, T. I.; Laine, R. M., Unpublished Work.
- [45]. Letard, J. F.; Lapouyade, R.; Rettig, W., Structure Photophysics Correlations in a Series of 4-(Dialkylamino)Stilbenes - Intramolecular Charge-Transfer in the Excited-State as Related to the Twist around the Single Bonds. *Journal of the American Chemical Society* **1993**, 115 (6), 2441-2447.
- [46]. Lewis, F. D.; Weigel, W., Excited State Properties of Donor-Acceptor Substituted Trans-Stilbenes: The Meta-Amino Effect. *Journal of Physical Chemistry A* **2000**, 104 (34), 8146-8153.
- [47]. Yang, J. S.; Chiou, S. Y.; Liou, K. L., Fluorescence Enhancement of Trans-4-Aminostilbene by N-Phenyl Substitutions: The "Amino Conjugation Effect". *Journal of the American Chemical Society* **2002**, 124 (11), 2518-2527.
- [48]. Murrell, J. N., The Electronic Spectrum of Aromatic Molecules .6. The Mesomeric Effect. *Proceedings of the Physical Society of London Section A* **1955**, 68 (11), 969-975.
- [49]. Yamaguchi, S.; Jin, R. Z.; Tamao, K., Modification of the Electronic Structure of Silole by the Substituents on the Ring Silicon. *Journal of Organometallic Chemistry* **1998**, 559 (1-2), 73-80.
- [50]. Tamao, K.; Ohno, S.; Yamaguchi, S., Silole-Pyrrole Co-Oligomers: Their Synthesis, Structure and Uv-Vis Absorption Spectral. *Chemical Communications* **1996**, (16), 1873-1874.
- [51]. Tamao, K.; Yamaguchi, S.; Ito, Y.; Matsuzaki, Y.; Yamabe, T.; Fukushima, M.; Mori, S., Silole-Containing Pi-Conjugated Systems .3. A Series of Silole-Thiophene Cooligomers and Copolymers - Synthesis, Properties, and Electronic-Structures. *Macromolecules* **1995**, 28 (25), 8668-8675.
- [52]. Tamao, K.; Yamaguchi, S.; Shiro, M., Oligosiloles - First Synthesis Based on a Novel Endo-Endo Mode Intramolecular Reductive Cyclization of Diethynylsilanes. *Journal of the American Chemical Society* **1994**, 116 (26), 11715-11722.
- [53]. Yamaguchi, S.; Tamao, K., Theoretical Study of the Electronic Structure of 2,2'-Bisilole in Comparison with 1,1'-Bi-1,3-Cyclopentadiene: Sigma*-Pi* Conjugation and a Low-Lying Lumo as the Origin of the Unusual Optical

Properties of 3,3',4,4'-Tetraphenyl-2,2'-Bisilole. *Bulletin of the Chemical Society of Japan* **1996**, 69 (8), 2327-2334.

- [54]. Todd, D. C.; Jean, J. M.; Rosenthal, S. J.; Ruggiero, A. J.; Yang, D.; Fleming, G. R., Fluorescence Upconversion Study of Cis-Stilbene Isomerization. *Journal of Chemical Physics* **1990**, 93 (12), 8658-8668.
- [55]. Meier, H., Blue Fluorescent Exciplexes Consisting of Trans-Stilbene and Antibodies. *Angewandte Chemie-International Edition* **2001**, 40 (10), 1851-1853.
- [56]. Sumitani, M.; Nakashima, N.; Yoshihara, K.; Nagakura, S., Temperature-Dependence of Fluorescence Lifetimes of Trans-Stilbene. *Chemical Physics Letters* **1977**, 51 (1), 183-185.
- [57]. Kubicki, A. A., Time-Resolved Emission Spectra of Stilbene Derivatives in Various Solvents. *Chemical Physics Letters* **2009**, 483 (4-6), 268-272.
- [58]. Lapouyade, R.; Czeschka, K.; Majenz, W.; Rettig, W.; Gilibert, E.; Rulliere, C., Photophysics of Donor-Acceptor Substituted Stilbenes - a Time-Resolved Fluorescence Study Using Selectively Bridged Dimethylamino Cyanomodel Compounds. *Journal of Physical Chemistry* **1992**, 96 (24), 9643-9650.
- [59]. Lapouyade, R.; Kuhn, A.; Letard, J. F.; Rettig, W., Multiple Relaxation Pathways in Photoexcited Dimethylaminonitro-Stilbenes and Dimethylaminocyanostilbenes. *Chemical Physics Letters* **1993**, 208 (1-2), 48-58.
- [60]. Letard, J. F.; Lapouyade, R.; Rettig, W., Multidimensional Photochemistry in 4-(N,N-Dimethylamino) Stilbene. *Chemical Physics* **1994**, 186 (1), 119-131.
- [61]. Letard, J. F.; Lapouyade, R.; Rettig, W., Relaxation Pathways in Photoexcited Electron-Rich Stilbenes (D-D Stilbenes) as Compared to D-a Stilbenes. *Chemical Physics Letters* **1994**, 222 (3), 209-216.
- [62]. Gustavsson, T.; Baldacchino, G.; Mialocq, J. C.; Pommeret, S., A Femtosecond Fluorescence up-Conversion Study of the Dynamic Stokes Shift of the Dcm Dye Molecule in Polar and Nonpolar-Solvents. *Chemical Physics Letters* **1995**, 236 (6), 587-594.
- [63]. Yoshihara, K.; Namiki, A.; Sumitani, M.; Nakashima, N., Picosecond Flash-Photolysis of Cis-Stilbene and Trans-Stilbene - Observation of an Intense Intramolecular Charge-Resonance Transition. *Journal of Chemical Physics* **1979**, 71 (7), 2892-2895.

- [64]. Rettig, W.; Majenz, W., Competing Adiabatic Photoreaction Channels in Stilbene Derivatives. *Chemical Physics Letters* **1989**, *154* (4), 335-341.
- [65]. Dekhtyar, M.; Rettig, W., Charge-Transfer Transitions in Twisted Stilbenoids: Interchangeable Features and Generic Distinctions of Single- and Double-Bond Twists. *Journal of Physical Chemistry A* **2007**, *111* (11), 2035-2039.
- [66]. LeBreton, H.; Bennetau, B.; Letard, J. F.; Lapouyade, R.; Rettig, W., Nonradiative Twisted Intramolecular Charge Transfer State in Polar Stilbenes: Photophysical Study of 4-Perfluorooctylsulfonyl-4'-N,N-Dimethylamino Stilbene and Two Bridged Derivatives. *Journal of Photochemistry and Photobiology a-Chemistry* **1996**, *95* (1), 7-20.
- [67]. Yang, J. S.; Lin, C. K.; Lahoti, A. M.; Tseng, C. K.; Liu, Y. H.; Lee, G. H.; Peng, S. M., Effect of Ground-State Twisting on the Trans -> Cis Photoisomerization and Tict State Formation of Aminostilbenes. *Journal of Physical Chemistry A* **2009**, *113* (17), 4868-4877.
- [68]. Ronchi, M.; Pizzotti, M.; Biroli, A. O.; Righetto, S.; Ugo, R.; Mussini, P.; Cavazzini, M.; Lucenti, E.; Salsa, M.; Fantucci, P., Second-Order Nonlinear Optical (Nlo) Properties of a Multichromophoric System Based on an Ensemble of Four Organic Nlo Chromophores Nanoorganized on a Cyclotetrasiloxane Architecture. *Journal of Physical Chemistry C* **2009**, *113* (7), 2745-2760.
- [69]. Fujiwara, T.; Lee, J.-K.; Zgierski, M. Z.; Lim, E. C., Intramolecular Charge Transfer in the Excited State of 4-Dimethylaminobenzaldehyde and 4-Dimethylaminoacetophenone. *Chemical Physics Letters* **2009**, *481* (1-3), 78-82.
- [70]. Singh, C.; Ghosh, R.; Mondal, J. A.; Palit, D. K., Excited State Dynamics of a Push-Pull Stilbene: A Femtosecond Transient Absorption Spectroscopic Study. *Journal of Photochemistry and Photobiology a-Chemistry* **2013**, *263*, 50-60.
- [71]. Savikhin, S.; Buck, D. R.; Struve, W. S., Pump-Probe Anisotropies of Fenna-Matthews-Olson Protein Trimers from *Chlorobium Tepidum*: A Diagnostic for Exciton Localization? *Biophysical Journal* **1997**, *73* (4), 2090-2096.
- [72]. Bradforth, S. E.; Jimenez, R.; Vanmourik, F.; Vangrondelle, R.; Fleming, G. R., Excitation Transfer in the Core Light-Harvesting Complex (Lh-1) of *Rhodobacter-Sphaeroides* - an Ultrafast Fluorescence Depolarization and Annihilation Study. *Journal of Physical Chemistry* **1995**, *99* (43), 16179-16191.
- [73]. Leegwater, J. A., Coherent Versus Incoherent Energy Transfer and Trapping in Photosynthetic Antenna Complexes. *Journal of Physical Chemistry* **1996**, *100* (34), 14403-14409.

- [74]. Yeh, A. T.; Shank, C. V.; McCusker, J. K., Ultrafast Electron Localization Dynamics Following Photo-Induced Charge Transfer. *Science* **2000**, 289 (5481), 935-938.
- [75]. Varnavski, O.; Samuel, I. D. W.; Palsson, L. O.; Beavington, R.; Burn, P. L.; Goodson, T., Investigations of Excitation Energy Transfer and Intramolecular Interactions in a Nitrogen Corded Distyrylbenzene Dendrimer System. *Journal of Chemical Physics* **2002**, 116 (20), 8893-8903.
- [76]. Wang, Y.; Ranasinghe, M. I.; Goodson, T., Ultrafast Fluorescence Investigation of Excitation Energy Transfer in Different Dendritic Core Branched Structures. *Journal of the American Chemical Society* **2003**, 125 (32), 9562-9563.
- [77]. Kopelman, R.; Shortreed, M.; Shi, Z. Y.; Tan, W. H.; Xu, Z. F.; Moore, J. S.; BarHaim, A.; Klafter, J., Spectroscopic Evidence for Excitonic Localization in Fractal Antenna Supermolecules. *Physical Review Letters* **1997**, 78 (7), 1239-1242.
- [78]. Swallen, S. F.; Zhu, Z. G.; Moore, J. S.; Kopelman, R., Correlated Excimer Formation and Molecular Rotational Dynamics in Phenylacetylene Dendrimers. *Journal of Physical Chemistry B* **2000**, 104 (16), 3988-3995.
- [79]. Wynne, K.; Hochstrasser, R. M., Coherence Effects in the Anisotropy of Optical Experiments. *Chemical Physics* **1993**, 171 (1-2), 179-188.
- [80]. Renger, T., Theory of Excitation Energy Transfer: From Structure to Function. *Photosynthesis Research* **2009**, 102 (2-3), 471-485.
- [81]. Soutar, I.; Swanson, L.; Christensen, R. L.; Drake, R. C.; Phillips, D., Time-Resolved Luminescence Anisotropy Studies of the Relaxation Behavior of Polymers .1. Intramolecular Segmental Relaxation of Poly(Methyl Methacrylate) and Poly(Methyl Acrylate) in Dilute Solutions in Dichloromethane. *Macromolecules* **1996**, 29 (14), 4931-4936.
- [82]. Jang, S.; Cheng, Y. C.; Reichman, D. R.; Eaves, J. D., Theory of Coherent Resonance Energy Transfer. *Journal of Chemical Physics* **2008**, 129 (10).
- [83]. Knox, R. S.; Gulen, D., Theory of Polarized Fluorescence from Molecular Pairs - Forster Transfer at Large Electronic Coupling. *Photochemistry and Photobiology* **1993**, 57 (1), 40-43.
- [84]. Schultefrohlinde, D.; Gorner, H., Cis-Trans Photoisomerization of 4-Nitrostilbenes. *Pure and Applied Chemistry* **1979**, 51 (2), 279-297.

- [85]. Fujiwara, T.; Lee, J. K.; Zgierski, M. Z.; Lim, E. C., Intramolecular Charge Transfer in the Excited State of 4-Dimethylaminobenzaldehyde and 4-Dimethylaminoacetophenone. *Chemical Physics Letters* **2009**, *481* (1-3), 78-82.
- [86]. Oberle, J.; Jonusauskas, G.; Abraham, E.; Lapouyade, R.; Rulliere, C., Time-Resolved Charge Transfer in "Push-Pull" Stilbenes. *Bulletin of the Chemical Society of Japan* **2002**, *75* (5), 1041-1047.
- [87]. Becker, H. C.; Kilsa, K., Size- and Solvent-Dependent Kinetics for Cis-Trans Isomerization in Donor-Acceptor Systems. *Spectrochimica Acta Part a-Molecular and Biomolecular Spectroscopy* **2009**, *72* (5), 1014-1019.
- [88]. Rice, J. K.; Baronavski, A. P., Ultrafast Studies of Solvent Effects in the Isomerization of Cis-Stilbene. *Journal of Physical Chemistry* **1992**, *96* (8), 3359-3366.
- [89]. Doany, F. E.; Hochstrasser, R. M.; Greene, B. I.; Millard, R. R., Femtosecond-Resolved Ground-State Recovery of Cis-Stilbene in Solution. *Chemical Physics Letters* **1985**, *118* (1), 1-5.
- [90]. Amatatsu, Y., Skeletal Relaxation Effect on the Charge Transfer State Formation of 4-Dimethylamino,4'-Cyanostilbene. *Journal of Physical Chemistry A* **2006**, *110* (28), 8736-8743.
- [91]. Nagasawa, Y.; Yartsev, A. P.; Tominaga, K.; Bisht, P. B.; Johnson, A. E.; Yoshihara, K., Dynamical Aspects of Ultrafast Intermolecular Electron-Transfer Faster Than Solvation Process - Substituent Effects and Energy-Gap Dependence. *Journal of Physical Chemistry* **1995**, *99* (2), 653-662.
- [92]. Oevering, H.; Paddonrow, M. N.; Heppener, M.; Oliver, A. M.; Cotsaris, E.; Verhoeven, J. W.; Hush, N. S., Long-Range Photoinduced through-Bond Electron-Transfer and Radiative Recombination Via Rigid Nonconjugated Bridges - Distance and Solvent Dependence. *Journal of the American Chemical Society* **1987**, *109* (11), 3258-3269.
- [93]. Kroon, J.; Verhoeven, J. W.; Paddonrow, M. N.; Oliver, A. M., Solvent Dependence of Photoinduced Intramolecular Electron-Transfer - Criteria for the Design of Systems with Rapid, Solvent-Independent Charge Separation. *Angewandte Chemie-International Edition in English* **1991**, *30* (10), 1358-1361.
- [94]. Marcus, R. A., On the Theory of Oxidation-Reduction Reactions Involving Electron Transfer .1. *Journal of Chemical Physics* **1956**, *24* (5), 966-978.

- [95]. Zgierski, M. Z.; Lim, E. C., The Role of Pi Sigma* State in Intramolecular Electron-Transfer Dynamics of 4-Dimethylaminobenzonitrile and Related Molecules. *Journal of Chemical Physics* **2004**, *121* (6), 2462-2465.
- [96]. Katan, C.; Terenziani, F.; Mongin, O.; Werts, M. H. V.; Porres, L.; Pons, T.; Mertz, J.; Tretiak, S.; Blanchard-Desce, M., Effects of (Multi)Branching of Dipolar Chromophores on Photophysical Properties and Two-Photon Absorption. *Journal of Physical Chemistry A* **2005**, *109* (13), 3024-3037.
- [97]. Rogers, J. E.; Slagle, J. E.; McLean, D. G.; Sutherland, R. L.; Sankaran, B.; Kannan, R.; Tan, L. S.; Fleitz, P. A., Understanding the One-Photon Photophysical Properties of a Two-Photon Absorbing Chromophore. *Journal of Physical Chemistry A* **2004**, *108* (26), 5514-5520.
- [98]. Li, B.; Tong, R.; Zhu, R. Y.; Meng, F. S.; Tian, H.; Qian, S. X., The Ultrafast Dynamics and Nonlinear Optical Properties of Tribranched Styryl Derivatives Based on 1,3,5-Triazine. *Journal of Physical Chemistry B* **2005**, *109* (21), 10705-10710.
- [99]. Beljonne, D.; Wenseleers, W.; Zojer, E.; Shuai, Z. G.; Vogel, H.; Pond, S. J. K.; Perry, J. W.; Marder, S. R.; Bredas, J. L., Role of Dimensionality on the Two-Photon Absorption Response of Conjugated Molecules: The Case of Octupolar Compounds. *Advanced Functional Materials* **2002**, *12* (9), 631-641.
- [100]. Ramakrishna, G.; Goodson, T., Excited-State Deactivation of Branched Two-Photon Absorbing Chromophores: A Femtosecond Transient Absorption Investigation. *Journal of Physical Chemistry A* **2007**, *111* (6), 993-1000.
- [101]. Mattori, M.; Mogi, K.; Sakai, Y.; Isobe, T., Studies on the Trapping and Detrapping Transition States of Atomic Hydrogen in Octasilsesquioxane Using the Density Functional Theory B3lyp Method. *Journal of Physical Chemistry A* **2000**, *104* (46), 10868-10872.

CHAPTER 5

OTHER PHOTOVOLTAIC MATERIALS: ENERGY MIGRATION IN DENDRITIC OLIGOTHIOPHENE- PERYLENE BISIMIDES

The work in this chapter was published at the following journal:

“Energy Migration in Dendritic Oligothiophene-Perylene Bisimides” Jin Zhang, Guda Ramakrishna, Markus K. R. Fischer, Peter Bäuerle and Theodore Goodson III, *The Journal of Physical Chemistry B*, 2013, 117, 4204–4215

Abstract:

A series of novel oligothiophene-peryene bisimide hybrid (DOTPBI) dendrimers up to the second generation (G0, G1, and G2) were investigated. Optical measurements such as nonlinear optical and time-resolved spectroscopy, including two-photon absorption, fluorescence upconversion, and excited state transient absorption were carried out. Results of these measurements revealed the ability of these molecules to undergo intramolecular fluorescence resonance energy transfer (FRET) from the dendritic oligothiophenes (DOT) to the perylene bisimide (PBI) moiety. The delocalization length and the photoinduced electron transfer (PET) were investigated as a function of dendrimer generation. A fast energy transfer process from the DOT dendron to the PBI core was observed. For the case of the G2 dendrimer, with relatively large thiophene dendrons attached to the bay area of the perylene bisimide, the PBI core is highly twisted and its ability to self-assemble into π - π stacked aggregates is destroyed. As a result,

among the three generations studied, G1, which has the best two-photon cross section and the most efficient energy transfer, is the best light harvesting material.

5.1 Introduction

Organic conjugated dendrimers are a class of materials with shape-persistent and defined, monodisperse structures that are highly reproducible.¹⁻³ These macromolecules, which have excellent optical and electrical properties, have been a focus of research for several years as they have tremendous potential applications in photovoltaic devices,⁴⁻⁵ light harvesting⁶⁻⁹ and organic electronics.¹⁰⁻¹¹ They have also shown enhanced nonlinear optical (NLO) and two photon absorption (TPA) properties.¹²⁻¹³ The geometry of dendrimers suggest a three dimensional order which might give rise to better overlap for energy transfer. Other structures have demonstrated this property as well. For example, several silsesquioxane (SQs) derivatives with perfect cubic symmetry, as well as corner and half partial SQs cages have been synthesized and their two photon cross sections have been measured.¹⁴⁻¹⁵ These results imply that the possible demonstration of three dimensional (3-D) conjugations through the core and the 3-D interaction in the excited state allows for their application as molecular transistors.¹⁴⁻¹⁵ Other geometries of organic conjugated macromolecules have gained tremendous interest and their non-linear optical properties have been studied. This includes branched chromophores,¹⁶ prion peptide nanostructures,¹⁷ porphyrin macrocycles¹⁸ and cyclothiophenes.¹⁹⁻²⁷ Among the different macromolecules investigated for enhanced NLO and TPA properties, both perylene bisimides and thiophene dendrimers have gained intense interests for their promising potential in organic electronic device application.²⁰⁻²¹

Perylene bisimide dyes (PBIs) have been developed in the past few years and are now one of the most useful classes of fluorescence materials.²³ PBI dyes exhibit exceptional water solubility, thermal stability, fluorescence intensity and photochemical stability with high fluorescence quantum yields up to 0.99.²² Perylene imide derivatives

are widely used as the electron acceptor component in the photoinduced energy and electron transfer effects.²⁴⁻²⁶ They can be easily functionalized both at the imide and at the bay area to achieve the desired optical and electrochemical properties by various chemical modifications, usually with different substituents. Due to the fully planar π -system shape, PBI are easily self-assembled into π - π stacking supramolecular architecture, as aggregates.²⁷⁻²⁹ Because of their strong delocalization and efficient charge hopping character, PBIs and other perylene imide derivatives have been suggested as candidates for organic electronics,³⁰⁻³³ with great potential for applications in light-harvesting systems,³⁴ solar cells³⁵ and field effect transistors.³⁶ PBIs have served as promising n-type organic semiconductor materials with measured remarkable electron mobilities.³⁷

Thiophene dendrimers or dendritic oligothiophenes (DOTs) have also drawn attention because of their versatile applications in organic light emitting diodes (OLEDs),³⁸⁻³⁹ light harvesting devices,⁴⁰⁻⁴¹ sensor materials,⁴² and field-effect transistors (FETs).⁴³⁻⁴⁷ Thiophene dendrimers with a highly branched three-dimensional architecture were first synthesized by Advincula *et al.*⁴⁸ Thiophene-based oligomers have been extensively studied theoretically and experimentally, both for applications such as light-emitting diodes.⁴⁹ Baeuerle *et al.*¹ developed a new class of large 3D-dendritic oligothiophenes that can be further functionalized at the periphery with other functional groups and easily attached to cores with three dimensional geometry and promising optoelectronic properties. Another series of functionalized 3D oligothiophene dendrimers have been synthesized by Baeuerle,⁵⁰ and Goodson *et al.*²¹ reported their time-resolved fluorescence upconversion and transient absorption properties. As these novel semiconducting macromolecules are monodispersed, they offer the significant advantage of reproducibility and unique photochemical properties, which is particularly important for organic electronic devices. The time-resolved spectra of oligothiophenes in solution have also been studied by several groups. Pfeffer *et al.*⁵¹ first observed the excited state absorption (ESA) and triplet absorption signal of terthiophenes using picosecond photoinduced absorption measurements. Lap *et al.*⁵² reported time dynamics of oligothiophenes using femtosecond time-resolved spectroscopy. Lanzani *et al.*⁵³ studied

the spectral-dynamic effect of ring rotation of the singlet excited state in oligothiophene derivatives. Unlike PBIs, thiophene dendrimers serve as p-type organic semiconductors.

Recently, a perylene-oligothiophene hybrid as a π -donor- π -acceptor system has been synthesized and studied by Baeuerle *et al.*⁵⁴ Both DOTs and PBIs are rigid and shape-persistent. As rigid and shape-persistent conjugated dendrimers, these materials represent a novel class of macromolecular materials with defined and monodispersed structures that are highly controllable due to precise synthetic approaches.⁴⁵ Because of their three dimensional structures consisting of a core and shell, these dendrimers possess numerous advantages compared to conventional polymers in offering a number of functionalization schemes. For example, functionalization of the exterior of the dendrimer has been shown to be a promising strategy for sensing applications,⁵⁵ while functionalization of the interior of the dendrimer has led to various applications in spectroscopy.⁵⁶ It will be very interesting to investigate the energy transfer process of the dendritic thiophene-peryene bisimides as donor-bridge-acceptor type supermolecules with different functional groups as the core and shell separately.

In this work, in order to understand and measure the extent of energy migration process, the two photon absorption cross section, fluorescence upconversion and excited state dynamics of a thiophene functioned perylene bisimide system up to the second generation (G0 to G2) have been investigated. The structures of these materials are shown in Figure 5.1. The TPA cross section in the near IR regions was measured. The fast energy transfer processes from dendron to core and from dendron to dendron are found. The results suggest the ultrafast energy migration in these systems is really efficient. With strong π - π stacking ability, perylene bisimide is excellent for energy trapping purpose. However, in the higher generation as G2, the tendency of H-aggregation is disrupted due to the highly twisted PBI core. As a result, G2 shows a larger possibility of energy delocalization between the DOT dendrons, lower quantum yield, lower two-photon cross section and lower energy transfer efficiency than G1. With a smaller size dendron, G1 is the best electron transfer material among those three systems.

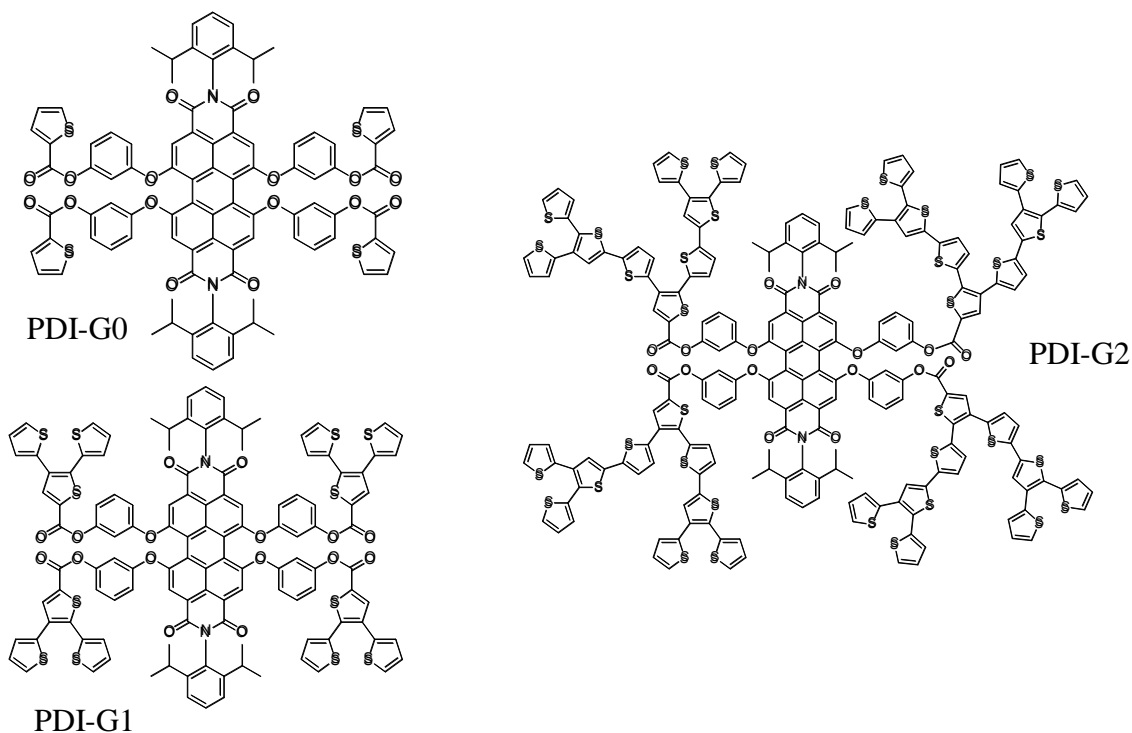


Figure 5.1 Molecular structure of investigated thiophene dendrimer functionalized perylene imides (PDI-G0, PDI-G1 and PDI-G2)

5.2 Results and Discussion

To investigate the optical properties of these oligothiophene-perylene bisimide, several spectroscopic measurements have been carried out, including steady state absorption and emission, two-photon excited fluorescence measurements, fluorescence upconversion dynamics and femtosecond transient absorption measurements. The synthesis of investigated dendritic oligothiophene-perylene bisimides DOTPBI-G0 (G0), DOTPBI-G1 (G1) and DOTPBI-G2 (G2) has been achieved by Baeuerle *et al.*, and the synthesis procedure was described previously.⁵⁵ All the measurements were carried out in dichloromethane (DCM) (Sigma-Aldrich, spectrophotometric grade). All compounds were used as received without any further purification.

5.2.1. Steady State Photophysical Properties

The measured optical absorption, fluorescence spectra and extinction coefficient spectra of the investigated systems dissolved in DCM solvent are shown in Figure 5.2. A summary of the corresponding steady state properties is shown in Table 5.1. Comparing these results with the absorption and emission spectra of thiophene dendrons²¹ and perylene bisimides,^{34, 57} the absorption spectra show the features of each moiety in the systems. The result is very clear that the absorption features can be assigned to four regions: below 300nm, 300nm-400nm, 400nm-500nm and 500nm-600nm. The absorption features below 300nm in all of these systems represent the π -to- π^* transition of pure monothiophene units. The absorption features from 300nm to 400nm are the π -to- π^* transition of dendritic thiophene units, and the intensity of these features increases with increasing the number of thiophene groups. The absorption region from 400nm to 500nm represents the S_0 to S_2 electronic transition caused by the dipole moment perpendicular to the long perylene axis. The absorption region from 500nm to 600nm is assigned to the S_0 to S_1 electronic transition caused by the dipole moment parallel to the long perylene axis. The absorption region from 500nm to 600nm is slightly blue shifted from 563nm (for both G0 and G1) to 558nm (G2). This small change may indicate a small change in the transition dipole moment and less conjugation character possibly as a result of twisting, but the relative sensitivity is not reliable to make a conclusion from steady state absorption alone. Ultrafast techniques or nonlinear optical techniques which are more sensitive can be used to investigate the conformational change of the perylene core.

The extinction coefficient values at different wavelengths are also shown in Table 4.1. These values in the 300nm-400nm region are dramatically increased by increasing the number of thiophenes. As expected, in 300nm-400nm region, the molar extinction coefficient of G2 is about 3 times higher than the G1, because the number of thiophene in G2 (36) is also three times more than in the G1 (12). The extinction coefficient values between 550 and 600 nm are almost the same.

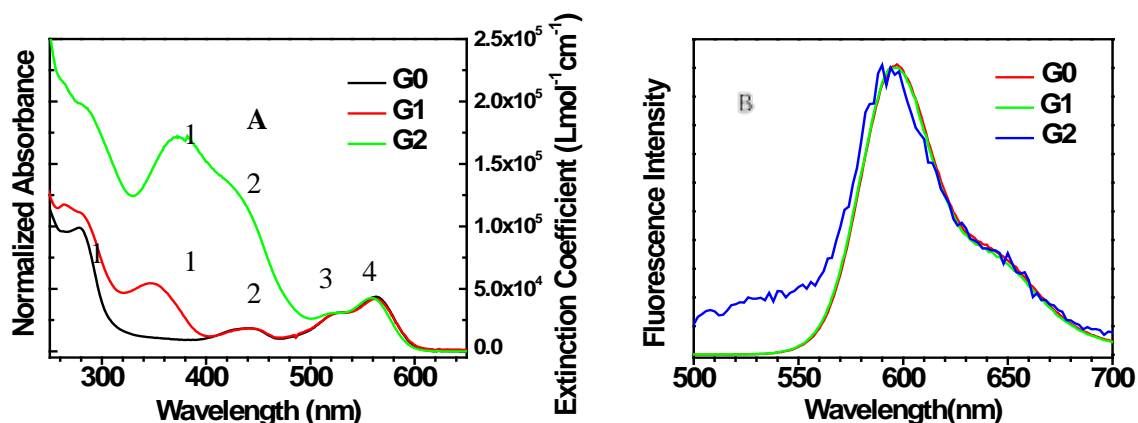


Figure 5.2 (A) Normalized optical absorption and extinction coefficient and (B) normalized steady-state fluorescence spectra of the investigated derivatives of G0, G1 and G2

Due to the charge transfer from the thiophene dendrons to the perylene, the absorption of the perylene in the 400nm-600nm region shows about a 13nm significant red shift in comparison to the (mono) PBIs. The fluorescence emission was excited at several different wavelengths for each compound, which gave very similar emission spectra. In the emission spectra, the peaks at 600nm with a shoulder at 640nm are observed as the mirror images of the longest wavelength perylene bisimides bands.³⁴ G2 has a broad shoulder on the left shoulder side of the emission peak, which is due to the residue of the insufficient charge transfer character from the DOT donor to PBI acceptor.

The quantum yield was measured at the wavelength of 495nm following a known procedure.⁵⁸ Rhodamine 6G was used as reference ($\Phi_f=0.93$ in MeOH). The fluorescence quantum yield of PBIs is reported as 0.99.⁵⁹ The reported fluorescence quantum yield for pure thiophene dendrons are as low as 0.02.²¹ The quantum yield of these three systems decreases significantly with increasing generation. The quantum yield of G2 is 0.004, which is much lower than G0 (0.53) and G1 (0.38). This is because, when

the larger thiophene dendrons are attached, the PBI core of G2 is highly twisted. The relatively bulky thiophene dendrons are highly overlapped and possibly self-quench the emission. As a result, the probability of energy delocalization throughout the entire thiophene dendrons of G2 is highly increased.

The extent of resonant energy transfer (E) is calculated using a known procedure.⁵⁹⁻⁶⁰ Results are noted in Table 5.1. In this calculation, the four thiophenes in G0 were neglected, and G0 was used as an acceptor without a donor group. The oligothiophene dendrimers we investigated previously were used as donor without acceptor.²¹ The resulting energy transfer efficiency is as high as 69% for G1 and 46% for G2. The efficiency results indicate the energy transfer process from DOT to PBI is more efficiently founded in the G1 system, and it corresponds well with the quantum yield results. In general, the steady-state absorption and emission results suggest the energy transfer from the PBI to DOT moieties. The energy transfer process in G2 is inefficient. Time-resolved nonlinear optical measurements were carried out to give a better understanding of the transition and mechanism of these systems.

Table 5.1 Steady-state properties of investigated dendrimer functionalized perylene bisimides.

Sample	$\lambda_{\text{abs}}(\text{nm})$	$\lambda_{\text{em}}(\text{nm})$	Φ_{f}^*	E(%)	Extinction Coefficient ($\text{Lmol}^{-1}\text{cm}^{-1}$) at different wavelengths	
G0	293(1),440(2),525(3),563(4)	597,645	0.53	~	N.A.	4.1×10^4 (563nm)
G1	347(1),440(2),525(3),563(4)	596,645	0.38	69	5.4×10^4 (347nm)	4.1×10^4 (563nm)
G2	374(1),441(2),525(3),558(4)	596,644	0.004	46	1.7×10^5 (374nm)	4.3×10^4 (558nm)

*Quantum yield is measured at the wavelength of 495nm.

5.2.2. Two-Photon Cross-Section Measurements

The TPA cross-section as a function of wavelength has been measured for all the investigated chromophores in the units of Goepfert-Mayer (GM), where 1 GM is $10^{-50} \text{ cm}^4 \text{ s photon}^{-1}$. It is an indication of charge transfer character and interaction between chromophores. The TPA cross sections of these systems are plotted in Figure 5.3 with the respect of wavelength in the range from 720nm-980nm. The TPA cross section per molecule and the TPA cross section per thiophene unit at selected wavelengths are listed in Table 5.2. Previous studies concerning the TPA cross section of perylene bisimides derivatives have been reported.^{20, 61} The TPA cross section of most PBI derivatives is ~ 100 GM within the scanned wavelength range 840nm-970nm. The TPA cross section of DOT dendrons with up to three monothiophenes has been reported.²¹ They range from ~6 up to ~150GM. A super linear relationship between the number of thiophene and the two-photon cross section was also found. This suggests a substantial increase in cross section with number of thiophene dendrons, and thus, it is expected that G2 would have a higher TPA cross section than G1. However this is not the case for our systems noted from Figure 5.3. When looking at the TPA cross section values between 700 and 780 nm, G1, with less thiophene on each dendron, has a higher TPA cross section than G2. This is due to less charge transfer character caused by the twisted perylene core of G2. The cross section “per branch” in these systems is not enhanced by the additional chromophores in the case of all compounds. In the higher generation, the twisted PBI core destroyed the charge correlation length from the external DOT dendron to the internal core. The TPA cross section at excitation of 1300nm has also been investigated. G1 shows a cross section of 16GM at 1300nm while two-photon absorption cross section is not detectable for G0 and G1 at this wavelength.

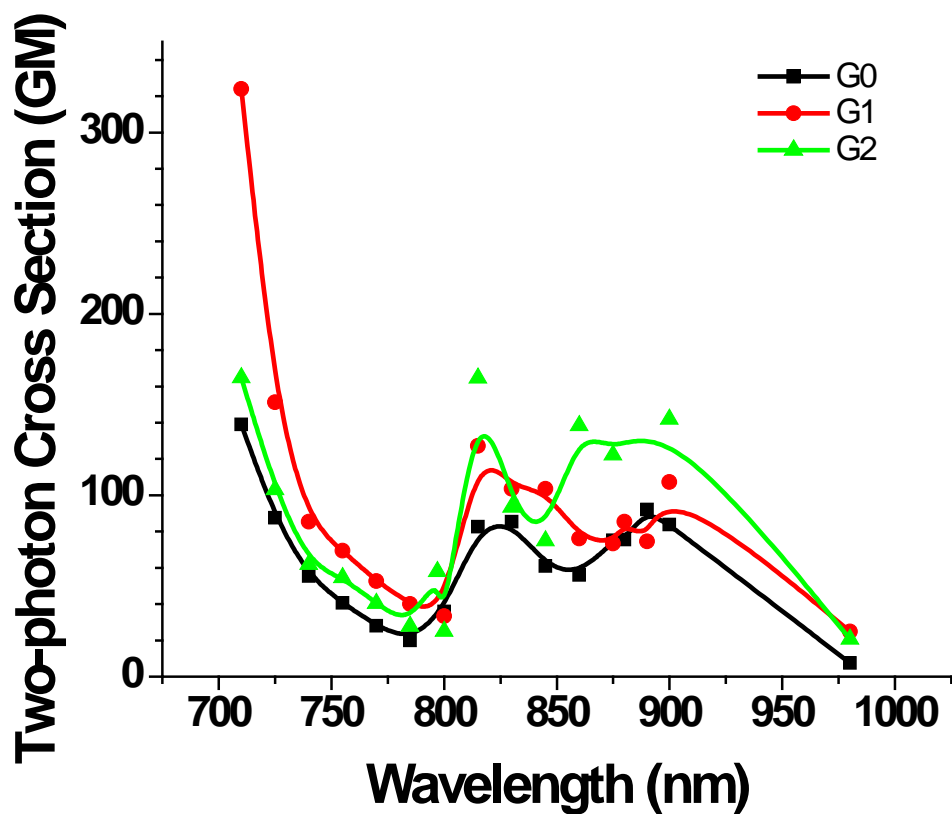


Figure 5.3 The two-photon absorption cross section for thiophene dendrimer functionalized perylene bisimides.

Table 5.2 TPA properties of silsesquioxane derivatives

Sample	$\lambda_{ex}=720\text{nm}$		$\lambda_{ex}=890\text{nm}$	
	δ (GM)	$\delta/\text{Thiophene}$ (GM)	δ (GM)	$\delta/\text{Thiophene}$ (GM)
G0	129	32	24	6
G1	324	27	43	4
G2	165	5	51	1

5.2.3. Fluorescence Up-Conversion Measurements

Time-resolved fluorescence measurements of the excited and relaxed states are used to investigate the conformational and electronic changes in these systems. Here, we are interested in the variation of fluorescence lifetime and anisotropy decay with excitation of different parts of the macromolecule by using different excitation wavelengths. This is a measurement of the energy transfer process, as well as the extent of the delocalization of the system. The fluorescence decay curve of the chromophores excited at different wavelengths, 420, 266 and 377nm are shown in Figure 5.4, Figure 5.6 and Figure 5.7 respectively. The fluorescence detection wavelength is 590nm. The lifetime results are listed in Table 5.3.

Table 5.3 Fluorescence lifetime of G0, G1 and G2 at different excitation wavelengths

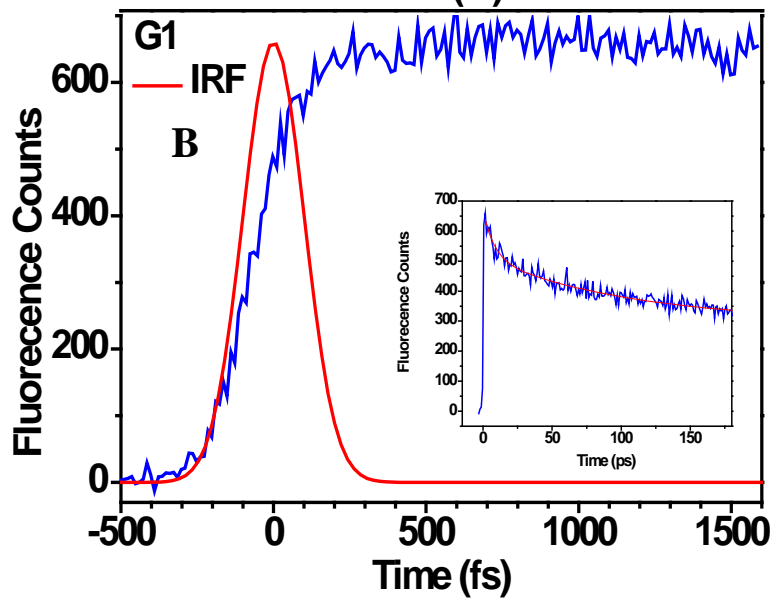
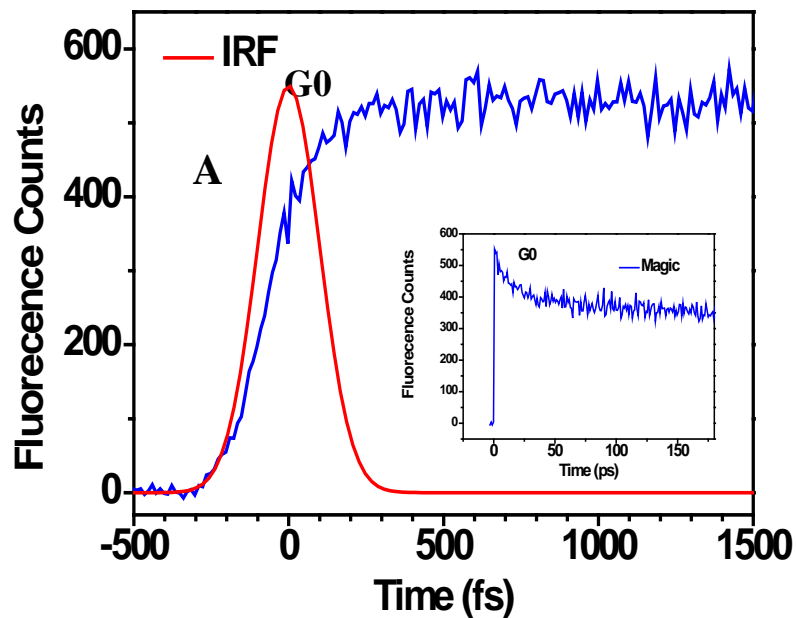
	Excitation Wavelength	Lifetime
G0	420nm	200fs, 24ps, 4.5ns
G1	420nm	255fs, 7.4ps, 95ps, 4.5ns
G2	420nm	200fs, 13ps, 66ps
G2	377nm	140fs, 5ps, 23ps, 425ps
G0	266nm	6.4ps, 61ps
G1	266nm	650fs, 45ps, 1ns
G2	266nm	14ps, 115ps

Shown in Figure 5.4 is fluorescence upconversion decay curve with an excitation at 420nm. The short time scale fluorescence decay of G0, G1 and G2 with the instrument response function is shown in Figure 5.4A, B and C, with the long time scale inserted respectively. The fluorescence anisotropy is shown in Figure 5.4D. In the case of G0 and G1, the systems are excited in the absorption band that is S_0 - S_2 electronic transition of perylene, where the dipole moment is perpendicular to the long perylene axis. As reported, the fluorescence lifetime of the singlet excited-state of the PDIs is 4.5ns.⁶² Under this excitation, the G0 and G1 both show a long-lived lifetime of 4.5ns. This result corresponds well with the reported fluorescence lifetime of perylene. G2, however, has a much shorter lifetime of 66ps which is much shorter than the typical fluorescence

lifetime of perylene. This discrepancy in the lifetime of G2 is due to the red shift of dendritic thiophene band which is overlapped with the S_0 - S_2 electronic transition of perylene core. In addition, the excitation is delocalized throughout the entire G2 molecule. The rise times after deconvolution are 200fs for G0, 255fs for G1 and 200fs for G2. The rise times of G0 and G1 imply the internal conversion of the perylene core. In the case of G2, the existence of fast rise time indicates that the energy has been transferred from the thiophene dendrons to the perylene core.

The fluorescence anisotropy curves are shown in Figure 5.4(D). It should be noted that, under this excitation wavelength, G0 and G1 have an interesting negative anisotropy while G2 shows a positive one. In order to dispel the possibility of aggregation, the steady state absorption and emission results are compared with those of known PBI monomer and π -stacked PBI.⁵⁷ Our results follow the trend of PBI monomer very well. Negative anisotropy of perylene with anisotropic rotation has been widely studied.⁶³ Under this excitation, the absorption and emission transition moments of perylene are nearly perpendicular to each other and the anisotropy at time zero is also reported as -0.14. As a nonspherical and disk-like molecule, perylene has different rotational rates around each axis. The in-plane rotation is much faster than the out-of-plane rotation, because out-of-plane motion requires displacement of solvent molecules. This explains the negative anisotropy of G0 and G1. Unlike planar PBI, G2 behaves as a spherical molecule and it gives rise to the positive sign of the anisotropy with decay. From the concern of conformational change, it also notes that with the introduction of a large bay substituent, such as DOT dendrons with 9 thiophene units, the center core in G2 is not as planar or disk-like. This is shown in Figure 5.5. This perylene bisimide core in G2 is highly twisted. The degree of the twist is dependent on the apparent overlap parameter of the bay substituents.⁶⁴ The dihedral angle is also reported to meet the situated value as 37° with dibromo-substituted PBI. These large dendritic thiophenes at the bay positions can cause core-twisted perylene bisimides. This discrepancy is due not only to the nonplanar geometry but also to excitation delocalization. By studying the fluorescence upconversion experiment under this wavelength, we can conclude that both DOT dendrons and PBI core are mainly isolated in the case G0 and G1. While in the case of

G2, it behaves quite different not only due to the interaction between those branches, but also the conformational change. Both shortening of lifetime (66ps) and the different sign of anisotropy decay suggests that, in the case of G2, the excitation is delocalized up to the thiophene dendrons.



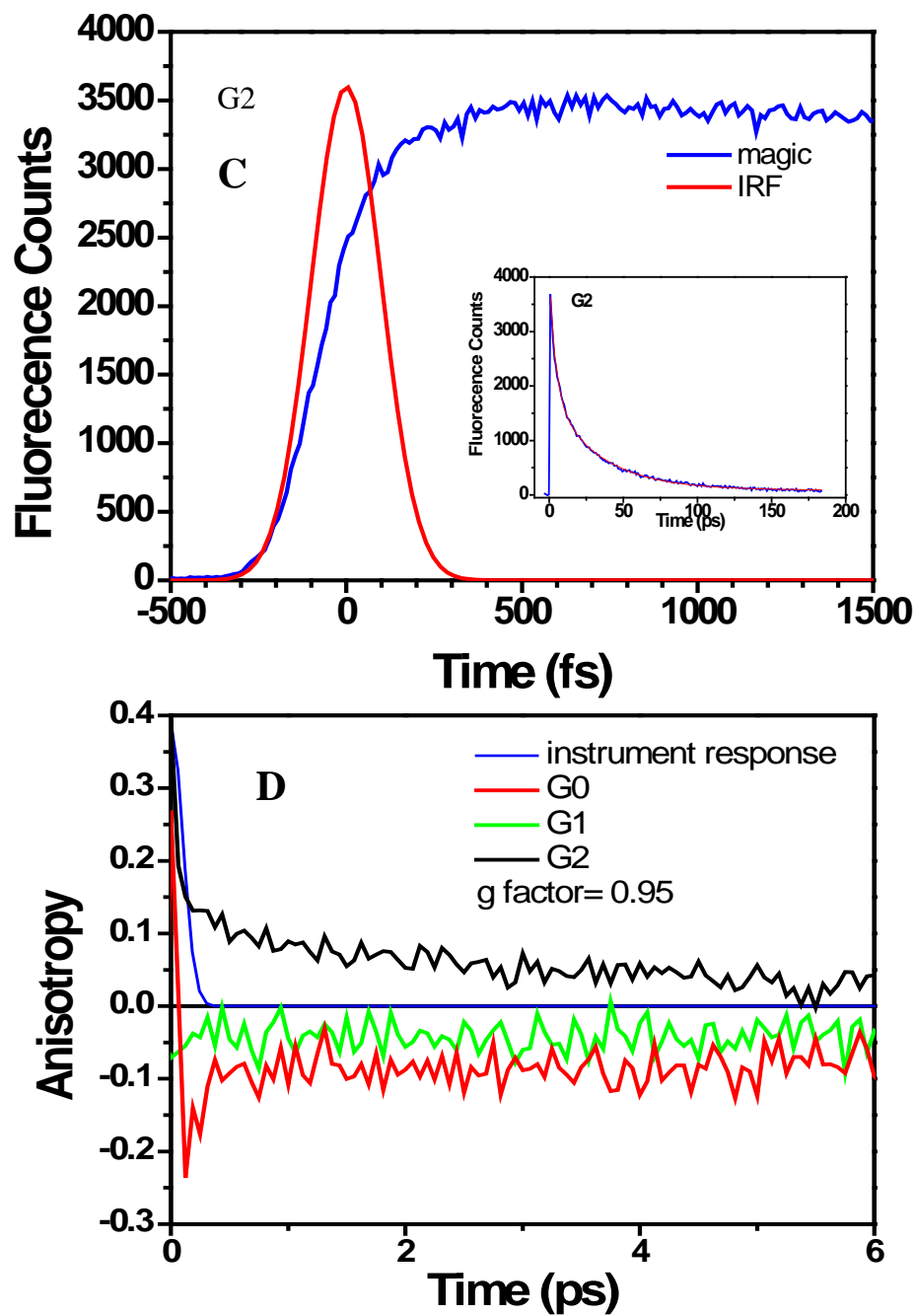


Figure 5.4 (A)G0 ,(B)G1 and (C)G2 fluorescence of different time scale with an excitation at 420nm, and (D)fluorecence anisotropy for G0, G1 and G2

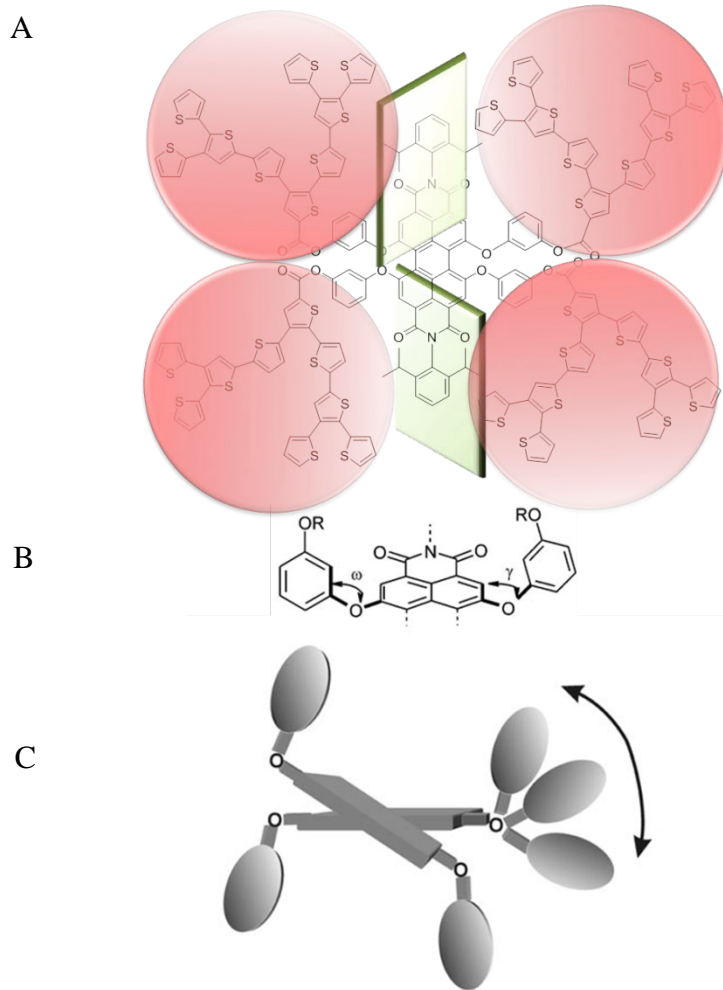
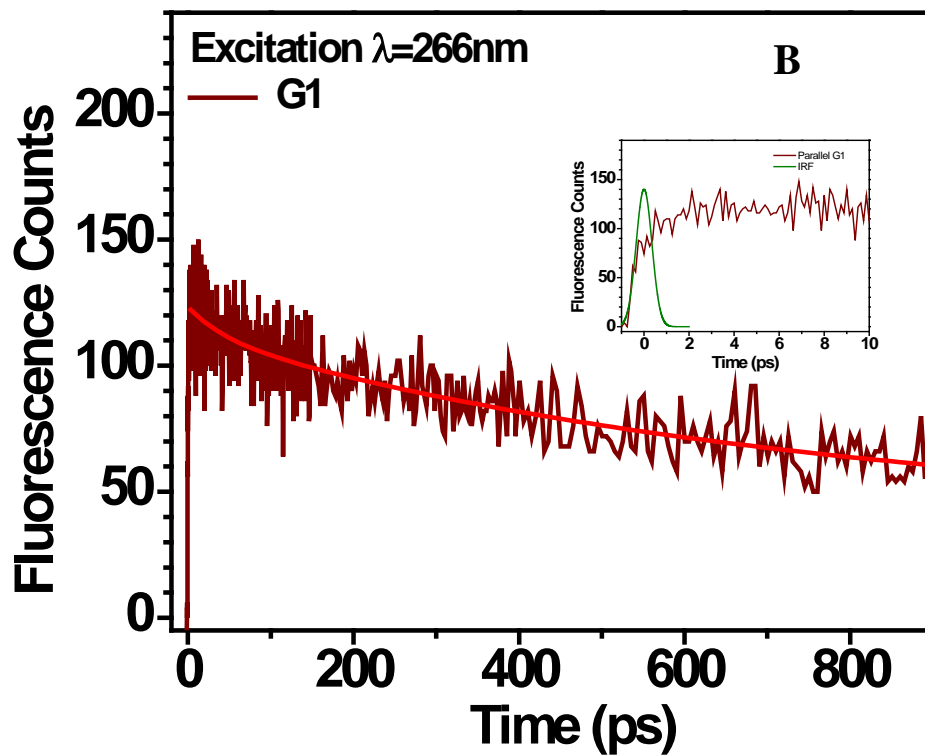
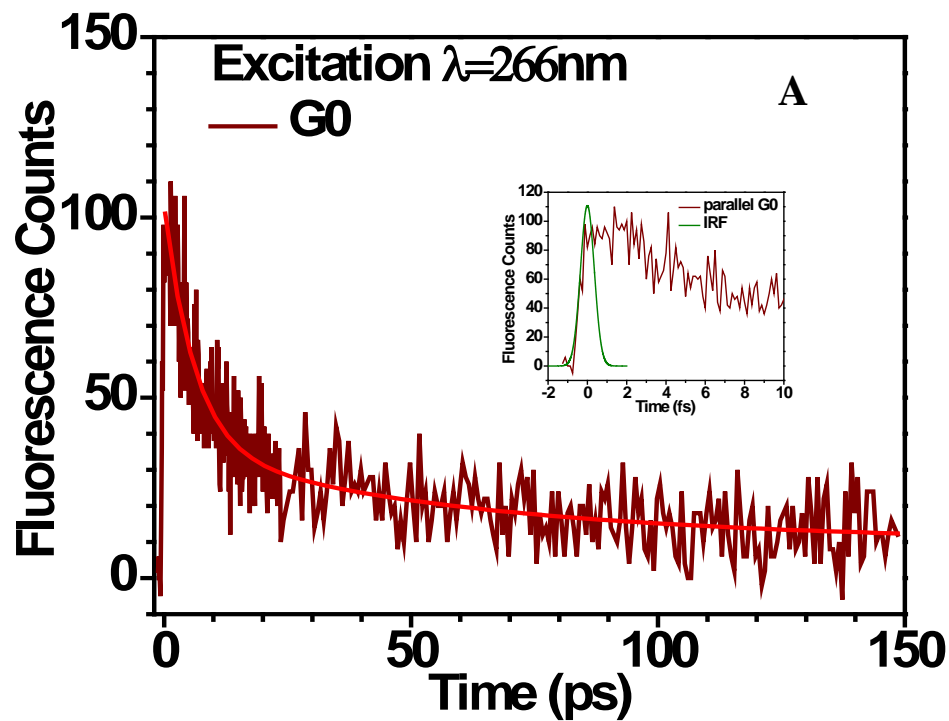


Figure 5.5 (A) Planar shape areas marked in G2, (B) Illustration the angle between the PDI and DOT and (C) Illustration of the twisting of the PDI

Figure 5.6 shows the fluorescence anisotropy and fluorescence decay curve with an excitation of 266nm. The long time scale fluorescence decay of G0, G1 and G2 are shown in Figure 5.6A, B and C with the short time scale figure inserted, respectively. Under this excitation, the systems are excited in the thiophene absorption band. The lifetime of G0 and G2 are 61ps and 115ps respectively, while the lifetime of G1 is in nanosecond which is much longer. As shown in Figure 5.6B, G1 shows a rise time of

650fs, while as shown in Figure 5.6A and C, G0 and G2 do not have a rise time. It may be because the rise time is faster than the FWHM of the instrument response function. It is also noted that in Figure 5.6D, the fluorescence anisotropy of G0 and G2 shows decay from 0.4 to 0, while G1 has a steady anisotropy value of 0. This result indicates that after the excitation, in the case of G0 and G2, the energy is highly delocalized throughout the entire molecule. In addition, dipole moments of G0 and G2 molecules are more likely randomly orientated at time zero, and then depolarization goes with time within 30ps. The results of G1, such as extreme long lifetime, localized excitation, and rise time of fluorescence intensity give the conclusion that the thiophene dendrons and perylene bisimides behave like individual molecules. In the case of G1, the energy is transferred from thiophene to the perylene and then localized at the perylene core which gives the long-lived fluorescence. These results may indicate that G1 is the most suitable one for bulk-heterojunction solar cells among these three materials.



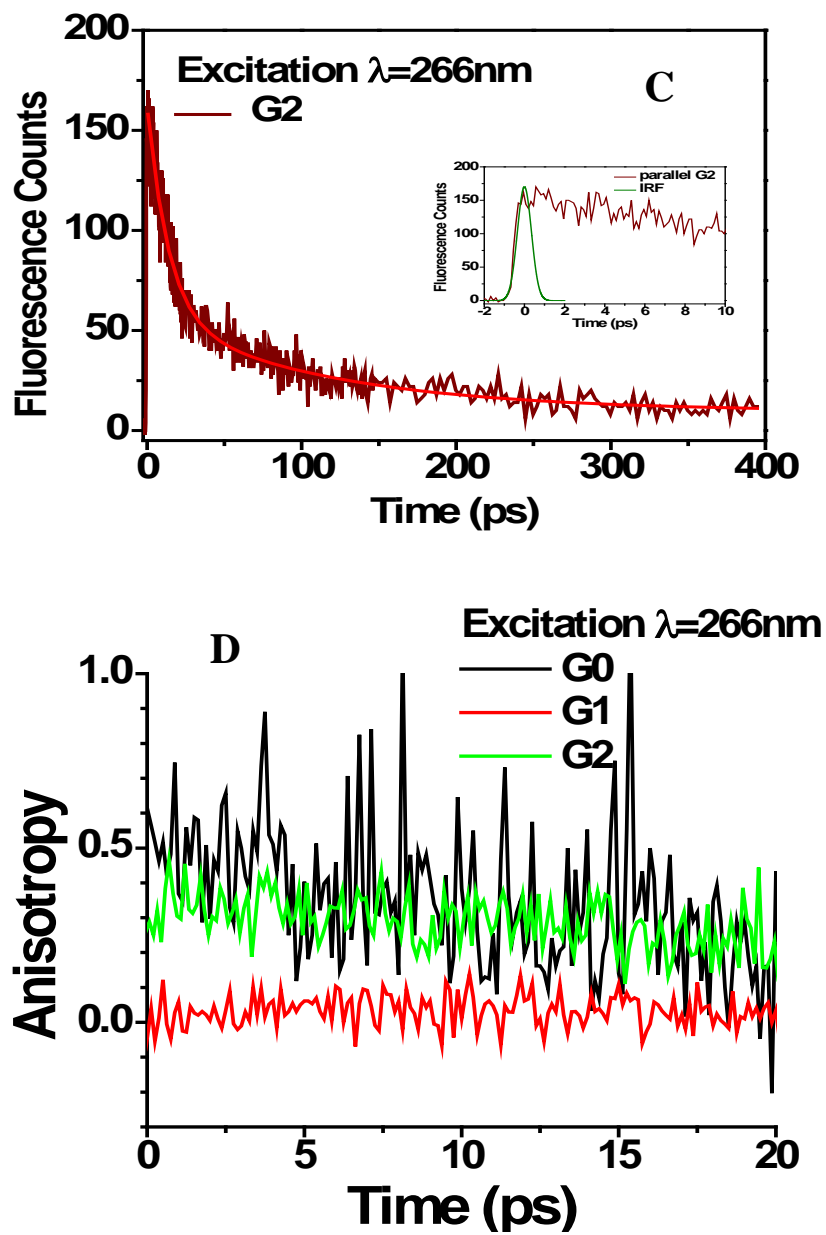


Figure 5.6 (A)G0, (B)G1 and (C)G2 fluorescence of different time scale with an excitation of 266nm and (D) fluorescence anisotropy for G0, G1 and G2

To see the excitation wavelength dependence of the G2 dendrimer, fluorescence upconversion at excitation of 377nm was also carried out. Shown in Figure 5.7A and B is the fluorescence decay and anisotropy, respectively. Under this wavelength, we are mainly exciting the thiophene dendrons. It is very interesting to observe that both the rise time (140fs) and the lifetime (425ps) of G2 are longer than the case of under excitation of 266nm. It is observed that the time-zero anisotropy is 0.06 instead of 0.4, in the case of 266nm excitation. This result suggests the degree of delocalization of G2 depends on the excitation wavelength or the incident photon energy. Numerous similar dynamical processes involving the interaction of excitons with donor and acceptor have been investigated by *Barbara et al.*⁶⁵⁻⁷¹ Figure 5.8 shows an illustration of the energy transfer in the G2 system. Both processes from the DOT to PBI and from DOT to DOT are observed. Charge transfer character is investigated by using ultrafast transient spectroscopy.

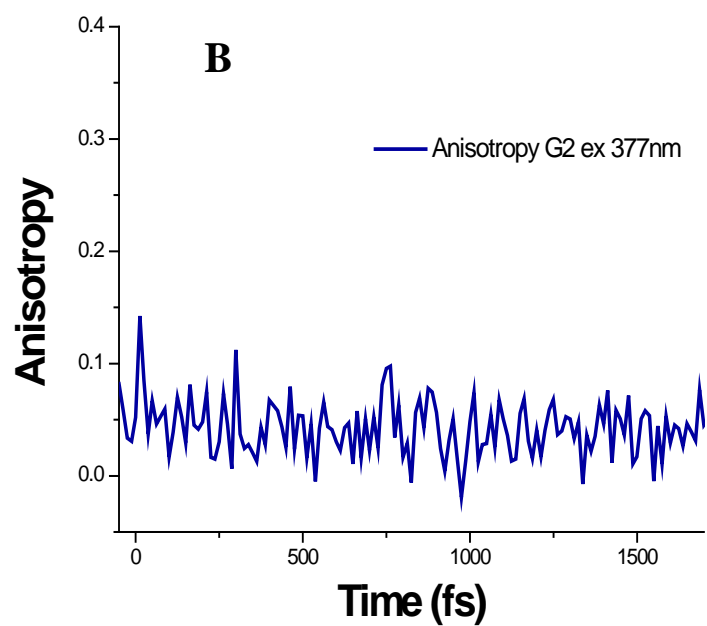
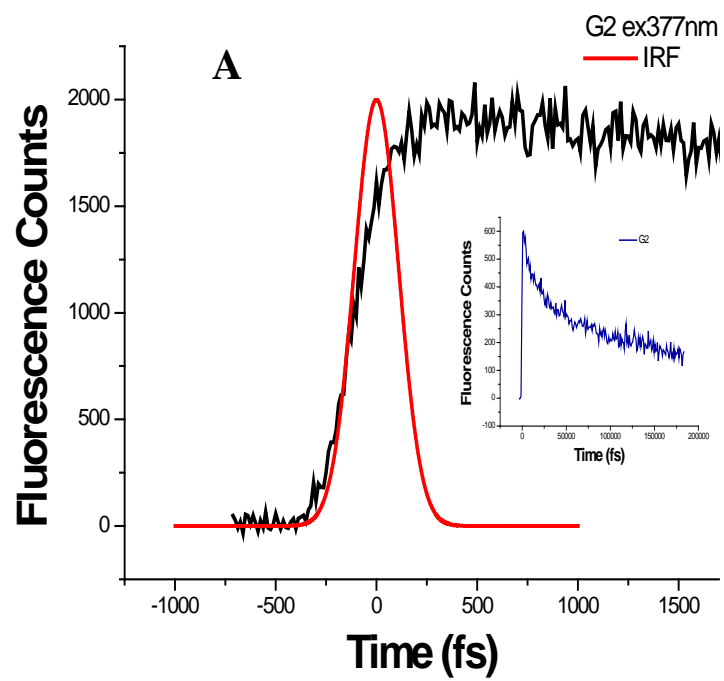


Figure 5.7 (A) Fluorescence intensity of G2 and (B) anisotropy of G2 at excitation of 377nm

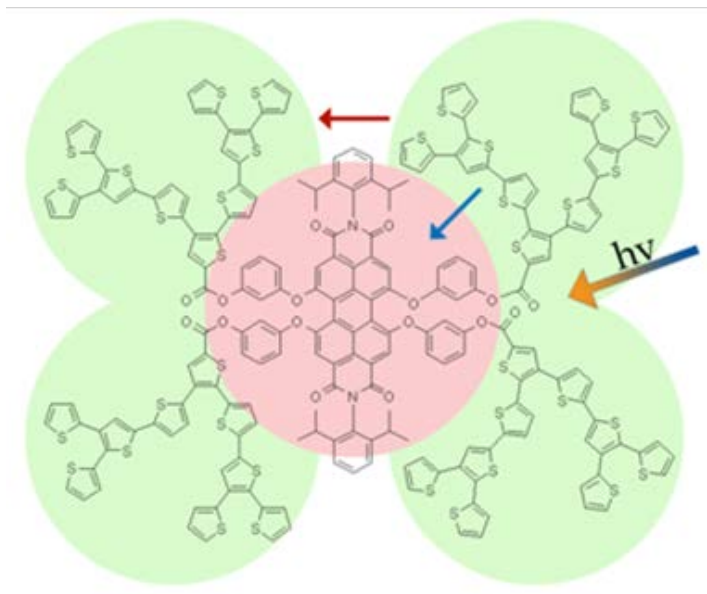


Figure 5.8 Illustration of energy transfer process in G2

5.2.4. Transient Absorption Measurements

Femtosecond transient absorption measurements have been carried out in order to understand the fundamental mechanisms of intramolecular excitation. These measurements probe the photoinduced energy and electron transfer processes and may confirm the participation of electron-transfer process from DOTs to PBIs in dendritic oligothiophene-phenylene bisimides. The transient absorption spectra of G0, G1, and G2 in dichloromethane under an excitation at 550nm are shown in Figure 5.9, Figure 5.10 and Figure 5.11, respectively, with the three dimensional transient absorption spectra and kinetic dynamics. There are several previous studies concerning femtosecond transient absorption measurement of PBIs reported in the literature.^{34, 48, 57, 72} Wasielewski *et al.* have studied versatile perylene derivatives using ultrafast pump-probe transient absorption.⁷³⁻⁷⁹ In the previous study, the transient absorption spectra with ground state bleaching bands from 400nm to 600nm and an excited state absorption band from 600nm

to 800nm have been obtained.⁵⁷ We compared our results with model PBI⁷⁰ (compound PDI0, N,N'-diphenyl-1,6,7,12-tetrakis[4-(1,1,3,3-tetramethylbutyl) phenoxy] perylene-3,4,9,10-tetracarboxdiimide), in which no electron donating group attached to perylene moiety, and thus no electron transfer process is expected in this molecule. This model compound exhibited a broad excited state absorption band at the wavelength above 680nm, as well as a ground state depletion overlapped with the stimulated emission centered at ~580nm. The transient absorption of the model PDI shows monoexponential decay at the wavelength about 700nm, with a lifetime around 5ns. The excited state absorption spectra of G0, G1 and G2 are shown in Figure 5.9A, Figure 5.10A and Figure 5.11A, B and C, with 3D excited state absorption spectra inserted. Compared with the model compound, all the three dendrimers result in a bleaching of the ground state absorption bands from 500 to 550nm, accompanied by a strong stimulated emission feature in the 550-600nm range. This ground state bleaching corresponds well to singlet-to-singlet transition of the perylene bisimides. As shown in Figure 5.9A and Figure 5.10A, both G0 and G1 show excited state absorption bands from 660 to 800nm. The intensity of the ESA bands of G0 and G1 rise initially and then decay quickly within a few picoseconds. Following this, the ESAs grow steadily with a long-lived lifetime. In the case of G2, which is shown in Figure 5.11A, B and C, there is an excited state absorption band in the range of 600-800nm, with blue-shifted ESA compared with G0 and G1. More interestingly, opposite to G0 and G1, the growth of ESA band of G2 is observed from 2.4 to 120ps, followed by decay from 120 to 780ps. This discrepancy can also be noted from the transient 3D spectra, shown in Figure 5.9A, Figure 5.10A and Figure 4.11A. Compared with the transient absorption features of all these three dendrimers with different generations, it looks like the G2, which has most thiophene dendrons, undergoes a different excitation mechanism. This will be discussed later in the section.

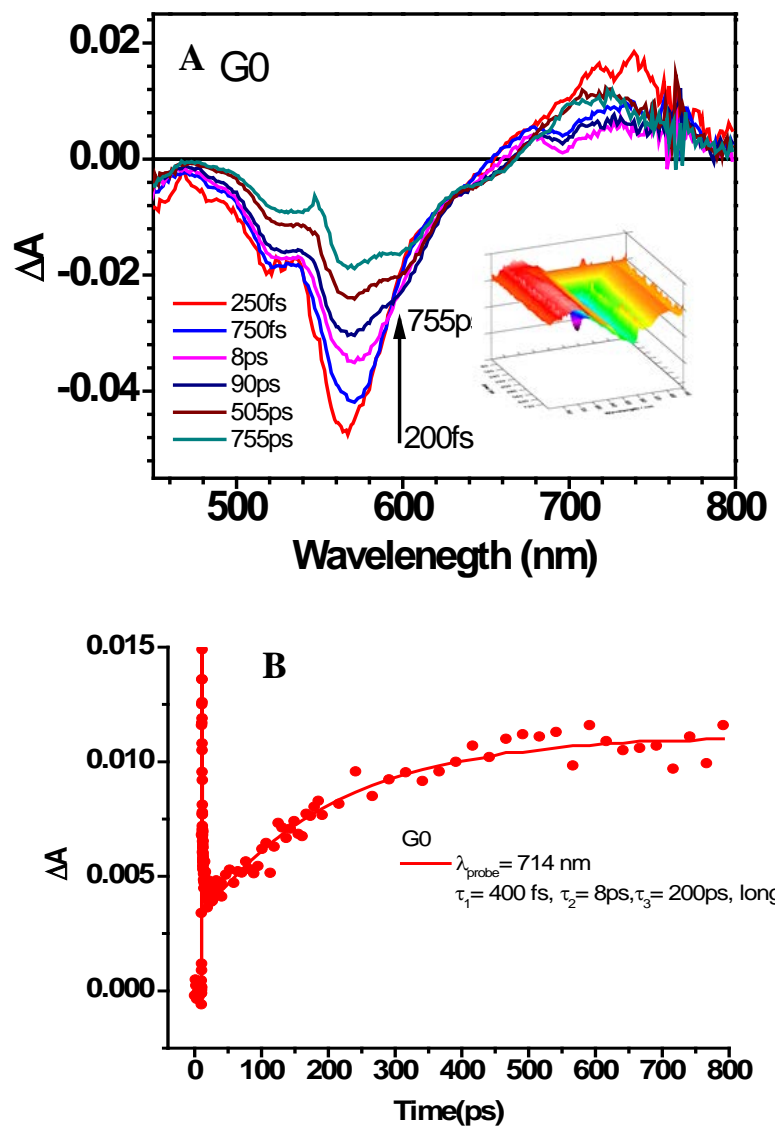


Figure 5.9 (A) Transient absorption spectra and 3-D spectrum (inserted) of compounds G0 with an excitation of 550nm. (B) Transient absorption kinetics of G0 at 714nm.

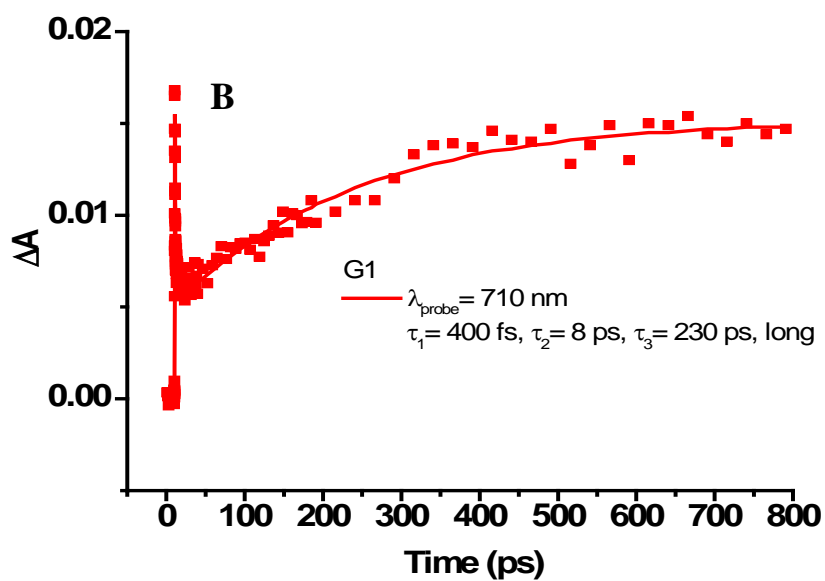
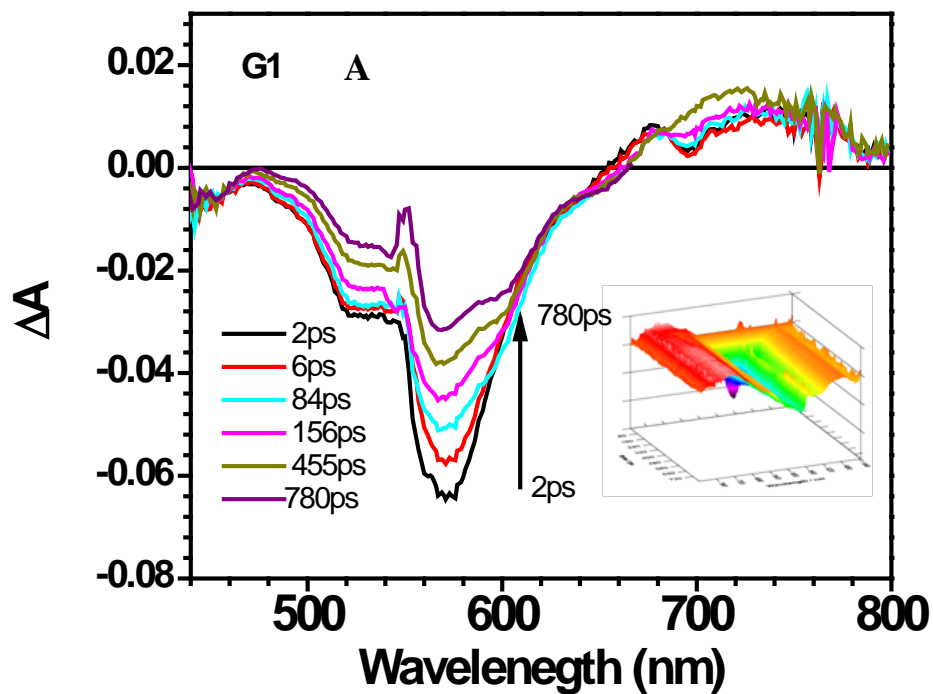


Figure 5.10 (A) Transient absorption spectra and 3-D spectrum (inserted) of compounds G1 with an excitation of 550 nm. (B) Transient absorption kinetics of G1 at 710 nm.

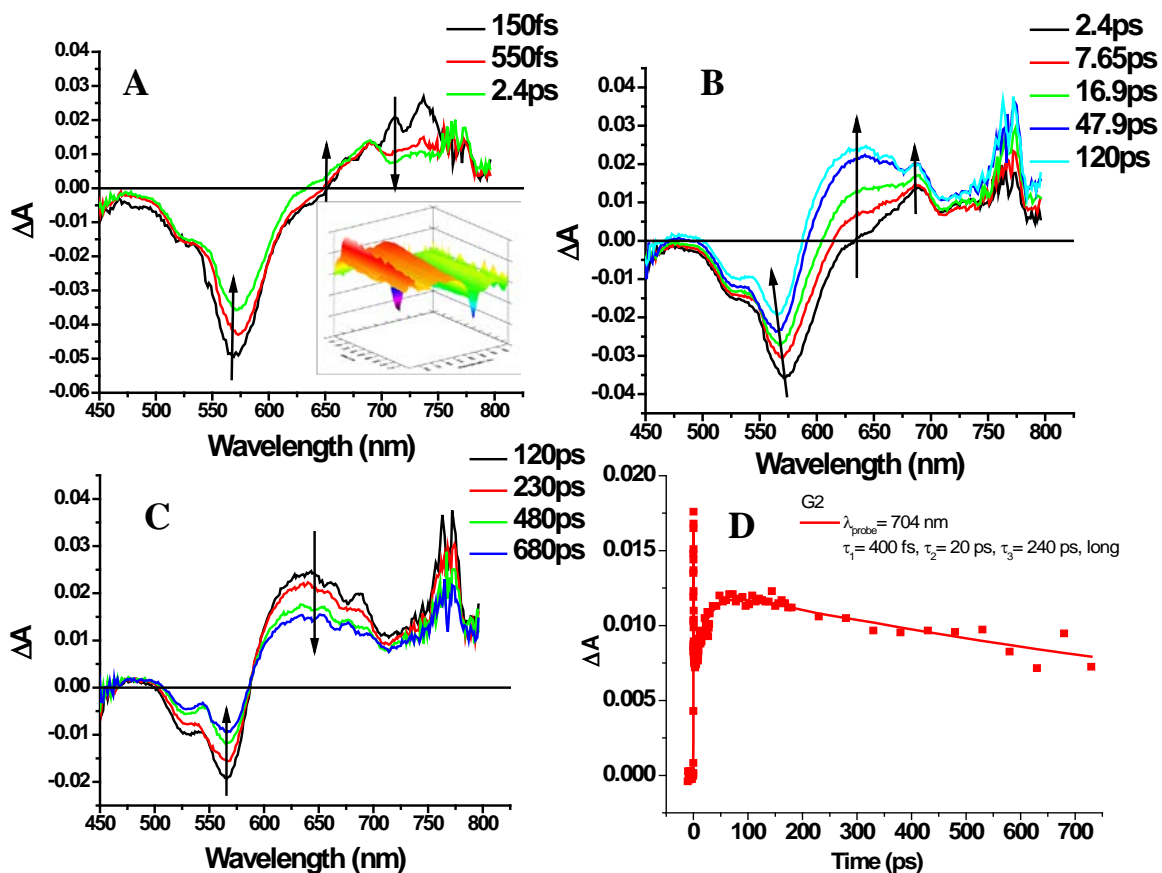


Figure 5.11 (A),(B) and (C) Transient absorption spectra of G2 of at different time. Inserted in(A) 3-D spectrum of compounds G2 with an excitation of 550nm. (D) Transient absorption kinetics of G2 at 704nm.

The dynamics of G0 and G1 systems are similar, as shown in Figure 5.9 B and Figure 5.10B. The kinetics of these two systems can be fitted with a triexponential with 400 fs, 8 ps, around 200 ps and a long time component. The lifetime of the dynamics for each system at different probe wavelength is shown in the Table 4.4. The fast component 400 fs can be attributed to the intramolecular excitation energy transfer from the delocalized state to the longest oligothiophene present in the dendron as found in the thiophene dendrimers.²¹ The other fast component $\sim 8 \text{ ps}$ can be assigned to

vibrational/solvent relaxation.^{72, 80-81} A 200 ps component is related with the absorption and formation of S_1 and the PDI radical anion. The ESA absorption above 680nm is the PDI S_1 -to- S_n absorption⁷² and the PDI radical anion absorption.⁸²⁻⁸⁴ Spectra of the ground-state bleaches did not evolve in time, indicating that the ground-state product of the photoinduced event is the same as the initial state. This also proves PDI radical anion formed after excited state excitation occurs. The absorption spectra of thiophene radical cations have been characterized, with absorption maxima at 530 nm.⁸⁵ An ESA at this wavelength caused by the formation of thiophene radical cation, is found overlapping with excited state bleaching.

The transient absorption spectra of G2, shown in Figure 5.11 A–C, give a broad excited state absorption that extends from 650 to 800 nm initially and then shifts to the blue side within 780 ps. This could indicate the charge separated state may be formed from 120 to 780 ps. As a result, the absorption from the charge separated state to the higher excited state happens after accumulation at this state. The longer time scale kinetics trace shows that the stimulated emission recovers with a time scale of 200 ps for the case of G2. The presence of a long-lived transient is observed and overlapped with the simulated emission region. This transient can be assigned to the long-lived triplet–triplet absorption. The recovery kinetics of stimulated emission is much faster than the actual single state lifetime.

G2 shows unique dynamics, which varies from what is found in G0 and G1. Considering G2 contains more thiophene than the other two systems, the transient absorption of thiophene dendrons must take into account. Several studies about the dynamics of excited states of oligothiophenes and polythiophene have been carried out using femtosecond transient absorption and time-resolved fluorescence techniques.^{51, 86} Lanzani *et al.*⁸⁶ have measured the excited state dynamics of oligothiophene and used a two-dimensional model involving vibrational relaxation and torsional relaxation to explain the two main components of the relaxation of the excited state other than the singlet state decay. Similar torsional relaxation has been found in several oligothiophenes and polythiophenes.^{51, 82, 87-90} Excited state dynamics of oligothiophene dendrons and the

coupling between the thiophenes within the dendrimer have also been investigated.²¹ The femtosecond transient absorption results have shown the excited state delocalization through the large part of thiophene dendron and ultrafast energy transfer to the longest oligothiophene in each dendritic unit. A torsional relaxation has also been observed in final emitting state. A Franck Condon (FC) state is found for the higher generation of thiophene dendrons, where delocalization happens through a large number of thiophenes in the dendrons. The excited state decays via intersystem crossing to the triplet state. In contrast with the linear oligothiophenes, the excited state dynamics of the thiophene dendrons are actually different due to the presence of a delocalized excited state, an ultrafast energy transfer, and a supplementary torsional relaxation. As shown in Figure 5.9A, Figure 5.10A and Figure 5.11C, while the amplitudes of ESA figure of G0 and G1 are increasing steadily after 120ps, the amplitude of G2 ESA decays from 120 to 680ps. This difference can also be easily observed from the kinetics trace curve in Figure 5.9B, Figure 5.10B, and Figure 5.11D. The kinetics of G2 at 704nm is fitted triexponentially with 400fs, 20ps and 240ps with a long time component. The fast component 400fs is attributed to the intramolecular excitation energy transfer from the delocalized excited state of the thiophene dendrons to the longest oligothiophene, as found in G0 and G1. And the 240ps component is related the rate of electron-transfer rate in G2. From a previous study, it is clearly noted that as the number of thiophene increased, the ESA feature in the range of 650-to-800nm is blue-shifted with increasing ESA intensity. And the excited state delocalization was complete instantly after photoexcitation. The kinetic time components of a series of pure thiophene dendrimers, which have the same structures as thiophene dendrons in G2 system, were reported with a long time component.²¹ The fast component of tens of picoseconds (20ps) is related to exciton annihilation between chromophores. The kinetic curve of G2 can also be explained by the charge recombination.

The optical properties of molecules containing multiple identical chromophores are strongly dependent on the relative orientation and distance between the adjacent chromophores. It has been found out that the zero-order molecular exciton model can be used to predict the coupling of the transition dipole moments by creating two new exciton

states.⁹¹ For those chromophores having parallel transition dipole moments, such as perylene bisimide dyes, the transition from the ground state to the higher energy state is fully allowed, while the transition to the lower exciton state is forbidden. As in all three of these three systems, the ground state bleaching band around 570nm is assigned to the transition from $v = 0$ vibronic level to the $v = 1$ vibronic band of the lower exciton state, while the band around 530 nm is assigned to the transition from the $v = 0$ vibronic level of the ground state to the $v = 0$ vibronic level of the upper exciton state. This bleaching is accompanied by a stimulated emission feature at about 570nm. The bleaching bands at 570 nm for G0 and G1 are narrower than that of G2. This suggests that the exciton coupling between adjacent chromophores in G0 and G1 is slightly stronger than that in G2, and the transition moments of G0 and G1 are more parallel than that of G2. As a result, the perylene core is much more twisted in G2 than the case of G0 and G1. There is also a weak excited state absorption change in the transient absorption spectra of perylene bisimides model at 730nm.⁵⁹ This feature is corresponds well with the ESA feature of G0 and G1, which shows less thiophene character than G2. In the case of G2, the different blue shift of the ESA indicates that, as the time goes, there is a certain state accumulating electrons, and after accumulation, these electrons actually go to the higher excited energy state. This blue-shift indicates a strong interaction between the excited PBI and its neighboring thiophene dendrons.

Table 5.4 Summary of transient lifetimes of G0, G1 and G2

		$\lambda_{\text{pump}}=550\text{nm}$		
		τ_1	τ_2	τ_3
G0	$\lambda_{\text{probe}}=716\text{nm}$	400fs	8ps	200ps
G1	$\lambda_{\text{probe}}=711\text{nm}$	400fs	8ps	230ps
G2	$\lambda_{\text{probe}}=704\text{nm}$	400fs	20ps	240ps

5.3 Conclusion

In conclusion, dendritic oligothiophene-perylene bisimide systems (G0, G1, and G2) have been measured and investigated for their application in light harvesting materials using several nonlinear optical methods. The TPA cross-section of the dendrimer systems is detected in the NIR spectral region. Ultrafast energy transfer and electron transfer from the thiophene dendrons to perylene core has been characterized and compared to model compounds. Femtosecond transient absorption measurements have shown the excited state charge formation of a perylene anion radical at ~700 nm and the formation of thiophene cation radical near 500 nm. The size of the thiophene dendron has a big influence in the excited-state processes as observed from the time-resolved measurements. For example, in comparing the G0 and G1 dendrimers to the G2 system, one observes an increase in the magnitude of torsional twist as a result of the larger bay substitutes. Thus, the thiophene dendrons overlap strongly. Because of this conformational effect, electrons in G2 are delocalized throughout the entire molecule after excitation. This delocalization process increases the number of pathways of electron transfer from DOTs to the PBI, and thus results in a much faster energy transfer rate, by as much as 8 times. On the other hand, while increasing the size and number of thiophene dendrons, the possibility of exciton annihilation is also increased substantially. Both of these effects have to be taken into account when building up PBI bay area substituted dendritic architectures for their application in the organic photovoltaic area.

References

- [1]. Ma, C. Q.; Fonrodona, M.; Schikora, M. C.; Wienk, M. M.; Janssen, R. A. J.; Bauerle, P., Solution-Processed Bulk-Heterojunction Solar Cells Based on Monodisperse Dendritic Oligothiophenes. *Advanced Functional Materials* **2008**, *18* (20), 3323-3331.
- [2]. Mishra, A.; Ma, C. Q.; Janssen, R. A. J.; Bauerle, P., Shape-Persistent Oligothiophene-Ethynylene-Based Dendrimers: Synthesis, Spectroscopy and

- Electrochemical Characterization. *Chemistry-a European Journal* **2009**, *15* (48), 13521-13534.
- [3]. Xia, P. F.; Lu, J. P.; Kwok, C. H.; Fukutani, H.; Wong, M. S.; Tao, Y., Synthesis and Properties of Monodisperse Multi-Triarylamine-Substituted Oligothiophenes and 4,7-Bis(2'-Oligothieryl)-2,1,3-Benzothiadiazoles for Organic Solar Cell Applications. *Journal of Polymer Science Part a-Polymer Chemistry* **2009**, *47* (1), 137-148.
- [4]. Granstrom, M.; Petritsch, K.; Arias, A. C.; Lux, A.; Andersson, M. R.; Friend, R. H., Laminated Fabrication of Polymeric Photovoltaic Diodes. *Nature* **1998**, *395* (6699), 257-260.
- [5]. Hagfeldt, A.; Gratzel, M., Molecular Photovoltaics. *Accounts of Chemical Research* **2000**, *33* (5), 269-277.
- [6]. Andrews, D. L.; Bradshaw, D. S., Optically Nonlinear Energy Transfer in Light-Harvesting Dendrimers. *Journal of Chemical Physics* **2004**, *121* (5), 2445-2454.
- [7]. Donehue, J. E.; Varnavski, O. P.; Cemborski, R.; Iyoda, M.; Goodson, T., Probing Coherence in Synthetic Cyclic Light-Harvesting Pigments. *Journal of the American Chemical Society* **2011**, *133* (13), 4819-4828.
- [8]. Jiang, D. L.; Aida, T., Photoisomerization in Dendrimers by Harvesting of Low-Energy Photons. *Nature* **1997**, *388* (6641), 454-456.
- [9]. Padinger, F.; Rittberger, R. S.; Sariciftci, N. S., Effects of Postproduction Treatment on Plastic Solar Cells. *Advanced Functional Materials* **2003**, *13* (1), 85-88.
- [10]. Forrest, S. R., The Path to Ubiquitous and Low-Cost Organic Electronic Appliances on Plastic. *Nature* **2004**, *428* (6986), 911-918.
- [11]. Hoeben, F. J. M.; Jonkheijm, P.; Meijer, E. W.; Schenning, A., About Supramolecular Assemblies of Pi-Conjugated Systems. *Chemical Reviews* **2005**, *105* (4), 1491-1546.
- [12]. Ramakrishna, G.; Bhaskar, A.; Goodson, T., Ultrafast Excited State Relaxation Dynamics of Branched Donor-Pi-Acceptor Chromophore: Evidence of a Charge-Delocalized State. *Journal of Physical Chemistry B* **2006**, *110* (42), 20872-20878.
- [13]. Goodson, T. G., Optical Excitations in Organic Dendrimers Investigated by Time-Resolved and Nonlinear Optical Spectroscopy. *Accounts of Chemical Research* **2005**, *38* (2), 99-107.

- [14]. Laine, R. M.; Sulaiman, S.; Brick, C.; Roll, M.; Tamaki, R.; Asuncion, M. Z.; Neurock, M.; Filhol, J. S.; Lee, C. Y.; Zhang, J.; Goodson, T.; Ronchi, M.; Pizzotti, M.; Rand, S. C.; Li, Y., Synthesis and Photophysical Properties of Stilbeneoctasilsesquioxanes. Emission Behavior Coupled with Theoretical Modeling Studies Suggest a 3-D Excited State Involving the Silica Core. *Journal of the American Chemical Society* **2010**, *132* (11), 3708-3722.
- [15]. Sulaiman, S.; Bhaskar, A.; Zhang, J.; Guda, R.; Goodson, T.; Laine, R. M., Molecules with Perfect Cubic Symmetry as Nanobuilding Blocks for 3-D Assemblies. Elaboration of Octavinylsilsesquioxane. Unusual Luminescence Shifts May Indicate Extended Conjugation Involving the Silsesquioxane Core. *Chemistry of Materials* **2008**, *20* (17), 5563-5573.
- [16]. Ramakrishna, G.; Goodson, T., Excited-State Deactivation of Branched Two-Photon Absorbing Chromophores: A Femtosecond Transient Absorption Investigation. *Journal of Physical Chemistry A* **2007**, *111* (6), 993-1000.
- [17]. Bhaskar, A.; Ramakrishna, G.; Lu, Z. K.; Twieg, R.; Hales, J. M.; Hagan, D. J.; Van Stryland, E.; Goodson, T., Investigation of Two-Photon Absorption Properties in Branched Alkene and Alkyne Chromophores. *Journal of the American Chemical Society* **2006**, *128* (36), 11840-11849.
- [18]. Raymond, J. E.; Bhaskar, A.; Goodson, T.; Makiuchi, N.; Ogawa, K.; Kobuke, Y., Synthesis and Two-Photon Absorption Enhancement of Porphyrin Macrocycles. *Journal of the American Chemical Society* **2008**, *130* (51), 17212-+.
- [19]. Bhaskar, A.; Ramakrishna, G.; Hagedorn, K.; Varnavski, O.; Mena-Osteritz, E.; Bauerle, P.; Goodson, T., Enhancement of Two-Photon Absorption Cross-Section in Macrocyclic Thiophenes with Cavities in the Nanometer Regime. *Journal of Physical Chemistry B* **2007**, *111* (5), 946-954.
- [20]. Piovesan, E.; Silva, D. L.; De Boni, L.; Guimaraes, F. E. G.; Misoguti, L.; Zalesny, R.; Bartkowiak, W.; Mendonca, C. R., Two-Photon Absorption of Perylene Derivatives: Interpreting the Spectral Structure. *Chemical Physics Letters* **2009**, *479* (1-3), 52-55.
- [21]. Ramakrishna, G.; Bhaskar, A.; Bauerle, P.; Goodson, T., Oligothiophene Dendrimers as New Building Blocks for Optical Applications. *Journal of Physical Chemistry A* **2008**, *112* (10), 2018-2026.
- [22]. Grimsdale, A. C.; Mullen, K., The Chemistry of Organic Nanomaterials. *Angewandte Chemie-International Edition* **2005**, *44* (35), 5592-5629.

- [23]. Neuteboom, E. E.; Meskers, S. C. J.; van Hal, P. A.; van Duren, J. K. J.; Meijer, E. W.; Janssen, R. A. J.; Dupin, H.; Pourtois, G.; Cornil, J.; Lazzaroni, R.; Bredas, J. L.; Beljonne, D., Alternating Oligo(P-Phenylene Vinylene)-Perylene Bisimide Copolymers: Synthesis, Photophysics, and Photovoltaic Properties of a New Class of Donor-Acceptor Materials. *Journal of the American Chemical Society* **2003**, *125* (28), 8625-8638.
- [24]. Zhao, Y. Y.; Wasielewski, M. R., 3,4 : 9,10-Perylenebis(Dicarboximide) Chromophores That Function as Both Electron Donors and Acceptors. *Tetrahedron Letters* **1999**, *40* (39), 7047-7050.
- [25]. Giacobbe, E. M.; Mi, Q. X.; Colvin, M. T.; Cohen, B.; Ramanan, C.; Scott, A. M.; Yeganeh, S.; Marks, T. J.; Ratner, M. A.; Wasielewski, M. R., Ultrafast Intersystem Crossing and Spin Dynamics of Photoexcited Perylene-3,4:9,10-Bis(Dicarboximide) Covalently Linked to a Nitroxide Radical at Fixed Distances. *Journal of the American Chemical Society* **2009**, *131* (10), 3700-3712.
- [26]. Kelley, R. F.; Shin, W. S.; Rybtchinski, B.; Sinks, L. E.; Wasielewski, M. R., Photoinitiated Charge Transport in Supramolecular Assemblies of a 1,7,N,N'-Tetrakis(Zinc Porphyrin)-Perylene-3,4 : 9,10-Bis(Dicarboximide). *Journal of the American Chemical Society* **2007**, *129* (11), 3173-3181.
- [27]. Wurthner, F., Perylene Bisimide Dyes as Versatile Building Blocks for Functional Supramolecular Architectures. *Chemical Communications* **2004**, (14), 1564-1579.
- [28]. Fuller, M. J.; Sinks, L. E.; Rybtchinski, B.; Giaimo, J. M.; Li, X. Y.; Wasielewski, M. R., Ultrafast Photoinduced Charge Separation Resulting from Self-Assembly of a Green Perylene-Based Dye into Pi-Stacked Arrays. *Journal of Physical Chemistry A* **2005**, *109* (6), 970-975.
- [29]. Wasielewski, M. R., Self-Assembly Strategies for Integrating Light Harvesting and Charge Separation in Artificial Photosynthetic Systems. *Accounts of Chemical Research* **2009**, *42* (12), 1910-1921.
- [30]. Newman, C. R.; Frisbie, C. D.; da Silva, D. A.; Bredas, J. L.; Ewbank, P. C.; Mann, K. R., Introduction to Organic Thin Film Transistors and Design of N-Channel Organic Semiconductors. *Chemistry of Materials* **2004**, *16* (23), 4436-4451.
- [31]. Tauber, M. J.; Kelley, R. F.; Giaimo, J. M.; Rybtchinski, B.; Wasielewski, M. R., Electron Hopping in Pi-Stacked Covalent and Self-Assembled Perylene Diimides Observed by Endor Spectroscopy. *Journal of the American Chemical Society* **2006**, *128* (6), 1782-1783.

- [32]. Ostroverkhova, O.; Cooke, D. G.; Shcherbyna, S.; Egerton, R. F.; Hegmann, F. A.; Tykwinski, R. R.; Anthony, J. E., Bandlike Transport in Pentacene and Functionalized Pentacene Thin Films Revealed by Subpicosecond Transient Photoconductivity Measurements. *Physical Review B* **2005**, *71* (3).
- [33]. You, C. C.; Hippus, C.; Grune, M.; Wurthner, F., Light-Harvesting Metallo-supramolecular Squares Composed of Perylene Bisimide Walls and Fluorescent Antenna Dyes. *Chemistry-a European Journal* **2006**, *12* (28), 7510-7519.
- [34]. Ahrens, M. J.; Sinks, L. E.; Rybtchinski, B.; Liu, W. H.; Jones, B. A.; Giaimo, J. M.; Gusev, A. V.; Goshe, A. J.; Tiede, D. M.; Wasielewski, M. R., Self-Assembly of Supramolecular Light-Harvesting Arrays from Covalent Multi-Chromophore Perylene-3,4 : 9,10-Bis(Dicarboximide) Building Blocks. *Journal of the American Chemical Society* **2004**, *126* (26), 8284-8294.
- [35]. Fortage, J.; Severac, M.; Houarner-Rassin, C.; Pellegrin, Y.; Blart, E.; Odobel, F., Synthesis of New Perylene Imide Dyes and Their Photovoltaic Performances in Nanocrystalline TiO₂ Dye-Sensitized Solar Cells. *Journal of Photochemistry and Photobiology a-Chemistry* **2008**, *197* (2-3), 156-169.
- [36]. Schmidt, R.; Oh, J. H.; Sun, Y. S.; Deppisch, M.; Krause, A. M.; Radacki, K.; Braunschweig, H.; Konemann, M.; Erk, P.; Bao, Z. A.; Wurthner, F., High-Performance Air-Stable N-Channel Organic Thin Film Transistors Based on Halogenated Perylene Bisimide Semiconductors. *Journal of the American Chemical Society* **2009**, *131* (17), 6215-6228.
- [37]. Tatemichi, S.; Ichikawa, M.; Koyama, T.; Taniguchi, Y., High Mobility N-Type Thin-Film Transistors Based on N,N'-Ditridecyl Perylene Diimide with Thermal Treatments. *Applied Physics Letters* **2006**, *89* (11).
- [38]. Lu, J. P.; Xia, P. F.; Lo, P. K.; Tao, Y.; Wong, M. S., Synthesis and Properties of Multi-Triarylamine-Substituted Carbazole-Based Dendrimers with an Oligothiophene Core for Potential Applications in Organic Solar Cells and Light-Emitting Diodes. *Chemistry of Materials* **2006**, *18* (26), 6194-6203.
- [39]. Vaterlein, C.; Neureiter, H.; Gebauer, W.; Ziegler, B.; Sokolowski, M.; Bauerle, P.; Umbach, E., Organic Light Emitting Devices Based on Vapor Deposited Films of End-Capped Sexithiophene: Evidence for Schottky Barriers and Transport Limitations. *Journal of Applied Physics* **1997**, *82* (6), 3003-3013.
- [40]. Chen, T. A.; Rieke, R. D., The 1st Regioregular Head-to-Tail Poly(3-Hexylthiophene-2,5-Diyl) and a Regiorandom Isopolymer - Ni Vs Pd Catalysis of 2(5)-Bromo-5(2)-(Bromozincio)-3-Hexylthiophene Polymerization. *Journal of the American Chemical Society* **1992**, *114* (25), 10087-10088.

- [41]. Brabec, C. J.; Sariciftci, N. S.; Hummelen, J. C., Plastic Solar Cells. *Advanced Functional Materials* **2001**, *11* (1), 15-26.
- [42]. Harpham, M. R.; Suzer, O.; Ma, C. Q.; Bauerle, P.; Goodson, T., Thiophene Dendrimers as Entangled Photon Sensor Materials. *Journal of the American Chemical Society* **2009**, *131* (3), 973-979.
- [43]. Torsi, L.; Dodabalapur, A.; Rothberg, L. J.; Fung, A. W. P.; Katz, H. E., Intrinsic Transport Properties and Performance Limits of Organic Field-Effect Transistors. *Science* **1996**, *272* (5267), 1462-1464.
- [44]. Sirringhaus, H.; Brown, P. J.; Friend, R. H.; Nielsen, M. M.; Bechgaard, K.; Langeveld-Voss, B. M. W.; Spiering, A. J. H.; Janssen, R. A. J.; Meijer, E. W.; Herwig, P.; de Leeuw, D. M., Two-Dimensional Charge Transport in Self-Organized, High-Mobility Conjugated Polymers. *Nature* **1999**, *401* (6754), 685-688.
- [45]. Schon, J. H.; Dodabalapur, A.; Bao, Z.; Kloc, C.; Schenker, O.; Batlogg, B., Gate-Induced Superconductivity in a Solution-Processed Organic Polymer Film (Retracted Article. See Vol 422 Pg 92 2003). *Nature* **2001**, *410* (6825), 189-192.
- [46]. Xia, C. J.; Fan, X. W.; Locklin, J.; Advincula, R. C., A First Synthesis of Thiophene Dendrimers. *Organic Letters* **2002**, *4* (12), 2067-2070.
- [47]. Garnier, F.; Hajlaoui, R.; Yassar, A.; Srivastava, P., All-Polymer Field-Effect Transistor Realized by Printing Techniques. *Science* **1994**, *265* (5179), 1684-1686.
- [48]. Ma, C. Q.; Mena-Osteritz, E.; Debaerdemaeker, T.; Wienk, M. M.; Janssen, R. A. J.; Bauerle, P., Functionalized 3d Oligothiophene Dendrons and Dendrimers - Novel Macromolecules for Organic Electronics. *Angewandte Chemie-International Edition* **2007**, *46* (10), 1679-1683.
- [49]. Charra, F.; Fichou, D.; Nunzi, J. M.; Pfeffer, N., Picosecond Photoinduced Dichroism in Solutions of Thiophene Oligomers. *Chemical Physics Letters* **1992**, *192* (5-6), 566-570.
- [50]. Lap, D. V.; Grebner, D.; Rentsch, S., Femtosecond Time-Resolved Spectroscopic Studies on Thiophene Oligomers. *Journal of Physical Chemistry A* **1997**, *101* (2), 107-112.
- [51]. Lanzani, G.; Nisoli, M.; Magni, V.; Desilvestri, S.; Barbarella, G.; Zambianchi, M.; Tubino, R., Femtosecond Spectral Relaxation of Alpha-Conjugated

- Hexamethylsexithiophene in Solution. *Physical Review B* **1995**, *51* (19), 13770-13773.
- [52]. Cremer, J.; Bauerle, P., Star-Shaped Perylene-Oligothiophene-Triphenylamine Hybrid Systems for Photovoltaic Applications. *Journal of Materials Chemistry* **2006**, *16* (9), 874-884.
- [53]. Trinchi, A.; Muster, T. H., A Review of Surface Functionalized Amine Terminated Dendrimers for Application in Biological and Molecular Sensing. *Supramolecular Chemistry* **2007**, *19* (7), 431-445.
- [54]. Hecht, S., Functionalizing the Interior of Dendrimers: Synthetic Challenges and Applications. *Journal of Polymer Science Part a-Polymer Chemistry* **2003**, *41* (8), 1047-1058.
- [55]. Fischer, M. K. R.; Kaiser, T. E.; Wurthner, F.; Bauerle, P., Dendritic Oligothiophene-Perylene Bisimide Hybrids: Synthesis, Optical and Electrochemical Properties. *Journal of Materials Chemistry* **2009**, *19* (8), 1129-1141.
- [56]. Maciejewski, A.; Steer, R. P., Spectral and Photophysical Properties of 9,10-Diphenylanthracene in Perfluoro-Normal-Hexane - the Influence of Solute Solvent Interactions. *Journal of Photochemistry* **1986**, *35* (1), 59-69.
- [57]. Giaimo, J. M.; Lockard, J. V.; Sinks, L. E.; Scott, A. M.; Wilson, T. M.; Wasielewski, M. R., Excited Singlet States of Covalently Bound, Cofacial Dimers and Trimers of Perylene-3,4 : 9,10-Bis(Dicarboximide)S. *Journal of Physical Chemistry A* **2008**, *112* (11), 2322-2330.
- [58]. Demas, J. N.; Crosby, G. A., Measurement of Photoluminescence Quantum Yields - Review. *Journal of Physical Chemistry* **1971**, *75* (8), 991-&.
- [59]. Wu, P. G.; Brand, L., Resonance Energy-Transfer - Methods and Applications. *Analytical Biochemistry* **1994**, *218* (1), 1-13.
- [60]. Selvin, P. R., Fluorescence Resonance Energy-Transfer. *Biochemical Spectroscopy* **1995**, *246*, 300-334.
- [61]. Margineanu, A.; Hofkens, J.; Cotlet, M.; Habuchi, S.; Stefan, A.; Qu, J. Q.; Kohl, C.; Mullen, K.; Vercammen, J.; Engelborghs, Y.; Gensch, T.; De Schryver, F. C., Photophysics of a Water-Soluble Rylene Dye: Comparison with Other Fluorescent Molecules for Biological Applications. *Journal of Physical Chemistry B* **2004**, *108* (32), 12242-12251.

- [62]. Bullock, J. E.; Vagnini, M. T.; Ramanan, C.; Co, D. T.; Wilson, T. M.; Dicke, J. W.; Marks, T. J.; Wasielewski, M. R., Photophysics and Redox Properties of Rylene Imide and Diimide Dyes Alkylated Ortho to the Imide Groups. *Journal of Physical Chemistry B* **2010**, *114* (5), 1794-1802.
- [63]. Barkley, M. D.; Kowalczyk, A. A.; Brand, L., Fluorescence Decay Studies of Anisotropic Rotations of Small Molecules. *Journal of Chemical Physics* **1981**, *75* (7), 3581-3593.
- [64]. Osswald, P.; Wurthner, F., Effects of Bay Substituents on the Racemization Barriers of Perylene Bisimides: Resolution of Atropo-Enantiomers. *Journal of the American Chemical Society* **2007**, *129* (46), 14319-14326.
- [65]. Denny, R. A.; Bagchi, B.; Barbara, P. F., Effects of Vibrational Energy Relaxation and Reverse Reaction on Electron Transfer Kinetics and Fluorescence Line Shapes in Solution. *Journal of Chemical Physics* **2001**, *115* (13), 6058-6071.
- [66]. Gesquiere, A. J.; Park, S. J.; Barbara, P. F., Photochemistry and Kinetics of Single Organic Nanoparticles in the Presence of Charge Carriers. *European Polymer Journal* **2004**, *40* (5), 1013-1018.
- [67]. Gesquiere, A. J.; Park, S. J.; Barbara, P. F., Hole-Induced Quenching of Triplet and Singlet Excitons in Conjugated Polymers. *Journal of the American Chemical Society* **2005**, *127* (26), 9556-9560.
- [68]. Kang, T. J.; Jarzaba, W.; Barbara, P. F.; Fonseca, T., A Photodynamical Model for the Excited-State Electron-Transfer of Bianthryl and Related Molecules. *Chemical Physics* **1990**, *149* (1-2), 81-95.
- [69]. Lammi, R. K.; Barbara, P. F., Influence of Chain Length on Exciton Migration to Low-Energy Sites in Single Fluorene Copolymers. *Photochemical & Photobiological Sciences* **2005**, *4* (1), 95-99.
- [70]. Lee, Y. J.; Zhang, T. Q.; Barbara, P. F., Kinetics of Electron Attachment to Reverse Micelles. *Journal of Physical Chemistry B* **2004**, *108* (17), 5175-5178.
- [71]. Tominaga, K.; Klinner, D. A. V.; Johnson, A. E.; Levinger, N. E.; Barbara, P. F., Femtosecond Experiments and Absolute Rate Calculations on Intervalence Electron-Transfer of Mixed-Valence Compounds. *Journal of Chemical Physics* **1993**, *98* (2), 1228-1243.
- [72]. Flors, C.; Oesterling, I.; Schnitzler, T.; Fron, E.; Schweitzer, G.; Sliwa, M.; Herrmann, A.; van der Auweraer, M.; de Schryver, F. C.; Mullen, K.; Hofkens, J.,

Energy and Electron Transfer in Ethynylene Bridged Perylene Diimide Multichromophores. *Journal of Physical Chemistry C* **2007**, *111* (12), 4861-4870.

- [73]. Ando, S.; Ramanan, C.; Facchetti, A.; Wasielewski, M. R.; Marks, T. J., Synthesis, Characterization, and Photoinduced Electron Transfer Properties of Core-Functionalized Perylene-3,4:9,10-Bis(Dicarboximide)s with Pendant Anthracenes. *Journal of Materials Chemistry* **2011**, *21* (47), 19049-19057.
- [74]. Gunderson, V. L.; Krieg, E.; Vagnini, M. T.; Iron, M. A.; Rybtchinski, B.; Wasielewski, M. R., Photoinduced Singlet Charge Transfer in a Ruthenium(II) Perylene-3,4:9,10-Bis(Dicarboximide) Complex. *Journal of Physical Chemistry B* **2011**, *115* (23), 7533-7540.
- [75]. Jones, B. A.; Facchetti, A.; Wasielewski, M. R.; Marks, T. J., Tuning Orbital Energetics in Arylene Diimide Semiconductors. Materials Design for Ambient Stability of N-Type Charge Transport. *Journal of the American Chemical Society* **2007**, *129* (49), 15259-15278.
- [76]. Miller, S. E.; Zhao, Y. Y.; Schaller, R.; Mulloni, V.; Just, E. M.; Johnson, R. C.; Wasielewski, M. R., Ultrafast Electron Transfer Reactions Initiated by Excited C_t States of Push-Pull Perylenes. *Chemical Physics* **2002**, *275* (1-3), 167-183.
- [77]. Odom, S. A.; Kelley, R. F.; Ohira, S.; Ensley, T. R.; Huang, C.; Padilha, L. A.; Webster, S.; Coropceanu, V.; Barlow, S.; Hagan, D. J.; Van Stryland, E. W.; Bredas, J. L.; Anderson, H. L.; Wasielewski, M. R.; Marder, S. R., Photophysical Properties of an Alkyne-Bridged Bis(Zinc Porphyrin)-Perylene Bis(Dicarboximide) Derivative. *Journal of Physical Chemistry A* **2009**, *113* (40), 10826-10832.
- [78]. Rybtchinski, B.; Sinks, L. E.; Wasielewski, M. R., Photoinduced Electron Transfer in Self-Assembled Dimers of 3-Fold Symmetric Donor - Acceptor Molecules Based on Perylene-3,4 : 9,10-Bis(Dicarboximide). *Journal of Physical Chemistry A* **2004**, *108* (37), 7497-7505.
- [79]. Sinks, L.; Fuller, M. J.; Liu, W. H.; Ahrens, M. J.; Wasielewski, M. R., Photoinduced Electron Transfer in a Donor-Acceptor Dyad Oriented by an Aligned Nematic Liquid Crystal Solvent. *Chemical Physics* **2005**, *319* (1-3), 226-234.
- [80]. Kaletas, B. K.; Dobraza, R.; Sautter, A.; Wurthner, F.; Zimine, M.; De Cola, L.; Williams, R. M., Photoinduced Electron and Energy Transfer Processes in a Bichromophoric Pyrene-Perylene Bisimide System. *Journal of Physical Chemistry A* **2004**, *108* (11), 1900-1909.

- [81]. Schweitzer, G.; Gronheid, R.; Jordens, S.; Lor, M.; De Belder, G.; Weil, T.; Reuther, E.; Mullen, M.; De Schryver, F. C., Intramolecular Directional Energy Transfer Processes in Dendrimers Containing Perylene and Terrylene Chromophores. *Journal of Physical Chemistry A* **2003**, *107* (18), 3199-3207.
- [82]. Ford, W. E.; Hiratsuka, H.; Kamat, P. V., Photochemistry of 3,4,9,10-Perylenetetracarboxylic Dianhydride Dyes .4. Spectroscopic and Redox Properties of Oxidized and Reduced Forms of the Bis(2,5-Di-Tert-Butylphenyl)Imide Derivative. *Journal of Physical Chemistry* **1989**, *93* (18), 6692-6696.
- [83]. Kircher, T.; Lohmannsroben, H. G., Photoinduced Charge Recombination Reactions of a Perylene Dye in Acetonitrile. *Physical Chemistry Chemical Physics* **1999**, *1* (17), 3987-3992.
- [84]. Wurthner, F.; Sautter, A., Highly Fluorescent and Electroactive Molecular Squares Containing Perylene Bisimide Ligands. *Chemical Communications* **2000**, (6), 445-446.
- [85]. Evans, C. H.; Scaiano, J. C., Photochemical Generation of Radical Cations from Alpha-Terthienyl and Related Thiophenes - Kinetic-Behavior and Magnetic-Field Effects on Radical-Ion Pairs in Micellar Solution. *Journal of the American Chemical Society* **1990**, *112* (7), 2694-2701.
- [86]. Lanzani, G.; Nisoli, M.; DeSilvestri, S.; Tubino, R., Femtosecond Vibrational and Torsional Energy Redistribution in Photoexcited Oligothiophenes. *Chemical Physics Letters* **1996**, *251* (5-6), 339-345.
- [87]. Lanzani, G.; Nisoli, M.; DeSilvestri, S.; Barbarella, G.; Zambianchi, M.; Tubino, R., Visible and near-Infrared Ultrafast Optical Dynamics of Hexamethylsexithiophene in Solution. *Physical Review B* **1996**, *53* (8), 4453-4457.
- [88]. Lanzani, G.; Nisoli, M.; DeSilvestri, S.; Tubino, R., Femtosecond Optical Dynamics of Alpha-Conjugated Hexamethylsexithiophene in Solution. *Synthetic Metals* **1996**, *76* (1-3), 39-41.
- [89]. Westenhoff, S.; Beenken, W. J. D.; Friend, R. H.; Greenham, N. C.; Yartsev, A.; Sundstrom, V., Anomalous Energy Transfer Dynamics Due to Torsional Relaxation in a Conjugated Polymer. *Physical Review Letters* **2006**, *97* (16).
- [90]. Westenhoff, S.; Daniel, C.; Friend, R. H.; Silva, C.; Sundstrom, V.; Yartsev, A., Exciton Migration in a Polythiophene: Probing the Spatial and Energy Domain by Line-Dipole Forster-Type Energy Transfer. *Journal of Chemical Physics* **2005**, *122* (9).

- [91]. Kasha, M.; Rawls, H. R.; El-Bayoumi, M. A., The Exciton Model in Molecular Spectroscopy. **1965**, *11* (3-4), 371-392.

CHAPTER 6

OTHER PHOTOVOLTAIC MATERIALS: $Z_N T_E O$ THIN FILMS – TWO PHOTON MEASUREMENTS USING NONLINEAR TRANSMISSION METHODS

6.1 Introduction

An intermediate band solar cell (IBSC) is a novel photovoltaic device concept that could potentially surpass the efficiency limit of single band gap solar cells. In an intermediate band material, electrons are excited into the forbidden band, so called intermediate band, as illustrated in Figure 6.1. The IBSC can be regarded as a set of two cells connected in series and one parallel. The intermediate band cells provide an increased absorption due to additional absorptions both from the valence band (VB) to the intermediate band (IB) and from the IB to the conduction band (CB). Therefore, in these type cells, short-circuit current (I_{SC}) can be increased, which leads to an improvement of overall power conversion efficiency without sacrificing the open circuit voltage (U_{OC}). Under the similar hypotheses used for the Shockley-Queisser limitation¹ of single gap cell (41%), the balance-limiting efficiency is as high as 63% for an IBSC, reported in 1997.² These cells offer better stability and tolerance when the solar spectrum is distorted by environment. In addition, they can be easily fabricated on the non-crystal substrate and offer a lower cost per unit power.

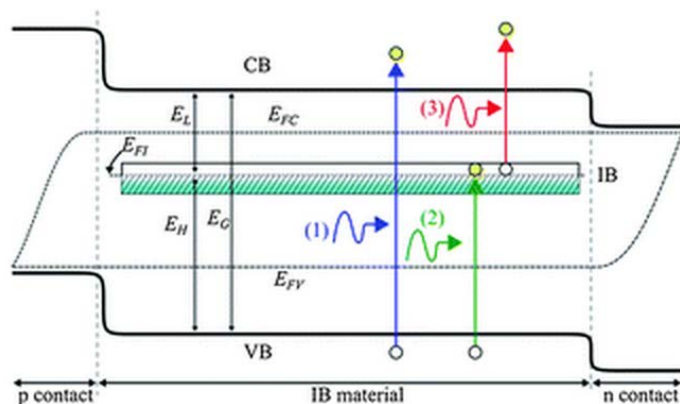


Figure 6.1 Schematic of optical transitions in intermediate band solar cells (CB: conduction band; IB: intermediate band; VB: valence band)³

The concept of introducing intermediate band to increase the maximum photocurrent was introduced by Wolf⁴ in 1960. However, this idea was initially rejected. Because an impurity or defect in the forbidden band gap caused by grain boundaries, dislocations, or other lattice imperfections, could act as non-radiative charge recombination centers, if it is capable to trap both the electron and the hole.¹ Interestingly, in 1970, Gutter and Queisser⁵ observed an enhancement of short-circuit current in an impurity silicon solar cell. They found out that splitting the Fermi level into three separate quasi-Fermi levels can maintain the high output voltage of a solar cell. Later on, prediction on intermediated band solar cell suggested that their theoretical overall power conversion efficiency could be up to 63%, which greatly exceeds the Shockley-Queisser limit.^{2, 6-9} The limiting efficiency is based on the assumption that all the charge carriers transport to the electrodes without non-radiative charge recombination, and absorption transition bands don't overlap with others. The first bulk intermediate band material reported was $\text{Zn}_{0.88}\text{Mn}_{0.12}\text{Te}_{0.987}\text{O}_{0.013}$, which was synthesized by Walukiewicz and his co-workers.¹⁰ The formation of intermediate band is due to the heavily mismatching in the alloys, and can be detected by spectral photo reflectance measurements. Later on, intermediate band materials were explored both experimentally and theoretically.¹¹⁻¹³ The intermediate band behavior is found in other materials such as $\text{GaN}_x\text{As}_{1-x-y}\text{P}_y$ alloys with

$y > 0.3$,¹⁴ and heavily titanium-doped silicon.¹⁵ Ab initio calculations have also been performed to identify the intermediate band materials.¹⁶⁻¹⁷ The first bulk intermediate band solar cell was made by Phillips *et al.*¹⁸⁻¹⁹ using oxygen-doped ZnTe in 2009.

An optimal intermediate band solar cell is achieved under the non-overlapping condition that the energy of absorbed photon covers most solar spectrum. Under this condition, the band gaps between the VB and the IB, and between the VB and the CB have to be greater than the bandwidth of conduction band. In addition, the bandgap between the IB and the CB has to be greater than the bandwidth of the VB. The optimal band gap of an intermediate band solar cell is shown in Figure 6.2 (a). The optimal IB solar cell has a total bandgap of about 1.95 eV. The two sub-bandgaps are proximately 0.71 eV and 1.24 eV. The bandwidth of conduction band is less than 0.5 eV, and the bandwidth of the valence band is less than 0.71 eV. In this way, all the photons with energy greater than 0.71 eV (wavelength less than 1771nm) will be absorbed. However, this ideal band structure is very difficult to obtain in the real device. Current research is focusing on reaching the spatial separation condition, as shown in Figure 6.2 (b).²⁰

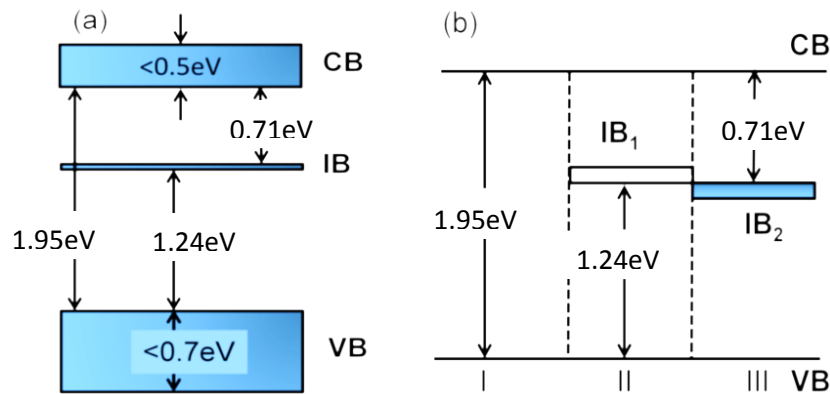


Figure 6.2 Non-overlapping band condition: (a) Optimal condition, (b) Spatial separation condition²⁰

This chapter focuses on intermediate band material, oxygen-doped ZnTe thin film which is fabricated by Dr. Weiming Wang from Prof. Phillip's group (Department of

Electrical Engineering, University of Michigan). ZnTe based materials have been investigated in great details for various applications, such as visible light emitters,²¹⁻²² x-ray detectors,²³ and sensitive infrared/mid-infrared detector.²⁴⁻²⁶ The band gap of ZnTe is 2.29eV.²⁷ Most wide band gap materials, such as ZnO, are typically n-type semiconductors. In contrast, ZnTe has established unique p-type behavior with controllable doping by nitrogen.²⁸⁻²⁹ This unique p-type behavior is due to the native defect in the crystal structure, such as zinc vacancy.³⁰⁻³¹ The basic characteristics of ZnTe are listed in the Table 6.1. Due to relative large difference of the electronegativity between Te and O atoms, the position of these atoms inside oxygen doped ZnTe alloy (ZnTeO) is highly mismatched. The presence of an intermediate band in ZnTeO has been suggested both theoretically and experimentally.¹⁰ The reported band gap of ZnTeO is ~1.9 eV with a defect band of ~0.5 eV, which is much lower than the band gap of ZnTe alloy (2.29eV).^{18, 32-35} Therefore, ZnTeO alloys with variable band gaps could absorb photons in a board range of solar spectrum, especially in the visible range. This feature makes this type of material very attractive to solar cell research area and provides great potential to enhance the power conversion efficiency.

Table 6.1 Basic characteristics of single crystal ZnTe^{27, 36}

Bandgap at room temperature	2.29 eV
Crystal structure	Zinc blende
Zinc blende density at 300K	5.65 g/cm ³
Lattice constant a_0 at 300K	0.610 nm
Zinc blende nearest-neighbor dist. at 300K	0.264 nm
Native defects	p-type
O _{Te} substitute	0.5 eV below E _c

The ZnTeO films investigated are fabricated by Molecular Beam Epitaxy (MBE) and Pulsed Laser Deposition (PLD) methods. The stoichiometry for ZnTeO deposited under 30 mTorr oxygen was determined to be Zn:Te:O=0.49:0.26:0.25, and that under 100 mTorr oxygen is Zn:Te:O=0.45:0.24:0.31. Zinc deficiency is found in samples deposited under higher oxygen pressure with oxygen densities higher than 10^{22} cm^{-3} . The possible oxygen sites of our investigated ZnTeO crystal are shown in Figure 6.3.

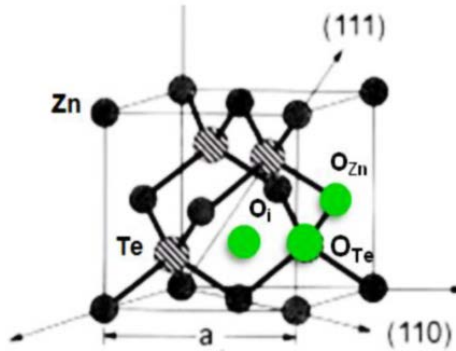


Figure 6.3 Schematics of possible oxygen sites in ZnTe crystal³⁶

Both single and two photon absorption has been investigated in bulk semiconductors in order to understand their coherent photocurrent generations.³⁷⁻³⁹ Two photon absorption coefficient of GaAs is measured by optical-pump terahertz-probe spectroscopy using femtosecond laser pulses with fluences up to 4.2 mJ/cm^2 .⁴⁰ Its estimated TPA coefficient is $220 \pm 50 \text{ cm/GW}$ using the Gaussian approximation of the temporal pulse shape.⁴⁰ The theoretical two-photon absorption coefficient of ZnTe is 0.89 cm/GM , reported by Vansteryland *et al.*⁴¹ Said *et al.*⁴² measured the two photon absorption coefficient of ZnTe ($4.2-4.5 \text{ cm/GM}$) using Z-scan experimental technique. The two photon coefficient is strongly dependent on the size of quantum dots.⁴³ In large CdSe quantum dots, the TPA coefficient approaches 55 cm/GM when the size of the exciton Bohr radius exceeds 10 nm .⁴³

6.2 Optical Properties of ZnTeO

The absorption coefficient spectra of ZnTe and ZnTeO have been reported, as shown in Figure 6.4.⁴⁴ ZnTeO under oxygen pressure at 10^{-5} Torr has an absorption coefficient of oxygen states as high as 10^4 cm^{-1} .

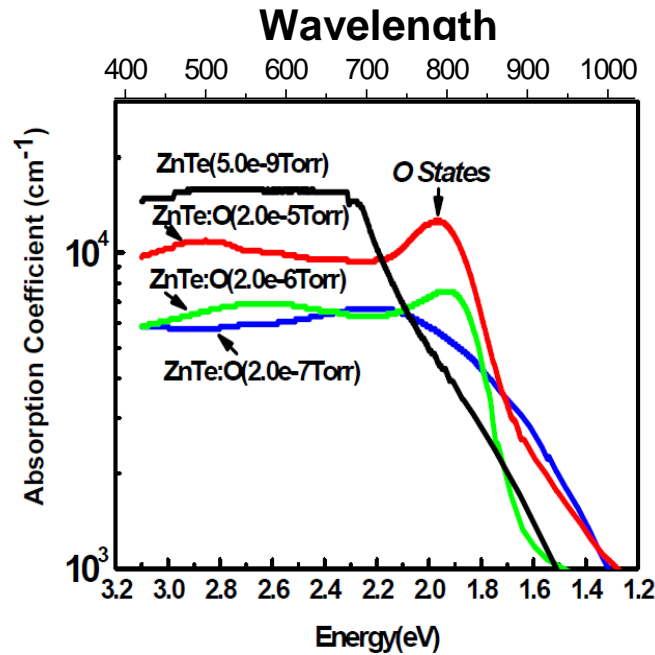


Figure 6.4 Absorption coefficients of ZnTe and ZnTeO⁴⁴

Photoluminescence spectra of ZnTe and ZnTeO are shown in Figure 6.5. A modified plot (logarithmic PL counts versus energy in eV) is presented in Figure 6.6.⁴⁴ The excitation wavelength is 325 nm. The PL spectrum of undoped ZnTe shows an emission band with maximum at 546 nm (~ 2.3 eV), whereas the emission band of ZnTeO dramatically shifts to the red with maximum at 686 nm (1.8 eV), which corresponds well with the PL band found in oxygen defects in ZnTe.⁴⁵ Comparing with the emission maximum with ZnTe, the significant red shift (~ 140 nm) of the ZnTeO is mainly due to the defects inside the crystal.⁴⁴ It also could be caused by the oxygen residue incorporated

in the alloy during the doping process.⁴⁴ In addition, the intensity of the emission at 686 nm of ZnTeO is significantly increased, suggesting the existence of the defect band with band gap $\sim 1.8\text{eV}$. In order to further examine this intermediate band, two-photon absorption measurements are carried out.

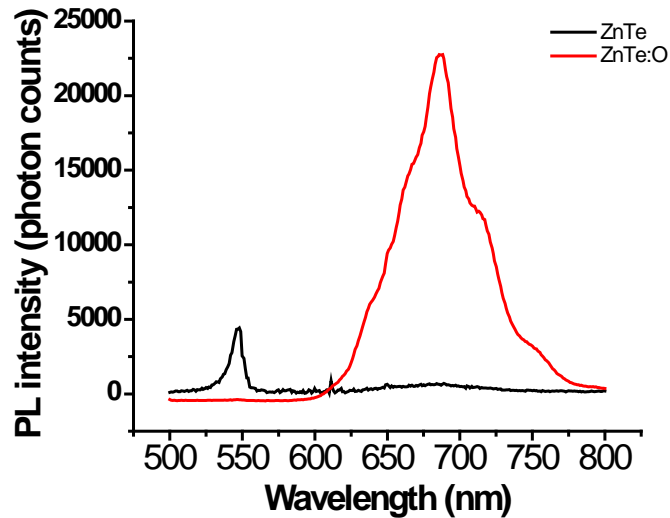


Figure 6.5 Photoluminescence spectra of ZnTe and ZnTeO

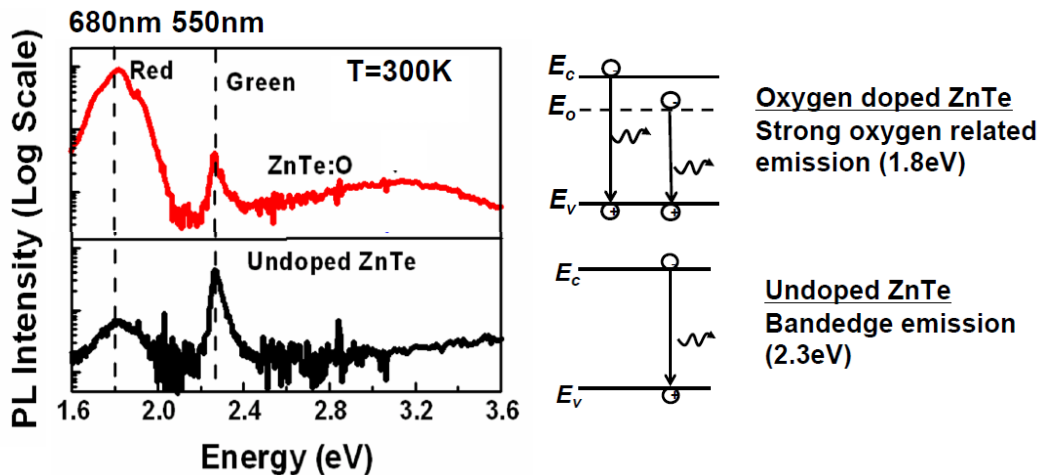


Figure 6.6 Photoluminescence spectra of ZnTeO and ZnTe (log scale)^{19,44}

6.3 Two Photon Transmission Measurement

The proposed band gap of investigated ZnTeO thin film is illustrated in Figure 6.7. The excitation wavelength of 1380nm provides the energy necessary for the transition from VB to IB with a band gap of 1.6eV.

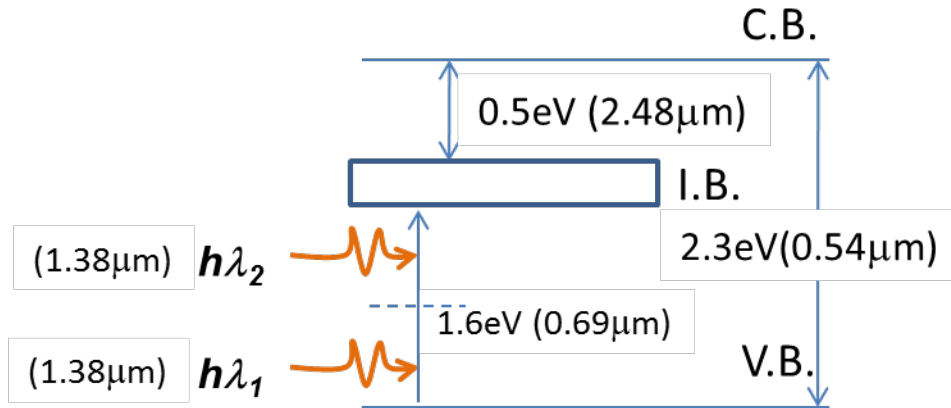


Figure 6.7 Schematic diagram of two photon excitation of ZnTeO

In this material, ZnTeO thin film is deposited on a sapphire substrate. Therefore, the reflection and transmission parameters for this two-layer system are considered. The detail experimental procedure was described in Chapter 2. A schematic drawing of reflection and transmission parameters of two-layer ZnTeO is illustrated in Figure 6.8.

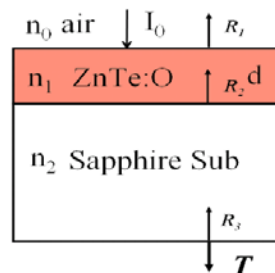


Figure 6.8 Schematic drawing of reflection and transmission parameters of two-layer ZnTeO

A model used for two-photon transmission for a two-layer film can be expressed below:⁴⁶

Equation 6.1

$$\frac{I'}{I_0} = T = \frac{(1 - R_1 T_x)^2 e^{-\alpha d}}{1 + \beta(1 - R_1 R_x) I_0 \left(\frac{1 - e^{-\alpha d}}{\alpha} \right)}$$

Where, α is the one-photon absorption coefficient, β is the two-photon absorption coefficient and d is the layer thickness of the two-photon absorbing material. T_x and R_x are the transmission and reflection coefficients, which are given by:

Equation 6.2

$$T_x = \frac{(1 - R_2)(1 - R_3)}{1 - R_2 R_3}$$

Equation 6.3

$$R_x = R_2 + \frac{R_3(1 - R_2)^2}{1 - R_2 R_3}$$

In Equations 6.1, 6.2 and 6.3, R_1 , R_2 and R_3 are the reflectivity of the interface for air/ZnTeO, ZnTeO/substrate and substrate/air, respectively. They are defined by: $R_1 = (1 - n_1)^2 / (1 + n_2)^2$, $R_2 = (n_1 - n_2)^2 / (n_1 + n_2)^2$ and $R_3 = (n_2 - 1)^2 / (1 + n_2)^2$. n_1 and n_2 are the refractive indices of the ZnTeO sample and the substrate, respectively. Here, we use the refraction index of ZnTe for ZnTeO sample.⁴⁷ In order to measure the two photon absorption coefficient, Equation 6.1 is rearranged as the following:

Equation 6.4

$$\frac{I_0}{I'} = \frac{1}{T} = \frac{1}{(1 - R_1 T_x)^2 e^{-\alpha d}} + \frac{\beta(1 - R_1 R_x) \left(\frac{1 - e^{-\alpha d}}{\alpha} \right)}{(1 - R_1 T_x)^2 e^{-\alpha d}} I_0 = a + b \times I_0$$

According to the equation above, a plot of $\frac{1}{T}$ with respect to I_0 should give us a linear relationship, and the resulting intercept a and slope b are used to further calculate two photon absorption coefficient. The expressions of a and b are described below:

Equation 6.5

$$a = \frac{1}{(1 - R_1 T_x)^2 e^{-ad}}$$

Equation 6.6

$$b = \frac{\beta(1 - R_1 R_x) \left(\frac{1 - e^{-ad}}{\alpha} \right)}{(1 - R_1 T_x)^2 e^{-ad}}$$

Based on the data from the experiment, a linear plot of the multiplicative inverse of transmission ($1/T$) against input beam intensity (I_0) is obtained, as shown in Figure 6.9. The values of a and b are 1.0072 and 0.0052, respectively. According to Equation 6.5, $e^{-ad} = 0.404$ and thus the linear absorption coefficient $\alpha = 1.8 \times 10^5 m^{-1}$. These values are taken into the following equation obtained from Equation 6.5 and 6.6:

Equation 6.7

$$\frac{b}{a} = \beta(1 - R_1 R_x) \left(\frac{1 - e^{-ad}}{\alpha} \right)$$

Given that the thickness (d) of ZnTeO sample is $5 \mu m$ and the concentration is $0.029 mol/cm^3$, according the equation above, the calculated two-photon absorption coefficient is $\beta = 1.6m/W = 1.6m/(J/s) = 1.6ms/J \times \frac{1J}{hc/\lambda} = 2.2 \times 10^{-17} cm \cdot s/photon$, and thus the two photon cross section of ZnTeO thin film is $\sigma_2 = \beta/(N_A c) = 1.2 \times 10^{-38} cm^4 s/photon = 1.2 \times 10^{12} GM$.

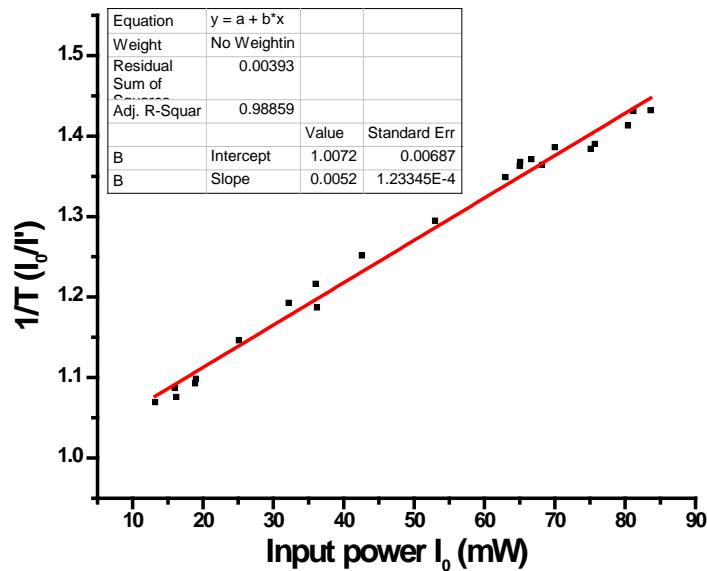


Figure 6.9 Plot of ZnTeO sample : input power I_0 verses $1/T$

6.4 Summary

In conclusion, ZnTeO thin film has exhibited enhanced absorbing and photoluminescent response to the solar spectrum in comparison to ZnTe. Sub-bandgap excitation experiments under 1380nm excitation demonstrate the two-photon response characteristic desired for intermediate band solar cells. The calculated two-photon cross-section of ZnTeO is as high as $1.2 \times 10^{12} \text{ GM}$. This observed two-photon phenomenon may serve as a basis for further efforts to develop ZnTeO and other dilute alloys or impurity materials for enhanced solar cell conversion efficiency.

There are also some further investigations on ZnTeO films that worth to explore. First of all, time-resolved fluorescence and transient absorption may provide an insight look on the energy and electron transport properties of these thin films. Secondly, based on concept of the up-conversion of sub-bandgap photons proposed by Trupke *et al.*⁴⁸, a layer of up-converting material can be added to the existing film. The predicted efficiency of the solar

cell are better than the original films, since reabsorbing process of up-converted emitting photons could happen in these films.

References

- [1]. Shockley, W.; Queisser, H. J., Detailed Balance Limit of Efficiency of P-N Junction Solar Cells. *Journal of Applied Physics* **1961**, 32 (3), 510-&.
- [2]. Luque, A.; Marti, A., Increasing the Efficiency of Ideal Solar Cells by Photon Induced Transitions at Intermediate Levels. *Physical Review Letters* **1997**, 78 (26), 5014-5017.
- [3]. Marti, A.; Antolin, E.; Linares, P. G.; Luque, A., Understanding Experimental Characterization of Intermediate Band Solar Cells. *Journal of Materials Chemistry* **2012**, 22 (43), 22832-22839.
- [4]. Wolf, M., Limitations and Possibilities for Improvement of Photovoltaic Solar Energy Converters .1. Considerations for Earths Surface Operation. *Proceedings of the Institute of Radio Engineers* **1960**, 48 (7), 1246-1263.
- [5]. Guttler, G.; Queisser, H. J., Impurity Photovoltaic Effect in Silicon. *Energy Conversion* **1970**, 10 (2), 51-&.
- [6]. Wurfel, P., Limiting Efficiency for Solar-Cells with Defects from a 3-Level Model. *Solar Energy Materials and Solar Cells* **1993**, 29 (4), 403-413.
- [7]. Keevers, M. J.; Green, M. A., Efficiency Improvements of Silicon Solar-Cells by the Impurity Photovoltaic Effect. *Journal of Applied Physics* **1994**, 75 (8), 4022-4031.
- [8]. Keevers, M. J.; Green, M. A., Extended Infrared Response of Silicon Solar Cells and the Impurity Photovoltaic Effect. *Solar Energy Materials and Solar Cells* **1996**, 41-2, 195-204.
- [9]. Brown, A. S.; Green, M. A., Impurity Photovoltaic Effect: Fundamental Energy Conversion Efficiency Limits. *Journal of Applied Physics* **2002**, 92 (3), 1329-1336.

- [10]. Yu, K. M.; Walukiewicz, W.; Wu, J.; Shan, W.; Beeman, J. W.; Scarpulla, M. A.; Dubon, O. D.; Becla, P., Diluted II-VI Oxide Semiconductors with Multiple Band Gaps. *Physical Review Letters* **2003**, *91* (24).
- [11]. Cuadra, L.; Marti, A.; Luque, A., Present Status of Intermediate Band Solar Cell Research. *Thin Solid Films* **2004**, *451*, 593-599.
- [12]. Seminovski, Y.; Palacios, P.; Conesa, J. C.; Wahnou, P., Thermodynamics of Zinc Insertion in CuGa_2Ti , Used as a Modulator Agent in an Intermediate-Band Photovoltaic Material. *Computational and Theoretical Chemistry* **2011**, *975* (1-3), 134-137.
- [13]. Bremner, S. P.; Honsberg, C. B.; Ieee, *Intermediate Band Solar Cell with Non-Ideal Band Structure under AM1.5 Spectrum*. Ieee: New York, 2012.
- [14]. Yu, K. M.; Walukiewicz, W.; Ager, J. W.; Bour, D.; Farshchi, R.; Dubon, O. D.; Li, S. X.; Sharp, I. D.; Haller, E. E., Multiband GaInP Quaternary Alloys. *Applied Physics Letters* **2006**, *88* (9).
- [15]. Gonzalez-Diaz, G.; Olea, J.; Martil, I.; Pastor, D.; Marti, A.; Antolin, E.; Luque, A., Intermediate Band Mobility in Heavily Titanium-Doped Silicon Layers. *Solar Energy Materials and Solar Cells* **2009**, *93* (9), 1668-1673.
- [16]. Wahnou, P.; Tablero, C., Ab Initio Electronic Structure Calculations for Metallic Intermediate Band Formation in Photovoltaic Materials. *Physical Review B* **2002**, *65* (16).
- [17]. Sanchez, K.; Aguilera, I.; Palacios, P.; Wahnou, P., Assessment through First-Principles Calculations of an Intermediate-Band Photovoltaic Material Based on Ti-Implanted Silicon: Interstitial Versus Substitutional Origin. *Physical Review B* **2009**, *79* (16).
- [18]. Wang, W. M.; Lin, A. S.; Phillips, J. D., Intermediate-Band Photovoltaic Solar Cell Based on ZnTe:O . *Applied Physics Letters* **2009**, *95* (1).
- [19]. Wang, W. M.; Lin, A. S.; Phillips, J. D.; Metzger, W. K., Generation and Recombination Rates at ZnTe:O Intermediate Band States. *Applied Physics Letters* **2009**, *95* (26).
- [20]. Wang, W.; Lin, A. S.; Phillips, J. D., Intermediate-Band Photovoltaic Solar Cell Based on ZnTe:O . *Applied Physics Letters* **2009**, *95* (1).

- [21]. Phillips, M. C.; Wang, M. W.; Swenberg, J. F.; McCaldin, J. O.; McGill, T. C., Proposal and Verification of a New Visible-Light Emitter Based on Wide Band Gap-II-VI Semiconductors. *Applied Physics Letters* **1992**, *61* (16), 1962-1964.
- [22]. Swenberg, J. F.; Wang, M. W.; Miles, R. J.; Phillips, M. C.; Hunter, A. T.; McCaldin, J. O.; McGill, T. C., Advances in the Development of Graded Injector Visible-Light Emitters. *Journal of Crystal Growth* **1994**, *138* (1-4), 692-696.
- [23]. Kang, Z. T.; Menkara, H.; Wagner, B. K.; Summers, C. J.; Durst, R.; Diawara, Y.; Mednikova, G.; Thorson, T., Oxygen-Doped ZnTe Phosphors for Synchrotron X-Ray Imaging Detectors. *Journal of Electronic Materials* **2006**, *35* (6), 1262-1266.
- [24]. Vaya, P. R.; Srinivasan, R.; Nsti, *Simulation Study of ZnTe-CdZnTe Based Asymmetric Step Strained Layer Quantum Well Infrared Photo-Detectors*. Computational Publications: Cambridge, 1999; p 377-379.
- [25]. Acharya, K. P.; Ullrich, B.; Erlacher, A., Responsivity of ZnTe/N-GaAs Heterostructures Formed by Infrared Nanosecond Laser Deposition. *Journal of Applied Physics* **2007**, *102* (7).
- [26]. Fishman, D. A.; Cirloganu, C.; Webster, S.; Padilha, L. A.; Monroe, M.; Hagan, D. J.; Van Stryland, E. W., Sensitive Mid-Infrared Detection in Wide-Bandgap Semiconductors Using Extreme Non-Degenerate Two-Photon Absorption. *Nature Photonics* **2011**, *5* (9), 561-565.
- [27]. Kasap, S. C., P., *Springer Handbook of Electronic and Photonic Materials*. Springer: 2007.
- [28]. Ferreira, S. O.; Sitter, H.; Faschinger, W.; Brunthaler, G., Growth of Highly Doped P-Type ZnTe Layers on GaAs Using a Nitrogen Dc Plasma-Cell. *Journal of Crystal Growth* **1994**, *140* (3-4), 282-286.
- [29]. Tao, I. W.; Jurkovic, M.; Wang, W. I., Doping of ZnTe by Molecular-Beam Epitaxy. *Applied Physics Letters* **1994**, *64* (14), 1848-1849.
- [30]. Brebrick, R. F., Deviations from Stoichiometry in Binary Ionic Crystals. *Journal of Physics and Chemistry of Solids* **1958**, *4* (3), 190-195.
- [31]. Mandel, G., Self-Compensation Limited Conductivity in Binary Semiconductors .1. Theory. *Physical Review a-General Physics* **1964**, *134* (4A), 1073-&.
- [32]. Hopfield, J. J.; Thomas, D. G.; Lynch, R. T., Isoelectronic Donors and Acceptors. *Physical Review Letters* **1966**, *17* (6), 312-&.

- [33]. Dietz, R. E.; Hopfield, J. J.; Thomas, D. G., Mirror Absorption and Fluorescence in ZnTe. *Physical Review Letters* **1962**, 8 (10), 391-&.
- [34]. Merita, S.; Kramer, T.; Mogwitz, B.; Franz, B.; Polity, A.; Meyer, B. K., Oxygen in Sputter-Deposited ZnTe Thin Films. In *Physica Status Solidi C - Current Topics in Solid State Physics, Vol 3, No 4*, Stutzmann, M., Ed. Wiley-Vch, Inc: New York, 2006; Vol. 3, pp 960-963.
- [35]. Nabetani, Y.; Okuno, T.; Aoki, K.; Kato, T.; Matsumoto, T.; Hirai, T., Epitaxial Growth and Optical Investigations of ZnTe Alloys. *Physica Status Solidi a-Applications and Materials Science* **2006**, 203 (11), 2653-2657.
- [36]. Wang, W. Intermediate Band Solar Cells Based on ZnTe. University of Michigan, 2010.
- [37]. McLaurin, E. J.; Greytak, A. B.; Bawendi, M. G.; Nocera, D. G., Two-Photon Absorbing Nanocrystal Sensors for Ratiometric Detection of Oxygen. *Journal of the American Chemical Society* **2009**, 131 (36), 12994-13001.
- [38]. Karatay, A.; Aksoy, C.; Yaglioglu, H. G.; Elmali, A.; Kurum, U.; Ates, A.; Gasanly, N., The Nonlinear and Saturable Absorption Characteristics of Ga_{0.90}In_{0.10}Se and Ga_{0.85}In_{0.15}Se Semiconductor Crystals and Their Amorphous Thin Films. *Journal of Optics* **2011**, 13 (7).
- [39]. Cui, H. Y.; Li, Z. F.; Ma, F. J.; Chen, X. S.; Lu, W., Two-Photon Absorption Coefficient Spectra of Indirect Transitions in Silicon. *Acta Physica Sinica* **2010**, 59 (10), 7055-7059.
- [40]. Kadlec, F.; Nemeč, H.; Kuzel, P., Optical Two-Photon Absorption in GaAs Measured by Optical-Pump Terahertz-Probe Spectroscopy. *Physical Review B* **2004**, 70 (12).
- [41]. Vanstryland, E. W.; Vanherzeele, H.; Woodall, M. A.; Soileau, M. J.; Smirl, A. L.; Guha, S.; Boggess, T. F., 2 Photon-Absorption, Nonlinear Refraction, and Optical Limiting in Semiconductors. *Optical Engineering* **1985**, 24 (4), 613-623.
- [42]. Said, A. A.; Sheikbaha, M.; Hagan, D. J.; Wei, T. H.; Wang, J.; Young, J.; Vanstryland, E. W., Determination of Bound-Electronic and Free-Carrier Nonlinearities in ZnSe, GaAs, CdTe, and ZnTe. *Journal of the Optical Society of America B-Optical Physics* **1992**, 9 (3), 405-414.
- [43]. Dakovski, G. L.; Shan, J., Size Dependence of Two-Photon Absorption in Semiconductor Quantum Dots. *Journal of Applied Physics* **2013**, 114 (1).

- [44]. Wang, W.; Bowen, W.; Spanninga, S.; Lin, S.; Phillips, J., Optical Characteristics of ZnTe Thin Films Synthesized by Pulsed Laser Deposition and Molecular Beam Epitaxy. *Journal of Electronic Materials* **2009**, *38* (1), 119-125.
- [45]. Schneider, M.; Tews, H.; Legros, R., Oxygen Diffusion in ZnTe During Laser Annealing. *Journal of Crystal Growth* **1982**, *59* (1-2), 293-296.
- [46]. Sutherland, R. L., *Handbook of Nonlinear Optics*. Marcel Dekker, INC.: New York 2003.
- [47]. Marple, D. T. F., Refractive Index of ZnSe, ZnTe, + CdTe. *Journal of Applied Physics* **1964**, *35* (3P1), 539-&.
- [48]. Trupke, T.; Green, M. A.; Würfel, P., Improving Solar Cell Efficiencies by up-Conversion of Sub-Band-Gap Light. *Journal of Applied Physics* **2002**, *92* (7), 4117-4122.

CHAPTER 7

OVERALL SUMMARY AND FUTURE DIRECTION

7.1 Overall Summary

Significant efforts have been made during the past a few years to surpass technological and material barriers in order to develop organic photovoltaic devices with improved power conversion efficiency and affordable cost. My thesis focuses on understanding the structure function relationship of OPV candidates utilizing various spectroscopy methods including steady state, two-photon absorption, and ultrafast nonlinear optical spectroscopy techniques. The steady state absorption and emission spectroscopy can reveal a wealth of information such as absorption extinction coefficients, quantum yield, and energy transfer efficiency. Two-photon absorption cross-section provides information about the ground and excited state transition dipole moments, changes in dipole moment term and therefore can be used to evaluate the charge transfer character. Fluorescence up-conversion provides information on exciton/energy migration dynamics and geometry of emitting states. Transient absorption spectroscopy has been widely used to study the nature of excited states in solar cells. This technique allows us to monitor all steps of device operations, such as absorption, exciton diffusion and dissociation, charge transport and charge collection. Understanding energy transfer and charge transfer processes has been crucial to tailoring structure of SQ based potential OPV materials, deeply understanding the photophysical and charge transfer properties, and guiding new research of designing novel OPV materials.

The main materials studied are chromophore substituted silsesquioxane derivatives. The background of silsesquioxanes is presented in Chapter 1. Major advantages offered by SQ core include enhanced thermal stability and improved mechanical properties. SQ materials studied were discussed in Chapter 3 and 4. There are three sets of SQ samples studied in this work, including octavinylstilbeneSQ derivatives, polyfunctional phenylSQ derivatives, and partial and full SQs. The basic characteristic properties, steady state properties, and two-photon absorption measurements of first two sets of SQ systems were discussed in Chapter 3. The UV-Vis and fluorescence emission spectra of the $[R'\text{-vinylStilbeneSiO}_{1.5}]_8$ compounds reveals exceptional red shifts, especially when a strong electron donating group, $R' = \text{NH}_2$ (120 nm) is introduced to the end of the chromophores. This large shift as well as excellent two photon absorption properties (up to 810GM when $R' = \text{NH}_2$) give evidence of the strongly enhanced charge transfer character among these systems. According to the linear and nonlinear optical study, both absorption property and charge transfer characters are significantly improved when strong electronic coupling of multichromophore takes place in a single nanostructure. Eventually, these enhancements could improve the power conversion efficiency.

Secondly, three sets of stilbene SQ derivatives: *o*-RStyr₈OPS, RStyr₁₆OPS, and RStyr₂₄OPS, [R = 4-methyl (Me), Boc-protected 4-amino (NBoc), or 4-acetoxy (Ace)], were studied in order to understand structure function relationship with increasing number of chromophores within one macrostructure. Mixtures of species with different numbers of chromophore substitutes are found in each system. These mixtures have great influence on absorption and fluorescence emission spectra, and cause broadening and multiple peaks of the absorption and emission bands. Interesting features in absorption spectra are also found. RStyr₁₆OPS exhibits blue shifted absorption spectra with respect to the RStyr₂₄OPS. Similar trends are also found in free dyes, which is caused by the steric interactions among the substituted chromophores. Relatively high two-photon cross-section values and TPA cross-section per chromophore values are found in NBocStyr₂₄OPS and AceStyr₂₄OPS. These results suggest that charge transfer character of the molecule could be dramatically enhanced by increased chromophore density in a

single nanostructure. This idea can be used to design molecular structure with better power conversion efficiency yield.

The photophysical properties of partial cages [*p*-Me₂NStilSi(OSiMe)₃] (corner) and [*p*-Me₂N-StilSi(OSiMe)]₄ (half), as well as full cage [*p*-Me₂NStil₈SiO_{1.5}]₈ (cube) are presented in Chapter 4. The emissions of all investigated SQs are greatly red-shifted with respect to the single chromophore, whereas the ground state UV-Vis absorptions are not significantly changed. The cube shows interesting red-shifted emissions (20nm) compared to dimethylaminostilbene, suggesting that the electronic coupling takes place within the chromophores and thus the excited state energy level is decreased. Similar observations are also found in half system. The theoretical calculation results suggest that 3-D symmetric LUMO involves contributions from all Si, oxygen atoms and the organic substituents. Two-photon absorption cross-section results suggest that the cube system (26 GM per chromophore) offer better charge transfer character with respect to the corner and half.

Energy transfer processes and excited state behavior of corner, half and cube are also discussed in Chapter 4. Fluorescence up-conversion measurements provide us an insight look into energy transfer process in these three systems. The kinetics results indicate that the twisting around the double bond of the substituted stilbene is more sensitive to the degree of its dipole moment than the size of its substitutes. In the case of corner, the twisting is retarded by the steric hindrance effect compared to stilbene free dye. In the case of half and cube, strong dipole moments are induced by the substitution which could facilitate the twisting process, overcome the steric hindrance effect and decrease the fluorescence lifetime. The ultrafast fluorescence anisotropy decay suggests substantial contribution of a coherent type interchromophore energy transport mechanism in the half and cube systems. The dynamics of the transient absorption show significant differences between the corner, and the half and cube. The pump-probe measurements have shown the presence of TICT state in 500nm-600nm region. The lifetimes of this emissive TICT state corresponds well with fluorescence lifetime of each system respectively. The transient absorption results also reveal a combination of charge transfer

dynamics and solvation process associated with excited-state absorption blue shifts, and resulting a solvent stabilized non emissive TICT' state. Ultrafast transient measurement have shown interesting trend with respect to the amount charge-transfer character with increasing number of chromophores. Both half and cube show enhanced charge transfer character compared to corner. This also explains the enhanced two-photon cross-section per chromophore in the half and cube systems. Upon photoexcitation, transient absorption measurements have shown the presence of a charge-transfer (TICT) state depending on the number of chromophores, suggesting the ultrafast delocalization of charge in half and cube systems.

Besides the silsesquioxanes derivatives, a series of core-shell system, dendritic oligothiophene-perylene bisimides, were investigated as promising candidate for heterojunction light-harvesting materials. The results are presented in Chapter 5. The TPA cross-sections in the NIR spectral region were measured. Ultrafast energy transfer and electron transfer from the thiophene dendrons to perylene core has been characterized and compared to model compounds. Charge separated states were observed under ultrafast transient absorption measurements with formation of perylene anion radical at ~ 700 nm and thiophene cation radical near 500 nm. The size of the thiophene dendron shell has a big influence on the excited-state energy and electron transfer mechanism. In contrast to G0 and G1, G2 has larger substitutes attached to the bay area of perylene. Therefore, the torsional twist around the center of the perylene is increased, and results strongly overlapping of the thiophene dendrons. Charge recombination of G2 is also observed. This can be explained by the PBI core lost its electron trapping ability caused by twisting. Due to this conformational effect, the excitation is delocalized throughout the thiophene dendrons. In the case of G2, both coherent energy transfer and Förster resonance energy transfer mechanisms contribute the energy transfer processes. Among the three generations studied, G1, which has the best two-photon cross section and the most efficient energy transfer (69%), is the best light harvesting material. As a result, both the strength and size of the electron donor have to be taken into account when building up perylene based architectures for their application in the organic photovoltaic area.

Other than organic photovoltaic systems, intermediate band ZnTeO thin films were also investigated (Chapter 6). Two-photon transmission experiment is designed with sub-bandgap excitation under 1550 nm excitation, and it demonstrates the two-photon response characteristic desired for these thin films. The two-photon investment of intermediate band solar cell can be utilized as a basis for developing dilute alloys or impurity materials with low costs for enhanced solar cell power conversion efficiency.

7.2 Future Direction

The technologies of the solar cell based on silsesquioxanes derivatives and other organic macromolecules are very promising but still in the early research stage. To make it competitive with other mature solar cell technologies, the following topics are worth exploring and developing.

Solid state measurements and real device applications

Currently all of our investigations are performed in the solution. To drive the research towards OPVs applications, it is very necessary to perform optical studies on the organic materials investigated in my research in solid state, such as thin films. In the solid state, the molecules are closely packed and therefore the interaction between the molecules is much stronger than the liquid phase. These phenomena could cause the photophysical properties that could be quite different than what is observed in solution phase.

Method of thin films deposition is crucial to the photovoltaic characteristics in solid state measurement. For example, it is well known that the perylene bisimides studied in this research are capable of forming self-assembled π -stacking nanostructures, as well as possessing liquid crystalline behaviors. It has been demonstrated that both crystallinity and photovoltaic performance can be affected by annealing time and temperature and type of solvents. To the best of our knowledge, a study of SQ

performance in OPV films has not been reported yet. It is very difficult to make a film using SQs.

Another possible approach to improving the power conversion efficiencies of the solid state device is increasing the electrical conductivity of organic materials by improving the crystal structure in solid state. Crystalline organic materials exhibit better charge transport capabilities than amorphous organic materials.

The properties and characterization methods that worth carrying out in the solid state include two-photon cross-section (fluorescence and transmission methods), time-resolved absorption and photoluminescence, dielectric constant, charge carrier mobility, conductive AFM, and electron tomography.

Optimizations of the band gaps with tailoring chromophore structures

The main contribution of my research is utilizing the linear and nonlinear optical technologies to understand structure function relationship in order to design and develop novel materials for solar cell applications. SQ nanostructured chemicals are hybrid organic–inorganic structures, monodispersed in size, consisting of a silicon oxide cage with a corona of organic substituents. It has been demonstrated that by introducing organic chromophores into the SQ cage, the band gap of the SQ hybrid can be dramatically lowered. The idea of designing and tailoring the organic shell on the SQ cage with a wide range of well-known light harvesting chromophores/oligomers gives the possibility for seeking candidates competitive to current state-of-the-art OPVs materials. Functionalizing SQ with conjugating polymers, oligomer or dendrimer might provide enhanced OPV characteristics. It has been reported that silsesquioxane molecules can facilitate the electron transfer and enhance current density when attached to semiconducting polymers.¹⁻² Some suggested functional structures worth exploring are illustrated in Figure 7.1. It will be very interesting to incorporate low band gap polymers into SQs, such as polythiophene and P3HT. Besides the possibility of improving the band gap, unique crystal structure might facilitate the charge transfer efficiency. For example,

a 2-dimensional crystallization of the SQ-macromer has been obtained, as illustrated in Figure 7.2. In addition, introducing rigid planar shape chromophores, such as perylene bisimides(PDI) derivatives could lead to a potential π -stacking aggregation and/or liquid crystalline behavior, as illustrated in Figure 7.3a. Another idea is using SQs as organic linkers for silsesquioxane-based polymers, as presented in Figure 7.3b. Varying the molecular structures and lengths of the organic linkers should provide us the ability to tailor the photophysical properties of the SQ based polymers, and thus giving access to multiple possible applications for this new set of materials.

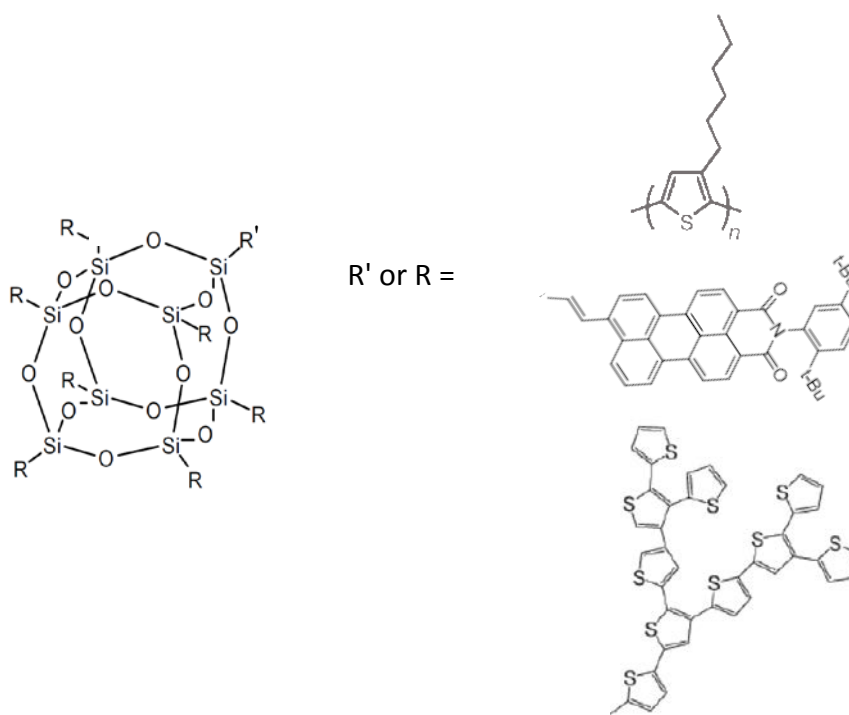


Figure 7.1 Proposed substituted chromophores

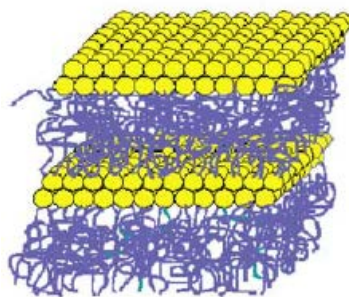


Figure 7.2 A model of the 2-D crystallization of the POSS macromers³

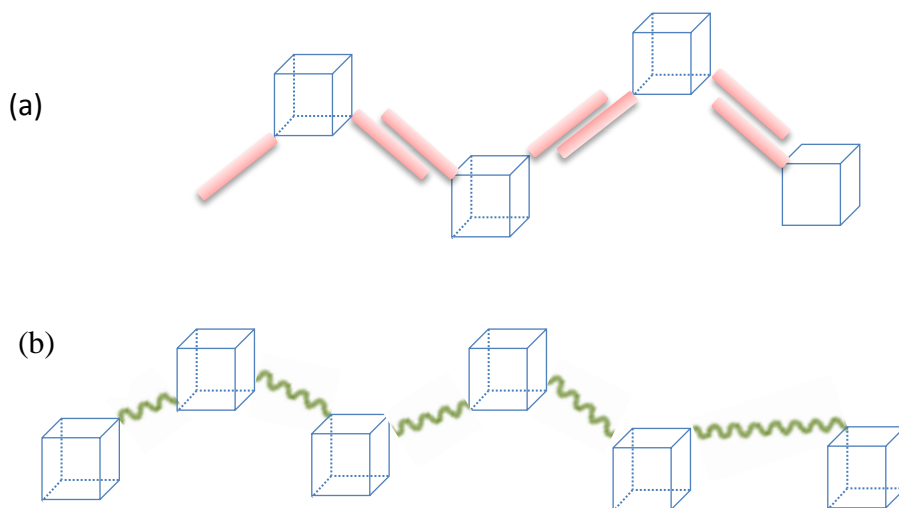


Figure 7.3 Schematic drawings of (a) silsesquioxane with π -stacking chromophores (b) silsesquioxane polymer

SQ-enhanced phase separation in bulk heterojunction photovoltaic systems

SQ materials can also be served as dispersing agents for organic and metallic nanoparticles. It has been reported that SQs can be used to obtain the desired nanostructure of polymeric matrices and develop performance improvements of solid state thin films.⁴⁻⁷ This can be achieved by altering the organic functional groups

substituted on the SQs, and incorporating it to the polymeric materials. In this way, one can control and modify the morphology, crystallinity and phase dispersion in polymeric blend systems. For example, polydimethylsiloxane (PDMS), a linear, long-chain macromolecule with siloxane backbone structure was incorporated into a low band gap polymer blend as bulk heterojunction solar cells.⁸ Advantages of utilizing PDMS additives include increasing J_{sc} by 50%, improving device power conversion efficiency by 70% and significantly reducing cell-to-cell variation.⁹ Small molecule SQ based additives with excellent miscibility also have been used to improve the performance of organic photovoltaic cells by controlling the morphology during the solvent evaporation process.¹⁰ However, unlike the rigid SQ molecules, they are removed during solvent evaporation process and cannot provide additional structural rigidity to the solid blends. Incorporation of SQ molecules may result in enhanced OPV performance. Therefore, developing of a full understanding of the nano scale morphology and mechanism of interaction between these complex blends is still very challenging and worth exploring.

References

- [1]. Xiao, S.; Nguyen, M.; Gong, X.; Cao, Y.; Wu, H. B.; Moses, D.; Heeger, A. J., Stabilization of Semiconducting Polymers with Silsesquioxane. *Advanced Functional Materials* **2003**, *13* (1), 25-29.
- [2]. Lee, J.; Hong, C. K.; Choe, S.; Shim, S. E., Synthesis of Polystyrene/Silica Composite Particles by Soap-Free Emulsion Polymerization Using Positively Charged Colloidal Silica. *Journal of Colloid and Interface Science* **2007**, *310* (1), 112-120.
- [3]. Phillips, S. H.; Haddad, T. S.; Tomczak, S. J., Developments in Nanoscience: Polyhedral Silsesquioxane (Poss)-Polymers Oligomeric. *Current Opinion in Solid State & Materials Science* **2004**, *8* (1), 21-29.
- [4]. Mattori, M.; Mogi, K.; Sakai, Y.; Isobe, T., Studies on the Trapping and Detrapping Transition States of Atomic Hydrogen in Octasilsesquioxane Using the Density Functional Theory B3lyp Method. *Journal of Physical Chemistry A* **2000**, *104* (46), 10868-10872.

- [5]. Jimenez, R.; Dikshit, S. N.; Bradforth, S. E.; Fleming, G. R., Electronic Excitation Transfer in the Lh2 Complex of Rhodobacter Sphaeroides. *Journal of Physical Chemistry* **1996**, *100* (16), 6825-6834.
- [6]. Becker, H. C.; Kilsa, K., Size- and Solvent-Dependent Kinetics for Cis-Trans Isomerization in Donor-Acceptor Systems. *Spectrochimica Acta Part a-Molecular and Biomolecular Spectroscopy* **2009**, *72* (5), 1014-1019.
- [7]. Rice, J. K.; Baronavski, A. P., Ultrafast Studies of Solvent Effects in the Isomerization of Cis-Stilbene. *Journal of Physical Chemistry* **1992**, *96* (8), 3359-3366.
- [8]. Doany, F. E.; Hochstrasser, R. M.; Greene, B. I.; Millard, R. R., Femtosecond-Resolved Ground-State Recovery of Cis-Stilbene in Solution. *Chemical Physics Letters* **1985**, *118* (1), 1-5.
- [9]. Furgal, J. C.; Jung, J. H.; Goodson, T.; Laine, R. M., Analyzing Structure-Photophysical Property Relationships for Isolated T-8, T-10, and T-12 Stilbenevinylsilsesquioxanes. *Journal of the American Chemical Society* **2013**, *135* (33), 12259-12269.
- [10]. Fujiwara, T.; Lee, J. K.; Zgierski, M. Z.; Lim, E. C., Intramolecular Charge Transfer in the Excited State of 4-Dimethylaminobenzaldehyde and 4-Dimethylaminoacetophenone. *Chemical Physics Letters* **2009**, *481* (1-3), 78-82.

APPENDIX I: MAITAI LASER CLEANING PROCEDURE

1. Set the MaiTai output wavelength to 800 nm, select *current* mode on the operation program and set the current to 70%.
2. Turn *PZTs OFF* from the operation menu and set their positions to 50:50.
3. Unscrew the outside cover of the MaiTai and open it.
4. Release the drying tube, which is located on the right side of the MaiTai.
5. Unscrew the MaiTai inside cover near the TPA setup.
6. Wear gloves.
7. Clean all the optics and the crystal with methanol (ACS spectrophotometric grade, >99.8%).
8. Place the inside cover back.
9. Check the color of the drying tube. It needs to be replaced if the color of the whole tube turns purple.
10. Place the drying tube back to its original position.
11. Turn *PZTs back ON* from the operation menu.
12. Dial the current back up to 100% step by step and then switch back to green power mode after stabilizing for about 15 mins.

APPENDIX II: RESET MAITAI PZTS POSITION

1. Start MaiTai and warm it up.
2. Set the output wavelength of MaiTai to 800 nm from the operation menu.
3. Turn *PZTs OFF* from the MaiTai operation menu and set PZTs positions to *50:50*.
4. Open the outside cover of the MaiTai box and release the drying tube.
5. Open the left side of the MaiTai inside cover only which is near output beam.
6. Open *RF controls* menu on the computer program, and find the values for *Fast Photodiode (FP)*; Open the *PZT controls*, and look at values for the *PZT positions (PP)* and *Qcell sum (QS)*.
7. Inside the MaiTai cavity, adjust the x and y positions of M_3 and P_2 mirror according to the Figure A 1, in order to increase the value of FP and QS. In the meantime, try to reach *PZTs positions* to *50:50*.
8. Adjust *slit*, *slit width* and *prism* from the MaiTai operation menu to obtain a Gaussian spectrum.
9. Repeat step 7 and 8 until both *FP* and *PP* reaching their maximum values together.
10. Put inside cover of the MaiTai back and put the drying tube back into place.
11. Cover the box of MaiTai.
12. Turn PZTs back on.

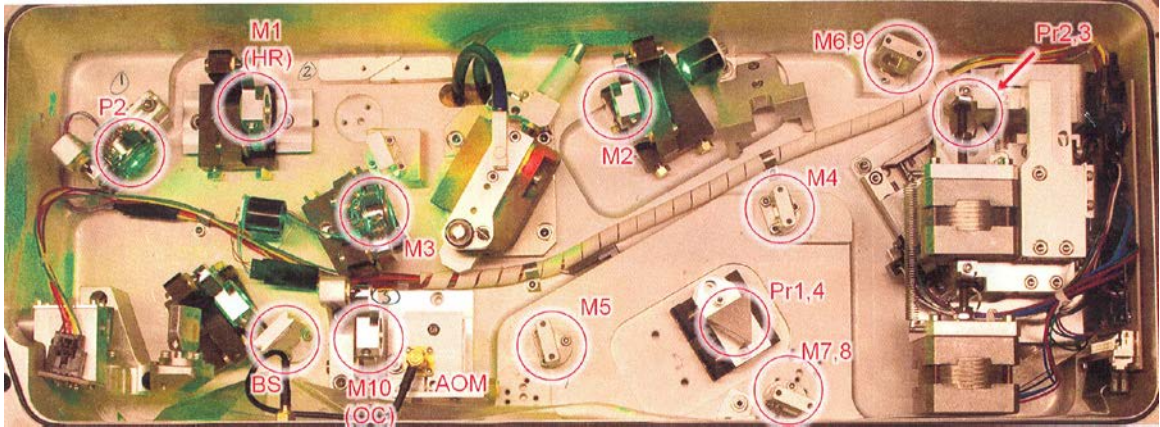


Figure A. 1 Cavity layout of MaiTai laser.

APPENDIX III: OPERATION PROCEDURE OF FEMTOSECOND SYNCHRONOUSLY PUMPED OPTICAL PARAMETERIC OSCILLATOR (OPAL)

To turn the system on,

1. Turn on the pump laser, MaiTai, and warm it up. At the same time, turn on the Opal electronics modules if it is not already on.
2. Check the MaiTai laser for power and mode. According to Table A. 1, set it to a wavelength appropriate for driving the Opal at the chosen wavelength.
3. Adjust the MaiTai output power to about 2W.
4. Set the Opal for normal operation. Select the *Setup* menu and run *Scan Length* to establish oscillation and perform a quick calibration of the Opal.
5. Use a spectrometer to measure the Signal wavelength. Recalibrate the wavelength if the wavelength shown on the Main menu is off by more than $\pm 3\text{nm}$.
6. To optimize the pulse width of the signal, use the *Adjust Temp* menu and make small temperature adjustments while monitoring the pulse width.
7. Adjust M_1 output coupler and optimize the output power from the Opal, regarding to Figure A. 2.

Table A. 1 Typical settings for several Opal wavelengths

Pump Wavelength (nm)	Opal Wavelength (μm)
750	1.1-1.2
775	1.2-1.35
810	1.4-1.6

If the system has not been used for a long time or if alternate wavelength ranges are desired,

1. Find the MaiTai and Opal cavity match point using the *Scan Length* function on the *Setup* menu.
2. Change the MaiTai pump wavelength.
3. Change the temperature of the crystal to optimize the performance at a given wavelength using the *Adjust Temp* menu.
4. Change optics sets to accommodate the desired Signal and Idler wavelength ranges. For this, Pr_1 and Pr_2 might need to be moved in or out of the beam, and the output coupler M_I might have to be adjusted to optimized cavity length.

To turn the system off,

1. Set the Opal to *Idle* mode from the *Configure* menu and leave the electronics on.
2. Turn off the MaiTai laser.

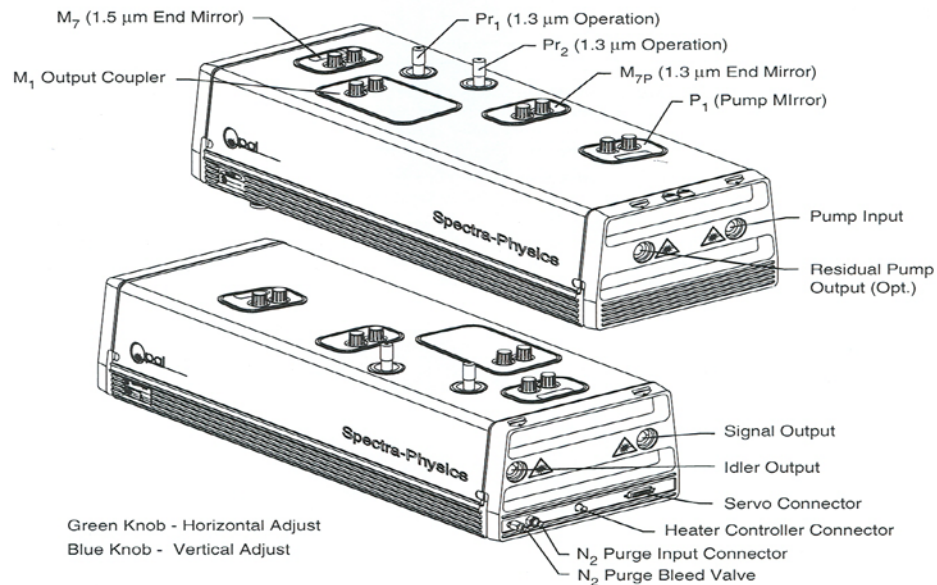


Figure A. 2 Opal head controls and connection

APPENDIX IV: OPAL ALIGNMENT PROCEDURE

Part I: Initial setup. All mirrors inside the Opal cavity are labeled in Figure A. 3

1. Set the MaiTai pump power to minimum.
2. Open the Opal shutter and verify the beam from MaiTai is centered on P_1 .

Part II: In this part, red beam from MaiTai is used.

3. Replace the output coupler M_1 mirror with 100% high reflector mirror.
4. Set the wavelength of MaiTai to 810nm and minimize the output power (with red color beam output but no pulsing).
5. Put away the *Waveplate* inside the Opal cavity.
6. Adjust the red beam to the center of P_1 using the big pinhole tool.
7. Adjust P_1 horizontally and vertically to direct the pump beam onto the center of P_2 .
8. Adjust P_2 horizontally and vertically in order to center the beam of P_3 and let the beam go through the center of iris I_1 in the meantime. Close the iris a little to verify the beam is centered. Repeat *Step 7-8* if necessary, until this condition is achieved.
9. Adjust P_3 horizontally and vertically to direct the beam onto the center of P_4 .
10. Adjust P_4 to direct the beam go through the *Crystal Assembly* and then reach the center of M_3 .
11. Adjust M_3 in order to center the beam on M_4 . Repeat *Step 10-11* until the pump beam goes through the crystal and is centered on the intracavity surfaces of M_3 and M_4 .
12. Observe the beam entering the crystal. If a bright spot on the surface of the crystal is observed, it is a high scattering site due to a surface flaw or burn. Then translate

the crystal slightly to an area that produces the least amount of reflectance. The beam should be close to the center of the crystal.

Part III: In this part, blue beam from MaiTai is used.

13. Adjust the pump power of MaiTai back to 12W, tune the wavelength to 810 nm and increase its output power to 2W.
14. Slide the *Waveplate* into the beam path.
15. Open iris I_1 all the way.
16. Rotate the *Waveplate* until the reflected beam from the front surface of the crystal has minimum intensity.
17. Adjust M_2 to direct the blue beam reach the center of M_1 , and then adjust M_3 to let the blue beam go through the center of the front face of iris I_2 , and reach the center of M_2 . Repeat this step until the blue beam goes through the center of I_2 and M_1 .
18. Adjust M_1 vertically and horizontally to direct the blue beam reflected from M_1 through the center of iris I_2 .
19. Fully open iris I_2 .
20. Adjust M_4 in order to direct the blue beam through the center of iris I_3 and onto the center of M_5 . Close I_3 a little to verify the beam is centered. Once centered, open it fully.
21. Adjust M_4 to direct the blue beam on the center of M_6 .
22. Adjust M_6 to center the blue beam onto the center of high reflector M_7 .
23. Adjust M_7 to let the reflected beam go back through I_3 . Repeat this step. Slightly close iris I_3 each time and observe the rear side of I_3 . Using small increments, adjust to center the reflected blue beam on the rear side of the iris. Open the iris fully when completed.
24. Fully open I_3 .
25. Adjust M_7 to direct the reflected blue beam from M_7 go through the center of iris I_2 .

Part IV: Remove the *Waveplate*, set the output wavelength of MaiTai to 775nm and set the crystal temperature of the OPAL to 55%.

26. Make sure using the high reflector on M_1 .
27. Move the motor position by hand carefully and try to obtain a flash from the *Crystal Assembly*.
28. If the flash is not obtained, repeat *Part II* and *Part III*.
29. Once catching a flash, go the OPAL control panel. From *Main Menu*, select *Configuration* and then choose *Manuel Control*. Adjust the *Motor Position* to the place where flash is observed.
30. Optimize the intensity of flashing by adjusting M_1 and M_7 .
31. Close I_3 a little bit each time. Let the beam go through the I_3 by adjusting M_1 and M_7 . Repeat this step several times until the red beam is fully centered through I_3 .
32. Replace the high reflector on M_1 back to the original mirror and try to catch a flash. If the flash is not observed, repeat from *Part III*.

Part V: Reset and calibrate Opal

33. After catching a flash using the original mirror on M_1 , cover the cavity of Opal carefully.
34. Go to the OPAL control panel. From the *Main Menu*, choose *Setup*.
35. Set the *Scan Length* to 1300nm manually.
36. Run *Scan Length* from the *Setup* menu again.
37. Select *Adj Temp* from *Main Menu*. Adjust the temperature offset up and down to optimize signal output power and stability. Optimum stability is achieved when *Temp Offset* is 0.5 to 1.0% below maximum power operation.

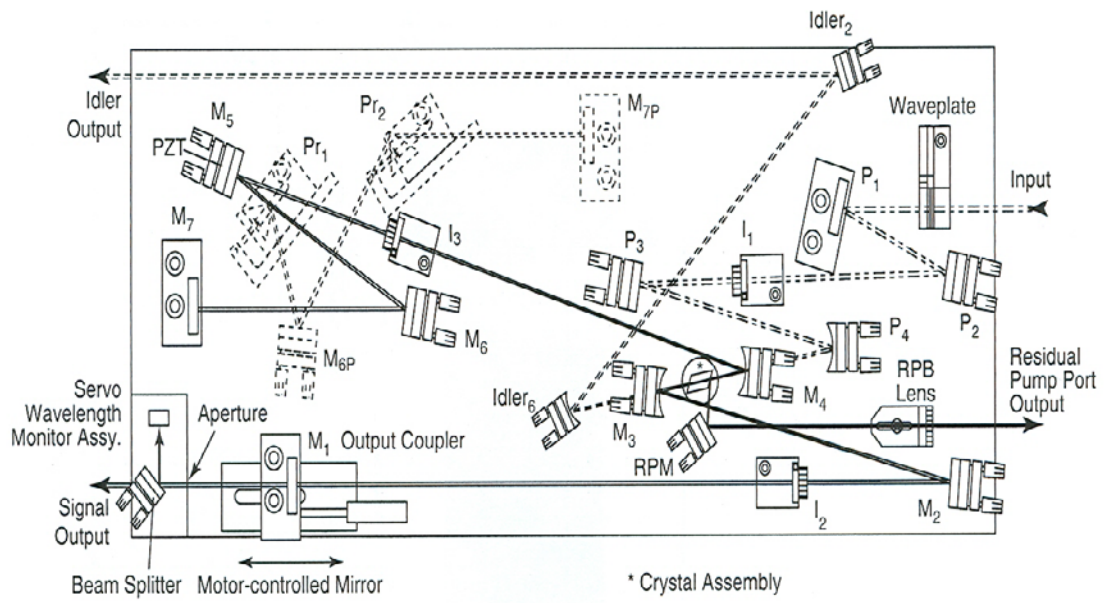


Figure A. 3 The cavity layout of Opal